Acta Universitatis Tamperensis 2391

MEERI MÄKINEN

Functionality of Brain in a Dish

Methods and study of electrophysiological phenomena in human pluripotent stem cell-derived neural networks

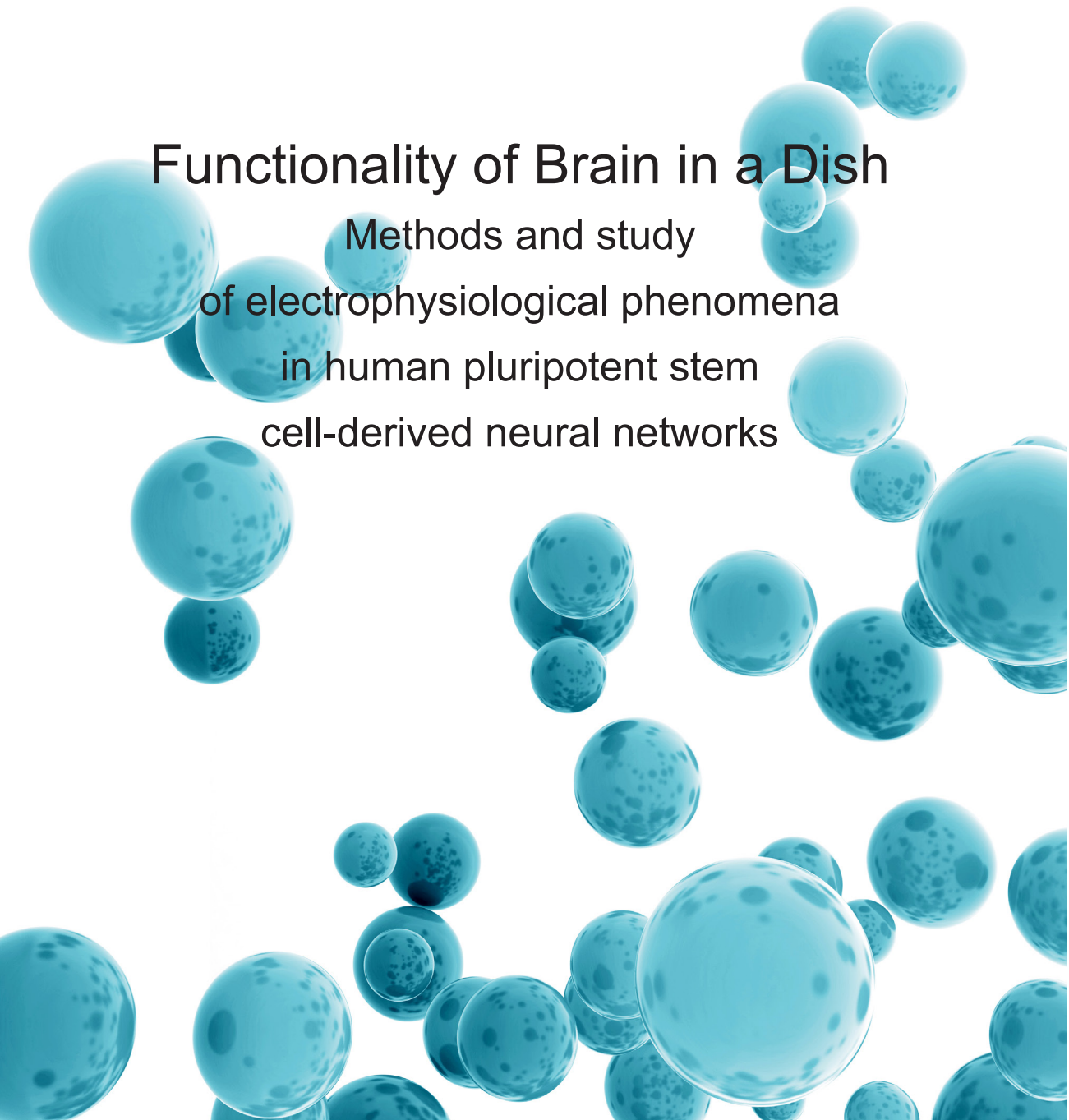

MEERI MÄKINEN

Functionality of Brain in a Dish

Methods and study of electrophysiological phenomena in human pluripotent stem cell-derived neural networks

■

ACADEMIC DISSERTATION
To be presented, with the permission of
the Faculty Council of the Faculty of Medicine and Life Sciences
of the University of Tampere,
for public discussion in the Jarmo Visakorpi auditorium
of the Arvo building, Arvo Ylpön katu 34, Tampere,
on 20 July 2018, at 12 o'clock.

UNIVERSITY OF TAMPERE

MEERI MÄKINEN

Functionality of Brain in a Dish

Methods and study of electrophysiological phenomena in human pluripotent stem cell-derived neural networks

Acta Universitatis Tamperensis 2391
Tampere University Press
Tampere 2018

UNIVERSITY
OF TAMPERE

ACADEMIC DISSERTATION
University of Tampere, Faculty of Medicine and Life Sciences
Finland

Supervised by
Supervised by
Docent Susanna Narkilahti
University of Tampere
Finland
PhD Laura Ylä-Outinen
University of Tampere
Finland

Reviewed by
Assistant Professor Joost le Feber
University of Twente
The Netherlands
Docent Sari Lauri
University of Helsinki
Finland

The originality of this thesis has been checked using the Turnitin OriginalityCheck service in accordance with the quality management system of the University of Tampere.

Cover design by
Mikko Reinikka

Acta Universitatis Tamperensis 2391
ISBN 978-952-03-0776-9 (print)
ISSN-L 1455-1616
ISSN 1455-1616

Acta Electronica Universitatis Tamperensis 1900
ISBN 978-952-03-0777-6 (pdf)
ISSN 1456-954X
http://tampub.uta.fi

Suomen Yliopistopaino Oy – Juvenes Print
Tampere 2018

"… (as any youthful study, it was poor and inclomplete, but demonstrated good intentions and a love of research) …"

~ Santiago Ramón y Cajal

ABSTRACT

The brain consists of electrically active circuits that carry out the functions of human cognition. These circuits are formed during development via structural and functional brain development. Our understanding of how the functional aspect arises from the cellular components remains incomplete. *In vitro* neuronal networks derived from human pluripotent stem cells (hPSCs) can be harnessed to repeat several key steps of structural brain development. Furthermore, hPSC-derived neurons are able to capture the development of functionality on an individual level and have been shown to display features of network activity.

The aim of this thesis was to aid the understanding of human specific cellular physiology underlaying network activity formation during neural development and generation of abnormal brain functions by studying the spontaneous emergence of network activity patterns in hPSC-derived neural networks. For studying the immature physiological properties of hPSC-derived neurons in the context the emerging network activity patterns, new experimental and analytical tools were developed.

In this thesis, hPSC-derived neural networks were characterized on morphological and molecular levels to ensure the generation of neural cells. Furthermore, the emergence of network activity patterns and the underlaying single neuron activity was investigated with microelectrode arrays (MEAs), calcium imaging and patch-clamp technique. To enhance the recordings of neural activity the effects of area and volume restriction by microfluidic devices were investigated. To asses the physiological properties of single neurons in the context the emerging network activity patterns, calcium imaging was combined with MEA measurements while performing pharmacological manipulations. Furthermore, new analytical tools for improving activity detection on MEAs and for collecting large scale single cell activity data from calcium imaging were developed and tested.

The activity measurements of hPSC-derived neural networks were found to be improved by restricting the growth area and volume. The developed analysis methods allowed two powerful measurement methods to be combined, providing improved temporal and spatial resolution. Furthermore, the hPSC-derived

networks were found to recapitulate general as well as species-specific features and mechanisms of network activity pattern development.

In conclusion, hPSC-derived networks in combination with the developed tools will be a valuable system for unraveling the detailed mechanisms of the formation of abnormal brain functions in the future studies.

TIIVISTELMÄ

Ihmisaivot koostuvat sähköisesti aktiivisista verkostoista. Nämä verkostot ovat aivotoimintamme perusta ja ne saavat alkunsa jo ennen syntymää. Aivojen kehityksen aikana ensimmäiset verkostot muodostuvat yksittäisistä hermosoluista. Samaan aikaan aivojen rakenne ja sähköinen toiminta muuttuvat vaiheittain. Emme kuitenkaan täysin ymmärrä kuinka yksittäisten hermosolujen toiminta johtaa aivotoimintaan. Tätä voidaan tutkia laboratoriossa, kasvattamalla hermosoluja ihmisperäisistä kantasoluista. Näin kasvatetut hermosolut muistuttavat ominaisuuksiltaan hermosoluja, joita voidaan löytää kehittyvistä aivoista eri vaihessa. Tämän lisäksi ihmisperäisistä kantasoluista tuotetut hermosolut kykenevät tuottamaan sekä yksittäin, että verkostona sähköistä aktiivisuutta.

Tämän väitöskirjan tavoitteena oli tutkia tarkemmin miten ja millaista sähköistä aktiivisuutta ihmisperäisistä kantasoluista kasvatetuissa hermoverkoissa muodostuu ja näin auttaa meitä tulevaisuudessa ymmärtämään kuinka aivotoiminta muodostuu terveissä ja sairaissa aivoissa. Tavoitteena oli myös selvittää eroja ihmisen ja eläinten aivotoiminnan kehittymisen välillä. Jotta hermosolujen kehittyviä sähköisiä ominaisuuksia voitiin seurata samaan aikaan kun mitattiin laajemman verkoston ominaisuuksia, kehitettiin väitöskirjassa uusia koe- ja analyysityökaluja.

Tässä väitöskirjatyössä varmistettiin ensin, että ihmisperäisistä kantasoluista kasvatetut solut todellakin olivat hermosoluja. Tämä suoritettiin tarkastelemalla solujen muotoa, sekä niissä esiintyviä proteiineja. Tämän lisäksi hermosolujen ja hermoverkkojen sähköistä aktiivisuutta ja sen kehittymistä seurattiin. Seuraaminen toteutettiin mittaamalla sähköistä aktiivisuutta useasta hermosolusta samaan aikaan mikroelektrodihilalla (MEA) tai kuvaamalla tiheään kalsiumionipitoisuusherkällä väriaineella värjätyä hermoverkkoa (kalsiumkuvannus). Yksittäisten hermosolujen solukalvon sähkönjohtavuuden muutoksia mittattiin solun sisään asetettavalla elektrodilla (patch clamp). Hermosolujen aktiivisuusmittausten tehostamiseksi, selvitettiin kasvattaako hermosolujen kasvupinta-alan ja nestetilavuuden rajoitus mittausherkkyyttä. Sähköisen toiminnan muodostumista tarkisteltiin yhdistämällä MEA-mittaukset ja kalsium-kuvannukseen, jotta voitaisiin selvittää kuinka yksittäisten hermosolut toimivat suhteessa verkoston toimintaan. Lisäksi verkostoja altistettiin erilaisille toimintaa häiritseville aineille, jotta saataisiin tarkempaa tietoa

siitä mitkä hermosolujen ominaisuudet ovat kriittisiä koko verkoston toiminnan kannalta. Väitöskirjatyön aikana kehitettiin ja testatiin uusia analyysiohjelmistoja, jotta voitaisiin tarkemmin erotella sähköistä aktiivisuutta MEA elektrodien mittaamasta signaalista, ja jotta voitaisiin automaattisesti tunnistaa ja päätellä kalsiumkuvannuksen tuottamista kuvasarjoista yksittäisten hermosolujen ja verkoston aktiivisuutta.

Hermosolujen kasvupinta-alan ja nestetilavuuden rajoituksen havaittiin lisäävän mittauksissa näkyvää aktiivisuutta. Avuksi kehitetyt analyysiohjelmistot mahdollistivat toisiaan täydentävän datan tuottamisen yhtäaikaisista MEA- ja kalsiumkuvannusmittauksista. Lisäksi sähköisen aktiivisuuden ja häiritsevien aineiden vaikutuksien tarkastelu paljasti ihmisperäisille hermoverkoille ominaisia piirteitä, mutta myös piirteitä, joita on havaittu muiden eliöiden aivojen kehityksen aikana.

Loppupäätelmänä voidaan sanoa, että ihmisperäististä kantasoluista kasvatetut hermoverkot ja kehitetyt mittaus- ja analyysityökalut muodostavat kokonaisuuden, joka tulevaisuudessa mahdollistaa aivoaktiivisuuden ja siihen vaikuttavien tekijöiden takana olevien yksityiskohtien selvittämisen.

LIST OF ORIGINAL PUBLICATIONS

This thesis is based on the following publications, which are referred to in the text using the following Roman numerals (I-IV):

I **Mäkinen M.***, Joki T.*, Ylä-Outinen L., Skottman H., Narkilahti S., Äänismaa R. (2013) "Fluorescent probes as a tool for cell population tracking in spontaneously active neural networks derived from human pluripotent stem cells." Journal of Neuroscience Methods. 2013 Apr 30;215(1):88-96. doi: 10.1016/j.jneumeth.2013.02.019. Epub 2013 Mar 7. PMID: 23473797.

II Kapucu F.E., **Mäkinen M.E.**, Tanskanen J.M., Ylä-Outinen L., Narkilahti S., Hyttinen J.A. (2014) "Joint analysis of extracellular spike waveforms and neuronal network bursts." Journal of Neuroscience Methods. 2016 Feb 1;259(1):143-55. doi: 10.1016/j.jneumeth.2015.11.022. Epub 2015 Dec 7. PMID: 26675487.

III Toivanen M.*, Pelkonen A.*, **Mäkinen M.**, Ylä-Outinen L., Sukki L., Kallio P., Ristola M., Narkilahti S., (2017) "PDMS tunnel devices on MEAs increase the measurable activity of human stem cell-derived neuronal networks." Frontiers in Neuroscience. 2017 Oct 31;606(11). doi: 10.3389/fnins.2017.00606

IV **Mäkinen ME.**, Ylä-Outinen L., Narkilahti S. (2018), GABA and Gap Junctions in the Development of Synchronized Activity in Human Pluripotent Stem Cell-Derived Neural Networks" Frontiers in Cellular Neuroscience. 2018 March 06; doi: 10.3389/fncel.2018.00056

* Authors contributed equally.

ABBREVIATIONS

AMPA/KA	α-amino-3-hydroxy-5-methyl-4-isoxazolepropionic acid- /kainate
BDNF	brain-derived neurotrophic factor
BIC	bicuculline
BSA	bovine serum albumin
B-TUB	βIII-tubulin
FGF2	basic fibroblast growth factor
CBX	carbenoxolone
C-MYC	c-Myc
CNS	central nervous system
CNTF	ciliary neurotrophic factor
CT	Cell Tracker Green
D-AP5	(2R)-amino-5-phosphonovaleric acid; (2R)-amino-5-phosphonopentanoate
DAPI	4',6-diamidino-2-phenylindole
DMEM	Dulbecco's modified Eagle's medium
dPBS	Dulbecco's phosphate-buffered saline
EAP	extracellular action potential
EEG	electroencephalography
EFG	epidermal growth factor
ENO	early network oscillation
ESC	embryonic stem cell
GABA	gamma-aminobutyric acid
GABAA receptor	ionotropic GABA receptor
GABAergic	pertaining to or affecting the neurotransmitter GABA
GDP	giant depolarizing potential
GFAP	glial fibrillary acidic protein
GLUT	glutamate neurotransmitter
hESC	human embyonic stem cell
hIPSC	human-induced pluripotent stem cell

hPSC	human pluripotent stem cell
IBI	inter-burst-interval
IPSC	induced pluripotent stem cell
ISI	inter-spike-interval
KLF4	Kruppel-like factor 4
LFP	local field potential
MAP-2	microtubule-associated protein
MCS	multichannel systems
MEA	microelectrode array
MUA	multiple unit activity
MZ	marginal zone
NDM	neural differentiation medium
NDS	normal donkey serum
NPC	neural precursor cell
NMDA	N-methyl-D-aspartate
OCT3/4	octamer-binding transcription factor 4
PB	phosphate buffer
PDMS	polymethylsiloxane
PFA	polyformaldehyde
PEI	polyethylimide
PSC	pluripotent stem cell
RT	room temperature
SPA	synchronous plateau assemblies
SOX2	SRY (sex determining region Y)-box 2
TTX	tetrodotoxin
TUT	Tampere University of Technology
UTA	University of Tampere
VZ	ventricular zone

TABLE OF CONTENTS

1 INTRODUCTION

The brain consists of electrically active circuits that carry out the functions of human cognition. These circuits are formed during development via a series of interacting, and partially overlapping, iterative biological processes of structural and functional brain development. Our understanding of how the functional aspect arises from the structural components remains incomplete. Understanding the functional aspect of normal human brain development can potentially provide insight into understanding the genesis of human neuropathologies.

The cellular and functional brain development has been excessively studied in rodents. However, the replication of human disease phenotypes in animal models has been questioned. The difficulty of replicating the functional changes can arise from the differences in the underlying cellular components, which has been observed recently. Thus, to understand the generation of clinical phenotypes manifesting as changes in functionality, it is essential to develop human cell models.

In vitro neuronal networks derived from human pluripotent stem cells (hPSCs) can be harnessed to model the developmental phases of structural brain development and should be investigated as an *in vitro* human model for replicating the functional changes. Furthermore, hPSC-derived neurons are able to capture the development of functionality on an individual level and have been shown to display features of network activity. Thus, studying the emergence of network activity patterns in hPSC-derived neural networks can improve the understanding of the human specific cellular mechanisms underlaying the network activity formation during neural development and generation of abnormal brain functions. However, current experimental and analytical tools for studying the immature physiological properties of hPSC-derived neurons in the context the emerging network activity patterns have been unable to provide answers.

2 LITERATURE REVIEW

The human brain is arguably the most complex functional structure among all living organisms. However, the mechanisms leading to this complexity and the reasons behind brain malfunctions remain incompletely understood. One of the main contributors to this lack of knowledge is the poor experimental accessibility of the embryonic human brain. Another reason is the lack of technologies to study all of the temporal and spatial scales of its activity.

2.1 Brain development

Brain development can be divided into the intertwined processes of structural and functional brain development. During structural brain development the cytoarchitechture of the brain is generated by cell differentiation, division and migration. This process consists of specification of the neuroectoderm, formation of the neural tube and ventricles, production of neuronal precursors, sequential generation of different populations of neurons and glia as well as their migration. Simultaneously, the functional brain development takes place and gives rise to the the circuits of the brain. The formation of functional neuronal circuits relies on neurite outgrowth, electrophysiological maturation and synaptogenesis. Structural and functional brain development are jointly regulated by genetic programs and surrounding gradients of signaling molecules, each with inhibitory or activating roles.

2.1.1 Structural brain development

The formation of the nervous system begins with the specification of the neuroectoderm. During this process, ectodermal cells are induced to neural lineage cells. These cells are known as neuroepithelial progenitors and they give rise to neural cells via differentiation (Muñoz-Sanjuán and Brivanlou, 2002; Weinstein and Hemmatibrivanlou, 1999).

Next, the neuroectoderm folds into the neural tube. The neural tube results from the self-organization of neuroepithelial progenitor cells (Zhang and Jiao, 2015). Following the formation of the neural tube, the rostral part of the neural tube bulges into three vesicles that will develop into the forebrain, midbrain, and hindbrain (Jessell and Sanes, 2000; Rash and Grove, 2006; Rhinn et al, 2006; Stern, 2001). These vesicles are delineated by neural precursors that arise from the neuroepithelial progenitor cells (Jessell and Sanes, 2000; Kornack and Rakic, 1995).

Finally, the neuronal precursors generate different populations of neurons and glia, in neurogenesis and gliogenesis, respectively. During this final differentiation step, the neural precursors undergo a sequential shift in their differentiation potency, generating the birthdate-linked neuronal populations of the various layers (Eckler et al., 2015; Frantz and McConnell, 1996; Gao et al., 2014; Guo et al., 2013). Furthermore, some neurons, such as inhibitory GABAergic neurons, are generated in specific locations of the developing brain tissue (McManus et al, 2004; Monk et al, 2001). Simultaneously to neurogenesis, the astrocytes are created in gliogenesis (Shen et al., 2006). This process intensifies as the neural precursors shift in their differentiation capacity.

Postmitotic neurons migrate outwards and form the layered structure of the brain in an inside-out manner, from the deeper layers to the more superficial ones in several different brain areas (Kornack and Rakic, 1995). Following the final cell division, neuronal cells mature and obtain their functional properties.

2.1.2 Functional brain development

Simultaneously to the generation of cytoarhitechture, the functionality of the brain emerges as patterns of electrical and calcium level activity (Allene and Cossart, 2010; Owens and Kriegstein, 1998). On the individual neuron level, the electrophysiological properties required for action potential firing mature. Action potential firing is required in the nervous system for carrying signals from one end of the neuron, the dendrite, to the other, the axon. The action potential is generated by voltage-gated ion channels on the neuronal cell membrane. Furthermore, for carrying signals across the nervous system, the neurons need to communicate with each other, carrying the signal from one neuron to another. The signal between neurons is transferred via synapses. Synapses can be electrical, connecting the insides of two neurons, or chemical. In chemical synapses, the presynaptic neuron releases neurotransmitters to the synaptic cleff and the postsynaptic receiving neuron reacts to the released neurotransmitters via neurotransmitter receptors also known as ligand-gated ion channels.

Neurotransmitters can encourage or discourage the postsynaptic neuron to fire action potentials and are called excitatory or inhibitory, respectively. On the individual neuron level, newborn neurons extend processes to form synaptic connections and express synaptic receptors. Synaptogenesis begins earlier in the deeper layers than in the more superficial ones. Thus, the earliest synaptic connections are formed by the earliest born neurons and are modiefied by the constant arrival of younger neurons (Bystron et al, 2008; Supèr et al, 1998).

As the maturation of both neuronal cell membrane properties and synapses proceeds during development, synchronous activity is generated as electrical and calcium level patterns. The properties of network activity pattern depend on the degree of network maturation (Kamioka et al., 1996) arising from the the maturity and connectivity of the neurons (Arnold et al., 2005; Ivenshitz and Segal, 2010; Latham et al., 2000), the excitatory/inhibitory neurotransmitter balance (Brunel and Wang, 2003), and the pacemakers within a neuronal network (Bazhenov et al., 2008; Latham et al., 2000). However, for the most part, the detailed mechanisms behind network activity patterns remain unclear (Barrnet et al., 2014).

2.1.2.1 Initial asynchronous activity

The earliest functionality emerges as uncorrelated activity. Initial asynchronous activity is generated by the earliest born neurons in the proliferative ventricular zone (VZ) and post-migratory marginal zone (MZ). The asynchronously active newborn neurons have immature membrane physiology and are thus unable to produce sodium conductances required for action potentials (Crépel et al., 2007). The uncorrelated activity is generated by asynchronous calcium transients and requires calcium release from intracellular stores (Owens et al., 2000).

2.1.2.2 Emergence of correlation

Next, a pattern of synchronous plateau assemblies (SPAs) emerges as the amount of neurons with uncorrelated activity decreases. SPAs are synchronous activity between a fraction of neurons (~20%, Crépel et al., 2007; Garaschuk et al., 1998; 2000; Allene et al., 2008; 2012; Corlew et al., 2004; Sun and Luhmann, 2007). SPAs are formed by synchronously occurring long-lasting calcium plateaus (duration: 9s, occurrence: 0.02 Hz) (Crépel et al., 2007). These correlated calcium elevations arise from synchronous membrane depolarizations and single-neuron bursting (Crépel et al., 2007; Alléne et al., 2008; 2012). Correlated activity emerges as the neural membrane physiology matures and neurons extent neurites.

SPAs depend on gap junctions and action potential generation (Crépel et al., 2007; Alléne and Cossart, 2010; Blankenship and Feller, 2010; Dupont et al., 2006; Kilb et al., 2011; Sun and Luhmann, 2007). The emergence of SPAs occurs parallel to the emergence of neurons with mature sodium conductance required for action potentials. These neurons initially fire action potentials asynchronously. Eventually gap junction formation between action potential firing and less mature neurons synchronizes activity into SPAs (Crépel et al., 2007). Electrical coupling by gap junctions mediates synchrony by passing changes in membrane potential directly from one cell to another via connexin formed electrical synapses (Schuchmann et al., 2006). SPAs occur independently of chemical synapses but, SPA participating neurons are exhibiting functional GABA receptors. However, despite the excitatory GABA response, GABA inhibits the generation of SPAs (Crépel et al., 2007). In adult tissue GABA is inhibitory neurotransmitter produced by GABAergic interneurons, and the developmental excitatory effects are due to reversed chloride gradient (Ben-Ari et al., 1989, 2002, 2007).

2.1.2.3 Network oscillations

Along the decrease of neurons participating in SPAs, a larger amount of neurons begins to participate in large-scale synchronized calcium transient waves and early network oscillations (ENOs) (Garaschuk et al., 1998; Weissman et al., 2004; Alléne and Cossart, 2010; Owens and Kriegstein, 1998). The activity pattern generated by SP neurons in the proliferating and neurogenic VZ (Dupont et al., 2006; Hanganu et al., 2009), and by Cajal-Retzius neurons in the post-migratory MZ (Schwartz et al., 1998; Aguiló et al., 1999; Allene and Cossart, 2010; Owens and Kriegstein, 1998). ENOs occur at low frequency (< 0.01 Hz) and consist of shorter burst of activity than SPAs, but are more regular and include more neurons (Khazipov et al., 2004; Kilb et al., 2011; Yang et al., 2010; Alléne et al., 2008; Garaschuk et al., 2000). ENOs are correlated to electrical changes in the field potential and increase of multiunit activity (Allené et al., 2008).

Similar to SPAs ENOs rely on action potentials and voltage-gated calcium channels (Corlew et al., 2004). In addition, ENOs are the first activity pattern relying on chemical synapses. ENOs emerge simultaneously with chemical synaptic mechanisms that are suppressing the expression of of SPAs (Crépel et al., 2007). The SP and MZ neurons, however, express different receptors, with SP neurons expressing functional nicotinic, muscarinic, glycine receptors (Hanganu and Luhmann, 2004; Kilb et al., 2008; Hanganu et al., 2009) and Cajal-Retzius neurons expressing AMPA and NMDA receptors (Garaschuk et al., 2000; Corlew et al., 2004; McCabe et

al., 2006). The synchrony in MZ is driven mostly by NMDA receptors with minor participation from AMPA receptors (Garaschuk et al., 2000; Corlew et al., 2004; McCabe et al., 2006). Both populations of neurons are expressing functional $GABA_A$ receptors (Hanganu et al., 2001; 2002; Aguiló et al., 1999) with excitatory response triggering action potentials (Kilb et al., 2002; Rheims et al., 2008; Cosgrove and Maccaferri, 2012; Sava et al., 2014).

2.1.2.4 Giant depolarizing potentials

ENOs gradually decrease in their occurrence and occurrence of giant depolarizing potentials (GDPs) increases (Allene et al., 2008). GDPs involve even larger numbers of neurons (up to 80%) and occur at much higher rates (0.1 Hz) (Ben-Ari et al., 1989; Allene et al., 2008; Allene and Cossart, 2010). GDPs are associated with synchronous calcium transient oscillations of faster kinetics (Allène et al., 2008; Ben-Ari et al., 1989, Khazipov et al., 2001; Garaschuk et al., 1998; Crépel et al., 2007). Neurons participating in GDPs generate the calcium transients with bursts of action potentials superimposed on strong membrane depolarizations (~1 s) (Allene and Cossart, 2010). Similar to ENOs GDPs are associated to field potential changes and even further increase in multiunit activity (Allene et al., 2008).

As the network activity pattern transition from SPAs to GDPs, GABAergic interneurons mature in their morphological and physiological properties (Allene et al., 2012). GDPs are strongly dependent on depolarizing $GABA_A$ receptor-mediated transmission and partially on glutamatergic transmission via AMPA/NMDA receptor (Allene et al., 2008). GDPs eventually disappear as GABAergic transmission matures and GABA changes from excitatory to inhibitory (Ben-Ari et al., 1989; Garaschuk et al., 1998; Tyzio et al., 2007). The change in the action of GABA arises from reversal of chloride gradient via increased expression of chloride transporter KCC2 (Rivera et al., 1999; Khazipov et al., 2004; Blaesse et al., 2009).

2.1.2.5 Role of synchronous activity

In clinical neuroscience, a range of disorders associated with early network dysfunction occur as developmental "oscillopathies" (Inta et al., 2011; Lisman et al., 2008; Uhlhaas and Singer, 2011). During development, synchronous activity appears spontaneously before the availability of external stimulus inputs from sensory organs (Moody and Bosma, 2005). Synchronous activity has been shown to affect neuronal

survival, migration, and differentiation (Allene and Cossart, 2010; Owens and Kriegstein, 1998). Furthermore, synchronous network activity has a critical role in development (reviewed in Moody and Bosma 2005). Synchronous activity has been shown to be important for the formation of synaptic connections which are the underlaying mechanim of functional networks (Maeda et al., 1995; Mayer et al. 2018). In addition, experimental and clinical evidence indicates that the early electrical activity measured by electroencephalography (EEG) is an important indicator of pathophysiological alterations at the earliest developmental stages (Vanhatalo and Kaila, 2006).

2.2 Modeling the human brain development

The series of developmental processes that lead to the formation of brain circuitries has been excessively studied in rodents. These studies have been carried out *in vivo* in living organisms, *ex vivo* in brain slices and *in vitro* in primary cell cultures. Each of these systems has their own advantages and limitations. *In vivo* studies are problematic because of their limited timeframe and requirement for anesthesia or other drug applications. However, the *in vivo* environment offers the possibility to preserve the cytoarchitecture of the brain as well as sensory inputs. The complex cytoarchitecture is also partially preserved in slice cultures (Humpel, 2015; Gähwiler et al., 1997; De Paola et al., 2003; Galimberti et al., 2006). As an advantage over *in vivo* model systems, brain slices allow a larger time window of observation, enabling the study of developmental changes in neural circuits over time (Henze et al., 2000). Furthermore, *in vitro* and *ex vivo* systems allow more precise pharmacological (Stoppini et al., 1997; Cho et al., 2007; Baraban et al., 2009) and genetic experimentation Ridoux et al., 1995; Thomas et al., 1998; Murphy and Messer, 2001; Jansen et al., 2011). However, animal models do not allow for the study of human-specific development.

2.2.1 Human-specific features of brain development

The human brain and its development display several species-specific features. On a crude scale, these features can be observed in the generation of neuroanatomical structures and in the pace of brain development. For example, the cerebral cortex which performs the human-specific cognitive functions has enlarged surface, thickness and specific gyration patterns (DeFelipe, 2011; Lui et al., 2011). These species-specific

structural features are thought to arise during development from differences in the employed mechanisms (Bystron et al., 2008; Fish et al., 2008; Lui et al., 2011; Taverna et al., 2014). These mechanisms include the presence of primate-specific stem and progenitor cells as well as the primate-specific neuronal cell types that are generated during neurogenesis.

The early progenitors cells, neuroepithelial progenitors, differ from their rodent counterparts (Lui et al., 2011; Taverna et al., 2014; Dehay et al., 2015) in having a longer period of amplification (Rakic, 1995) and greater diversity. This diversity has been linked to the generation of human specific structural features in the brain (Kriegstein et al., 2006; Fish et al., 2008; Fietz et al., 2010; Hansen et al., 2010; Lui et al., 2011; Taverna et al., 2014).

The generation of neurons from neural precursors, neurogenesis, takes also longer (Rakic, 1995) and produces an increased number and diversity of neurons (Rakic, 1995; Nimchinsky et al., 1999; Hill and Walsh, 2005; Roth and Dicke, 2005; Bystron et al., 2006; Lui et al., 2011). Some of the neurons generated from these precursors are primate-specific and not found in rodents (Clowry et al., 2010).

Human neurons also display prolonged morphological and electrophysiological maturation (Muguruma et al., 2010; 2015; Kriks et al., 2011; Muguruma and Sasai, 2012; Shi et al., 2012; Takazawa et al., 2012; Espuny-Camacho et al., 2013; Maroof et al., 2013; Nicholas et al., 2013; Studer et al., 2015). During morphological and electrophysiological maturation, neurite outgrowth, dendritic spine maturation and synaptogenesis occur (DeFelipe, 2011; Petanjek et al., 2011).

Thus, human models are needed to understand the full complexity of development underlying the function of the human brain. *In vitro* neuronal networks derived from human pluripotent stem cells (hPSCs) could be used to model the various developmental phases (Cavanaugh et al., 2014; Hunsberger et al., 2015; Pei et al., 2016).

2.3 Stem cell-based *in vitro* models

Stem cells can be used to derive neurons and neuronal networks in an *in vitro* environment. The derivation repeats the phases of *in vivo* brain development, producing a diversity that is equivalent to that of *in vivo* diversity and ending in functional maturation of the networks.

2.3.1 Stem cells

Stem cells are an unspecified cell type that has the capacity to proliferate indefinitely and differentiate into multiple cell types. There are two widely used types of PSCs: embryonic stem cells (ESCs), derived from the inner cell mass of blastocysts, and induced pluripotent stem cells (iPSCs), derived from differentiated adult somatic tissues via reprogramming. Somatic tissue reprogramming can be achieved via nuclear transfer, cell fusion or direct reprogramming (Hochedlinger and Jaenisch, 2006). Direct reprogramming is achieved by activating the expression of four pluripotency-associated transcription factors, Oct3/4, Sox2, c-Myc, and Klf4 (Takahashi and Yamanaka, 2006). Pluripotent stem cells can be differentiated into the cells of any of the three germ layers: ectoderm, mesoderm and endoderm (Martin, 1981). Differenatiation into neural cells, which are of ectodermal orgin, recapitulates the steps of *in vivo* brain development, which has led to their use in various applications.

2.3.2 Applications of hPSC-derived neurons

PSC differentiated *in vitro* into neural cells have been used to study human brain development, neurotoxicity, human-specific effects of different biomolecules, neuropathology and transplantation treatments.

PSCs can be used to study the basic mechanisms of brain development, specifically human brain development and its evolutionary background. PSC-derived neural models have revealed that the cell diversity and patterning can be recapitulated *in vitro* (Wunderlich et al., 2014). Furthermore, the intrinsic self-organization allows for the generation of structures that strikingly resemble human brain subregions (Muruguma and Sasai et al., 2012; Lancaster and Knoblich, 2014).

hPSC-derived neural cells can also be used for drug and teratologic agent screenings *in vitro* (Dolmetsch and Geschwind, 2011; Brennand and Cage, 2012; Tabar and Studer 2014). Moreover, some biomolecules, such as steroids, that are effective in the human CNS are not as effective in rodents, and differ in their signaling mechanisms or expression during development (Azcoitia et al., 2011). Additionally, hPSC-derived neurons could be used for transplantation treatment (Oki et al., 2012; Lindvall, 2015). Such treatments have been shown to have functional benefits in animal models (Wernig et al., 2008; Hallett et al., 2015).

hPSC-derived neural cells have been used to model neurological diseases (Mungenast et al., 2016). IPSCs generated from a patient carrying a mutation that is strongly linked to a particular phenotype allow for the study of underlying disease

mechanisms (Egashira et al., 2011). Several diseases depend on synaptic function and thus on network function, making the proper formation of networks important *in vitro*. Synaptogenesis and synaptic activity have been assessed in patient iPSC-derived neural cultures (Dolmetsch and Geschwind, 2011; Sandoe and Eggan, 2013). Additionally, *in vitro,* genes associated with different neuropathologies can be inactivated via molecular biology tools (Rubio et al., 2016). Diseases belonging to the neurodegenerative, neurodevelopmental and psychopathological classes have been modeled (Heman-Ackah et al., 2016). The studied neurodegenerative diseases include Parkinson's disease (Byers et al., 2012), Huntington's disease (Nekrasov et al., 2016), amyotrophic lateral sclerosis (Chestkov et al., 2014), and Alzheimer's disease (Mungenast et al., 2016). Neuropsychiatric conditions include Rett syndrome (Marchetto et al., 2010), Timothy syndrome (Paşca et al., 2011), sporadic schizophrenia (Brennand et al., 2011) and Phelan–McDermid syndrome (Shcheglovitov et al., 2013). These studies demonstrate the possibility of using PSC-based *in vitro* models to study synaptic development in the humans. However, a desirable *in vitro* model would require being able to distinguish the normal versus disease features *in vitro*. Table 1 summarizes the differences in functionality in patient hPSC-derived neural cultures.

Table 1. Manifestation of functionality in hPSC-based in vitro models. The table describes original works where functional phenotype of patient derived hPSC-derived neural cells was studied with network activity measurements. Studies with calcium imaging and MEA were included. The in vitro phenotype of the disease is listed together with functional differences observed. Functional differences in spike firing frequency, synchronous bursting or synchronous calcium transients, number of spikes in bursts or size of calcium transients and network connectivity were reported between healthy and patient derived cell lines.

Reference	Disease type (disease)	Method	Phenotype	Functional differences			
				Firing frequency	Bursting frequency	Spikes in bursts	Connectivity
Canals et al., 2015	degenerative (Sanfilippo C)	calcium imaging	-	-	decreased	decreased	altered
Vessoni et al., 2016	developmental (Cockayne Syndrome B)	MEA	reduced synapse density	decreased	less synchronized	-	-
Flaherty et al., 2017	psychiatric (Schizophrenia)	MEA	altered synaptic gene expression	increased	-	-	-
Nageshappa et al., 2016	developmental (MECP2dup)	MEA	increased number of glutamatergic synapses	increased	increased	-	-

2.3.3 PSC-derived neurons recapitulate *in vivo* neurogenesis

ESCs and iPSC can differentiate into ectodermal cells, including neural cells. The process of producing neural cells *in vitro* from PSCs recapitulates *in vivo* brain development described in Chapter 2.1.1 Structural brain development. Similar to *in vivo,* neural induction *in vitro* is a default pathway for stem cells and depends on the deprivation of external signals, growth factors and morphogens, and the *in vitro* differentiation of stem cells to neurons begins with the deprivation of external signals (Chambers et al., 2009). Additionally, the self-organization capabilities are conserved *in vitro* as neuroepithelial progenitor cells organize into structures called neural rosettes (Elkabetz et al., 2008; Germain et al., 2010). Neural rosettes then give rise to neural stem cells and precursors (Malchenko et al., 2014), which are specific to humans (Lancaster et al., 2013; Shi et al., 2012). The ability of neural progenitors to sequentially generate neurons in neurogenesis is also recapitulated during *in vitro* differentiation (Eiraku et al., 2008; Gaspard et al., 2008). Furthermore, despite the specific generation of inhibitory interneurons, the generation of inhibitory neurons is repeated *in vitro* (Watanabe et al., 2005; Danjo et al., 2011; Maroof et al., 2010, 2013; Germain et al., 2013; Hansen et al., 2013;). Also, the gliogenesis is preserved as the *in vitro* differentiated neural precursors generate astrocytes in a similar sequential manner (Itsykson et al., 2005; Johnson et al., 2007; Hu et al., 2010; Lappalainen et al., 2010). In conclusion, PSC-derived neural cultures capture several components of the *in vivo* structure. Thus, it could be expected that the functional aspects arise as well.

2.3.4 Generation of electrical functionality in PSC-derived neural cultures

As the neurons are generated *in vivo*, they begin to mature electrophysiologically as described in Chapter 2.1.2 Functional brain development. Initially electrophysiological maturation consists of the expression of voltage-gated ion channels, which allow neurons to fire action potentials. The *in vitro* differentiated PSC-derived neurons develop mature firing properties similar to *in vivo,* starting from the ablitity to produce abortive action potentials, then full action potentials, and finally to bursts of action potentials (Telezhkin et al., 2016; Gunhanlar et al., 2017; Lam et al., 2017). The temporal aspects of brain development are also captured, as longer culture periods increase the proportion of electrophysiologically mature active neurons (Shi et al., 2012; Cornelissen et al., 2013; Nicholas et al., 2013; Rushton et al., 2013; Hartfiel et al., 2014). Furthermore, astrocytes, from the ongoing gliogenesis or as externally supplied,

Table 2. Maturation of spontaneous activity in hPSC-derived neural networks derived from different cell sources with varying differentiation methods and follow up times (network age). During network maturation (age), the number of active electrodes is generally observed to increase, but remain low. Similarly the frequency of spikes measured from the networks increases and bursts of action potentials emerge or their occurrence increases. As the networks mature (age), the number of spikes in bursts and the duration of bursts increases. Absolute values are listed when available.

Reference	Source	Differentiation	Network age (weeks)	Active electrodes	Firing frequency	Bursting frequency	Spikes in bursts	Burst duration
Odawara et al., 2014	hiPSC	Odawara et al., 2014	1, 2, 3, 4	increased < 10%	increased	-	increased	-
Odawara et al., 2016	hNPC	predifferentiated	2–10	increased	increased	increased	-	-
Kayama et al., 2018	hNPC	predifferentiated	-	-	-	6.6 / min	-	-
Matsuda et al., 2018	hNPC	predifferentiated	8	-	6 kHz	2 / min	12 000	8 s
Ishii et al., 2017	hNPC	predifferentiated	4 & 8	increased	increased from 1 Hz to 3 Hz	emerged	-	-
Fukushima et al., 2016	hPSC	Fukushima et al., 2016	2, 5, 6, 8	increased < 20%	increased	increased	-	-
Vessoni et al., 2016	hiPSC	Vessoni et al., 2016	5	-	-	emerged	-	-
Heikkilä et al., 2009	hESC	Nat et al., 2007	1-5	-	-	emerged > 5w	-	-
Odawara et al., 2016	hNPC	predifferentiated	10-36	-	increased to 5 Hz	increased 1/min to 3/min	increased	increased 400 ms
Nageshappa et al., 2016	hiPSC	Espuny-Camacho et al., 2013	-	-	-	1/min	-	-
Napoli and Obeid, 2016	human primary	-	up to 5	-	-	none	-	-
Yamazaki et al., 2016	hiPSC	Falk et al., 2012	7	increased < 20%	increased	increased	-	-
Tukker et al., 2016	hPSC	Tukker et al., 2016	2	6-17%	0.083-0.33 Hz	-	-	-
Telezhkin et al., 2016	hiPSC	Telezhkin et al., 2016	-	-	2–3 Hz	-	-	-

have been shown to promote functional maturation (Pfrieger and Barres, 1997; Johnson et al., 2007; Eroglu et al., 2009; Allen et al., 2012; Paşca et al., 2015).

Electrophysiological maturation occurs in parallel to synaptogenesis, which is upregulated as the neurogenesis proceeds and proliferation decreases in hPSC-derived neural cultures (Odawara et al., 2016). Synaptogenesis allows individual neurons to connect and generate network activity patterns. The formation of synapses correlates with the amount of electrical activity, both of which initially increase, followed by a plateau in both synapse density and activity in hPSC-derived neural cultures (Ito et al., 2013). Studies of the emergence of spontaneous activity in hPSC-derived neural cultures are listed in Table 2. The hPSC-derived cultures are able to form both GABAergic (Table 3 and Table 4) and glutamatergic (Table 5 and Table 6) synapses. Currently, there are no studies assessing the gap junctions in hPSC-derived neural networks. Thus, the framework and functional capacities of the major neurotransmitter systems established early in development are, for the most part, successfully captured in the PSC-derived neural networks. However, proper synaptogenesis and network formation remains debatable and requires further assessment.

Similar to *in vivo* differentiated neurons, PSC-derived neuronal networks self-organize to display activities that resemble those observed in the brain (Nimmrich et al., 2005; Illes et al., 2007; 2009; Heikkilä et al., 2009; Gullo et al., 2010). One of these activities is spontaneous synchronous bursting (Illes et al., 2007; 2009; Eiraku et al., 2008; Heikkilä et al., 2009). Due to the recurrent emergence of bursting observed in these networks, PSC-derived neuronal networks are a good model to study the basic mechanisms of network activity development, such as how synchronization is achieved and what its underlying connectivity is. However, the *in vivo* parallel of synchronous activity observed in PSC-derived neural cultures is not known. Furthermore, it has not been shown if the synchronous activity transitions from one pattern to another *in vivo* are also observed *in vitro*.

Uncovering the undelaying mechanisms of synchrony in hPSC-derived neural netoworks would contribute to the understanding of network functions and help elucidate the genesis of physiological and pathological activity. Thus, studying the mechanisms of early network function and dysfunction is of importance for both basic and clinical neurosciences. Furthermore, determining the mechanisms that mediate the network activity in hPSC-derived networks would allow us to draw conclusions about which *in vivo* activity is its parallel.

Table 3. Studies of stimulation of GABAergic signaling in hPSC-derived neural networks generally report decreased action potential firing. The effect on bursting frequency, spikes in bursts and burst duration are also decreased but not frequently reported. The effect on or the number of active electrodes is commonly not reported.

Reference	Firing frequency	Bursting frequency	Spikes in bursts	Burst duration	Active electrodes
Fukushima et al., 2016	decreased	-	-	-	-
Heikkilä et al., 2009	decreased	-	-	-	-
Yamazaki et al., 2016	decreased	decreased	decreased	decreased	-
Tukker et al., 2016	decreased	-	-	-	-

Table 4. Studies of blockade of GABAergic signaling in hPSC-derived neural networks generally report increased firing and bursting frequency as well as increased burst durations. The reports on the effect of number of spikes in bursts differ. The effect on or the number of active electrodes is commonly not reported.

Reference	Pharmacological target receptor	Firing frequency	Bursting frequency	Spikes in bursts	Burst duration	Active electrodes
Odawara et al., 2014	$GABA_A$	increased	-	-	-	-
Ishii et al., 2017	$GABA_A$	increased	increased	increased	increased	
Fukushima et al., 2016	$GABA_A$	increased	increased	-	-	-
Heikkilä et al., 2009	$GABA_A$	increased	increased	-	-	-
Odawara et al., 2016	$GABA_A$	increased	increased	increased	increased	-
Tukker et al., 2016	$GABA_A$	increased	-	-	-	-
Telezhkin et al., 2016	$GABA_A$	increased	-	-	-	-

Table 5. Studies of stimulation of glutamatergic signaling in hPSC-derived neural networks generally report increased firing frequency. The effect on bursting frequency, number of spikes in bursts, burst duration or the number of active electrodes is commonly not reported.

Reference	Firing frequency	Bursting frequency	Spikes in bursts	Burst duration	Active electrodes
Fukushima et al., 2016	increased	-	-	-	-
Odawara et al., 2016	increased	-	-	-	-
Tukker et al., 2016	decreased	-	-	-	-
Telezhkin et al., 2016	increased	-	-	-	-

Table 6. Studies of blockade of glutamatergic signaling in hPSC-derived neural networks generally report decreased action potential firing and decreased occurrence of bursts of action potentials. The effect on number of spikes in bursts, burst duration or the number of active electrodes is commonly not reported.

Reference	Pharmacological target receptor	Firing frequency	Bursting frequency	Spikes in bursts	Burst duration	Active electrodes
Odawara et al., 2014	AMPA/kainate + NMDA	silenced	-	-	-	-
Ishii et al., 2017	AMPA/kainate + NMDA	decreased	decreased	-	-	-
Fukushima et al., 2016	AMPA/kainate + NMDA	decreased	decreased	-	-	-
Heikkilä et al., 2009	AMPA/kainate + NMDA	decreased	silenced	-	-	-
Odawara et al., 2016	AMPA/kainate + NMDA	decreased	silenced	-	-	-

2.4 Measurement of functionality in neural network cultures

Studying early network function and dysfunction has the potential to be of major importance for clinical, basic and developmental neurosciences. Thus, studying the emergence of spatial and temporal network activity in these networks can lead to a better understanding of the functioning of the brain (Penn and Shatz 1999; Bi and Poo 2001; Zhang and Poo 2001; Hua and Smith 2004; Chiappalone et al. 2006; Göbel and Helmchen, 2007; Blankenship and Feller 2010; Kerschensteiner 2014). Synchronous network activity that produces network oscillations is of interest in neuroscience, as it has a role in both the development and function of adult neural circuits. Synchronized network activity has also been observed *in vitro* (Cohen et al., 2008; Ivenshitz and Segal, 2010). Synchronized network bursts are considered an important parameter to assess the physiology and pathophysiology of neurons *in vitro* (Martinoia et al., 2005).

Studying the patterns of neuronal activity in a large population is required to understand the operating principles of neural circuits. The two most widely used methods for measuring the activity of many neurons simultaneously are multichannel electrophysiology and population calcium imaging.

2.4.1 Measurement of functionality with MEA

Recording from multiple sites across a large area simultaneously is required to resolve the spatiotemporal patterns of synchronous firing. This can be achieved with MEA measurements. In MEA measurements, the electrophysiological activity of a neural culture is measured via electrodes in an array. Each of the electrodes measures neural activity simultaneously from many neurons at high (kHz) temporal resolution (Buzsaki, 2004). Furthermore, due to their noninvasive nature, MEA measurements can be utilized to record electrophysiological activity recordings over several weeks or months (Illes et al., 2009). MEAs have been used to the study spontaneous activity patterns of both developing (Wagenaar et al., 2006; Charlesworth et al., 2015) and mature neuronal networks (Ito et al., 2014). MEA recordings have been utilized to understand basic brain functions such as functional connectivity (Ito et al., 2014) and structure-function relationship (Buzsaki, 2004; Nicolelis and Lebedev, 2009).

2.4.1.1 Biological basis of MEA signals

The MEA-recorded extracellular electrophysiological activity contains extracellular voltage changes that are produced by the neural cell culture growing on top of the electrodes. When the neurons of the population are electrically active they produce voltage changes across their cell membrane. These voltage changes are mediated by ion flow across the cellular membrane and will generate sharp changes in the voltage of the extracellular field. (Buzsáki et al., 2012; Anastassiou et al., 2013) The extracellular voltage changes are recorded by the undelaying electrodes, which are able to record even from distant sources (Bakkum et al., 2013). Thus, the electrodes are thought to record the average voltage of the area at each recording site (Nelson et al., 2008).

The voltage signals recorded by the electrodes contain three types of signals: single-unit activity, multiunit activity and local field potentials (LFPs). The single-unit activities represent extracellular action potentials (EAPs). EAPS are generated by initial and rapid Na^+ ion influx, followed by slow K^+ efflux. These ion flows produce a large negative deflection, followed by a small positive deflection in the extracellular

field. The EAPs are usually tens to hundreds of microvolts in amplitude and are <2 ms in duration (Buzsáki et al., 2012). In contrast to EAPS, the multiunit activity originates from several simultaneously active neurons generating action potentials nearby the electrode (Einevoll et al., 2012). The third component of the signal, the LFP, is recorded from large neuronal population as the synchronous net activity of several hundreds to thousands of neurons (Giacomello et al., 2011; Mahmud et al., 2012; Khodagholy et al., 2015). Due to this complex nature, the desired component is isolated from the rest of the signal and background noise.

2.4.1.2 Neuronal spike activity detection and noise

The success of EAP detection depends on the amplitudes of the extracellular spikes relative to background noise. The sources of noise that affect the final signal-to-noise ratio (SNR) arise from biological background noise, the properties of the MEA electrodes, analog signal processing and digital signal processing.

Biological noise, also known as background noise, arises from the electrical activity of large numbers of neurons too far from the electrode to produce detectable spikes. Signals from sources that are closer than 200 μm are still detectable (Egert et al., 2002; Frey et al., 2009). Thus, increase in general action potential firing leads to the smaller ratio of the amplitudes of the nearby neurons compared to the distant cells, lowering the SNR (Martinez et al., 2009; Harris et al., 2016).

MEA electrode noise is affected by the electrode geometry, impedance and thermal noise (Gesteland et al., 1959; Liu et al., 2007). Furthermore, when the voltage signal is transferred from the microelectrode to the amplifier, it is subject to the 50-60 Hz hum from power lines. This arises from the high impedance in the electrode-to-amplifier-connection at these frequencies. The distance between the electrode and the amplifier is minimized to reduce this so called mains noise. (Kim et al., 2008)

Finally, analog signal processing in the amplifier itself (gain, bandwidth, systems behavior outside the cut-off frequencies), quantization noise during analog to digital conversion (sampling rate, digital processing) and any lossy compression during signal transfers will add additional sources of noise.

2.4.1.3 Extracellular space and the recording

The electrode array on the bottom of the MEA dish covers a varying proportion of the surface available for cell growth. Due to this setup, the seeded neurons form a network randomly and the network might be too distant from electrodes to be measured effectively. This results in a low percentage (often <20%) of activity-

detecting electrodes (Ylä-Outinen et al., 2010; Shein-Idelson et al., 2011; Tukker et al., 2016; Mayer et al., 2018). However, simply plating more neurons to increase cell density has a decreasing effect on the activity (Biffi et al., 2013). Thus, measurements could be improved by restricting the growth area (Erickson et al., 2008; Ylä-Outinen et al., 2010). The restricted growth area shortens the distance between the signal source and the measuring electrode (Obien et al., 2015). Cell growth has been previously restricted successfully with microscale structures made from polydimethylsiloxane (PDMS) (Berdichevsky et al., 2009; Cimetta et al., 2009; Korin et al., 2009; Teixeira et al., 2009).

MEA measurements can also be improved by restricting the extracellular space, or medium volume, around the neurons (FitzGerald et al., 2009; Wieringa et al., 2010; Wang et al., 2012). The limited medium volume improves the measurements by Ohmic amplification. Ohmic amplification increases the extracellular electrical signals due to increased resistance of the volume conductor (medium) (FitzGerald et al., 2008; 2009; Wieringa et al., 2010; Wang et al., 2012). Restriction of the volume was suggested in 1968 by Robinson. He argued that since the resistance of the paths around the glial cells are lower (for signals at 1 kHz) than the paths through them (due to the membranes), the extracellular signals would flow between the cells, not through them. Thus, the tissue or the culture itself can cause directional differences in the conduction of signals (Rice et al., 1993; Okada et al., 1994). However, due to fluidic isolation (Taylor et al., 2005), the restrictive structures can prevent the observation of neural parts, such as the soma or neurites, via immunocytochemistry. This can be overcome by utilizing small dye molecules (Taylor et al., 2005; Narula et al., 2017).

In conclusions, there exist options to improve the current setup for performing MEA measurements, both by guiding the neurons and by amplifying the signal.

2.4.1.4 Spike waveforms

Each of the detected EAPs has a waveform. This waveform consists of the subsequent voltage values produced by the action potential. Typical spike waveforms (EAP waveforms) are 1-2 ms in duration. (Somogyvári et al., 2005, 2012; Frey et al., 2009; Delgado Ruz and Schultz, 2014) The size and shape of the detected spike waveform on a microelectrode depends on the properties of the neuronal signal source, the properties of the medium conductor and the properties of the electrode.

The magnitude, sign, and distance of the current flow source from the measuring electrode are known to affect the recorded waveform. The shape of the waveform is produced by linear distance dependent summation of sources of different magnitudes and signs. The sources are created by currents through ion channels. (Nunez and

Srinivasan, 2006) Thus, spike waveforms differ depending on the relative locations of specific neural parts to the electrode (Henze et al., 2000; Gold et al., 2006).

As a result, the differences in the waveform shapes and amplitudes have been used to classify the activity recorded by a single electrode into the activity of individual neurons. This classification is called spike sorting. The distance between the electrode and the spike source (neuron) has a large impact on the peak amplitude and the stability of the waveform (Egert et al., 2002; Frey et al., 2009). Additionally, changes in individual neurons during the measurement can result in changes in the recorded waveform (McCormick et al., 1985; Henze et al., 2000; Delescluse and Pouzat, 2006; Stratton et al., 2012). Changes to waveforms are directly produced by complex-spike bursts (Harris et al., 2001) or prolonged firing (Quirk and Wilson, 1999), and indirectly by firing history, intrinsic inhibition and neuromodulation (Spruston et al., 1995). Thus, changes in spike waveforms can potentially reflect changes in individual neurons or the firing of the network and are an interesting aspect to study.

2.4.1.5 Bursting

The EAPS detected from MEA recordings can be used to investigate changes in the firing patterns in networks of dissociated neurons. The development of firing patterns is hallmarked by the transition from asynchronous EAPs to a synchronous series of EAPs called bursts (Van Pelt et al., 2004; Wagenaar et al., 2006). Several parameters such as burst frequency and duration are generally used to characterize burst activity (Bal-Price et al., 2010; Lappalainen et al., 2010; Defranchi et al., 2011; Hogberg et al., 2011). The emergence of bursts reflects the development of neural network connections *in vitro*. Furthermore, several preparations, including hPSC-derived neuronal cells, show dynamically varying changes in their bursting patterns during the maturation of cells and networks (Illes et al., 2014; Kapucu et al., 2012), and can be studied to understand the development and functioning of neuronal networks.

2.4.2 Calcium imaging

Similar to MEA, calcium imaging can be used to record patterns of neuronal activity across large populations of neurons simultaneously (Stosiek et al., 2003; Ohki et al., 2005). Calcium imaging is based on monitoring calcium fluxes resulting from series of action potentials (Smetters et al., 1999). To monitor the calcium fluxes, the cells are loaded with a calcium sensitive dye. The dye changes its light emitting properties upon

binding and unbinding from calcium. The binding is weak, and thus the fluctuations of calcium concentration are reflected by the properties of light emitted by the dye. In neurons, action potentials can cause the opening of a group of voltage-sensitive calcium channels. The opening of channels produces a fast and transient flow of calcium into the neuron and this is reflected as a change in the light emitted by the calcium indicator dye (Clapham, 2007). Thus, the dye measured by imaging functions as an indirect indicator of neuronal action potentials (Yaksi and Friedrich, 2006; Vogelstein et al., 2010).

The kinetics of the obtained calcium signal, however, are slower than the currents inside and outside of the neuron. The fastest phase of the calcium signal is the rising phase (~10 ms) (Yaksi and Friedrich, 2006; Vogelstein et al., 2010), but even that is several times slower than the whole duration of the MEA recorded action potential (~2 ms). The kinetics of dissociation are even slower, producing a slow decay phase after the peak (Yaksi and Friedrich, 2006; Vogelstein et al., 2010). Furthermore, the precise relationship between calcium signaling and neuronal spiking is variable (Theis et al., 2016). The variability of this relationship can be observed during bursts of spikes where the size of the calcium signal depends on the inter-spike interval (Pnevmatikakis et al., 2016). Despite this, calcium indicators are able to relatively reliably report the occurrence of spiking or spike burst (Smith and Hausser, 2010; Chen et al., 2013) and they can be treated as somewhat linear reflectors of activity (Rose et al., 2014).

2.4.3 Simultaneous recordings

A complete understanding of how brain circuits function will require measurements that monitor large scale network activity simultaneously with the activity of local neural populations (Shew et al., 2010). Due to the lack of spatial resolution, standard MEAs cannot reveal inactive neurons or the exact locations of active neurons (Cossart et al., 2005; Akerboom et al., 2012). In contrast, calcium imaging is able to provide information on both of these parameters (Tian et al., 2009; Akerboom et al., 2012; Zariwala et al., 2012). However, calcium imaging is not capable of monitoring a neural population in a very large area and it suffers from poor temporal resolution compared to MEA recordings, revealing individual spikes. Furthermore, downstream signals of electrical activity are often mediated by intracellular calcium concentration changes. Thus, combining these two measurement methods might provide valuable insight into the function of the neural network.

2.5 Analysis of neural network activity measurements

2.5.1 MEA analysis

The complexity of data collected by MEA recordings requires sophisticated analysis approaches. Several software tools have been developed by individual laboratories, while several analysis scripts are kept private, reducing the transparency and reproducibility of the analyses (Schofield et al., 2009). MEA analysis is usually performed by subsequent steps of filtering, spike detection, optional spike sorting and spike train analysis. In the end of the analysis pipeline the data can reflect either general activity levels or very specific features of the neurons and network. Many of the methods that are now used for a wide variety of preparations have been initially optimized for primary cultures.

2.5.1.1 Filtering and spike detection

Raw MEAsignals are recorded with a wide-band filter to avoid phase distortion. This signal can then be refined by further filtering. In MEA analyses that focus on the EAP and multiunit activity, the fast EAPs are separated from LFPs with a bandpass filter (Quiroga, 2007). Filtering is used to increase the signal-to-noise-ratio (SNR) for detecting spikes. The SNR dictates how well spikes from neurons can be detected.

In spike detection the voltage traces corresponding to extracellular action potentials are detected from the filtered voltage signal. Amplitude thresholding is the most commonly used method. In amplitude thresholding a spike is detected when the recorded voltage crosses a set value. However, there are also other spike detection-methods such as the two-point procedure (Borghi et al., 2007; Maccione et al., 2009) and template matching (Kim and McNames, 2007). The threshold amplitude is usually set as a multiple of 5 of the background noise level. This noise can be calculated as the root mean square of the voltage signal. However, the threshold can also be estimated using a root median square. The median is less sensitive to outliers, such as the spikes themselves, and is thus more robust with changing spike rates. (Quiroga et al., 2004). The quality of the spike detection determines the quality of the following steps and is thus critical for the whole analysis (Rey et al., 2015). It is also the most time consuming phase as the data will undergo significant reductions.

2.5.1.2 Spike waveform sorting

The timestamps of detected spikes can be used to extract the corresponding waveform of voltage values from the raw signal. In spike sorting, these waveforms recorded by single electrodes are separated into clusters that represent the activity from an individual neuron. This new hidden level arises from sparse coding of single neurons. It became evident in experiments by Quiroga and colleagues (2007) that while the total number of spikes showed no difference in response to stimuli, there was a response masked by the sparse coding of single neurons. This response was only visible after sorting the mixed activity into clusters representing single neurons.

Spike sorting consists of three analysis phases. First, a set of features from each waveform is gathered. These features can be the peak amplitude or width, or can be more complex features evaluated by the principal component analysis (Quiroga et al., 2007) and wavelet transform (Mallat, 1989). Next, the clusters are separated based on grouping of the features to classify similar waveforms representing the activity of an individual neuron (unit). This can be done manually or automatically. Finally, auto- and cross-correlograms are manually used to evaluate the clustering. Fully automatic algorithms, however, have been known to suffer from a lack of sufficient robustness. (reviewed in Harris et al. 2016)

2.5.1.3 Spike train analysis

Extracted time stamps from the MEA data can be used to reconstruct a spike train representing the activity produced by the recorded network. This spike train can then be quantified to make comparisons between networks. The simplest spike train analysis is the summing of total spikes or the calculation of the total spike rate for the recording. A more sophisticated analysis exists and is focused on analyzing clusters of spikes called bursts. Bursting is typically described as periods of intense spiking separated by quiescent periods. Bursts are thought to be the *in vitro* manifestation of network activity and connectivity. However, the definition of a burst lacks consensus (Gourévitch and Eggermont 2007), and several different methods and criteria are used to quantify burst-related parameters from spike trains.

Bursts can be detected based on the threshold between the subsequent spikes in the spike train or sudden changes in the underlying firing rate (Legéndy and Salcman, 1985; Gourévitch and Eggermont, 2007; Ko et al., 2012). Threshold-based methods are most commonly used and they define the minimum firing rate or maximum interspike interval (ISI) allowed for spikes in burst. The methods for determining thresholds vary from fixed values (Chiappalone et al., 2005) to values derived from the properties of the spike trains. The derived values can be based on the total spiking rate

(Pimashkin et al., 2011) or the distribution of ISIs (Kaneoke and Vitek, 1996; Wagenaar et al., 2006; Mazzoni et al., 2007; Selinger et al., 2007; Pasquale et al., 2010; Kapucu et al., 2012; Bakkum et al., 2014).

Furthermore, spike trains can be analyzed for a single channel or for the whole network. A simple visualization of network activity is a raster plot, which contais a single tic for each recorded spike. Another option is to form network-wide spike trains, which have enhanced SNR compared to single-channel spike trains (Bakkum et al., 2014). Burst detection for network-wide spike trains is performed by either detecting the bursts separately for each channel or by calculating the network bursts based on simultaneous bursting (Wagenaar et al. 2006; Pasquale et al., 2010). However, the evaluation of bursting as a network behavior may give further insight into the function of the network as a whole.

2.5.1.4 Analysis of MEA data from hPSC stem cell-derived networks

The neurons derived from human stem cells have been analyzed with previously published methods (Table 7). The analysis methods currently used for a wide variety of preparations were initially optimized for primary neuronal cultures (Cotterill et al., 2016), which contain fully mature neurons. However, newborn neurons have been shown to greatly differ in their spike generation properties compared to fully mature neurons.

Compared to mature neurons with mature spiking properties, young neurons acquire their spiking properties gradually (Lam et al., 2017), and the obtained spikes from hPSC-derived neural cultures have been observed to differ in size from those from primary cultures (Bakkum et al., 2014; Heikkila et al., 2009). Due to low SNR in hPSC-derived networks, a high number of neuronal signals with small amplitudes are not detected (Mayer et al. 2018). Furthermore, there is lack of studies of extracellular spike waveform behavior in cultures with hPSC derived neurons. Furthermore, hPSC-derived neural networks exhibit more variable bursting behavior than rodent neuronal networks (Kapucu et al. 2012). This places an additional burden on accurately choosing parameters for burst detection in recordings spanning a large range of developmental ages (Bakkum et al., 2014). Several research groups have added their own criteria on existing burst detection to cope with these variations (Table 7, last

Table 7. Analyses used for hPSC-derived neural networks with MEA generally involve similar filtering and static threshold based spike detection. Waveform analysis and burst detection are more rarely carried out. Burst detection is most commonly based on inter spike intervals.

	Filtering	Spike detection	Waveform analysis	Burst detection
Heikkilä et al, 2009	200 Hz high-pass	Threshold 5.5 * SD	none	none
Saito et al., 2009	100 Hz-20 kHz	LabView software (National Instruments)	none	none
Ylä-Outinen et al., 2010	nd	Threshold -5 * SD	none	none
Odawara et al., 2014	Mobius software (Alpha Med Scientific Inc.)			
Ylä-Outinen et al., 2014	200 Hz high-pass	MC Datatool (MCS) and MATLAB	none	none
Amin et al., 2016	nd	Threshold 9 * SD	Shoham et al., 2003	none
Fukushima et al., 2016	nd	Threshold 5.5 * SD	none	Li et al., 2007
Nageshappa et al., 2016	nd	none	none	none
Odawara et al., 2016a	nd	Threshold ±5 * SD	none	ISI threshold with additional criteria
Odawara et al., 2016b	nd	Threshold ±5 * SD	none	none
Tukker et al., 2016	200-5000 Hz	Threshold 6 * SD	none	none
Vessoni et al., 2016	10–5000 Hz	Adaptive threshold 5.5 * SD	none	Poisson surprise algorithm
Yamazaki et al., 2016	MED64 Mobius software	Threshold 5.5 * SD	none	Fukushima et al., 2016
Frega et al., 2017	custom software package (Bologna et al., 2010)			
Hyysalo et al., 2017	nd	Threshold ±5 * SD	none	ISI threshold with additional criteria
Ishii et al., 2017	nd	Threshold 5.5 * SD	none	ISI threshold with additional criteria
Kasteel and Westerink, 2017	nd	Threshold 6 * SD	none	none
Kayama et al., 2018	1 kHz low-pass	Threshold 10 μV	none	none
Matsuda et al., 2018	nd	Threshold ±5 * SD	none	ISI threshold
Paavilainen et al., 2018	200 Hz high-pass	Threshold -5 * SD	none	ISI threshold with additional criteria

nd = not defined, SD = standard deviation, none = not performed

column). Thus, the current analysis scheme might not be the most optimal analysis for recordings from hPSC-derived neural cultures. MEA can be improved by refining both the measurements and analysis.

2.5.2 Calcium imaging analysis

Similar to MEA data analysis, the calcium imaging recordings require further processing. In calcium imaging analysis, a time stack of fluorescence images are analyzed to produce activity data for each region of interest (ROI). The ROIs usually correspond to individual neuronal somata, but parts of neurons can also be used. Calcium imaging requires extensive processing to obtain final numbers that reflect activity. The processing can consist of image alignment and motion correction, segmentation, time course extraction of intensities, spike or event detection, and population synchronization analysis.

Image alignment and motion correction are performed to correct for the movement of the whole sample or tissue during the experiment. However, for the movement of individual neurons, more complex tools such as tracking are required. Such tools are needed especially for very migratory neurons, such as young neurons (Paredes et al., 2016). Segmentation is performed to find the pixels that correspond to each ROI. Segmentation can be done manually by drawing each ROI, automatically, or semiautomatically (Ohki et al., 2005). Automatic segmentation such as watershedding or the active contour method can be used to delineate the boundaris of ROIs (Caselles et al., 1997; Chan and Vese, 2001). Additionally, activity-dependent detection algorithms, such as independent component analysis can be used (Mukamel et al., 2009). However, activity-dependent detection and manual detection are biased towards active neurons (Patel et al., 2015; Peron et al., 2015). This can be overcome by labeling cell nuclei with static fluorescence (Peron et al., 2015) or by detecting the resting fluorescence of inactive cells (Reynolds et al., 2017). Similar to spike detection for MEA analysis, segmentation is the most time consuming step in calcium imaging analysis.

Segmentation is followed by time course extraction of the intensity values from pixels defined by ROI from each frame for each cell. The obtained values are summed or averaged to obtain a single value per frame to create a trace for each cell. The time trace is then often normalized due to uneven loading of cells with calcium indicator dye (Paredes et al., 2008). Normalization can be performed relative to known calcium levels or to the baseline level of each cell (Paredes et al., 2008). *In vitro* automated

analysis tools are usully limited to segmentation and normalized fluorescence time course extraction (Ozden et al., 2008; Mukamel et al., 2009; Tomek et al., 2013).

The normalized or nonnormalized intensity traces are analyzed to estimate the underlying neuronal activity. Each transient event in the trace is associated with one or more action potentials within the neuron (Kerr et al., 2005; Dombeck et al., 2007; Greenberget al., 2008; Akerboom et al., 2009). In action potential train estimation, the transient events are extrapolated into numbers representing action potentials. However, automated event detection is problematic due to high variety of events occurring in a neuron as the transient events differ in amplitude and duration and occur at irregular intervals (Patel et al., 2015). The intensity traces can also be used to distinguish between neuronal and nonneuronal cells. Neurons can be distinguished based on their steady-state response to glutamate as opposed to the transient response in other cell types (Pickering et al., 2008).

Spike train estimates can be further used to compute the synchronization and functional connectivity of the network. However, automated analysis tools lack quantitative representations of neural activity patterns. Furthermore, the few tools that exist are focused on the analysis of network connectivity and not on the overall level of network activity (Jee Jang and Nam, 2015; Patel et al., 2015).

The acquisition of neural activity data via calcium imaging has advanced both *in vivo* and *in vitro*. These advances have led to massive image sets, the analysis of which is challenging with current methods (Jee Jang and Nam, 2015). Therefore, tools to automate the whole analysis flow from the single-neuron to the network level are needed.

3 AIMS

The broad aim of this thesis was to explore the topic of modeling brain functionality *in vitro* in hPSC-derived neural networks. This aim was further divided into two more specific aims as follows.

1) To investigate the emergence of electrical activity of single neurons and networks derived from hPSCs (Studies I-IV).

2) To investigate the synaptic connections mediating the patterns of electrical network activity in hPSC-derived neural networks (Studies II and IV).

To fulfill these aims, three supporting aims were set as follows.

3) To evaluate if restricting growth and medium volume available for neural cultures increases the electrical activity measured from the cultures (Study III).

4) To develop and optimize MEA and calcium imaging data analysis for more accurate detection of electrical activity from the networks (Studies II and IV).

5) To develop and evaluate MEA and calcium imaging analysis methods for investigating network level electrical activity (Study IV).

4 MATERIALS AND METHODS

4.1 Deriving neural networks

To obtain neural network cultures, previously established hPSC lines were differentiated into neurons. The lines were derived, characterized, and maintained in house. Both, hESC and hIPSC lines were differentiated into neural precursor cells in suspension. The neural precursor cells were seeded for adherent cell culture. During the adherent culturing, neural precursors matured into neural cells and formed neural networks.

4.1.1 Pluripotent stem cells

4.1.1.1 Derivation and characterization

Three different hESC lines (Regea 08/056, 06/040, 08/023) and one hIPSC line (04311.WT) were used in the studies (Table 8). The derivation and pluripotency characterization of these hPSC lines has been described earlier (Rajala et al., 2010; Skottman, 2010). The hESC lines can be found in the European Human Embryonic Stem Cell Registry (http://www.hescreg.eu/; 09.01.2012). The studies were conducted at tBioMediTech, University of Tampere, Finland. BioMediTech holds an approval from the Ethics Committee of Pirkanmaa Hospital District for derivation, characterization, and differentiation of hESC and hIPSC lines (R05051, R05116, R08070) as well as permission from Valvira, the National Authority for Medicolegal Affairs in Finland, to conduct research on human embryos (1426/32/300/05).

Table 8. hEPSC and hIPSC lines used in the studies carried out in this thesis. The references to the original work characterizing each line is provided when excisting.

Line	Type	Study	Characterized
Regea 08/056	hESC	I	Skottman, 2010
Regea 06/040	hESC	I	Rajala et al., 2010
Regea 08/023	hESC	I, II, III, IV	Skottman, 2010
UTA.04311.WT	hIPSC	III	-

4.1.1.2 Maintenance

The maintenance of the hPSC lines was performed as described by Rajala and colleagues, 2007. The undifferentiated hESC lines were grown as colonies over a mitotically inactivated human foreskin fibroblast (CRL-2429, ATTC, Manassas, VA) feeder cell layer. The hPSC culture medium is described in Table 9. The colonies were enzymatically or mechanically passaged and reseeded on top of a fresh fibroblast cell layer 1-2 times per week. The maintenance of the undifferentiated hESC lines, as described here, was performed by lab technicians. The quality of the hESC lines was determined by frequent gene and protein expression analyses (OCT-3/4, NANOG, Tra-1-81, Tra-1-60), and embryonic body formation, karyotype, and mycoplasma assays. All used cultures maintained normal karyotypes and were mycoplasma free. This study was conducted in accordance with the Ethics Committee of Pirkanmaa Hospital District to establish, culture, and differentiate hiPSC lines (R08070).

Table 9. Compositions of culture mediums used during cell culture as undifferentiated hPSC-colonies, aggregate culture of neural differentiation and adherent culture of neural maturation.

Reagent	hPSC-culture medium	Neural differentiation medium	Neural maturation medium	Enhanced neural maturation medium	Manufacturer
Dulbecco's modified Eagle's medium (DMEM)	75% (v/v)	48% (v/v)	48% (v/v)	48% (v/v)	Gibco
Neurobasal	-	48% (v/v)	48% (v/v)	48% (v/v)	Gibco
knockout serum replacement	20% (v/v)	-	-	-	Gibco
B27	-	0.02% (v/v)	0.02 % (v/v)	0.02 % (v/v)	Gibco
N2	-	0.01% (v/v)	0.01% (v/v)	0.01% (v/v)	Gibco
GlutaMAX	2 mM	2 mM	2 mM	2 mM	Gibco
nonessential amino acids	1% (v/v)	-	-	-	Lonza
penicillin/streptomycin	50 U/ml	25 U/ml	25 U/ml	25 U/ml	Lonza
2-mercaptoethanol	0.1 mM	-	-	-	Gibco
bFGF	8 ng/ml	20 ng/ml	-	4 ng/ml	R&D
BNDF	-	-	-	5 ng/ml	Gibco

Manufacturer references: Gibco = Gibco, Thermo Fisher Scientific, Waltham, MA, USA; Lonza = Lonza Group Ltd., Basel, Switzerland; R&D = R&D Systems Inc., Minneapolis, MN, USA

4.1.2 Derivation of neural networks

4.1.2.1 Differentiation

Neural precursor cells were derived as described by Lappalainen and colleagues (2010). Briefly, neural differentiation was initiated by mechanically cutting adherent undifferentiated hESC and hIPSC colonies. The cut pieces were transferred onto plastic cell culture dishes (low attachment 6-well plates, Nunc, Thermo Fisher Scientific, Rochester, NY) for suspension culture in neural differentiation medium (see Table 9 for components). During differentiation, the cut pieces rounded up and formed spherical floating neural aggregates, called neurospheres. The neurospheres were kept in the neural differentiation medium for 8-33 weeks (Table 10). Half of the medium was replaced three times per week and the neurospheres were mechanically cut 1-2 times per week.

For adherent culturing, the neurospheres were manually dissected into small cell aggregates (Ø ~50 - 200 μm). Approximately 5-20 small aggregates were seeded to the coated cell culturing dish (Table 12). Each aggregate contained approximately 3000 cells (Lappalainen et al., 2010). For coculturing (Study I), the adherent fluorescence labeled cultures were dissected enzymatically (TrypLe Select™, Gibco). After the seeded cells were attached, the culture medium was changed to neural maturation medium (see Table 9 for components). In Studies II and III, the neural maturation medium was supplemented with BDNF and bFGF (enhanced neural maturation medium) after 1 week of adherent culturing.

Table 10. Differentiation and maturation times for each of the studies described in this thesis. During suspension differentiation, the hPSC-derived neurospeheres were kept in the neural differentiation medium. During adherent culture the neurospheres were grown in the neural maturation medium which was changed to the enhanced neural maturation medium in two studies.

Study	Suspension differentiation (weeks)	Adherent culturing (weeks)	Enhanced medium
I	9-33	2-8	-
II	9	7	after 7 days
III	8-10	7	after 7 days
IV	8	5	-

4.1.2.2 PDMS structures

Three different kinds of PDMS devices were utilized in the cell culturing (Table 11) to enhance (Studies I, II and IV) and investigate the enhancement of spiking during MEA recordings (Study III). The PDMS devices were used in combination with MEA dishes. 1-well PDMS devices were manufactured as described by Kreutzer and colleagues (2012). 6 well-devices (SpikeBoosters) were obtained from BioMediTech, Tampere, Finland. PDMS tunnel devices were manufactured at Tampere University of Technology.

A rapid prototyping method described by Park and colleagues (2006) was utilized to manufacture the PDMS tunnel devices. Briefly, a mold was made from SU (SU-8 3050, Micro Resist Technology GmbH) on top of a silicon wafer. The mold was used to produce a PDMS replica. This PDMS replica of the mold was in turn used to produce the final PDMS tunnel device. Both PDMS structures were made using a soft lithography process. For further processing, individual structures were punched out of the PDMS sheets with a 15-mm-diameter punching tool and cell plating areas were punched with 3-mm-diameter manual punching tool.

Table 11. Different PDMS cell culture devices were used during adherent culture in the studies. The devices differed in medium volume and culture area available for cell growth and dimensions of restriction of cell growth between cell culture areas. Devices with no restriction had separate cell culture areas.

	1-well PDMS	6-well device	PDMS tunnel			
Medium volume	1 ml	200 µl	1 ml			
Cell culture area (electrode grid)	4 mm (8 x 8)	3 mm (3 x 3)	3 mm (partial 8 x 8)			
Restriction (w x h x l µm)	-	-	100 x 43 x 1000	500 x 43 x 1000	750 x 43 x 1000	1500 x 43 x 1000
			100 x 105 x 1000	500 x 105 x 1000	750 x 105 x 1000	1500 x 105 x 1000
Study	I, III, IV	II, III	III			

4.1.2.3 Coating for seeding

To enhance the attachment of cells, the culture devices were treated prior to cell seeding (4.1.2.1 Differentiation). The preparation and coating was performed differently depending on the initial sterility and hydrophilicity culture platform (compared in Table 12). Plastic culture dishes were used as such and coated with laminin. Glass cover slips were cleaned with ethanol, dried and coated with laminin. MEA dishes were cleaned with ethanol, dried and then sterilized with UV light inside laminar flow for at least 30 min at room temperature. MEAs were double coated, first

with polyethyleneimine (PEI, Sigma-Aldrich), which was rinsed with sterile water, and next with laminin. PDMS 1 and 6-well devices were attached before PEI coating and PDMS tunnel devices were attached after PEI coating. PDMS devices were hydrophilized with oxygen plasma in a PICO plasma system (Diener electronic) for 3 min at 50 W and finally combined with MEA dishes. The combined device was then coated with laminin.

Laminin was either from mouse or human (both purchased from Sigma–Aldrich, St. Louis, MO). All coatings were performed overnight at +4°C or for two hours at +37°C in a 5% CO_2 humidified atmosphere. After the final laminin coating, the excess laminin was removed from all culture platforms.

Table 12. Preparation of the cell culture platforms for culturing. hPSC-derived neural networks were cultured in several culture formats. The culture dishes were obtained as sterile or were cleaned by ethanol or plasma. To support cell adhesion the hydrophobic cell culture areas were hydrofilized and hydrophilic cell culture areas were coated with laminin. The cells were seeded as pieces of aggregates to an area that was smaller than the culture area available for cell growth.

Culture format	Ethanol wash (%)	Hydrofilization	Laminin (μg/ml)	Seeding density (10^3/cm^2)	Study
Plastic	-	-	10	15-53	I, II, III
Glass cover slip	90	-	20	19-53	I, III, IV
MEA	70	0.1% or 0.05% PEI	20	7-53	I, II, III, IV
1-well and 6-well PDMS devices	70	-	20	30-212	I, II, III, IV
PDMS tunnels	-	oxygen plasma	20	160-212	III

4.2 Functionality measurements

To investigate the functional maturation of neurons and neural networks, the activity was studied with MEA measurements, calcium imaging and patch-clamp technique.

4.2.1 MEA measurements

MEA measurements were made to obtain noninvasive long-term measurements of network activity. During MEA measurements, the cell cultures growing on top of an electrode array were sealed for sterility and placed into a recording system. The

recording system amplifies, filters, digitizes and stores the recorded voltage values from the cell culture on top.

For the recording, the cells were cultured on a dish with electrodes. Three types of MEA dishes with different electrode configurations and cell culture areas were utilized (see Table 13, all purchased from Multi Channel Systems, MCS, Reutlingen, Germany). The microelectrodes had 30 µm diameter and 200 µm inter-electrode distances on all MEA dishes. After the experiments, the MEA dishes were washed with distilled water and placed into Tergazyme solution (4 g/200 ml, Z273287, Sigma-Aldrich) for at least overnight. Tergazyme was washed off with distilled water and the MEA dishes were air dried and stored for reuse.

Table 13. A variety of MEA dishes were used for cell culturing in the studies. The dishes had similar electrode spacing, while the size of the electrode grid and the amount of electrodes per network varied.

MEA property	Study I	Study II		Study III		Study IV
Spacing (µm)	200	200		200		200
Grid	8x8	3x3	8x8	3x3	8x8	8x8
Electrodes	59	9	59	9	59	59

For the MEA measurements, the dishes were sealed during the recordings to avoid contamination. Sealing was performed within a laminar flow hood with 70% ethanol cleaned semipermeable membrane (ALA MEA-MEM, ALA Scientific Instruments Inc., Westbury, NY), glass circles or PDMS circles. After the measurements, the seals were removed, cleaned with 70% ethanol and reused, while the MEA dishes containing the cell cultures were returned to incubator. For the Study IV end-point experiments, the MEA measurements were performed in open culture dishes on gravity fed perfusion. After placing the MEA dish into the amplifier, the system was allowed to settle for one minute before the recording was started.

The MEA measurements were made with two filter amplifiers; with or without a preamplifier. The temperature of the measurement system was controlled during the experiments. Details of the recording systems are listed in Table 14.

Table 14. Two different MEA measurement systems were used in the studies. One of the systems had a separate preamplifier and the extracellular voltages were recorded with different filter amplifiers and at different sampling rates. The temperature during measurements was controlled with same controller but different settings.

MEA system	Preamplifier	Filter amplifier	Temperature controller	Study
I	MEA1060-Inv-BC	FA60S-BC, sampling rate 20 kHz	TC02 (+ 38°C)	I, II
II	-	MEA2100, sampling rate 25 kHz (III), 50 kHz (IV)	TC02 (+ 37-38°C)	III, IV

4.2.2 Calcium imaging

Calcium imaging was perfomed to provide higher spatial resolution while recording from multiple neurons. Cultures grown on top of MEA dishes or on top of cover slips were used. The calcium indicator-labeled (4.3.1 Live-labeling) neural cultures on MEA dishes were attached to the MEA amplifier, and coverslips were placed into an imaging chamber. The neural cultures were then imaged under perfusion (Table 15). Ringer's solution was prepared by dissolving all the reagents (Sigma-Aldrich) in dH_2O, adjusting pH to 7.4 with NaOH.

Table 15. Different salt concentrations were present in solutions used during different measurements and can potentially affect the neural function. The extracellular solutions, Ringer's solution and neural maturation medium, differed in the concentration of several key ions and glucose. The intracellular solution was used only during patch clamp experiments.

Salt	Ringer's solution	Neural maturation medium	Intracellular solution
NaCl	140 mM	93 mM	5 mM
HEPES	10 mM	5 mM	10 mM
D-glucose	10 mM	21 mM	-
KCl	3.5 mM	4.7 mM	-
NaH_2PO_4	1.25 mM	1.3 mM	-
$CaCl_2$	2 mM	1.4 mM	0.1 mM
$MgCl_2$	1 mM	0.8 mM	-
$KMeSO_4$	-	-	140 mM
EGTA	-	-	1 mM
Mg-ATP	-	-	2 mM
Na-GTP	-	-	0.5 mM

4.2.2.1 Preparation

The coverslips were labeled with the calcium indicator (Fluo-4) and placed into a recording chamber (RC-25, Warner Instruments, Hamden, CT) with a preglued glass bottom. The chamber was filled with Ringer's solution and attached to a holder (P3, Luigs and Neumann, Ratingen, Germany). The holder was mounted with a stage adapter to the micromanipulator-controlled stage (SM 5-9, Luigs and Neumann, Ratingen, Germany) of the imaging microscope (10x objective, NA = 0.5, Olympus IX51 microscope). The MEA amplifier was similarly attached to the stage. The fluorescence was confirmed via microscope oculars. After confirming the presence of fluorescence and cells, the perfusion chamber was connected to a gravity fed perfusion system with a peristaltic suction pump (Minipuls 3, Gilson, Limburg, Germany).

4.2.2.2 Collecting image series

During calcium imaging, neural network activity was imaged every 0.5 s (2 Hz). The excitation wavelength was produced with a software-controlled monochromator (Polychrome V, TILL Photonics, Gräfelfing, Germany) and emission was filtered with a filter cube. The emitted fluorescence signal was imaged with a cooled charge-coupled device (CCD) camera (iXion+ 885, Andor Technology, Belfast, Ireland), which was controlled by software (TILLvisON v.4.5.65, TILL Photonics or TILL Photonics Live Acquisition software). Images were exported into TIFF-stacks from TILL Photonics Offline Analysis software and loaded into MATLAB.

4.2.3 Patch-clamp

To study the electrophysiological maturation of individual neurons whole-cell patch-clamp recordings were performed to measure the currents and voltages occurring at a single cell membrane. The coverslips containing neurons were placed into a recording chamber (RC-25) with a preglued glass bottom. The chamber was filled with Ringer's solution (Table 15) and attached to the platform (P3). The platform was mounted with a stage adapter to micromanipulator-controlled stage (SM 5-9) of the imaging microscope (10x objective, NA = 0.5, Olympus IX51 microscope). The perfusion chamber was connected to a gravity fed perfusion system with a peristaltic suction pump (Minipuls 3).

Glass capillaries were pulled with a flaming micropipetter puller (MODEL P1000, Sutter Instruments) from glass stoves (Harvard Apparatus Ltd., 1.5 mm O.D x 1.16

mm I. D). Capillaries were filled with intracellular solution (Table 15). The filled capillary was attached to a pipette holder. The pipette resistances were 3-8 MΩ and only cells that had a seal resistance >1 GΩ were measured. Whole cell voltage clamp measurements were made with 500 ms voltage steps from -80 mV to +50 mV in 10 mV of increments. Whole cell current clamp measurements were made sequentially from unclamped membrane potential (45-55 mV), -70, -80 and -90 mV holding potential with 200 ms current injection from 0 to 160 pA with 20 pA increments. All measurements were made at room temperature. The pipette holder was attached to a preamplifier, and the combination was attached to a micromanipulator (SM 5-9). A chlorinated silver wire electrode was used as a measuring electrode inside the glass capillary. A silver peller was used as a ground and placed in the recording chamber. Signals were amplified with an Axopatch 200B amplifer with 5-10 kHz filtering (Axon CNS, Molecular Devices) and digitized with DigiData 1440A (Axon CNS, Molecular Devices). The whole system resided inside a faraday cage. The system was controlled and the recordings were made with Axon PClamp (Molecular Devices) at 20 kHz sampling rate. Analysis was performed in Clampfir 10.2 (Molecular devices).

4.2.4 Pharmacological studies

Pharmacological substances were applied to block the function of specific channels or receptors, or to study the cell physiology. To obtain a point of comparison, baseline was measured after replacing the cell culture medium with fresh medium at the start of the experiment. The drugs (Table 16) were applied manually (Studies II and III) or via perfusion system (Study IV). The manually applied drugs were added in very small volumes (≤ 5 µl) from the drug stock solution to the cell culturing solution on the MEA dish (800 µl). After drug application, the MEA dishes were incubated (times in Table 16) in an incubator (+37°C, 5% CO_2, humidified atmosphere) before the MEA measurements were performed. During washout, the medium was replaced with fresh preheated (+37°C) cell culturing medium to obtain conditions similar to those during baseline recording. Using gravity fed perfusion system the drugs were diluted to their final concentration with Ringer's solution. Each drug was assigned a separate perfusion line (2 ml/min, ALA Scientific).

Table 16. Several pharmacological agents were used in different studies. The final concentrations, incubations times and related studies are summarized here. The abbreviations, expected function and manufacturer are also listed.

Drug	Concentration	Incubation	Study	Abbreviation	Function	Manufacturer
Tetrodotoxin	1 μM	acute	III	TTX	sodium channel antagonist	Tocris Bioscience
L-glutamic acid	30 μM	1-2 min	IV	glut	glutamic receptor agonist	Sigma
Potassium	5 mM	1 min	IV	K^+	component of ion gradient	Sigma-Aldrich
γ-Aminobutyric acid	100 μM	5 min, 3 min	II, IV	GABA	GABA receptor agonist	Sigma
Bicuculline methiodide	30 or 10 μM	5 min, 3 min	II, IV	Bic	$GABA_A$ receptor antagonist	Sigma
Carbenoxolone	25 μM	10 min	IV	CBX	gap junction blocker	Sigma-Aldrich
6-cyano-7-nitroquinoxaline-2,3-dione	20 μM	5 min	II	CNQX	AMPA/KA receptor antagonist	Abcam
2-amino-5-phosphonopentanoic acid	30 μM	5 min	II	D-AP5	NMDA receptor antagonist	Abcam

4.3 Cell labeling

Living cells were labeled for functional studies and growth assessment. For immunochemical binding-based protein expression studies (immunocytochemistry), the cells were fixed before labeling.

4.3.1 Live-labeling

For the calcium imaging, the neural cultures were loaded with a calcium indicator Fluo-4 AM (4 μM, F14201, Thermo Fisher Scientific). The dye was diluted in fresh cell culture medium and incubated for 30 min at 37°C and 5% CO_2. During this time, the acetoxymethyl (AM) tail is cleaved by intracellular esterases and the dye becomes trapped. After dye incubation, the remaining extracellular dye was removed by a wash with fresh Ringer's solution for 30 min at 37°C and 5% CO_2. The emission of Fluo-4 is increased upon binding of calcium ($K_d(Ca^{2+})$ of 345 nM). Thus, the intensity of Fluo-4 reflects the intracellular calcium concentration changes.

To visualize neurites within PDMS devices, a lipophilic carbocyanine molecule 1,1'-Dioctadecyl-3,3,3',3'-tetramethylindodicarbocyanine perchlorate (DiD) is was used. In

a hydrophilic environment, DiD is weakly fluorescent but in the lipophilic lipid environment of the cell membrane, DiD becomes strongly fluorescent (Molecular Probes® Handbook). DiD has an absorption maximum at 644 nm and an emission maximum at 665 nm (Molecular Probes® Handbook, Section 14.4). For labeling, a 20 mM DiD stock was prepared from DiD oil (D-307, Lot 461358, 25 mg, Molecular Probes Invitrogen) by dissolving it into 99.8% ethanol. The final DiD concentrations were prepared from the stock on the day of use. The culture medium was replaced with DiD containing fresh medium and incubated at +37°C, 5% CO_2, humidified atmosphere. After labeling, the medium was replaced with fresh culture medium and the cells were imaged at varying periods after labeling.

To visualize the location of somas within PDMS devices a DNA binding small molecular dye 4',6-Diamidino-2-phenylindole (DAPI, D1306, Molecular Probes Invitrogen) was used to label the nuclei. The dye was tested at 0.1 mM and 1 mM concentrations for 5 min, 30 min and 24 hours. The final concentration used to label the nuclei in the PDMS devices was 0.1 mM for 24 hours.

4.3.2 Immunocytochemistry

To study the protein expression of proliferation, neuronal and astrocyte markers indirect immunocytochemistry was performed on adherent cultures. Medium was removed, and cells were rinsed with Dulbecco's phosphate-buffered saline (RT, DPBS, Bio Whittaker, MD, USA) to remove extracellular proteins. Cells were fixed with cold (+4°C) paraformaldehyde (4%, 15 min, RT). Paraformaldehyde was washed twice with DPBS and the protocol was continued immediately or the cultures were stored at +4°C for later use. To prevent nonspecific antibody binding, nonspecific sites were blocked with normal donkey serum solution (10%, NDS, Millipore, 0.1% Triton X-100, Sigma or 0.1% saponin Sigma–Aldrich, 1%, bovine serum albumin BSA, Sigma, DPBS). Cells were incubated with primary antibody dilutions (1% NDS, 1% BSA in DPBS with 0.1% Triton X-100 or 0.1% saponin) overnight at +4°C. The unbound primary antibodies were removed by washing with 1% BSA in DPBS without or with 0.1% saponin. The secondary antibodies were added (in 1% BSA in DPBS without or with 0.1% saponin). Due to the photosensitive nature of secondary antibody conjugates, the cultures and reagents were kept in the dark during the following phases. Secondary antibodies were incubated at room temperature for one hour. The excess secondary antibodies were removed by washing with PBS and phosphate buffer without saline. Nuclei were stained and the cultures were mounted

with Vectashield containing 4,6-diamidino-2-phenylindole (DAPI, H1200, Vector laboratories, Peterborough, UK).

Permeabilizing agents were used to guarantee the access of the antibodies to their intracellular targets. To avoid fluorescent dye loss while keeping the cytochemical staining optimal, two different permeabilizers were studied. Triton X-100 was used at a 0.1% dilution in blocking and primary antibody solutions. Saponin (7900-25 g, Sigma-Aldrich) was used as 1% and 0.1% solutions and was added to the blocking, primary antibody, washing and secondary antibody solutions. The immunocytochemical staining protocol was also performed with no permeabilization.

Neuronal cell bodies and processes were detected based on being bound by antibeta-III Tubulin (β-tub) (rabbit, 1:2000; GenScript) or, anti-MAP-2 primary antibody (rabbit, 1:600 or 1:400, AB5622, Millipore, Billerica, MA, USA); anti-GFAP primary antibody (sheep, 1:600, AF2594, R&D Systems, Minneapolis, MN, USA) for was used for detecting astrocytes. The proliferating cells were identified based on nuclear binding of anti-Ki-67 (rabbit, 1:800, AB9260, Millipore). AlexaFluor-488, -568 or -680 conjugates of antirabbit or antisheep secondary antibodies (1:600, Molecular Probes Invitrogen) were used as secondary antibodies.

4.3.3 Imaging systems

To observe the cell morphologies, a phase contrast imaging in all experiments was performed with a Nikon Eclipse TE2000-S (Nikon Corporation).

To obtain images from fluorescent marker labeled cells, fluorescence imaging was performed with an Olympus IX51 inverted microscope, using PlanFLN 4×, 10×, 20×, and 40× objectives and an Olympus DP30BW CCD camera. The light was filtered with U-MNU2 (excitation filter 360–370; emission filter 420; dichromatic filter 400), U-MNB2 (excitation filter 470–490; emission filter 520; dichromatic filter 500), U-MWG2 (excitation filter 550-510; emission filter 590; dichromatic filter 570), or U-N41023 (excitation filter 625–675; emission filter 710; dichromatic filter 680) filter cubes.

To obtain desired illumination and imaging speed, the calcium imaging was performed with an Olympus IX61 inverted microscope (10x objective, NA = 0.5), an Andor iXon 885 EMCCD camera (Andor 169 Technology, Belfast, Northern Ireland) and a Polychrom V monochromator (TILL 170 Photonics, Munich, Germany). Images were acquired with TILL Photonics Live Acquisition software.

4.4 Analysis

4.4.1 MEA data analysis

MEA recordings produce high sampling rate voltage data. To obtain meaningful information the MEA data analysis consisted of several subsequent phases (Table 17). Two of the phases were common to all studies. First, the spikes, representing action potentials recorded by the electrodes, were detected (Table 18) from the recorded voltage traces. When MEA recordings were made in conjunction with perfusion and imaging, a noise removal was used to remove the noise caused by the perfusion and imaging. Next, the spike timestamps provided by spike detection were used to generate raster plots and total spike counts for evaluating the ongoing action potential firing in the network. In Studies II-IV, burst detection was applied to detect and evaluate network activity patterns. Furthermore, in Study III, waveform clustering was utilized to investigate the shapes of detected action potentials.

Table 17. Comparison of components and outputs of the MEA data analysis flow in each study. The methods used for different detections are highlighted with grey background and the number in the brackets refers to the section where the method is described. The parameters gained out from the analysis are on while background. The spike and burst detection setup consisted of similar methods and output parameters only between Studies II and III.

Analysis phase	Study I	Study II	Study III	Study IV
Noise removal	-	-	-	median (4.4.1.1)
Spike detection	MCS (4.4.1.2)	Quiroga (4.4.1.3)	Quiroga (4.4.1.3)	windowed Quiroga (4.4.1.4)
Burst detection	-	Kapucu (4.4.1.6)	Kapucu (4.4.1.6)	prominence (4.4.1.6)
Waveform clustering	-	-	WaveClus (4.4.1.5)	-
Network activity	raster plot	bursts	bursts	network activity peaks
Raster plots	black and while	black and while	black and while	grayscale
Event occurrence	-	burst count	burst count	interval
Event duration	-	burst duration	burst duration	peak width
Activity during event	-	spikes in burst	spikes in burst	prominence, max spiking frequency
Whole recording	total spikes,% of active electrodes	total spikes,% of active electrodes	total spikes,% active electrodes	-

4.4.1.1 Noise removal

When MEA recordings were made in conjunction with perfusion and imaging, noise removal was used to remove the noise caused by perfusion and imaging. To remove the noise the digitized recordings were imported to MATLAB (MathWorks, Inc., Natick, MA, USA) with NeuroShare library (NeuroShare Library, 2003). Noise was removed by subtracting the median voltage of all electrodes from the voltage of each individual electrode.

4.4.1.2 MCS spike detection

To extract the frequenzies containing fast action potential spikes, digitized recordings were preprocessed before spike detection with 50 Hz (notch) band reject and 200 Hz high pass (a second order Butterworth) filter. Spike detection was performed in MC_Rack and spike detection was set to 5 times standard deviation. Most of the spikes visualized by eye were upwards, thus only upwards spikes were detected. The detected spike timestamps were extracted with NeuroExplorer (Nex Technologies, Littleton, MA) for further analysis.

4.4.1.3 Quiroga-based spike detection

To detect both upwards and downwards spikes, Quiroga-based spike detection was used. The signal was bandpass filtered (200-3000 Hz). Spikes were detected as events that crossed 5 times the median noise similar to Quiroga and colleagues (2004). The median noise was calculated by taking the median of the absolute values in the analyzed signal window and dividing this with 0.6745. After threshold crossing, a detector dead time was applied counting from the peak amplitude of the waveform. Spike timestamps and cut-out waveforms were stored for further analysis.

4.4.1.4 Adaptive spike detection

To detect spikes from recordings with varying level of noise, the Quiroga-based spike detection was implemented with windowed spike detection. The signal was bandpass filtered (200-3000 Hz). Several windows (0.05, 0.1, 0.5, 1, 10, 30, 50, 70, 90, 100, 300 s) with different overlaps (30%, 50% and 80%) were compared for optimal spike detection. Finally, the signal was analyzed in 30-s windows with an 80% overlap with Quiroga-based detection. The windows were used to calculate the median noise for spike detection.

Table 18. The spikes representing action potentials were detected differently in each of the studies. The prefiltering was performed similarly while two different methods were used. All of the methods were based on threshold but only one of them was adaptive. When applying Quiroga-based spike detection different parameters were used for detector dead time and different time window for cutting out spike waveforms was used.

Spike detection parameter	Study I	Study II	Study III	Study IV
Method	MCS	Quiroga (4.4.1.3)	Quiroga (4.4.1.3)	Quiroga (4.4.1.3)
Prefiltering	200-3000 Hz	200-3000 Hz	200-3000 Hz	200-3000 Hz
Basis	Static threshold (only positive)	Static threshold (both)	Static threshold (both)	Adaptive threshold (both)
Threshold (window)	5 * SD (300s)	5 * noise (300 s)	5 * noise (600 s) 500 * noise as top	5 * noise (30 s)
Detector dead time		1.48 ms	1.48 ms	1.5 ms
Waveforms		1 ms before, 2.2 ms after	0.8 ms before, 1.76 ms after	1 ms before, 2.2 ms after

4.4.1.5 Waveform clustering

To analyze the shapes of the action potentials, a waveform clustering analysis was performed. First, each of the recordings was sorted into clusters separately. Second, representative waveforms were determined. Finally, clusters form each recording were associated with each other based on a correlation analysis.

The waveforms stored during spike detection were analyzed and sorted into clusters based on their shape. Thus, each cluster contained spike waveforms with similar shapes. Waveform sorting consisted of an automatic and manual phase and was based on the Wave Clus algorithm (Quiroga et al., 2004). For the automatic clustering, the minimum cluster size was initially set to 5 or 50 spikes for waveforms from a single electrode or for waveforms pooled from all electrodes in a single culture. After automatic clustering, the temperature parameter was manually tuned to ensure that no more clusters with distinct average spike waveforms could be formed. If the tuning produced new clusters, the new clusters were used instead of the automatic clustering results. After clustering, an average cluster waveform, together with lower and upper standard deviation waveforms, were stored.

The waveforms from different pharmacological treatments were each clustered separately. To associate clusters detected from different recordings from the same electrode or culture, representative waveforms needed to be selected. For the single electrode analysis, the most distinguished average spike waveforms occurring during the entire pharmacological experiment were selected by visual assessment. For

waveforms pooled from the entire network, the clusters present during the baseline recordings were considered the representative waveforms.

To associate clusters between pharmacological treatments, a correlation analysis was performed. In the correlation analysis, a cross correlation was calculated for average waveforms and their standard deviation waveforms between the representative clusters and the rest of the clusters. The waveforms with the highest cross correlation were assumed to be the corresponding cluster in a separate recording. If the highest cross-correlation did not occur between the same clusters for an average waveform and its standard deviation waveforms no association was assumed and the cluster was marked as a representative of a new spike type.

4.4.1.6 Burst detection

To quantify the network activity patterns, two methods for detecting the temporal clustering of spikes into bursts were applied. In Studies II and III, an adaptive inter spike interval-based algorithm, developed by Kapucu and colleagues (2012), was utilized. Briefly, for the adaptive, burst detection a cumulative moving average (CMA) was calculated for inter-spike intervals (ISIs). From this, a spike frequency threshold (or inter-spike interval threshold) was determined for the bursts and burst tails. Spikes were labeled burst spikes if their interval to a nearest spike was shorter than the threshold. Finally, sequences of burst spikes that consisted of less than three spikes were rejected as bursts. Only electrodes with more than 50 spikes during a 300 s recording were included in the analysis. Burst detection provided values for the average spikes in a burst, the number of spikes inside and outside bursts, the average burst duration and the number of bursts.

In Study IV, a new spike rate-based algorithm for detecting the temporal clustering of spikes was developed to be able to compare quantified MEA data to calcium data. To obtain a combined spike rate for the network, all the recorded timestamps from a network were pooled into a single vector. Next, the combined spike rate vector (10 s bins, 80% overlap) was calculated from the timestamps. Peaks in the spike rate were detected from the combined spike rate vector using the peak detection function of the MATLAB Signal Processing Toolbox. A threshold prominence of 0.05 Hz was used as a criterion. Prominence-based detection was used to detect events when the spike rate in the whole network increased temporally from the baseline level of activity. Network activity peak detection provided values for the peak width, prominence, height and timing.

4.4.1.7 Joint analysis

The joint analysis was developed by combining spike sorting and burst detection to unravel the changes in the spike waveform composition of the bursts. First, spikes were detected (as described earlier, 4.4.1.3). Next, the spikes were sorted into clusters and bursts were detected in parallel and independent of each other. Finally, the sorted spikes were labeled burst spikes or individual spikes based on the burst detection. The networks that did not exhibit any bursting were excluded from the analysis. The joint analysis provided values for the number of each spike waveform inside and outside the bursts.

4.4.2 Image analysis

4.4.2.1 Quantification of calcium imaging

Calcium imaging was quantified to allow comparisons between networks, neurons and to allow comparison to MEA recordings. For the calcium imaging analysis, the intensity fluctuations were extracted, normalized and quantified for neural cultures and for single neurons. To extract the calcium sensitive dye intensity fluctuations, an automatic segmentation of the imaged frames was performed together with tracking the motion of the neurons from frame to frame. A custom MATLAB algorithm was built for these tasks. The amount of data processed and produced by each step is summarized in Table 19.

Table 19. Amount of data as bytes on hard drive and as frames together with time required for segmentation and tracking. The values for total segmentation and tracking are estimates based on the average recording.

	n (networks)	Data	Frames	Segmentation	Tracking	n (traces)
Total	30	77 GB	133200	77 days	14 days	18659
Average	-	2.56 GB	4440	50 s per frame	9 s per frame	622

Segmentation

Image segmentation consisted of preprocessing, followed by foreground and background marker-guided watershed transformation. Segmentation provided values for centroid location, belonging pixels and area for each detected cell in each frame.

The image sequences were preprocessed to enhance the fluorescence in the image used for foreground and background marker detection. The preprocessing was

performed by averaging 50 subsequent frames (25 s) and the scaling pixel values to range [0, 1]. Overall, 10, 100, 200 and 500 frame windows were tested for averaging. Fifty frame window was the best compromise between enhancing cell fluorescence and cell motion affecting the segmentation. Preprocessing was performed only to obtain segmentation data and the traces were collected from the unprocessed image sequences.

Marked guided watershedding reguires markers, but instead of manually providing the markers an automated method was developed to decrease the amount of manual work and human bias. Morphological operations are often used in different image segmentation applications and were evaluated for suitability to segment fluorescence images. Foreground markers were generated by a sequence of morphological operations. A morphological opening was applied to the preprocessed images, and a threshold was used to identify the high intensity objects. The pixels of the identified objects were subtracted from the averaged and scaled images. The resulting images were eroded with a flat morphological disk-shaped structuring element (radius 2) and regional maxims were identified from the resulting images. The identified regional maxims were eroded and subsequently dilated using a 3-by-3 neighborhood for both operations. Background markers were generated by utilizing the identified foreground markers in a watershed operation. First, the foreground markers were set to an equal value in the preprocessed images. Next, the resulting images were converted to binary images by thresholding with Otsu's method (Otsu, 1979). The watershed was performed with Fernand Meyer watershed algorithm (Fernand, 1994) using Euclidean distance transform computed from the binary images. Background markers were generated by setting the watershed regions to 0. The background markers were postprocessed by morphological dilation (flat disk-shaped structuring element of radius 2). The resulting pixels were removed from the set of foreground pixels to ensure the separation of foreground and background markers.

Watershedding provides a way to detect complex structures, such as cell boundaries. Thus, for the final segmentation, a watershed was performed onto the filtered images containing foreground and background markers. First, the preprocessed images were filtered with two filters in parallel. The filtering was performed with a predefined Sobel horizontal edge-emphasizing 2D-filter and its transpose. The values outside the bounds were assumed to be equal to the array border value for both filtering operations. The exponents of the filtered images were summed and a square root was taken from the sum. The foreground and background markers identified earlier were utilized to impose regional minimums onto the resulting images. Finally, a watershed operation was performed.

Tracking

Due to the cell migration during the imaging, the motion of the cells needed to be accounted for when evaluating their fluorescence trace. This was done by performing tracking. The centroids resulting from segmentation were connected between frames to obtain intensity traces from frame to frame for each cell. The connection was determined by minimizing the distance simultaneously between all of the centroids of the detected cells on the subsequent frames. The optimal association between centroids was calculated with the James Munkres's variant of the Hungarian assignment algorithm (Munkres, 1957). A cost matrix was calculated from distances between all centroid pairings. A gating threshold of 20 was used for distances together with a gating cost of 5000. The cost of nonassignment was set to 500. The minimum track age was set to 20 frames and the visibility to 0.5 of the time. Fluorescence intensity traces for each cell were collected based on the tracking information.

Trace exclusion and quantification

To exclude noisy traces from the analysis, the collected traces were filtered with a Butter bandpass filter (0.0013 Hz-0.02 Hz), and traces with a standard deviation greater than 0.05 were removed as having a noisy baseline. To exclude dysfunctional neurons, traces with less than a 10% increase in fluorescence during the application of high potassium were removed as inactive or as originating from cells other than neurons. The amount of remaining traces in a network was always more than 98% of the initial traces.

To quantify the slow GABA-induced depolarization, all of the included traces were refiltered from unfiltered traces (0.024-Hz lowpass). To quantify the properties of fast activity peaks and for forming the network responses, the traces were refiltered (0.005 Hz-0.2 Hz) from unfiltered traces and normalized [0 1]. To obtain an overview of the calcium level fluctuations, all of the individual filtered and normalized calcium traces were converted back to intensities and aligned for each network. To form the network response, the filtered and normalized traces were summed and the sum was normalized [0 1].

Automated prominence based peak detection was evaluated to automate the network and single neuron activity detection Network activity peaks were identified when the peak prominence exceeded 0.025. The same criterion was used for the individual traces. Peak detection for both the individual traces and network traces was performed with the MATLAB Signal Processing Toolbox. Peak detection provided values for each peak for width, prominence, height and timing. The distributions of the peak parameters were collected into histograms with 0.005 prominence or 1-s

inter-peak-interval binning. Change distributions were also represented as histograms; all with 5% binning. Cumulative sums were obtained from the aforementioned histograms.

4.4.2.2 Quantification of neurite orientation

To investigate the effect of PDMS devices on the neurite growth, the orientation of neurites was analyzed. Images were collected with a phase contrast microscope from 5-week-old cultures. The images were taken either from neurites inside the tunnels or from freely growing networks on cell culture plates. The images were preprocessed to exclude electrodes and their tracks from the analysis. This processing was performed in MATLAB by replacing the pixels corresponding to the electrodes and their tracks with the local mean intensities. The local mean intensities were calculated from the corresponding regions of each image. The analysis was performed with CytoSpectre 1.2 software (http://www.tut.fi/cytospectre) (Kartasalo et al., 2015). The used parameters can be found in Table 20. The software calculated the orientations of the image components based on the spectral analysis. The orientation is described with a circular variance value from 1 for randomly aligned components to 0 for completely unidirectional components.

Table 20. The settings used for performing neurite orientation analysis with CytoSpectre.

CytoSpectre Setting	Value
component mode	mixed
spectral resolution/noise	balanced
component size (min/max)	1 μm/30 μm

4.4.2.3 Quantification of cytochemical labelings

To quantify the cytochemically labeled networks, a minimum of 6 images were obtained (from at least 2 parallel wells and at least 3 images per well). To quantify the percentage of dividing cells, DAPI- and Ki-67-positive nuclei were manually counted from the images. The proportion of Ki-67-positive nuclei from all nuclei (DAPI) was calculated.

4.4.3 Statistical analysis

The data gained from the manual cell counting of the Ki-67-labeled networks were analyzed with nonparametric Kruskal-Wallis tests followed by the Mann-Whitney U-test (post hoc test). A p-value less than 0.05 was considered significant. If more than two groups were analyzed, the resulting p-values were multiplied by the number of comparisons performed (Bonferroni correction). Linear regression analysis between activity pattern peak parameters as median values from 5 networks with 95% confidence intervals was performed to investigate the relationship between parameters obtained with different methods. GraphPad Prism version 5.02 was used for all analyses.

5 SUMMARY OF THE RESULTS

In this section, the main results of the publications (I, II, III, IV) are summarized and combined under three general topics. The first topic, "Validation of functional neurons and networks in the *in vitro* model", summarizes the results, pointing to the existence of functional neurons and networks in the model. The second topic, "Engineering the analysis and measurements of functionality in the *in vitro* model", summarizes the major improvements engineered to advance the analysis and measurement of neural functionality in the model. The third topic, "Biological studies of functionality in the *in vitro* model", summarizes the most important results related to the biology behind the functionality in the model.

5.1 Validation of functional neurons and networks in the *in vitro* model

To ensure that differentiation produced functional neurons and networks, the neural properties of the neurons derived from hPSCs using the suspension differentiation method were assessed during Studies I, II, III and IV. The neural nature of the differentiated cells was verified on a molecular level and the neuronal functionality was assessed on both the single-neuron and network levels.

5.1.1 Neural marker expression

The neural differentiation of cells was confirmed by the emergence of neural morphology assessed with light microscopy observations 2-3 times a week in Studies I-IV. An example phase contrast image is shown in Figure 1A (unpublished). Most of the cells in the adherent cultures displayed neural morphology as evidenced by compacted soma and long thin processes. The second most common morphological group was cells with slightly larger soma and astrocyte morphology. Occasionally, flat cells with no star-like morphology and round cells with no morphology were also observed. The neural differentiation of cells was confirmed on a molecular level with immunocytochemical stainings

(Studies I and III). The stainings were made for neuronal markers (MAP2, βtubIII) and an astrocyte marker (GFAP). The neural markers revealed the cells had a neural morphology with thin long processes. Exemplary fluorescence microscopy images are shown in Figure 1B-D (Study I and III). Furthermore, proliferation in neural networks was studied, and the networks were found to contain cells that were actively dividing (Study I). The amount of dividing cells was 20%.

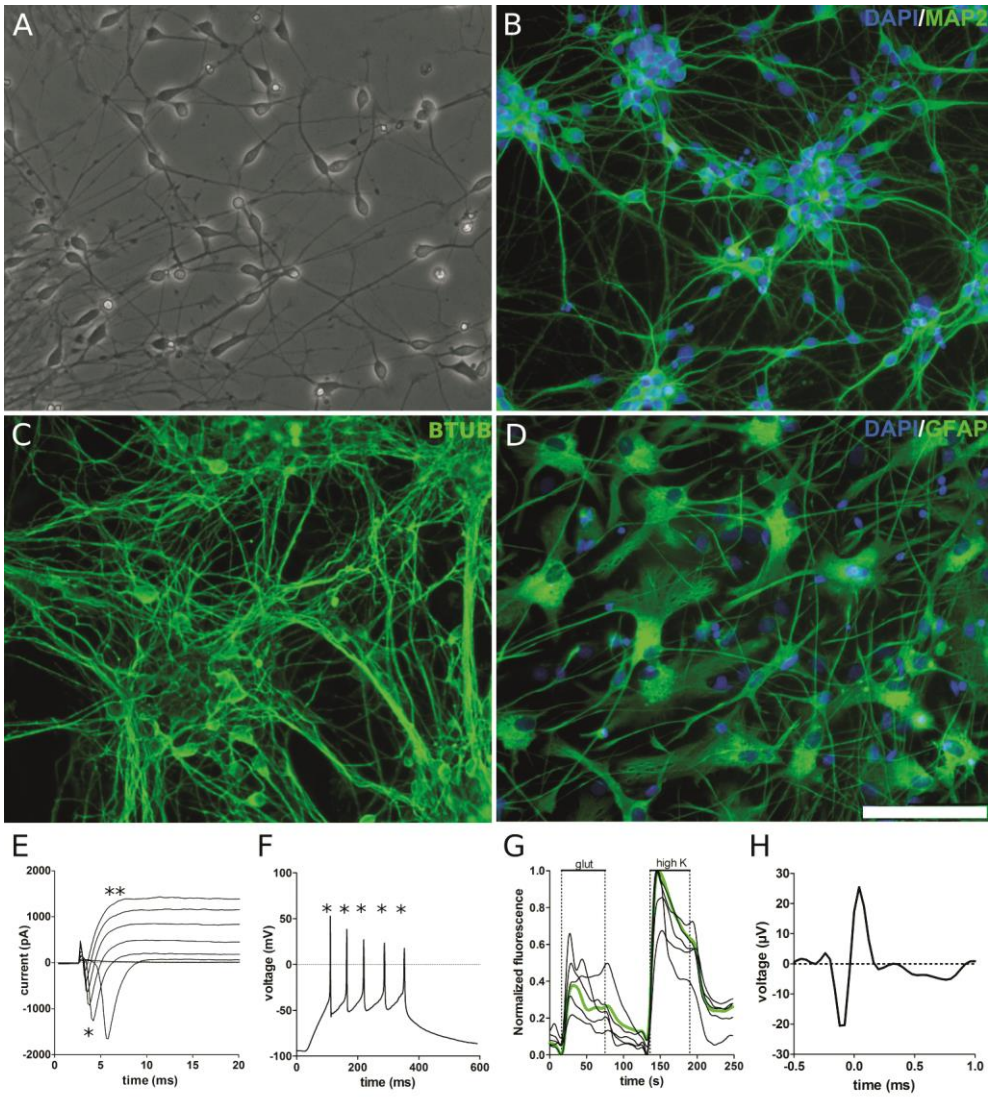

Figure 1. The differentiated cells exhibited morphological, molecular and electrophysiological features of neuronal cell types. (A) Phase contrast image demonstrating that the cells displayed neural morphologies. (B-D) Immunocytochemical staining of a neural cell culture revealed that the cultures were expressing neural markers MAP2- (B, green) and βtubIII- (C, green), and astrocyte marker GFAP (D, green). The scale bar in A-D is 100 μm. (E) Single-neuron whole-cell voltage-clamp recordings displayed current responses typical to neurons after 3 weeks of adherent culture. * marks the fast inward currents and ** marks the outward rectifying currents. The recorded current responses (y-axis) are shown as a function of time (x-axis) through a series of depolarization steps (F) Single-neuron whole-cell current-clamp recordings displayed neuronal voltage responses, action potential trains after 3 weeks of adherent culture. The recorded voltage response (y-axis) is shown as a function of time (x-axis) in response to a current injection. * marks the action potentials. G) Neurons produced calcium transients as reponse to glutamate and high potassium after 3 weeks of adherent culture. The intracellular calcium level (y-axis) is shown as a function of time (x-axis) from 5 simultaneously measured neurons (black traces) and the whole population (green trace). The bars with glut and high K mark the time windows of glutamate and high potassium concentration application. H) Neurons produced fast extracellular voltage fluctuations corresponding to extracellular action potentials. The extracellular voltage change (y-axis) is shown as a function of time (x-axis) during a single spike waveform recorded via a single MEA electrode.

5.1.2 Expression of electrical functionality

The emergence of electrical functionality was confirmed with patch-clamp (unpublished), calcium imaging (Study IV), and MEA measurements (Studies I-IV). The whole-cell patch-clamp measurements were made in voltage-clamp mode to revealed currents typical to neurons. The voltage-clamp measurement from one neuron showing inward and outward currents is shown in Figure 1E. These currents were observed to grow in size during the adherent culture (more carefully studied in Prajapati (2014). Furthermore, the current-clamp measurements from the differentiated neurons were made to reveal voltage responses typical to neurons. A train of action potentials measured in response to a depolarization pulse is shown in the Figure 1F. Neurons with multiple action potentials were rare. Calcium imaging revealed neuronal responses to stimulation with glutamate and high potassium (Figure 1G). Some cells showed a maximal response to both glutamate and high potassium, while some responded only to potassium. Furthermore, MEA measurements revealed sharp extracellular voltage signals (Figure 1H). Thus, the three separate methods showed behavior typical of neurons. Waveforms were few tens of microvolts in amplitude and on the millisecond scale in duration. The amount of spiking increased during the first few weeks in culture.

5.1.3 Emergence of functional networks

The emergence of neuronal network functionality was investigated with MEAs (Studies I-IV) and calcium imaging (Study IV). The emergence of network activity progressed through three phases. During the first and second week of adherent culturing, the neural cultures developed scarce asynchronous activity. This was seen as asynchronous, infrequent extracellular voltage spikes in the MEA recordings (Figure 2A, unpublished). In the calcium imaging, single neurons showed asynchronous infrequent intracellular calcium transients (Figure 2B and C). Next, neural cultures developed semisynchronous activity. On MEA the recordings, this was observed as more frequent extracellular voltages and partial synchrony between electrodes (Figure 2D). On the calcium imaging, this was indicated by more frequent more aligned intracellular calcium rises with loose temporal associations (Figure 2E and F). Finally, the neural networks developed strong synchronous activity. On the MEA recordings, this was observed as bursts of activity separated with periods of silence (Figure 2G). On calcium imaging, this was indicated by tightly synchronous intracellular calcium rises (Figure 2H and I). The synchrony was very strong between the neuronal traces and the intervals between events of synchronous activity were devoid of spikes. The emergence of synchronity on MEA was generally observed after three weeks of adherent culture. The activity on MEA, even when synchronous, was not temporally very strongly correlated between different electrodes. Individual spikes occurred closer to each other than during the event intervals, but with clear silent periods in between events. Furthermore, single electrodes occasionally detected bursts of activity. The bursts were distinguishable because of a clearly higher spike rate center.

Figure 2. Synchronous activity emerged in the neural cell cultures as a function of network age and was visible in both MEA recordings and calcium imaging. (A, D, G) Raster plots from MEA recordings showed initially random spikes (black bars) which grouped during the network maturation. Detected spikes from each of the MEA electrodes (y-axis, 59 electrodes) are shown as a raster plot during a 5 min recording (x-axis). (B, E, H) Individual intracellular calcium fluctuations synchronized between neurons. The intracellular calcium levels (y-axis) from 6 neurons are shown as a function of time (x-axis). (C, F, I) The aligned traces of intracellular calcium fluctuations as intensities showed an increasing proportion of neurons with synchronous elevations in intracellular calcium during network maturation. The intracellular calcium levels as intensity from all neurons (y-axis) in the imaged field are shown as a function of time (x-axis). Representative recordings shown from networks displaying (A, B, C) asynchronous activity, (D, E, F) semisynchronous activity, and (G, H, I) synchronous activity. Moments of synchrony are labeled with *.

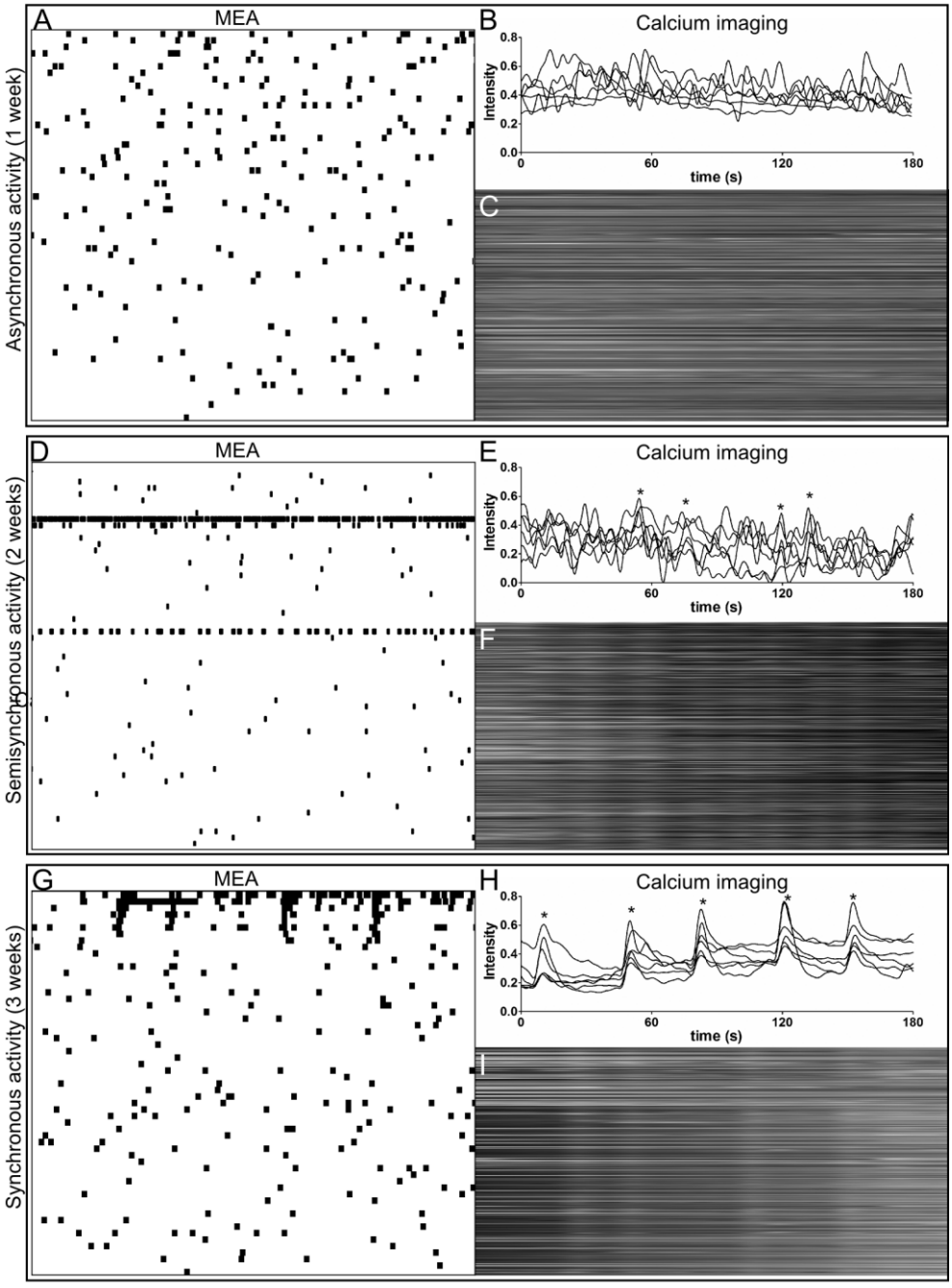
A
MEA
B
Calcium imaging
Intensity
0.8
0.6
0.4
0.2
0.0
0
60
120
180
time (s)
C
Asynchronous activity (1 week)
D
MEA
E
Calcium imaging
Intensity
time (s)
F
Semisynchronous activity (2 weeks)
G
MEA
H
Calcium imaging
Intensity
time (s)
I
Synchronous activity (3 weeks)

5.2 Engineering the analysis and measurements of functionality in the *in vitro* model

5.2.1 Refining the culture system

Recordings frequently showed only a few active electrodes (Figure 3A, starting from 6th week on MEA, Study I). The effect of restricting the space with PDMS devices on guiding the growth of neurons and increasing the amount of activity detected from the neural cultures was studied by culturing the neurons in PDMS devices with space restricting wells and tunnels (Study III, unpublished). Phase contrast imaging was utilized to confirm that devices did not prevent the growth of neurites. Neurites were observed to fill the restricted space of devices (Figure 3C). In the very narrow tunnels the evaluation of cell soma location by phase contrast microscopy was unreliable and immunocytochemistry that is generally used for observing the somas and neurites was unsuccessful. Finally, the effect of restriction via PDMS devices on the amount of activity measured was assessed by comparing the amount of active electrodes (Figure 3F) and SNR (Figure 3G) between different PDMS devices. Restriction increased the number of active electrodes and enhanced the SNR. The number of the active electrodes was highest in the PDMS tunnel devices, while the open 1-well and 6-well structures did not provide similar improvement.

Figure 3. To enhance the detection of spikes, the culture system was refined by retricting space with PDMS-devices. (A) 8 weeks follow up redording as a raster plot of detected spikes detected from 59 electrodes (y-axis) during 9 5-min (x-axis) recordings demonstrating the low levels of recorded activity. Properly active electrodes can be seen as dense packing of spikes into black bars during 5-minute recordings. These electrodes begun emerging after 6 weeks and were low in numbers compared to the total number of electrodes (here 2-5 out of 59). (B) The designed PDMS device had a restricting tunnel between two cell plating areas. When the PDMS devices were attached to MEA, the electrodes were located in the tunnel, under the PDMS lid and under the PDMS device itself. (C) Phase contrast imaging revealed that the neurons willingly grew into the tunnels. The scale bar is 100 µm. (D) The immunocytochemical stainings were unable to penetrate into the PDMS-devices, while live staining with small molecular dyes enabled the observation of both neurite and soma penetration into the restrictive devices. On the left, BTUB-antibody- (green) and small molecular dye DiD- (red) labeled neural cells growing through the PDMS tunnels. The scale bar is 100 µm. Small molecular dye DAPI-labeled nuclei outside the PDMS channels. The scale bar is 100 µm. (E) The tunnel width dependent orientation of neurites in the restricting structures was revealed by decreased circular variance. The statistical differences were analyzed using univariatate analysis of variance. The *-symbols indicate significance based on Bonferroni's post hoc test versus open cultures (* $p < 0.05$; ** $p < 0.01$; *** $p < 0.001$). (F) The proportion of active electrodes increased faster in restricting devices during network maturation. Percentage of active electrodes (y-axis) is shown as as a function of restriction (x-axis)

during different weeks of culture. (G) SNR (y-axis) was increased by restricting devices (x-axis). The statistical differences between groups were analysed using the 1-way ANOVA. The * symbols indicate significant differences using Dunn's post hoc test versus the 1-well control (** $p < 0.01$; *** $p < 0.001$). (H) The biological source of activity in restricting PDMS-devices was confirmed by shutting down neural activity with strong neurotoxin (TTX) application. The effect of TTX on the percentage of active electrodes (y-axis) in different devices. (F-H) The numbers indicate cross-section diameter of the tunnel in µm; 1w is 1-well device, 6w is 6-well device, o is outside tunnels and under the lid.

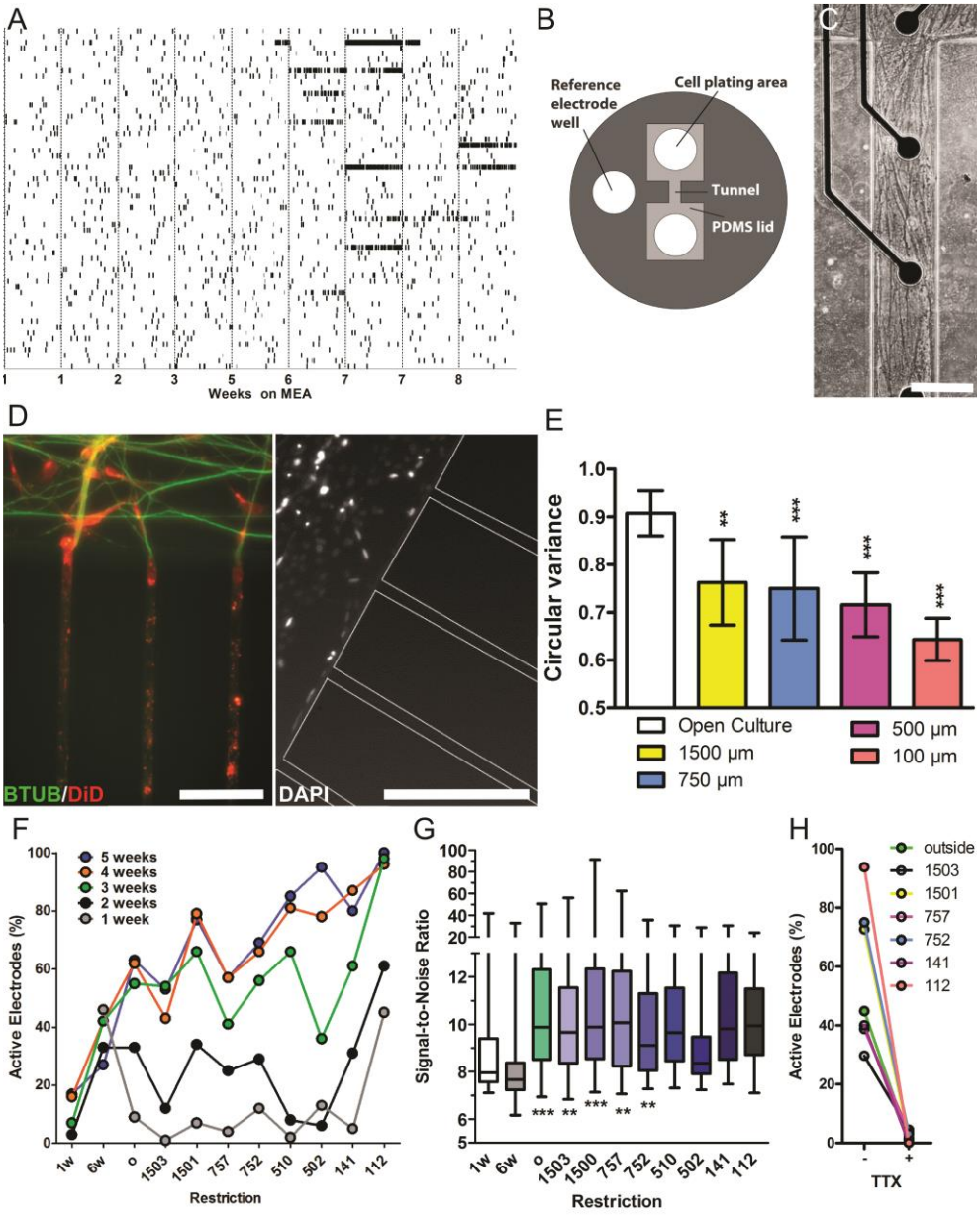

The SNR was improved by implementation of the PDMS tunnel devices. The noise detected by the electrodes in the cultures grown in the PDMS tunnel devices was increased compared to the control measurements. An increase was also observed in the median peak-to-peak amplitude. Both the noise and amplitude were increased in both the inside and outside tunnels. To confirm, that the signal was arising from biological sources, TTX was applied to block the sodium channels underlying the neural action potential formation (Figure 3H).

5.2.2 Improving the MEA analysis

To enhance the amount of detected neural activity, the MEA analysis was improved by refining the detection of spikes from the voltage data. Spike detection was observed to suffer from noise arising from perfusion and calcium imaging performed simultaneously with MEA recordings (Figure 4A, left). To decrease the effect of noise on spike detection, a noise removal based on the median voltage value of the electrodes was applied (Study IV, unpublished). An example of a noisy recording before and after noise removal is shown in Figure 4A (unpublished). The background noise is clearly decreased as a result of the noise removal. Median noise removal was able to remove large-scale fluctuations while retaining the fast spikes representing action potentials.

The spike detection used in all studies was based on utilizing a static threshold for each recording. To ensure that the threshold used for spike detection is optimal, several thresholds were compared in unpublished studies. The thresholds were compared based on the number of true spikes detected and the ratio between true and false detections (Figure 4B, unpublished). The number of true detections was evaluated by subtracting the rate of false detections from the measured spike rate. The rate of false positive detections was evaluated from recordings made in the presence of TTX. Five times noise provided the best compromise between true detections and the ratio between true and false detections.

To investigate the source of spikes recorded from networks, spike waveforms were sorted for a single electrode (n=1) and networks (n=10) in Study II. Spike waveform sorting from the single electrode revealed four waveforms of approximately equal peak-to-peak amplitudes (Figure 4D). The fourth waveform emerged only after pharmacological treatment. Spike waveform sorting from data

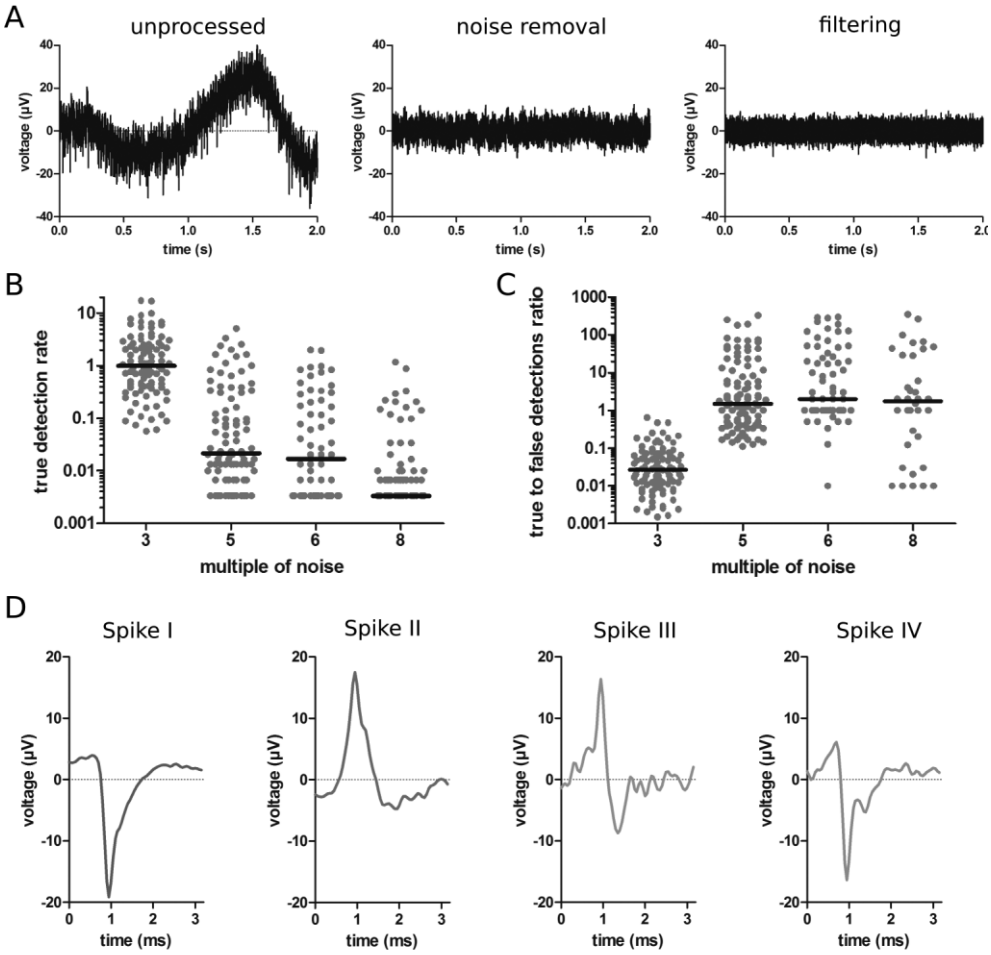

Figure 4. More accurate detection of spiking activity from networks was provided by improving MEA data analysis. (A) Comparison between voltage signals recorded from single electrode showed that median based noise removal allowed the perfusion noise to be effectively removed. The same extracellular voltage (y-axis) signal is shown as a function of time (x-axis) from one electrode before (left) and after (middle) the noise removal, and after filtering (right). (B-C) Evaluation of different multiples of noise for spike detection revealed that multiple of 5 provided best compromise between the detected number of true and false spikes. (B) The rate of true positives (y-axis) is shown from individual electrodes (n=97) analyzed with different multiples of noise. Electrodes with no spikes detected at specific SD were excluded (1, 1, 35 and 24 for SD of 3, 5, 6 and 8, respectively). (C) The ratio of detected true positive spike rate and false detection rate measured during TTX (y-axis) using different multiples of noise (x-axis) for individual electrodes (n=97). Electrodes with no spikes detected at specific SD were excluded (0, 0, 31 and 53 for SD of 3, 5, 6 and 8, respectively). D) Clustering used to analyse spike waveshapes revealed multiple clearly distinct spike waveforms recorded by single electrode. Averaged extracellular voltages (y-axis) detected from the same electrode are shown as a function of time (x-axis) from four clusters (Spike I, II, III, IV).

pooled per network revealed five different spike waveforms in each of the networks (Study II). Two of these spike waveforms (III and IV) had approximately 70-90 μV peak-to-peak amplitude compared to the other two waveforms, which had considerably smaller peak-to-peak amplitude (20 μV). The majority (99%) of the spikes waveforms detected during the baseline had peak-to-peak amplitudes of ~20 μV.

To investigate the source of spikes temporally clustering into bursts, spike sorting was performed jointly with burst detection (n=10 networks). Sorting revealed that the bursts of activity consisted of spikes with different waveforms. The bursts (24 in total, average 8.5 spikes each) recorded before pharmacological manipulation consisted of Spike I (174 spikes), Spike II (17 spikes) and Spike III (12 spikes).

5.2.3 Improving network activity pattern analysis

Raster plots of spikes seemed to saturate during the bursting activity (Figure 6A). This saturation hindered the visualization of network activity pattern recorded via MEAs. Grayscale spike rate-based raster plots were tested to enhance the visualization of the network activity in Study IV. Grayscale spike rate raster plots allowed the desaturation of burst spikes and revealed clear silent and highly active periods during the network-wide MEA recordings (Figure 6B).

To allow comparison between networks, drug applications and to calcium imaging, network activity pattern quantification method based on summed spike rate was investigated. Summed spike rate for whole a MEA with 10 s binning is shown in Figure 6C. The formed spike rate trace showed sharp peaks of sudden high increases in the spike rate. Inspired by these transient peaks, an alternative prominence-based burst detection method for MEA data was studied (Figure 6C). The prominence-based burst detection method (Figure 6C and F, asterisks) was found to correlate with the ISI-based burst detection method (Figure 6C, Study IV).

5.2.4 Improving the calcium imaging analysis

To investigate generation of network activity patterns on single neuron level in developing networks with migrating neurons, an automated segmentation and tracking algorithm was developed in Study IV. For investigating calcium

fluctuations in all of the cells in the imaged field of view an automated segmentation was implemented. A segmentation algorithm based on marker guided watershedding was able to successfully segment the cell somas (region of interest, ROIs) from the image series (Figure 5A-D, Study IV). The parameters of the algorithm were optimized to maximize the similarity of the ROI counts between the frames and minimize the detection of overlapping ROIs. The algorithm was applied on an averaged set of images to allow neurons with fluctuating fluorescence levels to be detected more reliably. A moving average of 50 frames produced the best results with respect to the robustness of the ROI count and the amount of overlap during detection. The frame-to-frame location information produced by segmentation was provided for the tracking algorithm. Munkres assignment algorithm was investigated for assigning tracks to follow neurons during their migration (Figure 5E, unpublished). The highest number of unique tracks with highest track lengths was used to evaluate the performance of tracking. A gating threshold of 20, gating cost of 5000, cost of nonassignment of 500, minimum track age of 20 frames and minimum visibility of 50% of frames produced the highest number of unique tracks with the highest length. Discontinuous tracks were joined by matching the intensity and location.

This tracking information was used to extract single cell fluorescent intensity traces (Figure 5F, unpublished). The single cell traces contained noise and the level of measured intensity was dependent on the loading of the calcium indicator. To compare the activity of neurons, the calcium traces were filtered, normalized and quantified. A normalization based on the maximum fluorescence of the neuron was investigated. A typical trace from a single-neuron after processing is shown in Figure 5G. For quantifying the activity patterns of the single neurons, an automated algorithm based on peak detection with a prominence threshold was investigated (Figure 5G, asterisks). Visual inspection revealed that peak detection was able to distinguish peaks. The single-neuron data for single-neuron peak height, prominence, duration and interval was automatically collected from the detected peaks.

Raster plots from calcium level fluctuations (example in Figure 6D) showed traces of network bursts when highly oversaturated (not shown). To better visualize the network activity patterns of calcium increases, raster plots from normalized neural traces were investigated (Figure 6E). Normalized raster plots allowed for the network-wide rises in intracellular calcium to be easily visualizable. To compare the network activity patterns between networks, to single neurons and to MEA recordings, an algorithm for quantifying network activity patterns was

investigated. To obtain a trace for the activity pattern visualized in the raster plot a simple summation of traces was investigated (Figure 6F, trace). Summed trace successfully displayed peaks corresponding to the synchronous intracellular calcium rises of the network activity pattern. This trace resembled the single neuron traces, which were succesfully quantified by an automated algorithm based on prominence threshold, thus the use of this algorithm for network activity quatification was investigated (Figure 6F, dots). Visual inspection revealed that peak detection was able to distinguish peaks. The data for peak height, prominence, duration and interval were automatically collected. Comparison between MEA and calcium-data collected simultaneously from the same network revealed that network activity peaks were detected similarly from both types of data.

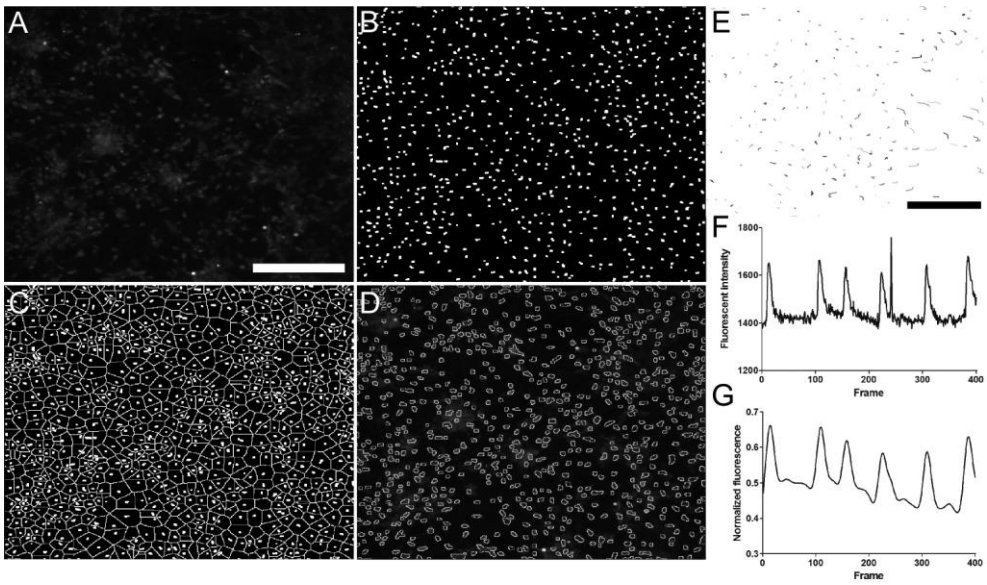

Figure 5. The developed and optimized calcium imaging data analysis allowed automated evaluation of single neuron activities. (A-D) The developed stepwise segmentation allowed cells to be automatically detected. The scale bar is 200 µm. (A) An example of initial image formed by averaging from fifty subsequent frames (25 s, 0.5 s interval) would have been difficult to analyze manually. (B) Demonstration of how morphological operations allowed foreground markers (white areas, derived from A) to be derived from the averaged image. (C) Demonstration of how morphological operations allowed background markers (white lines, derived from B) to be derived from the foreground markers. (D) Demonstration of how watershedding utilizing the foreground and background markers allowed segmentation of cells (areas lined with while, derived from B and C). (E) The visual inspection of cell tracks from full recordings revealed succesfull tracking. Tracks connecting ROIs detected from a one 30-min recording. Each colored line represents the motion of a single cell as movement of its centroid. The scale bar is 200 µm. (F) Demonstration of succesfull collection of calcium fluctuations as intensity of the dye (y-axis) in single neurons after the automated collection of the intensities from each frame

of the recording (x-axis). (G) Demonstration of succesfull detection of peaks (*) from the normalized and filtered intensity (y-axis) trace for the same cell as in F during the recording (x-axis).

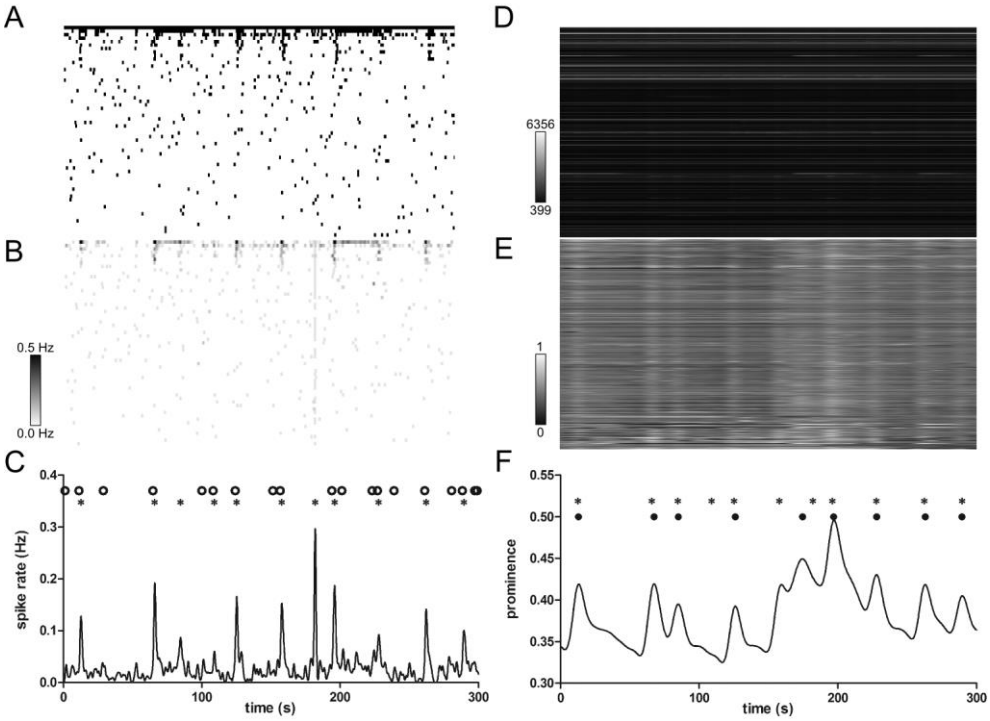

Figure 6. Analysis of network activity patterns with optimized analyzis for evaluation and quantification of MEA and calcium imaging data revealed that both methods were able to detect similar network activity patterns. (A-B) Representation of MEA recorded spikes for each channel (n = 59, y-axis) from 5-minute (x-axis) recording as grayscale spike rate (B) instead of black and white timestamps (A) allowed better visualization of synchronous spiking. (C) Summed spike rate for the whole MEA resulted in peaks of spike rate (*) that were detectable, quantifiable and in agreement with previously published method (○). The summed network spike rate (y-axis) shown as a function of time (x-axis). The asterisks and the circles indicate the network bursts as detected with the prominence-based method and the method developed by Kapucu and colleagues (2012), respectively. The two burst detection methods were able to detect the network bursts similarly. (D-C) Enhanced visualization of the network activity pattern was revealed by comparison of recorded intracellular calcium fluctuations (gray scale bars) during 5 minutes of calcium imaging rfrom the whole field of view as unprocessed intensity changes of the calcium indicator (D) and as normalized and filtered calcium level fluctuations (E). The recording was performed simultaneously with the MEA recording represented on A-C. (F) Summed calcium level fluctuations (y-axis) from the imaged field resulted in peaks of intracellular calcium increases (•) that were detectable, quantifiable and in agreement with the pattern of spike rate peaks (*) detected from the simultaneously performed MEA recording. The asterisks indicate the network bursts as detected using the prominence based method from MEA-recording. The dots indicate the network bursts detected using the prominence-based method from calcium fluctuations. Most of the network bursts were detected by both of the methods.

5.3 Biological studies of functionality in the *in vitro* model

To investigate the emergence of neural network activity patterns from single neurons in hPSC-derived neural networks, activity was simultaneously studied on the population and single-neuron levels in Studies II and IV. Furthermore, to investigate the synaptic mechanisms mediating the network activity patterns pharmacological studies were carried out. This section summarizes the results related to the biology of the *in vitro* model under three distinct topics. The first topic, "Combined measurements of population activity", summarizes the results of the correlations between the MEA measurements and calcium imaging. The second topic, "Behavior of single neurons during population activity", summarizes the observations related to the participation of single neurons in the network events. Finally, the third topic, "Mechanisms mediating the network activity of the in vitro model", summarizes the results obtained using pharmacological tools.

5.3.1 Combined measurements of population activity

Both MEA and calcium imaging reflect the activity of neurons in the measured network. However, MEA measurements lack of spatial resolution, while calcium imaging lacks temporal resolution. The benefit of performing simultaneous MEA and calcium imaging measurements was investigated in Study IV. The correlation between MEA measured network activity patterns of synchronous action potentials and calcium imaging measured network activity patterns of synchronous intracellular calcium fluctuations was investigated to ensure that both methods are measuring the same patterns of synchronous activity. The network activity patterns recorded by both methods were visually compared. The comparison of grayscale plots produced from the spike rates of individual microelectrodes (Figure 6B) or from the normalized calcium signals of individual neurons (Figure 6E), revealed that both methods detected similar network activity patterns. Furthermore, to ensure that the automatic detection is detecting similar network activity pattern the quantified network activity patterns were aligned for comparison (Figure 6F, asterisks and dots). Visual comparison of the quantitated population level signals revealed that the MEA recorded population events and the network level calcium rises were occurring together. However, some temporal differences and method-specific peaks of network activity were also observed. In some cases, this was due to the already high calcium level. High calcium baseline lowered the peak

prominence thus preventing prominence threshold being crossed. In other cases, MEA spike rate was smaller than the population bursts and were associated with no or very negligible summed calcium trace peaks.

To compare the network patterns of action potential and calcium fluctuations between methods and networks, durations, prominences and intervals were obtained for each peak in the network activity pattern from five networks measured with simultaneous MEA and calcium imaging recording (Figure 7A-C). The comparison of parameters of network activity patterns between networks revealed that networks generated similar patterns with respect to duration of action potential firing and calcium transients. In addition, networks generated calcium transient patterns of similar prominence and interval. Network bursts measured with MEA were shorter, more prominent from background activity and occurred slightly more frequently. The relationship between the network activity patterns obtained via MEA and population level calcium fluctuations were quantified with linear regression analysis (Table 21) to investigate the correlation of parameters measured for the network pattern with different methods. Linear regression analysis revealed that the increase in the number of spikes during bursts of spikes measured via MEA was strongly and significantly ($p < 0.05$) predicted by increase in the prominence of network calcium fluctuation.

Table 21. Linear regression analysis of association between MEA and calcium imaging measured network burst parameters from 5 networks revealed burst prominence as the most significantly and strongly replicated parameter. Relationship describes the equation obtained from linear regression analysis. y is the expected parameter value for MEA recording as a function of measured parameter value from calcium imaging (x).

Parameter	Relationship	Strength (r^2)	Significance (p)
Peak duration	y = 3.53 - 0.20x	0.51	-
Peak prominence	y = 0.026 + 0.21x	0.81	< 0.05
Inter-peak-interval	y = -220 + 8.8x	0.61	-

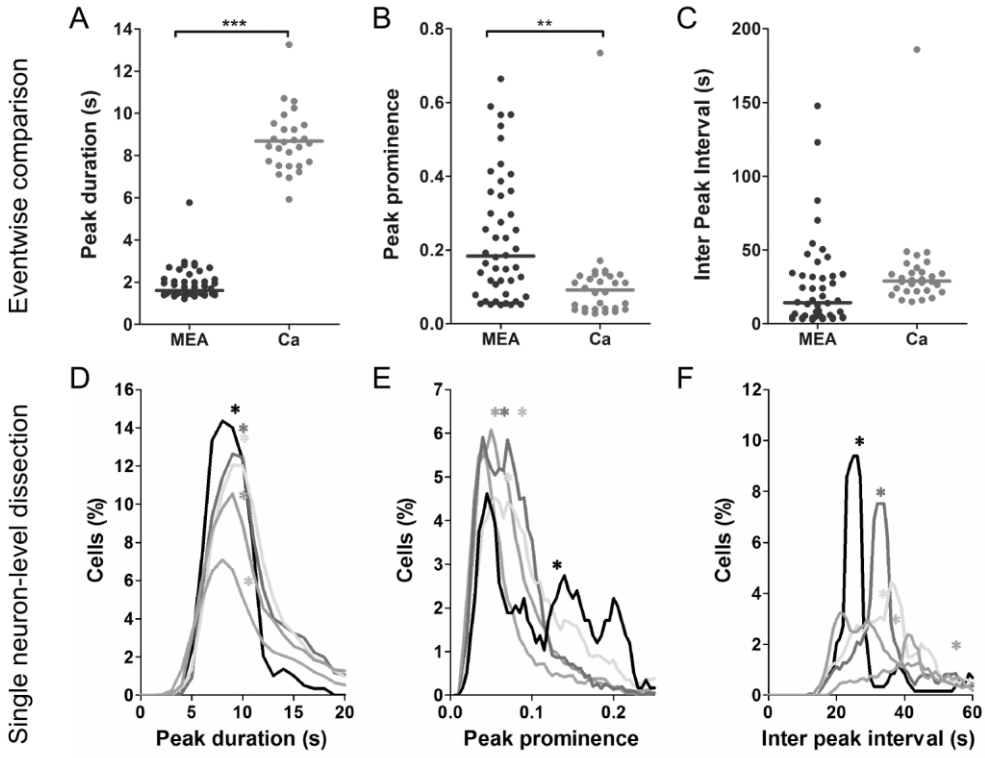

Figure 7. The comparison of parameters of network patterns measured via MEA and calcium imaging revealed that networks generated similar patterns. Furthermore, the comparison of single neuron distributions of activity parameters revealed similar distributions between different networks. (A-C) Each replicate is a peak of network activity (46 events for MEA and 30 events for calcium imaging, both from the same 5 networks). (A) Network activity peak durations were similar between different networks but differed greatly between methods. Durations (y-axis) of the peaks of network activity (bursts) as measured with MEA (median 1.6 s) and calcium imaging (Ca, median 9 s) for the networks. Significant difference was observed between MEA and calcium imaging (*** $p < 0.001$). (B) The activity during network activity peaks measured by MEAs were widely varying while network wide calcium transient peaks were more uniform. Prominence of the peaks of network activity as measured with MEA (median 0.18) and calcium imaging (Ca, median 0.09) for the networks. Significant difference was observed between MEA and calcium imaging (** $p < 0.01$) were observed. (C) Interval between peaks of activity was similar between networks when measured from calcium transients but shorter and more varying for those measured from MEAs. Inter-peak-interval (y-axis) of the peaks of network activity as measured with MEA (median 14 s) and calcium imaging (Ca, median 29 s) from networks. There was no significant difference between MEA and calcium imaging. (D-F) Values from individual neurons from each network are represented as a distribution with the same color as their median (*). The medians are numerically listed in Table 23. (D) Comparison of distributions of durations of calcium transients in individual neurons revealed very similar overall shape and location between networks. Percentage of neurons (y-axis) with respect to the single-neuron activity peak widths (x-axis) for 5 networks. (E) Comparison of distributions of peak prominences of calcium transients in individual neurons revealed similar overall shape between majority of networks.

Percentage of neurons (y-axis) with respect to the single-neuron activity peak prominence (x-axis) for 5 networks. (F) Comparison of distributions of intervals between calcium transients in individual neurons revealed a similar overall shape with a sharp peak between majority of networks. Percentage of neurons (y-axis) with respect to the single-neuron activity inter-peak-intervals (x-axis) for 5 networks.

5.3.2 Behavior of single neurons during population activity

To investigate how the neural network activity patterns emerge from single neuron activity in hPSC-derived neural networks, calcium traces from single neurons were compared to the calcium trace pattern obtained from the network in Study IV. Peaks of calcium traces, corresponding to bursts of neuronal activity, from individual neurons and from networks were detected based on prominence. Values for peak duration, prominence and interval between peaks were obtained and compared (Figure 7D-F and Table 23). Comparison of durations of peaks revealed similarity between the patterns of calcium transients of single neurons and the network, as well as between different networks (Figure 7D). The distributions of the durations of activity during network events in single neurons had one peak, which was skewed towards longer durations. Skewedness was smallest in the network with the most activity during synchronous events. Comparison of the amount of activity during peaks, reflected by the peak prominence, revealed similarity between the patterns of calcium transients of the network and the constituent neurons (Figure 7E). The prominence distributions in general were skewed, and the highest activity network had multipeaked distribution. Most neurons displayed peak prominence corresponding to calcium transient less than 10% of their maximum calcium transient (measured as a response to high potassium). Only the most active network had a large proportion of neurons showing over a 10% of maximum increase in their intracellular calcium levels. Very few neurons produced their maximum during events. Comparison of inter-peak-intervals revealed that the interval between peaks in network calcium trace pattern corresponded to a subgroup of neurons (Figure 7F). This group was proportionally the largest in the network with highest peak prominences. Furthermore, the peak prominence seemed to be associated with the variability in the inter-peak-interval between neurons and the most active network had the smallest variability in the inter-peak-interval between neurons.

The relationship between the single neuron calcium traces and the network calcium trace was quantified with linear regression analysis, to investigate the association between parameters on single neuron and network level (Table 22).

Emergent network properties were expected to be poorly associated. Linear regression analysis revealed that the inter-peak-interval and the peak prominence as strongly replicated parameters between network and single neuron level. Duration of calcium transients was poorly associated, thus being strong candidate for emergent network property.

Table 22. Linear regression analysis of association between peak parameters obtained from network calcium trace (n = 5 networks) and single neuron calcium traces revealed inter-burst-interval and burst prominence as the most significantly and strongly replicated parameters between network and single neuron level. Relationship describes the equation obtained from linear regression analysis. y is the expected parameter value for the network level as a function of measured parameter value on single neuron level (x).

Parameter	Relationship	Strength (r^2)	Significance (p)
Peak duration	y = 9.68 + 0.042x	0.016	-
Peak prominence	y = 0.040 + 0.59x	0.86	< 0.05
Inter-peak-interval	y = 7.50 + 0.80x	0.93	< 0.05

Table 23. Comparison of the properties of network bursts (grey) and the single-neuron bursts reveal that peaks of activity on network and single neuron level are similar. The network event values are medians calculated for events (n=30) from all five networks. The single neuron event values are medians calculated from medians for each neuron (numbers in table on the bottom row) in the specified network.

	Network events (I-V)	Single neuron events				
		Network I	Network II	Network III	Network IV	Network V
Median duration (s)	9	9	10	11	10	10
Median prominence	0.09	0.13	0.06	0.09	0.07	0.07
Median inter-event-interval (s)	29	27	55	38	33	34
Events/neurons (n)	30	117	823	670	393	571

5.3.3 Mechanisms mediating the network activity of the *in vitro* model

To investigate the synaptic connections mediating the patterns of electrical network activity in hPSC-derived neural networks, the hPSC-derived neural networks were pharmacologically treated in Studies II and IV. The pharmacological treatments were targeted to GABAergic, glutamatergic and gap junction mediated signaling. These mechanisms have been shown to participate in the generation of the earliest forms of network activity. Network level responses to pharmacological treatments were recorded with MEAs and calcium imaging. Furthermore, changes

in spike waveforms and the distributions of single-neuron responses arising from pharmacological treatments were studied.

5.3.3.1 GABA response

The presence of functional GABA receptors in neurons participating in the generation of network activity in hPSC-derived neural networks was investigated by studying the responses to GABA application. Responses to GABA application were studied with MEA recordings and calcium imaging. The presence of functional GABA receptors in neurons participating in the generation of network activity was studied by measuring the effect of GABA application on the network activity assessed by MEA measurements and calcium imaging. The network activity patterns were quantified via burst detection for MEAs and by network calcium trace peak detection for calcium imaging. Comparison of network activity pattern properties between baseline and GABA treatment revealed an inhibitory response (Figure 8A-D, Study II and IV).

It was observed that single electrodes within the same network responded differently to GABA application (Study II). In further accordance, the single channel spike sorting revealed that some of the spike waveforms were not observed during GABA application while others were present. This observed heterogeny was further investigated by assessing the responses of single neuron calcium transients to GABA application. The distribution of single-neuron response revealed that most of the neurons were inhibited by GABA, but to different degrees (Figure 9A and 10A). In addition, some of the neurons were depolarized by GABA application (Figure 9A, top). Both inhibited and depolarized neurons were found during the experiments from the same networks and despite the response difference to GABA, both inhibited and depolarizing neurons participated in the network activity pattern (Figure 9B). Spatial distribution of the differently responding neurons was studied to see if neurons responding similarly to GABA formed clusters. However, completely mixed cultures devoid of such clusters were observed (Figure 9C).

GABA application decreased the size of calcium transient generated by synchronous activity in networks with high initial transients (Figure 8B). To investigate if this was due to single neuron responses or due to an emergent network response, the correlation between size of baseline transients and the magnitude of the response was studied on the single neuron level (Figure 11A).

Response to GABA was found to be dependent on the activity of the neuron; the higher prominence of the neuron, the more strongly it was blocked by GABA.

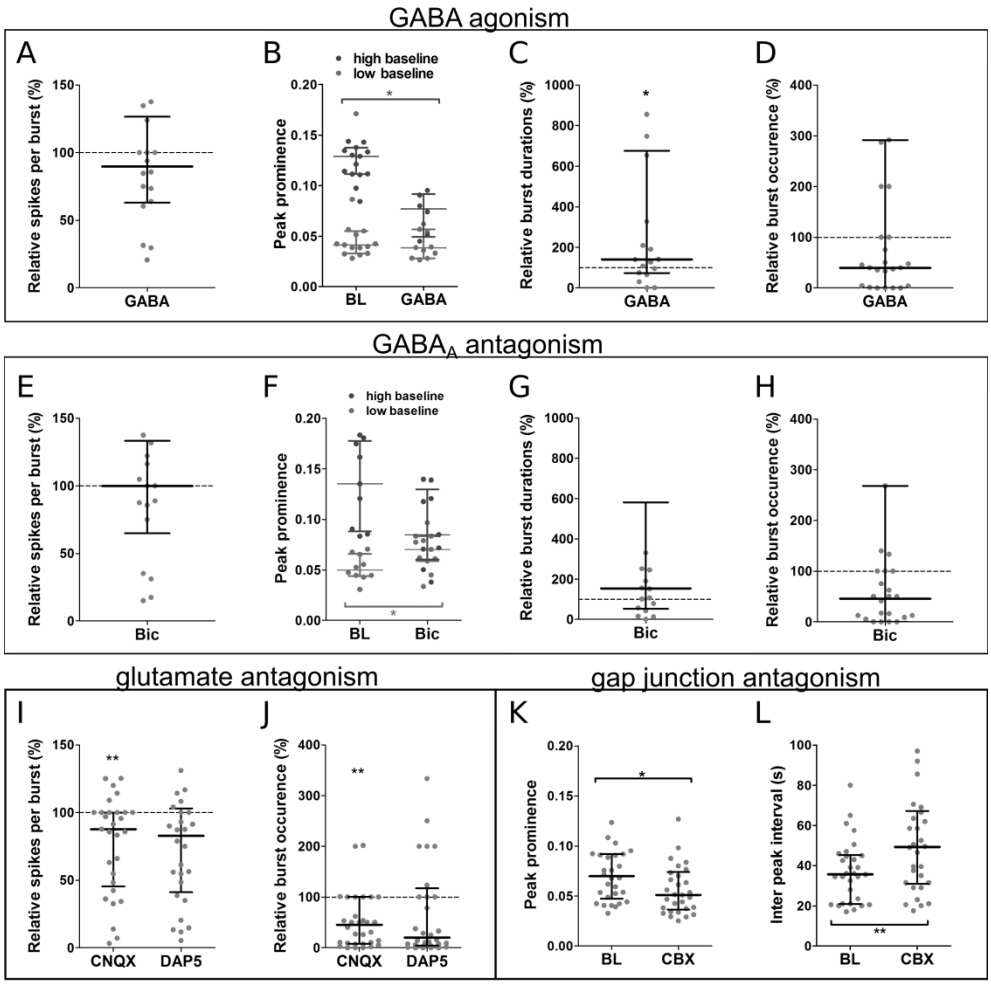

Figure 8. The participation of chemical and electrical synapses in the generation of network activity pattern was confirmed by comparison of the effects of different pharmacological agents. The horizontal bars represent the medians with the interquartile range marked by whiskers. (A-D) The presence of functional GABA receptors in neurons participating in the generation of network activity was confirmed by GABA application. (A) The GABA application mainly decreased but occasionally increased the number of spikes in burst relative to baseline (y-axis). Each entry represents an average per network (B) The GABA application decreased the size of calcium transient generated by synchronous activity in networks with high initial transients. Peak prominence (y-axis) of network activity peaks with GABA application. GABA application caused a significant (* $p < 0.05$) decrease in the prominence of events from the high baseline activity networks. GABA application had also varying

effects on burst duration (C) and the number of bursts (D) in different networks compared to baseline (y-axis). GABA application caused a significant (* $p < 0.05$) increase in burst duration. Each entry represents an average per network. (E-H) The participation of functional $GABA_A$ receptors in the generation of network activity pattern was confirmed by $GABA_A$ antagonist application. (E) The $GABA_A$ antagonist (Bic) application both decreased and increased the number of spikes in burst relative to baseline (y-axis). Each entry represents an average per network. (F) The $GABA_A$ antagonist (Bic) application increased the size of network calcium transients generated by synchronous activity in networks with low initial transients and decreased the size of network calcium transients in networks with high initial transients. Peak prominence (y-axis) of network activity peaks during the baseline and $GABA_A$ antagonist (Bic) application. Bic application caused a significant (* $p < 0.05$) decrease in prominence of events from low baseline activity networks. $GABA_A$ antagonist (Bic) application had also varying effects on burst duration (y-axis) (G) and bursts occurrence (y-axis) (H) relative to baseline. Each entry represents an average per network. (I-J) The participation of functional glutamate receptors in the generation of network activity pattern was confirmed by sequential application of glutamate receptor antagonists. (I) The glutamatergic AMPA/kainate receptor antagonist (CNQX) application mainly decreased the number of spikes in burst (y-axis) while the glutamatergic NMDA receptor antagonist (DAP5) decreased the number only slightly further. (J) AMPA/kainate receptor antagonist CNQX also decreased the occurence of bursts (y-axis) while NMDA receptor antagonist DAP5 clearly decreased the occurrence of bursts further. CNQX application caused a significant (** $p < 0.01$) decrease in spikes per burst and burst occurence. Each entry represents an average per network relative to baseline. (K-L) The participation of functional gap junctions in the generation of network activity pattern was confirmed by gap junction blocker application. (K) The application of gap junction blocker CBX decreased the peak prominence (y-axis) and (L) inter-peak-interval (y-axis) of network activity peaks compared to baseline. CBX application caused a significant (* $p < 0.015$ and ** $p < 0.01$) decrease in network burst prominence and increase in inter-peak-interval.

5.3.3.2 Role of GABAergic signaling

To investigate the role of GABAergic signaling in the generation of network activity pattern, the network activity pattern properties were compared between baseline and $GABA_A$ antagonist application in Studies II and IV (Figure 8E-H). The $GABA_A$ antagonist bicuculline was never observed to completely disrupt the network activity pattern in Studies II and IV. However, blockade of $GABA_A$ signaling was observed to both increase and decrease the amount of spikes in bursts and prominence of network calcium trace peaks (Figure 8E-F). The effect on burst duration (Figure 8G) and occurrence (Figure 8H) was also observed to be decreased in some and increase in some networks. On the other hand, some of the networks were unaffected by treatment. Demonstrating varying effects of $GABA_A$ antagonist.

The distribution of single-neuron responses as change in the prominence of calcium transients duringe $GABA_A$ antagonist application was studied, to investigate if all neurons were affected similarly (Figure 10B). The single-neuron response distribution was bell shaped and the peak aligned with the network

response. $GABA_A$ antagonist application increased the size of calcium transient generated by synchronous activity in networks with low initial transients (Figure 8F).

To investigate if this was due to single neuron responses or due to an emergent network response, the correlation between size of baseline transients and the magnitude of the response was studied on the single neuron level (Figure 11B). On the single-neuron level the responses were observed to be more dependent on the network the neuron resided in than on the size of the initial calcium transients.

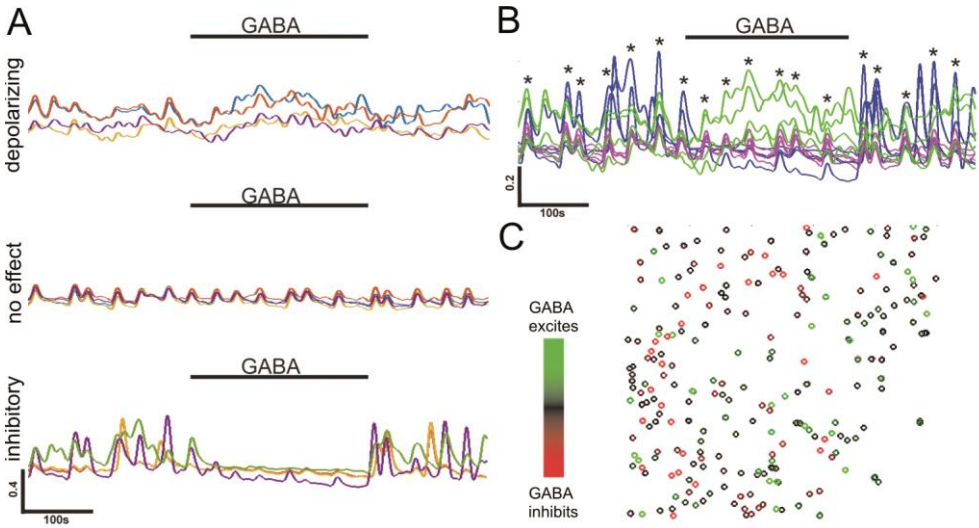

Figure 9. The investigation of neuronal responses to GABA application on single cell level revealed that the network activity pattern was generated by a heterogenous mixture of neurons with different responses to GABA. (A) Three distinct responses to GABA application were observed. Intracellular calcium level (y-axis) shown as a function of time (x-axis) from individual neurons depolarized by GABA (top), with no response to GABA (middle) and inhibited by GABA (bottom). All neurons are from the same network. (B) Neurons responding differently were in synchrony, together generating the network pattern. The traces in A shown together. Green traces from depolarized, pink from non-responders and blue from neurons inhibited by GABA. * indicates the moments of synchronous activity during a network event. (C) Neurons with different responses to GABA were completely mixed in the culture. Neurons from one field of view marked with a colored circle representing their GABA response (color scale bar).

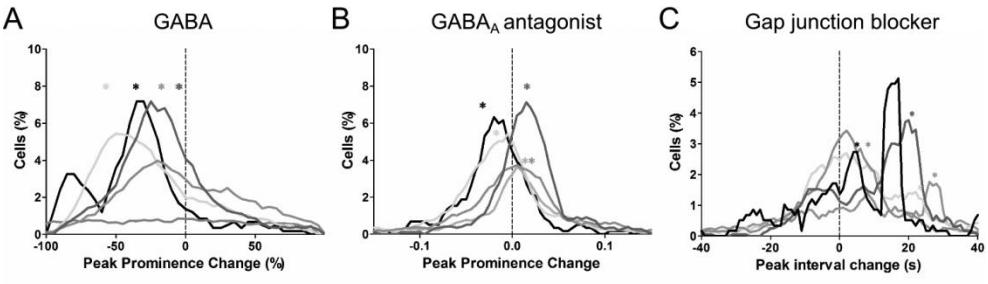

Figure 10. Comparison of distributions of individual neuron responses and the network response (*) to pharmacological agents showed association between network and individual neuron level reponses. (A) Comparison of network responses (*) and single neuron response distributions to GABA showed a peak of single neuron response distributions aligning with respective network response. Percentage of neurons (y-axis) with respect to the single neuron peak prominence change during GABA application compared to baseline (x-axis) for 5 networks. (B) Comparison of network responses (*) and single neuron distributions to $GABA_A$ antagonist showed a peak of single neuron response distributions aligning with respective network response. Percentage of neurons (y-axis) with respect to the single neuron peak prominence change during $GABA_A$ antagonist application compared to baseline (x-axis) for 5 networks. (C) Comparison of network responses (*) and single neuron distributions to gap junction blocker showed a peak of single neuron response distributions aligning with respective network response. Percentage of neurons (y-axis) with respect to the single neuron inter-peak-interval change during gap junction antagonist application compared to baseline (x-axis) for 5 networks.

5.3.3.3 Role of glutamate and gap junctions

The participation of functional glutamate receptors in the generation of network activity pattern was investigated by sequential application of glutamate receptor antagonists in Study II. The glutamatergic AMPA/KA receptor antagonist CNQX was observed to significantly ($p < 0.01$) decrease the occurrence of bursts and the amount of spikes in bursts (Figure 8I-J). The effect was somewhat permanent with poor recovery, and the addition of the glutamatergic NMDA receptor antagonist D-AP5 further decreased the activity slightly, but unsignificantly ($p > 0.05$).

The participation of functional gap junctions in the generation of network activity pattern was investigated by gap junction blocker application in Study IV (Figure 8K-L). The gap junction antagonist CBX increased the interval between network calcium transients by visibly decreasing the occurrence of network level calcium transients. Furthermore, the promincence of network calcium transients was decreased. The distribution of single-neuron responses as change in the inter-peak-interval of calcium transients to gap junction blockade was studied, to investigate if all neurons were responding similarly (Figure 10C). The single-neuron

response distribution revealed a sharp peak corresponding to a subgroup of neurons with response similar to respective network response.

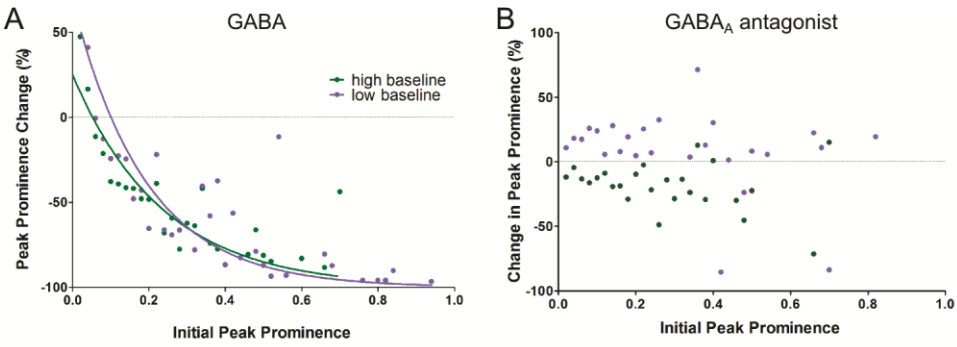

Figure 11. Comparison of single-neuron responses to pharmacological treatments in different network groups revealed two patterns. (A) Single-neuron response to GABA was similarly dependent on the amount of spontaneous activity of that neuron in different networks. Neurons with more activity were more strongly inhibited by GABA. This was independent of the network the neuron resided in. Median peak prominence change in response to GABA (y-axis) as a function of the initial peak prominence (x-axis) of individual neurons in either the high baseline (green) or the low baseline activity networks (purple). Lines represent exponential fit. (B) Single-neuron response to $GABA_A$ antagonist was dependent on the amount of spontaneous activity in the network the neuron resided in. Neurons in networks with high spontaneous activity (green) were generally inhibited by $GABA_A$ antagonist while neurons in networks with low level of spontaneous activity (purple) were generally stimulated by $GABA_A$ antagonist. Median peak prominence change in response to the $GABA_A$ antagonist (y-axis) is shown as a function of the initial peak prominence (x-axis) of individual neurons in either the high baseline (green) or the low baseline activity networks (purple).

6 DISCUSSION

Human cognition is based on electrically active circuits in the brain. Today, our understanding of the formation and detailed function of these electrically active circuits remains incomplete. Understanding the processes of brain circuitry generation could provide valuable insight into the genesis of human neuropathologies. The formation of functional human neural networks can be studied *in vitro* in hPSC-derived networks. This *in vitro* model allows us to assess the cellular and network mechanisms involved in neural development and abnormal brain function.

In this thesis, an electrically functional *in vitro* model consisting of a networks formed by hPSC-derived neural cells was utilized to study the formation of electrical activity in human neuronal networks. This chapter discusses first the improvements made in the experimental and analytical tools used to study hPSC-derived neural network activity. Next, the *in vitro* model and formation of electrical activity is discussed. Finally, the biological findings regarding the cellular and network mechanisms involved in the formation of network functionality are discussed.

6.1 Analysis and measurements of functionality in the *in vitro* model

The electrical network activity *in vitro* can be studied by performing MEA measurements and calcium imaging. However, MEA measurements from hPSC-derived neural networks are challenging due to the low amount of detected activity. In this thesis, improvements for experimental and analytical tools for studying hPSC-derived neural networks with MEA were investigated to enhance the detection of electrical activity from the networks. Furthermore, it was investigated if calcium imaging analysis methods can be developed, optimized and evaluated to obtain more accurate detection of electrical activity on the network level.

6.1.1 Improving the culture system

One of the most notable challenges in performing MEA measurements is the low number of activity detecting electrodes. In this thesis, the improvement of the number of active electrodes by refining the culture system was investigated. The refinement was studied in Study III, where PDMS devices were used to refine the culture system by restricting the growth area and medium volume available for neurons. This was hypothesized to guide the growth of neural cells and enhance the signal detected by electrodes. The PDMS devices were able to guide and restrict the growth of neural cells. It was observed that both cell somas and neurites willingly grew into the restricted areas. Furthermore, the PDMS tunnel devices seemed to induce parallel alignment of the neurites. Previously, random alignment has been observed (Goyal and Nam, 2011). Furthermore, PDMS devices were able to restrict the somas into one compartment. However, immunocytochemistry, which is generally used for observing the somas and neurites, was unsuccessfull in the crowded areas of PDMS tunnel devices. This phenomenon was most likely due to the hindrance in diffusion imposed by the combined volume restriction of the PDMS devices and crowded cell culture.

The PDMS tunnel devices enhanced the spike detection via electrodes. The most important improvement observed was the increase in the number of activity detecting electrodes. This increase was observed to occur most strongly in the PDMS tunnel devices, while the open 1-well and 6-well structures did not provide similar improvement. The increase in the number of active electrodes is most likely due to more cells being in close proximity to the electrodes (Obien et al., 2015). Furthermore, the SNR was improved by PDMS tunnel devices. The noise detected by the electrodes in the PDMS tunnel device cultures was increased compared to the control measurements. In addition to noise, the median peak-to-peak amplitude was also increased. The increase of both these parameters has been previously reported for smaller tunnels (Morales et al., 2008; Dworak and Wheeler, 2009; FitzGerald et al., 2009; Goyal and Nam, 2011; Habibey et al., 2015). Both the noise and amplitude were increased in both the inside and outside tunnels. These changes could be explained by amplification of the signals that were previously part of the background noise. Such amplification would lead to an increase in the spike detection threshold and an increase in the amplitude of the detected spikes. However, these effects can be ruled out by the increase in the number of active electrodes. Thus, the increase in the SNR is most likely due to real amplification of the neuronal signal originating from near the electrode combined with the increased likelihood of a neuron being near an electrode.

In summary, PDMS devices studied guided the growth of neural cells and enhanced the signals detected by electrodes. The combined effect of the noise and the enhancement in measured signals increased the general sensitivity of the measurement system. Furthermore, the PDMS tunnel devices increased the number of active electrodes, thus significantly improving the measurement system. From the perspective of further engineering of the measurement system, it remains to be determined whether the desired effect is due to the guiding properties, or the volume restriction or both.

6.1.2 Improving the microelectrode data analysis

Another notable challenge in utilizing MEA measurements is the analysis and interpretation of measured data signals and the lack of efficient network activity pattern analysis methods. The analysis of the MEA data was refined in Studies II and IV.

6.1.2.1 Noise removal and spike detection

It was hypothesized, that MEA data analysis could be refined by noise removal and spike detection optimization to enhance the detection of electrical activity. In Study IV, median noise subtraction removed large-scale fluctuations from the measured signals. Median noise subtraction is well suited for MEA signals when only the fast spikes are analyzed as the desired part of the signal - the action potentials - are local and thus detected only by a single electrode; thus, the same signals measured from multiple electrodes at exactly the same time must be noise.

Spike detection with static thresholding suffers from fluctuations in the background noise. To address this problem, the spike detection was improved by implementing windowed spike detection in Study IV. When utilizing threshold based detection, the window used for determining the noise plays a critical role. MCS MC_Rack spike detection calculates the detection threshold from the 500 ms of the data acquired after the experimenter presses the button and is thus strongly dependent on data used for calculation. MED64-associated Mobius relies on the user to define the spike detection thresholds and is thus sensitive to experimenter decisions. From the commercial tools, only Axion Biosystem Axis software is adaptive. Thus, spike detection algorithms not accounting for changes in the background noise are widely used (Table 7) and are an important point to improve on.

Currently, there are no studies comparing different spike detection thresholds. To find out the most optimal spike detection threshold, spike detection thresholds from 3 to 8 times the noise were studied. Detection threshold of 5 times the noise provided the best performance. This is inline with the generally used threshold of 5-6 times the noise (Table 7).

6.1.2.2 Waveform sorting

The exact relationship between signal source and MEA detected signal remains unclear. In Study II spike waveforms recorded by the electrodes were sorted based on their shape to gain insight into the sources of detected spikes trains and whether sorting works in human-derived cultures.

It is unclear whether single MEA electrodes record signals from single sealed neuron or from multiple neurons. The spike waveforms recorded by single electrodes were sorted according to their shape, to investigate whether multiple shapes representative of multiple neural sources were present. Spike sorting revealed that single electrodes record signals from multiple neurons. Sorting spike waveforms from the single electrode revealed four waveforms of roughly equal peak-to-peak amplitude. Similar numbers (1-4) of waveforms have been previously observed from single electrodes in mouse PSC-derived neural networks (Illes et al., 2014). Furthermore, the spike waveforms had small peak-to-peak amplitudes and thus likely represent recordings from neurons far from the electrode rather than neurons forming seal with the electrode (Egert et al., 2002; Frey et al., 2009). Taken together, these observations highlight the notion that each individual MEA electrode represents signal recorded from a small-scale network surrounding the electrode.

Bursts recorded by single electrodes can in theory arise from intense firing of single neurons or from the synchronous firing of multiple neurons. The burst participation of sorted spike waveforms was studied by combining spike waveform sorting with burst detection. This joint analysis revealed that the bursts of spikes recorded by the single electrode consisted of spike waveforms of different shapes. Bursts of spikes consisting of multiple spike waveforms have also been previously reported (Illes et al., 2014). Thus, the bursts of spikes recorded by MEA arise from multiple sources. From the perspective of analyzing burst parameters the idea that single electrode recorded bursts consists of spikes from multiple sources implies that the changes in burst properties, such as burst duration, reflect changes in the communication between neurons.

To investigate whether the neural types can be distinguished based on the shape of the extracellular spike waveform, spike waveforms pooled from all electrodes from individual networks were sorted. Five different spike waveforms emerged from the data pooled from all the electrodes in one network. Spikes I, II and V had small amplitudes and likely represent neurons too far to be classified (Egert et al., 2002; Frey et al., 2009). The large peak-to-peak amplitude spikes (III and IV) more likely represent neurons close to the electrodes. However, it is unlikely that they represent different types of neurons as classification into large and small amplitude neurons is usually an indicator of faulty spike sorting (Van Dijck et al., 2012). Thus, pooling waveforms without any prior exclusion criteria for spike waveform parameters, such as amplitude, did not produce neural type segregation in spikes recorded from hPSC-derived neural networks.

In conclusion, the MEA analysis pipeline has several aspects that can be refined to enhance the detection of neural activity. First, based on the results of applying the windowed spike detection, adaptive thresholding is advised. Second, single channel spike sorting can improve the resolution of MEA recordings while pooling waveforms seems to be unable to produce neural type segregation. Third, the bursts recorded by single electrodes can arise from the synchronous activity of multiple neurons. Furthermore, the spike waveform analysis suggests that each MEA electrode recording should be treated as a population signal from small-small scale network.

6.1.3 Quantification of calcium imaging analysis

To obtain more accurate detection of electrical activity on the single neuron and network level, and to investigate generation of network activity patterns on single neuron level in developing networks with migrating neurons, an automated segmentation and tracking algorithm for calcium imaging analysis was developed, optimized and evaluated in Study IV. To extract activity traces from all of the neurons in the captured image series, an automated segmentation based on morphological operations and watershedding was implemented. Morphological operations have been previously utilized in calcium imaging analysis (Jee Jang and Nam, 2015; Muhammed et al., 2016). However, compared to pure morphological feature extraction that produces circular ROIs (Jee Jang and Nam, 2015), watershedding allows measurement from the whole complex-shaped soma. Furthermore, segmentation based on morphological openings is able to provide a

considerably higher analysis speed (up to 12 times) compared to independent and principal component analysis-based segmentation methods (Muhammed et al., 2016). Thus, morphological operations complemented with watershedding are a strong candidate as a basis for automated fluorescent microscopy image segmentation.

To compare nonratiometric calcium traces between neurons, the feasibility of normalization relative to the maximum fluorescence of a cell was investigated. The resulting output using this normalization represents the fraction of maximum activity of single neuron at any given moment. Generally, normalization to baseline or minimum is used (Patel et al., 2015; Jee Jang and Nam, 2015; Cornelissen et al., 2013). This minimum based intensity then represents the fluorescence changes as deviations relative to baseline. However, normalizing to the maximum revealed an unexpected benefit as the population activity pattern became clear from the aligned track rasters. Thus, the maximum fluorecense based normalization is usefull for studying the network wide calcium transient patterns.

To compare patterns of calcium trace behavior between neurons and networks, threshold-based peak detection was investigated. Threshold-based peak detection was able to robustly detect transients from individual neurons. Previously, Patel and colleagues (2015) argued that threshold-based peak detection methodology was not robust enough to identify both small and large amplitude transients. However, their concerns involved percentile-based threshold, whereas a prominence-based threshold was used in Study IV. Unlike percentile-based threshold prominence-based threshold is insensitive to slow fluctuations in the basal calcium level. This allows prominence-based threshold to detect small spikes during low and high basal calcium. Jee Jang and Nam (2015) extracted the small spikes by combining thresholding and template matching. This methodology could be an interesting addition to the algorithm represented in Study IV. In conclusion, prominence-based peak detection is promising approach for quantifying calcium transients.

6.1.4 Analysis and comparison of population activity between MEA and calcium imaging

The downside of MEA measurements is the lack of spatial resolution, while calcium imaging lacks temporal resolution. It was investigated if simultaneous MEA recordings and calcium imaging would provide crossvalidation of the methods and insight into the network activity measured. The electrical activity

measured simultaneously with both methods was compared, to confirm that both MEA and calcium imaging were reflecting the same electrical activity patterns of neurons and neuronal networks.

The MEA raster plots, used to visualize network wide activity patterns, suffer from desaturation during high frequenzy spiking. In study IV spike rate based grayscale raster plots were compared to black and white raster plots, to investigate if spike rate based plots would provide better visualization. The spike rate based grayscale spike rate rasters allowed the desaturation of the burst spikes and revealed clear silent and highly active periods on the network-wide MEA recordings.

It was hypothesized that calcium transient rasters obtained from calcium imaging would also show network patterns. Unprocessed calcium indicator intensity and normalized calcium indicator intensity raster plots were compared in Study IV to investigate which provided better visualization. The normalized raster plots showed synchronous network-wide rises in intracellular calcium. Comparison of raster plots obtained from simultaneous MEA recordings and calcium imaging revealed similar network activity patterns.

The tools to quantify the network activity pattern consisting of rhythmic and correlated increase of activity of individual neurons emerging during neural network formation are scarse. It was investigated if a quantification method to analyze network activity patterns captured simultaneous by both MEA and calcium imaging could be developed. In Study IV, the feasibility of simple windowed summation of spike rate and calcium transients was investigated. Summed traces representing the activity measured by both methods showed sudden peaks of neuronal activity. These peaks were temporally correlated between the methods. Few of the network activity peaks were shown by only one of the methods. This was most likely resulting from the differences in temporal resolution (Takayama and Kida, 2016) and spatial coverage between the methods (Illes et al., 2014). Summation based population activity analysis differs greatly from the connectivity analysis more commonly used for calcium imaging data. In connectivity analysis traces from individual neurons are compared to estimate their temporal correlation (Li et al., 2010; Lutcke et al., 2013; Mukamel et al., 2009; Stetter et al., 2012; Tibau et al., 2013; Patel et al., 2015). However, summing neuronal traces and separately detecting peaks from the summed network activity pattern does not suffer from the accuracy requirement of peak detection from the individual neurons that is used to derive the temporal correlations in connectivity analysis. Thus, simple summation was sufficient to allow for detection of network wide activity increases.

In conclusion, the MEA measurement of hPSC-derived neural networks can be improved by restricting the available space and volume. Furthermore, the MEA analysis can be improved by median-based noise removal and windowed spike detection. However, the benefits of adding spike waveform sorting are not clear and require further studies. Calcium imaging analysis can be performed automatically for a mass of moving neurons. The comparison between simultaneous MEA and calcium recordings revealed that the two methods for measuring population activity from the same network are in general agreement. Thus, both methods can be reliably and comparably used to study network level activity.

6.2 The *in vitro* model and its functionality

6.2.1 Neural differentiation

The neural differenation by withdrawal of external signaling molecules in hPSCs was confirmed by neural morphology and protein expression analysis. Similar to i*n vivo,* the same neural precursor cells were expected to produce both neurons and glia. The morphology of the cells during *in vitro* differentiation was assessed in studies I-IV. Differentiation produced mainly cells with neuronal morphology with compacted soma and long thin processes and a minor population of cells with slightly larger soma and astrocyte morphology. Occasionally flat cells with no star-like morphology and round cells with no morphology were observed. These morphologies have been previously associated to neural identity (Nat et al., 2007; Lappalainen et al., 2010). Thus, the withdrawal of external signaling molecules produced neural cells with proper morphologies. The expression of neuronal (MAP-2 and βtubIII) and astrocytic (GFAP) proteins in cells with neuronal and astrocytes morphologies was investigated in Studies I and III. Cells with neuronal morphology were observed to express markers of neuronal processes, MAP-2 and βtubIII as a result of neural differentiation, as reported earlier by Lappalainen and colleagues (2010) and by Paavilainen and colleagues (2018). Cells with astrocytic morphology expressed GFAP. The proportion and effect of astrocyte content of these cultures has been more carefully studied by Paavilainen and colleagues (2008). Astrocytes in hPSC-derived neural cultures have been suggested to enhance the maturation of the neural network by supporting synaptogenic mechanisms

(Pfrieger and Barres, 1997; Johnson et al., 2007; Eroglu et al., 2009; Allen et al., 2012; Paşca et al., 2015).

The presence of proliferating cells, typical to *in vivo* developing brain tissue, was confirmed in neural cultures arising from the *in vitro* differentiation in Study I. 20% of the cells in the neural cultures were proliferating. A mixture of neurons of different developmental ages (proliferating versus non-proliferating) in hPSC-derived neural cultures has also been reported by others (Shi et al., 2012; Lam et al., 2017; Gunhanlar et al., 2017). Thus, there exists heterogeneity regarding the maturational stage of the neurons.

In conclusion, the neuronal differentiation of hPSCs, based on withdrawal of external signaling molecules and neurosphere culturing, produces a heterogenous neural population. This population consists of neuronal and astrocytic cells, in addition to proliferating fraction of cells. Thus, the obtained cultures contained neurons and other cellular components required for functional network formation.

6.2.2 Functional characterization of the differentiated cultures

In addition to support from the cellular components, successful synapse formation requires the maturation of the electrophysiological properties of neurons. The maturation of electrophysiological properties of neurons was investigated (Studies I-IV and unpublished) to asses the ability of hPSC-derived neurons to produce typical neuronal electrical activity.

The electrophysiological properties of single neurons were studied with patch clamp and calcium measurements. Neurons produced typical neuronal currents (Coyne et al., 2011) when measured with whole-cell voltage-clamp. Both Na and K currents were observed starting at the first week of adherent culture. Furthermore, the current-clamp measurements from the differentiated neurons revealed voltage responses typical of neurons. Single and multiple action potentials were measured in response to depolarization. Multiple action potentials were rare, however, reflecting the young age of the neurons or the smaller proportion of more matured neurons. The number of fired action potentials has been shown to increase as hPSC-derived neurons mature (Lam et al., 2017). The calcium transients measured from single neurons revealed that neuronal cells had different responses to potassium and glutamate application. The responses to glutamate and high potassium were similar to those reported previously (Forostyak et al., 2013;

Paavilainen et al., 2018). Some of the cells showed a maximal response to both glutamate and high potassium, while some responded only to potassium. Furthermore, the glutamate to potassium response ratio varied between cells. Thus, the neural cultures consisted of neurons of different electrophysiological maturity.

The emergence of neural activity as extracellular voltage changes was studied with MEA recordings in Studies I-IV. Neural activity emerged in the cultured networks after the first week of plating as sharp voltage changes with different waveforms. The waveforms were a few tens of microvolts in amplitude and on the millisecond scale in duration. The amount of spiking increased during the first few weeks in culture. Increase in spiking is generally observed (Vessoni et al., 2016; Odawara et al., 2014; Fukushima et al., 2016), and can result from more neurons firing action potentials, more neurons firing more than one action potential (Lam et al., 2017) or more synaptic connections (Canals et al., 2015) causing either or both of the first two behaviors (Lam et al., 2017).

In summary, the heterogenous environment of maturing neurons, astrocytes and proliferating cells supports the functional maturation of neurons and development of spontaneous activity which increases as the culture time is increased. However, the neurons exhibit different levels of functional maturity.

6.2.3 Network activity patterns

Synapse formation is associated with the production of synchronous network activity. The emergence of network activity patterns in the hPSC-derived cultures containing electrophysiologically functional neuronal cells was investigated in Studies I-IV, to confirm synapse formation.

6.2.3.1 Emergence of network activity patterns

The gradual synapse formation occurring during network formation was investigated by measuring the neural spiking and calcium transients during the maturation of hPSC-derived neural networks.

Similar to previous studies (Heikkilä et al., 2009; Kirwan et al., 2015), the first pattern of activity seen in MEA recordings and calcium imaging was asynchronous. Much like has been reported for the first maturing neurons in rodent cortex and hippocampus (Crépel et al., 2007; Allene et al., 2008). However, the calcium

transients in hPSC-derived neurons were constant fluctuations compared to rodents where the transients were separated by clear periods of silence (Crépel et al., 2007; Allene et al., 2008). This can be a real difference, or arise from the extracellular solution and thus would require further studies to be confirmed.

When the hPSC-derived neural cultures matured further, the activity became semisynchronous. Semisynchronization was seen as loosely correlated spiking between the different electrodes of MEA (Studies I and IV) and as loose temporal association of calcium transients (Study IV). The rodent SPAs are similar to the observed activity in terms of loose synchrony, proportion of participating neurons and association with action potentials (Allene et al., 2008). However, the observed calcium transients in hPSC-derived neurons are shorter and much more frequent with no clear periods of silence.

Finally, the networks displayed synchronous activity, seen as synchronous spiking between the different electrodes of MEAs, typical to hPSC-derived neural cultures (Heikkilä et al., 2009; Kirwan et al., 2015) and synchronous calcium transients between neurons. This activity was similar to ENOs in rodents in terms of increased proportion of participating neurons, tightness of synchrony, frequency of occurrence and association with bursts of action potentials (Garaschuk et al., 2000; Allene et al., 2008).

The arising neural spiking activity pattern was expected to be associated with similar pattern of calcium transients. However, during the early asynchronous phase, MEA detected scarse spikes nested in long silent periods, while calcium imaging revealed frequent asynchronous calcium transients. Studies utilizing only one these methods report similar findings (Heikkilä et al., 2009; Patel et al., 2015; Cohen et al., 2008; Ivenshitz and Segal, 2010). The initial lack of correlation between MEA and calcium imaging could arise from calcium transients that are not associated with action potentials. Similar to what has been reported to occur in *ex vivo* recordings from rodents (Crépel et al., 2007). This could be linked to the electrophysiological maturity of the neurons. The low amount of electrophysiologically mature neurons, capable of producing spikes, would also explain low amount of spikes detected by MEA.

However, as the network activity synchronized both spikes measured by MEA and calcium traces recorded by calcium imaging organized into periods of intense activity and periods of silence. On MEA measurements this was seen as bursts of spikes on both single electrode and as peaks of spike rate on network level. On calcium fluctuations, the synchronous activity was seen as strong correlated increases in calcium level on individual neurons and as peaks of network level

calcium trace. The single neuron calcium transients could be arising from brusts of action potentials reported to appear gradually after 3 weeks (Lam et al., 2017).

Thus, synchronous neural activity pattern arose in a stepwise manner partially resembling the activity emerging in the developing brain. However there were clear differences in the calcium transients compared to *ex vivo* recordings from rodents. This warrants further studies to confirm if this is true difference of results from experimental setup. Furthermore, as the extracellular action potentials and calcium transients correlated with each other only during the synchronous period this should be taken into consideration when assessing and comparing the activity of immature neural networks recorded with different techniques. Lastly, the gradual emergence of synchronous activity and synapses could be linked to the maturation of calcium signalling systems in the neurons and should be more carefully studied.

6.2.3.2 Properties of synchronous activity

Synchronous activity is commonly studied with either microelectrodes or calcium imaging. Microelectrodes record the extracellular spikes with high temporal resolution while the sources of spiking activity remain unclear. On the other hand, calcium imaging is able to record individual cells or even subcellular parts, but lack in temporal resolution. The properties of the network activity patterns were compared between simultaneous MEA measurements and calcium imaging in Study IV to increase the resolution of the recordings allowing a more in depth study of the network activity pattern.

To evaluate the extent of correlated spiking seen on MEA recordings, calcium imaging was used to investigate the single neuron participation. Simultaneous calcium imaging revealed that large proportions of neurons covering the entire field of view were active during the correlated bursts of action potentials recorded by MEA. Thus, the synchronous activity measured by MEAs is wide spread and several neurons around the electrodes are active and can potentially contribute to the MEA signal. Shew and colleagues (2010) also reported that the activity recorded by MEA was accompanied with a simultaneous rise in nearly all neurons. This is in contrast to the scarse calcium rises reported to occur in conjunction with the bursts of spikes on MEA by Illes and colleagues (2014). This could reflect differences in the early activity between species. A possible cause could be the lack of voltage-gated calcium channels producing the flow of calcium in mouse PSC-derived neurons (Robinson et al., 1993; Smetters et al., 1999).

Due to the lack of temporal resolution during calcium imaging, the timing between action potentials generating the calcium transients has remained unclear. MEA recordings were performed simultaneously with calcium imaging, to improve the temporal resolution for resolving the spike trains occurring during calcium transients. Correlated window for calcium transients was observed, while the spiking within this window was not tightly correlated between different areas of network and spiking pattern varied from transient to transient. Previously, strong synchrony between calcium traces (Shew et al., 2010) and lack of exact synchrony between spikes (Satuvuori et al., 2017) has been separately observed. Furthermore, the intervals between correlated calcium transients were largely devoid of both spikes and transients. Thus, it could be suggested that the network activity pattern consists of correlated windows of silence and activity while the activity within the windows of activity is not strongly correlated.

The properties of network activity patterns in different networks were compared, to investigate if the emergence of network activity pattern is a part of developmental program manifesting itself *in vitro*. Furthermore, the activity patterns measured via MEA recordings and calcium imaging were compared, to investigate if both methods are measuring the same patterns of synchronous activity. For these purposes, the duration, prominence and interval of spike rate peaks and network calcium trace peaks were compared in Study IV. The duration of occurences of correlated spiking and network calcium traces were similar between networks. In addition, the intervals between network calcium trace peaks were similar between networks. In contrary to the wide range (0.0005 Hz to 0.18 Hz) of occurrence previously reported by Kirwan and colleagues (2015). The amount of activity, measured as increase in spiking frequency and calcium levels, however, varied a lot between networks. Thus, it can be argued that the timing related network properties, such as duration and interval, are regulated by a genetic program. This would also make them important aspects to study between healthy and diseased networks.

Comparison between the properties of network patterns of action potentials and calcium fluctuations revealed that while both methods were recording the same pattern of synchronous activity, MEA was more sensitive to activity originating from few neurons. This was seen as slightly shorter inter-peak-interval due to smaller peaks of activity in between larger network calcium transient correlated peaks. These extra peaks most likely reflect the activation of a few high activity neurons, but they are not visible in calcium imaging, which is not affected by a few high activity neurons.

In summary, the comparison of network activity patterns recorded with MEA and calcium imaging revealed that both methods were recording the same pattern of synchronous activity while MEA was more sensitive to activity of few neurons. The synchronous activity was widespread and consisted of correlated windows of silence and activity while the activity within the windows was not strongly correlated. The timing of these windows was similar between different networks suggesting an inherent biological mechanism in tight control of the network activity patterns.

6.2.3.3 Distribution of single-neuron responses within networks

To investigate how the neural network activity patterns emerge from single neuron activity in hPSC-derived neural networks, calcium traces from single neurons were compared to the calcium trace pattern obtained from the networks. The neural network population activity was measured as a sum of the normalized calcium transients of each individual neuron. It was hypothesized that the neural network activity pattern would be seen to be faithfully replicated by the single neurons. The single neurons behave similarly to the network with respect to the calcium transient duration and prominence. However, only portion of neurons behave similarly to networks with respect to inter-peak-interval. This could represent neurons that were producing calcium transients strictly during the correlated transients and thus the properties of the inter-peak-interval histogram could be used to evaluate the proportion of neurons participating in the network activity pattern. Previously, network activity pattern has been suggested to be regulated by a distinct population of neurons (Kirwan et al 2015; Illes et al., 2014). It is plausible that this population is the group of neurons that are active only during synchrony. However, this would need to be assessed in more detail.

Comparison of distributions between networks revealed that networks with most prominent network calcium transients displayed least varied durations and had sharpest peak in distribution of inter-peak-intervals on the single neuron level. Thus, the most distinct network activity pattern could be suggested to arise from the most tightly correlated timing of individual neurons. The correlation of timing can arise only from communication between neurons, thus the prominence of networks calcium transients might reflect the amount of synaptic connections which has been shown to increase during neuronal maturation (Lam et al., 2017).

Furthermore, clear majority of neurons in all networks were spontaneously producing calcium transients of only fraction of size of the maximum transient.

Spontaneous spiking of only proportion of maximum spiking has also been observed in patch-clamp measurements (Gunhanlar et al., 2017). No previously published large-scale single cell *in vitro* calcium imaging studies were found.

In conclusion, the network activity pattern emerged from the transients of individual neurons that were organized into windows of activity with similar duration and inter-window-interval across neurons of different networks. The activity during windows, however, was not organized into repeating patterns or tight synchrony most likely implying that in developing networks activation in general was more important than the exact sequence of firing. The size of transients in the network activity pattern was associated with the proportion of neurons employed in this window and could reflect the amount of synaptic connectivity.

6.3 Mechanisms mediating activity in maturing networks

To investigate the mechanism giving rise to synchronous activity and synchronous silence, three commonly observed mechanisms were studied (Studies II and IV) by pharmacologically stimulating or removing their participation.

6.3.1 GABA

The neurotransmitter GABA has been shown to have varying roles in the formation of neural networks. In *in vitro* studies, GABA has been shown to extensively excite developing networks. However, varying results have been reported by different research groups. In Studies II and IV, the networks were exposed to GABA and a $GABA_A$ receptor antagonist to study the maturity and role of the inhibitory GABAergic system.

6.3.1.1 The dual effect of GABA in hPSC-derived neural networks

The presence of functional GABA receptors in neurons participating in the network activity was investigated by studying network activity pattern changes during GABA application. GABA application produced inhibitory response, by reducing the occurrence of bursts of spikes and size of network calcium transients. Inhibitory effect in hPSC-derived neural networks has been also observed by

Kirwan and colleagues (2015) and Fukushima and colleagues (2016). This suggests presense of GABA receptors in neurons participating in the network activity, thus resembling the developing rodent brain where the generation of SPAs is inhibited by GABA (Crépel et al., 2007).

The response to GABA was studied in more detail by spike sorting to investigate the uniformity of responses within the networks. Spike sorting revealed differences in the response between spike types. Varying changes in spiking as response to GABA have been shown also by Illes and colleagues (2014). Only the highest amplitude spikes were completely blocked by GABA. The increase in the amplitude of action potentials in hPSC-derived neurons has been linked to the maturation stage of the neurons (Telezhkin et al., 2016; Gunhanlar et al., 2017; Lam et al., 2017). Thus, the highest amplitude spikes could originate from the most mature neurons. However, due to the unreliability of sorting, the distribution of amplitudes would be a better measure to investigate. The amount of spikes completely blocked by GABA was low compared to the other spike types. This possibly reflects the low amount of neurons with mature GABA response. The proportion of high amplitude mature neurons has been observed to increase up until 8 weeks of adherent culture (Lam et al., 2017).

The response to GABA was studied in more detail by investigating single neuron calcium traces to investigate the uniformity of responses of neurons participating in the synchronous network activity patterns. Most of the neurons were inhibited by GABA. However, the amount of inhibition, measured as decrease in synchronous calcium transients, was variable. Some of the neurons were depolarized by GABA. Previously, it has been suggested that depolarizing effects of GABA in immature neuronal tissues is a consequence of errors during the experiments (Holmgren et al., 2010; Mukhtarov et al., 2011; Rheims et al., 2009; Dzhala et al., 2012). However, the GABA depolarized neurons were found from the same networks as inhibited ones and were participating in the synchronous network activity. The depolarizing GABA responses during the maturation of hPSC-derived neurons were also observed by Telezhkin and colleagues (2016). Thus, it can be argued that GABA depolarized neurons exists in the developing neural networks is not a result of the experimental setup. In the developing rodent brain GABA is reported to be excitatory/depolarizing up until postnatal disappearance of GDPs (Ben-Ari et al., 1989; Garaschuk et al., 1998; Tyzio et al., 2007). This is clear difference to the heterogeny of depolarizing and inhibitory responses in hPSC-derived networks. Thus the observed heterogeny might be specific to hPSC-derived neurons, but requires further studies.

Furthermore, in rodents the GABA switch occurs as a response to oxytocin (Leonzino et al., 2016), suggesting that the human GABA switch is not oxytocin dependent. The role of depolarizing GABA in these networks is likely to promote functional maturation of the neurons (Rushton et al., 2013, Lam et al., 2017) that are newly generated from the dividing cells. The promotion of functional maturation by depolarizing GABA most likely occurs via communication with astrocytes (Perea and Araque, 2010; Telezhkin et al., 2016).

The GABA response and size of calcium transients were compared on single neuron level to investigate if the GABA response was related to the ability to produce transients during synchronous activity. GABA response of single neurons was found to be dependent on the size of the spontaneously produced synchronized calcium transients. Neurons with higher transients were proportionally more sensitive to GABA. The number of action potential spikes in a neuronal burst correlates with the size of the observed calcium transient (Robinson et al., 1993; Smetters et al., 1999). The ability of neurons to burst has been linked to the maturation stage in hPSC-derived neurons (Telezhkin et al., 2016; Gunhanlar et al., 2017; Lam et al., 2017). Furthermore, the proportion of GABA inhibited neurons and the initial size of network calcium transients were associated with the overall network activity pattern change in response to GABA. Thus, it can be suggested that as the neurons functionally mature within the network the network produces higher calcium transients and becomes more sensitive to GABA.

6.3.1.2 The role of GABA in mediating network activity

To investigate the role of GABAergic signaling in the generation of network activity pattern, the network activity pattern changes to $GABA_A$ antagonist application were studied. The network activity pattern changes were varied, in some networks the $GABA_A$ antagonist increased the spiking in bursts or increased the size of network calcium transients, thus increasing the activity during windows of synchrony. In others no effect, or opposite response, was observed. The increase in activity, disinhibition, is indicative of functional GABAergic inhibition (Arumugam et al 2008). Both disinhibition (Heikkilä et al., 2009; Telezhkin et al., 2016; Fukushima et al., 2016), and lack of it (Kirwan et al., 2015) have been previously observed in hPSC-derived neural networks. A varying effect of the $GABA_A$ receptor antagonist has been previously reported by Patel and colleagues (2015), who demonstrated that in the early phase of network formation in rats, GABA blockade reduces activity and synchrony, while at later stages, $GABA_A$ receptor blockade results in enhanced synchrony. Both of these observations are

most likely linked to transition from GDP-like activity to more mature type activity following the GABA switch in developing rodent brain (Ben-Ari et al., 1989; Garaschuk et al., 1998; Tyzio et al., 2007). Interestingly, the hPSC-derived neural networks displayed calcium transient kinetics very different from GDPs. However, the networks with lack of disinhibition had larger calcium transients which were suggested (6.3.1.1) to be indicative of functionally more mature neurons. This discrepancy might arise from differences in the maturity of GABAergic systems, such as lack of GABAergic neurons, GABA biosynthesis or fewer or more immature $GABA_A$ receptors. This is supported by the observation that disinhibited networks were not exhibiting synchronous network activity pattern initially (Telezhkin et al., 2016; Illes et al., 2007; Heikkila et al., 2009; Fukushima et al., 2016). This would need to be assessed in more detail. However, the presense of synchronous activity pattern in networks with lack of disinhibition warrants the conclusion that inhibitory $GABA_A$ mediated signaling is not required for its generation (Baltz et al., 2010).

To investigate if single neuron disinhibition correlates with the network activity pattern disinhibition as suggested by Arumugam and colleagues (2008), single neuron calcium transients in response to $GABA_A$ were studied. Both disinhibition and inhibition were observed as increase or decrease in calcium transients during synchrony, respectively. However, the timing of synchronous calcium transients was unaffected. It was investigated whether the more disinhibited neurons had also smaller transients during baseline, indicative of ongoing inhibition. The cellwise comparison of transients during initial baseline measurements and the response to $GABA_A$ antagonist revealed that single-neuron responses were more dependent on the network the neuron resided in than on the size of the initial calcium transients. Thus, the effect of $GABA_A$ antagonist can be argued to arise from a component of network, such as the GABAergic neurons and their functionality. Possible reasons could thus be the amount of GABAergic neurons, the maturity of GABAergic neurons, the amount of output synapses made by GABAergic neurons and the activity of these synapses. The generation of GABAergic neurons from PSCs seems to differ between laboratories and the observations regarding the GABAergic system vary (Table 24). Some laboratories are claiming large fractions of GABAergic neurons (Eiraku et al., 2008; Illes et al., 2009; Watanabe et al., 2005), while others are reporting a lack of GABAergic neurons (Kirwan et al., 2015; Shi et al., 2012c) or few GABAergic synapses (Gunhanlar et al., 2017). In our lab, some GABAergic neurons are produced during differentiation (Paavilainen et al., 2018). With respect to the human time frame, the lack of GABAergic neurons is to be

expected. Thus, further studies are required to determine the time frame for the generation of GABAergic neurons in this system. In conclusion, GABA does not seem to be required for the generation of initial synchronous network activity pattern, but seems to participate in the control of transients during windows of synchronous activity.

Table 24. The relationship between reaction to GABA, $GABA_A$ inhibition and the proportion of GABAergic neurons in different preparations of maturing neural networks. The depolarizing effect of GABA has been reported to be present in networks where $GABA_A$ blockade disinhibits. However, no reports where there would be a disinhibition without the presense of synapses to GABAergic neurons were found.

Preparation	Reaction to GABA	$GABA_A$ block	GABAergic neurons	Reference
hPSC	depolarizing	disinhibition	majority	Telezhkin et al., 2016
rat embryo	inhibitory	increase in peaks	13%	Jee Jang and Nam, 2015
rat embryo	depolarizing	disinhibition	3-5%	Baltz et al., 2010
rat embryo	depolarizing	no effect	0 % (blocked)	Baltz et al., 2010
rat embryo	inhibitory	disinhibition	-	Jungblut et al., 2009
rat embryo	-	decrease / increase	-	Patel et al., 2015
hPSC	complete block	no effect	none	Kirwan et al., 2015
hPSC	inhibitory	disinhibition	-	Fukushima et al., 2016
hPSC	complete block	disinhibition	-	Heikkila et al., 2009
hPSC	depolarizing	-	some	Paavilainen et al., 2018
hPSC	-	increased activity	-	Odawara et al., 2014
mPSC	-	disinhibition	-	Illes et al., 2014
adult rat	-	disinhibition	-	Shew et al., 2010

In conclusion, the neurons participating in the network activity pattern responded differently to GABA and this might be a feature unique to hPSC-derived networks. The neurons inhibited with GABA showed larger amplitude spikes and higher calcium transients during network events. The response of neurons to GABA could be linked to their functional maturity. However, neurons with higher calcium transients did not become more disinhibited by $GABA_A$ receptor antagonism. Instead, the neuron wise response seemed more dependent on the network the neuron resided in. Thus, the effect of $GABA_A$ antagonist can be argued to arise from a component of network, such as the amount of GABAergic neurons. However, it is possible that the disinhibition increases with more GABAergic neurons, and is reflected in the disinhibition commonly seen in other preparations. Furthermore, GABAergic signaling did not seem to participate

in the temporal control of the synchronous activity pattern suggesting that the recorded activity patterns represent less immature activity than rodent GDPs.

6.3.2 Glutamate

The effect of glutamate antagonistm on the synchronous network activity pattern was studied, to investigate if excitory neurotransmitter glutamate is a mediator of the network activity pattern. The occurrence of bursts of spikes was greatly diminished by glutamatergic blockers. Additionally, the spikes in bursts were decreased. Glutamatergic signaling has been shown to appear (Gunhanlar et al., 2017) after 2 weeks (Lam et al., 2017). Thus, glutamate most likely participates in the initiation and spike rate production during the network events in hPSC-derived neural networks (Fukushima et al., 2016; Kuijlaars et al., 2016) and can be argued to be the mechanism providing the excitation required for the network activity.

The actions of glutamate in these networks could be mediated via AMPA/kainate receptors as the activity inhibiting effect was already observed during AMPA/kainate receptor antagonism, and NMDA receptor blockade did not produce clear changes. This effect has also been observed with patch-clamp measurements from hPSC-derived neurons, where AMPA/kainate receptors are located synaptically and NMDA receptors extrasynaptically (Lam et al., 2017). Thus, it can be argued that AMPA/kainate receptors have a more important role in mediating network activity. The lack of NMDA-mediated activity could reflect the immaturity of neurons (Fukushima et al., 2016). Altought the mediating glutamatergic receptors were not studied in more depth, Kirwan and colleagues (2015) observed that hPSC-derived neurons express synchronous network activity in cultures where neurons express a mixture of mature and immature functional glutamate receptors. This would be an interesting detail to confirm in the future. In developing rodent brain both ENOs and GDPs are dependent on NMDA-receptor mediated signaling (Garaschuk et al., 2000; Corlew et al., 2004; McCabe et al., 2006; Allene et al., 2008). Thus, the strong AMPA/kainate dependency is might be novel to hPSC-derived neural networks.

6.3.3 Gap junctions mediate network activity

The participation of gap junctions in the generation of synchronous network activity pattern was investigated by applying a gap junction blocker in Study IV.

The occurrence of synchronous calcium transients was greatly diminished by a gap junction blocker application. The size of the calcium transients during synchronous windows of activity was slightly but not as clearly affected, and might not be biologically significant. Thus, gap junctions seem to participate in the interval upkeep and to have a minor role in spike rate production during the windows of synchronous activity. Gap junctions could be a potential candidate as the intrinsic chemical synapse-independent mechanism observed in PSC-derived neural networks (Illes et al., 2014; Kirwan et al., 2015; Fukushima et al., 2016). In the developing rodent brain, SPAs have been reported to be mediated via gap junctions (Allene et al., 2008).

To study how the behavior of individual neurons is affected by the gap junction blockade the inter-peak-interval change in calcium transients was further studied on the single neuron level. A subgroup of neurons seemed to correspond to the change in the network activity pattern. Thus, gap junction blockade can be suggested to affect a specific group of neurons and this group of neurons has a major role in determining the network pattern interval.

In conclusion, hPSC-derived neural networks are a mixture of neurons with different molecular and functional maturities with more mature neurons contributing more to the synchronous activity pattern. In addition, the amount of activity during network events is governed by the excitation/inhibition balance between glutamatergic excitation and GABAergic inhibition. Finally, synchronized neurons are silent during the intervals between events, and the length of this period is regulated by glutamate and gap junctions. The observed dependency of the network activity pattern on different mechanisms did not have clear equivalent in the developing rodent brain. The hPSC-derived neural network activity pattern has gap junction dependency similar to SPAs, but was also mediated by chemical synapses. Thus the found activity pattern could correspond to transition from SPAs to ENOs. However, unlike ENOs the activity pattern was more dependent on AMPA/kainate receptor than on NMDA receptor mediated signaling. Furthermore, the network response to GABA and $GABA_A$ antagonist suggested that the hPSC-derived networks could be transitioning from ENO- to GDP-like activity. Thus, the activity pattern generated during brain development in human could be suggested to be different from the rodent, but requires further studies confirming that this is not an *in vitro* artifact.

6.4 Future perspectives

Despite the advancements made, some questions remain unanswered and new questions were evoked. From the perspective of further engineering of the measurement system, it remains to be determined whether the increase in measured spiking is due to the guiding properties, due to the volume restriction or both. Understanding these findings would allow further engineering of the measurement system. Additionally, spike sorting provides an important level in the study of heterogeneous networks by offering a means to assess differently behaving neurons. However, the criteria for sortable spikes would need to be more carefully considered and applied.

From the perspective of further biological studies, the detailed mechanisms allowing networks to take more control over individual neurons as they mature remains unknown. Furthermore, the molecular level details of how gap junctions and glutamate cooperate to form the pattern of network activity are unassessed. Finally, although GABAergic signaling did not participate in the generation of network activity, the response to GABA repeatedly showed a developmental profile and thus is likely to play are role in either single-neuron or network maturation.

7 CONLUSIONS

The broad aim of this thesis was to explore the topic of modeling brain functionality *in vitro* in hPSC-derived neural networks to better understand human-specific developmental processes and mechanisms.

Based on the findings presented in this thesis, the following are concluded:

1) The activity measurements of the *in vitro* model consisting of functional human PSC-derived neural networks were improved by restricting the growth area and volume with PDMS devices.

2) The analysis of MEA data can be refined by adding median noise removal and windowed spike detection. Additionally, heterogeneous networks can be more effectively assessed with spike sorting.

3) MEA and calcium imaging, which are generally utilized for measuring population activity from the same network, were in general agreement and are comparable via the analyses developed. Additionally, details of network activity pattern can be obtained from large-scale single-neuron measurements.

4) The neuronal differentiation of hPSCs produces a heterogenous neural population. This population consists of neuronal and astrocytic cells, in addition to a proliferating fraction of cells. The heterogenous environment supports the functional maturation of neurons and development of spontaneous activity which increases as the culture time is increased. However, the neurons exhibit different levels of functional maturity.

5) The network activity pattern in human PSC-derived neurons arises from a mixed but cooperating population of neurons of different functional maturity. As the neurons mature, they gradually become more active while simultaneously becoming less independent. The network activity generated

reflects intrinsic biological mechanisms in the temporal organization of network activity patterns. The activity pattern was widespread and consisted of correlated windows of silence and activity while the activity within the windows was not strongly patterned.

6) The windows of activity and silence are regulated by glutamate and gap junctions, but not by $GABA_A$ receptors. The activity of individual neurons during the windows of activity is regulated by glutamate, gap junctions and GABA. The mechanisms patterning the network activity in hPSC-derived neural networks are more overlapping than the ones exhibited during rodent brain development.

ACKNOWLEDGMENTS

The research for this thesis was carried out at the Institute of Biosciences and Medical Technology (BioMeditech), University of Tampere. I want to thank all the personnel who helped me along the way. I would like to thank Tampere Graduate Program in Biomedicine and Biotechnology (TGPBB) and Oskar Öflund foundation for financially supporting my research and participation in international conferences.

I want to thank my supervisor Adjunct professor Susanna Narkilahti for the opportunity to work in NeuroGroup, including participation in several projects, international conferences and courses and for organizing funding for the research. I wish to express my gratitude to my supervisor PhD Laura Ylä-Outinen for the kind advice and scientific guidance during all these years. I want to thank her especially for the intriguing conversations related to network activity, MEA measurements and statistics. I wish to acknowledge the members of my follow-up group; PhD Dmitriy Fayuk and PhD Kati Juuti-Uusitalo for their encouragement, valuable comments and discussions at the annual meetings. Furthermore, I am in deep gratitude to my external reviewers; Assistant professor Joost le Feber and Adjunct professor Sari Lauri for their suggestions and comments which significantly improved the Thesis.

I wish to acknowledge my co-authors; PhD Tiina Joki, PhD Laura Ylä-Outinen, Adjunct professor Heli Skottman, Adjunct professor Susanna Narkilahti, PhD Riikka Äänismaa, PhD Emre Kapucu, PhD Jarno Tanskanen, Professor Jari Hyttinen, MSc Maria Toivanen, PhD Anssi Pelkonen, MSc Lassi Sukki, Professor Pasi Kallio and PhD Mervi Ristola for their contribution to the subworks of this Thesis.

I want to state my warm gratitude to all the past and current members of the NeuroGroup. It has been a privilege to share the research and life with you. I want

to warmly thank my dear colleague, friend and fellow PhD student PhD Tiina Joki for all the adventures in science and philosophy, both in theory and in the lab. I wish to express my gratitude to my dear colleagues, friends and and fellow PhD students; PhD Anu Hyysalo and MSc Tanja Hyvärinen for all the support both in science and in life. I want to express special gratitude to my dear friend, laboratory technician Juha Heikkilä for all the technical discussions, assistance and mental support in the lab as well as in private life. I want to thank laboratory technician Eija Hannuksela for encouragement and the kind words that have brought me warmth during the darkest and coldest hours.

I am grateful to my dear friend and mentor PhD Jarno Tanskanen for the deep and plentiful discussions about the MEA recordings and their analysis. I also want to acknowledge him for all the advice regarding philosophy of science that he has given me along these years. I want to thank my students MSc Chandra Prajapati and MSc Maria Toivanen, teaching and working with you significantly contributed to my Thesis. It was a pure pleasure to be able to participate in your guidance. I want to thank my friend and colleague MSc Disheet Shah for stimulating conversations and new perspectives. I also want to express my gratitude to MSc Heini Huhtala for lengthy discussions about statistics and Sari Orhanen for the support in finalizing the Thesis.

Haluan kiittää äitiäni Pirkko Mäkistä kaikesta siitä ahkeruudesta, päättäväisyydestä ja sinnikkyydestä, jotka hän on esimerkillään minuun istuttanut. Voin vain toivoa, että jonain päivänä olen edes osin yhtä rautainen kuin sinä. Tahdon myös kiittää isääni Antero Mäkistä kaikesta kekseliäisyydestä ja pelottomuudesta, joita hän on minulle lapsesta asti opettanut. Olen äärettömän kiitollinen rakkaalle veljelleni Manu Mäkiselle kaikesta siitä vastuuntunnosta ja itsevarmuudesta, joita hän on minulle opettanut. Haluan myös kiittää häntä vertaistuesta lopputyön kirjoituksessa. Ilman Teitä minulla ei olisi ollut niitä henkisiä apuja, joiden voimin tämä väitöskirja tutkimuksineen rakennettiin.

I also want to acknowledge my friends Aapo Maijanen, Alexandr Jacko, Henna Andelin, Chris Cohen and Niko Kukkamäki for the support and determination they gave to push me forwards and out of the pits of despair. Finally, I wish to

thank my life partner Fredrik Nelin for the words of wisdom and the immense mental support that was required for me to survive writing this Thesis.

Tampere, June 2018

8 REFERENCES

Aguiló, A., Schwartz, T. H., Kumar, V. S., Peterlin, Z. A., Tsiola, A., Soriano, E., & Yuste, R. (1999). Involvement of cajal-retzius neurons in spontaneous correlated activity of embryonic and postnatal layer 1 from wild-type and reeler mice. *The Journal of Neuroscience : The Official Journal of the Society for Neuroscience*, *19*(24), 10856–10868. https://doi.org/10.1016/S0896-6273(00)80993-9

Akerboom, J., Chen, T.-W., Wardill, T. J., Tian, L., Marvin, J. S., Mutlu, S., … Looger, L. L. (2012). Optimization of a GCaMP Calcium Indicator for Neural Activity Imaging. *Journal of Neuroscience*, *32*(40), 13819–13840. https://doi.org/10.1523/JNEUROSCI.2601-12.2012

Akerboom, J., Rivera, J. D. V., Rodríguez Guilbe, M. M., Malavé, E. C. A., Hernandez, H. H., Tian, L., … Schreiter, E. R. (2009). Crystal structures of the GCaMP calcium sensor reveal the mechanism of fluorescence signal change and aid rational design. *Journal of Biological Chemistry*, *284*(10), 6455–6464. https://doi.org/10.1074/jbc.M807657200

Allen, N. J., Bennett, M. L., Foo, L. C., Wang, G. X., Chakraborty, C., Smith, S. J., & Barres, B. A. (2012). Astrocyte glypicans 4 and 6 promote formation of excitatory synapses via GluA1 AMPA receptors. *Nature*, *486*(7403), 410–414. https://doi.org/10.1038/nature11059

Allene, C., Cattani, A., Ackman, J. B., Bonifazi, P., Aniksztejn, L., Ben-Ari, Y., & Cossart, R. (2008). Sequential Generation of Two Distinct Synapse-Driven Network Patterns in Developing Neocortex. *Journal of Neuroscience*, *28*(48), 12851–12863. https://doi.org/10.1523/JNEUROSCI.3733-08.2008

Allene, C., Picardo, M. A., Becq, H., Miyoshi, G., Fishell, G., & Cossart, R. (2012). Dynamic Changes in Interneuron Morphophysiological Properties Mark the Maturation of Hippocampal Network Activity. *Journal of Neuroscience*, *32*(19), 6688–6698. https://doi.org/10.1523/JNEUROSCI.0081-12.2012

Allene, C., & Cossart, R. (2010). Early NMDA receptor-driven waves of activity in the developing neocortex: Physiological or pathological network oscillations? *Journal of Physiology*, *588*(1), 83–91. https://doi.org/10.1113/jphysiol.2009.178798

Amin, H., Maccione, A., Marinaro, F., Zordan, S., Nieus, T., & Berdondini, L. (2016). Electrical Responses and Spontaneous Activity of Human iPS-Derived Neuronal Networks Characterized for 3-month Culture with 4096-Electrode Arrays. *Frontiers in Neuroscience*, *10*(MAR), 121. https://doi.org/10.3389/fnins.2016.00121

Anastassiou, C. A., Perin, R., Buzsáki, G., Markram, H., & Koch, C. (2015). Cell type- and activity-dependent extracellular correlates of intracellular spiking. *Journal of Neurophysiology*, *114*(1), 608–623. https://doi.org/10.1152/jn.00628.2014

Arnold, F. J. L., Hoffmann, F., Bengtson, C. P., Wittmann, M., Vanhoutte, P., & Bading, H. (2005). Microelectrode array recordings of cultured hippocampal networks reveal a simple model for transcription and protein synthesis-dependent plasticity. *Journal of Physiology*, *564*(1), 3–19. https://doi.org/10.1113/jphysiol.2004.077446

Arumugam, H., Denisova, J. V., Neve, R. L., Corriveau, R. A., & Belousov, A. B. (2008). Use of calcium imaging for analysis of neuronal gap junction coupling. *Neuroscience Letters*, *445*(1), 26–30. https://doi.org/10.1016/j.neulet.2008.08.075

Au, E., & Fishell, G. (2008). Cortex shatters the glass ceiling. *Cell Stem Cell*, *3*(5), 472–474. https://doi.org/10.1016/j.stem.2008.10.013

Azcoitia, I., Yague, J. G., & Garcia-Segura, L. M. (2011). Estradiol synthesis within the human brain. *Neuroscience*, *191*, 139–147. https://doi.org/10.1016/j.neuroscience.2011.02.012

Bakkum, D. J., Frey, U., Radivojevic, M., Russell, T. L., Müller, J., Fiscella, M., … Hierlemann, A. (2013). Tracking axonal action potential propagation on a high-density microelectrode array across hundreds of sites. *Nature Communications*, *4*. https://doi.org/10.1038/ncomms3181

Bakkum, D. J., Radivojevic, M., Frey, U., Franke, F., Hierlemann, A., & Takahashi, H. (2014). Parameters for burst detection. *Frontiers in Computational Neuroscience*, *7*(January), 1–12. https://doi.org/10.3389/fncom.2013.00193

Bal-Price, A. K., Hogberg, H. T., Buzanska, L., Lenas, P., van Vliet, E., & Hartung, T. (2010). In vitro developmental neurotoxicity (DNT) testing: Relevant models and endpoints. *NeuroToxicology*, *31*(5), 545–554. https://doi.org/10.1016/j.neuro.2009.11.006

Baltz, T., de Lima, A. D., & Voigt, T. (2010). Contribution of GABAergic interneurons to the development of spontaneous activity patterns in cultured neocortical networks. *Frontiers in Cellular Neuroscience*, *4*(June), 15. https://doi.org/10.3389/fncel.2010.00015

Baltz, T., de Lima, A. D., & Voigt, T. (2010). Contribution of GABAergic interneurons to the development of spontaneous activity patterns in cultured neocortical networks. *Frontiers in Cellular Neuroscience*, *4*(12), 15. https://doi.org/10.3389/fncel.2010.00015

Baraban, S. C., Southwell, D. G., Estrada, R. C., Jones, D. L., Sebe, J. Y., Alfaro-Cervello, C., … Alvarez-Buylla, A. (2009). Reduction of seizures by transplantation of cortical GABAergic interneuron precursors into Kv1.1 mutant mice. *Proceedings of the National Academy of Sciences*, *106*(36), 15472–15477. https://doi.org/10.1073/pnas.0900141106

Barnett, H. M., Gjorgjieva, J., Weir, K., Comfort, C., Fairhall, A. L., & Moody, W. J. (2014). Relationship between individual neuron and network spontaneous activity in developing mouse cortex. *Journal of Neurophysiology*, *112*(12), 3033–3045. https://doi.org/10.1152/jn.00349.2014

Bazhenov, M., Rulkov, N. F., & Timofeev, I. (2008). Effect of Synaptic Connectivity on Long-Range Synchronization of Fast Cortical Oscillations. *Journal of Neurophysiology*, *100*(3), 1562–1575. https://doi.org/10.1152/jn.90613.2008

Ben-Ari, Y., Gaiarsa, J.-L., Tyzio, R., & Khazipov, R. (2007). GABA: A Pioneer Transmitter That Excites Immature Neurons and Generates Primitive Oscillations. *Physiological Reviews*, *87*(4), 1215–1284. https://doi.org/10.1152/physrev.00017.2006

Ben-Ari, Y., Cherubini, E., Corradetti, R., & Gaiarsa, J.-L. L. (1989). Giant synaptic potentials in immature rat CA3 hippocampal neurones. *The Journal of Physiology*, *416*, 303–325. https://doi.org/10.1113/jphysiol.1989.sp017762

Ben-Ari, Y., Khazipov, R., Leinekugel, X., Caillard, O., & Gaiarsa, J. L. (1997). GABAA, NMDA and AMPA receptors: a developmentally regulated "ménage à trois". *Trends in Neurosciences*, *20*(11), 523–529. https://doi.org/10.1016/S0166-2236(97)01147-8

Ben-Ari, Y. (2007). GABA excites and sculpts immature neurons well before delivery: modulation by GABA of the development of ventricular progenitor cells. *Epilepsy Currents*, *7*(6), 167–169. https://doi.org/10.1111/j.1535-7511.2007.00214.x

Ben-Ari, Y. (2006). Basic developmental rules and their implications for epilepsy in the immature brain. *Epileptic Disorders : International Epilepsy Journal with Videotape*, *8*(2), 91–102. Retrieved from http://www.ncbi.nlm.nih.gov/pubmed/16793570

Ben-Ari, Y. (2002). Excitatory actions of gaba during development: the nature of the nurture. *Nature Reviews. Neuroscience*, *3*(9), 728–739. https://doi.org/10.1038/nrn920

Ben-Ari, Y. (2001). Developing networks play a similar melody. *Trends in Neurosciences*, *24*(6), 353–360. https://doi.org/10.1016/S0166-2236(00)01813-0

Berdichevsky, Y., Sabolek, H., Levine, J. B., Staley, K. J., & Yarmush, M. L. (2009). Microfluidics and multielectrode array-compatible organotypic slice culture method. *Journal of Neuroscience Methods*, *178*(1), 59–64. https://doi.org/10.1016/j.jneumeth.2008.11.016

Bi, G., & Poo, M. (2001). Synaptic modification by correlated activity: Hebb's postulate revisited. *Annual Review of Neuroscience*, *24*, 139–166. https://doi.org/10.1146/annurev.neuro.24.1.139

Biffi, E., Regalia, G., Menegon, A., Ferrigno, G., & Pedrocchi, A. (2013). The influence of neuronal density and maturation on network activity of hippocampal cell cultures: A methodological study. *PLoS ONE*, *8*(12). https://doi.org/10.1371/journal.pone.0083899

Blaesse, P., Airaksinen, M. S., Rivera, C., & Kaila, K. (2009). Cation-Chloride Cotransporters and Neuronal Function. *Neuron*, *61*(6), 820–838. https://doi.org/10.1016/j.neuron.2009.03.003

Blankenship, Aaron G.; Feller, M. B. (2010). Mechanisms underlying spontaneous patterned activity in developing neural circuits. *Nature Reviews Neuroscience*, *11*(1), 18–29. https://doi.org/10.1038/nrn2759.Mechanisms

Bolton, M. M., & Eroglu, C. (2009). Look who is weaving the neural web: glial control of synapse formation. *Current Opinion in Neurobiology*, *19*(5), 491–497. https://doi.org/10.1016/j.conb.2009.09.007

Bonifazi, P., Goldin, M., Picardo, M. A., Jorquera, I., Cattani, A., Bianconi, G., … Cossart, R. (2009). GABAergic hub neurons orchestrate synchrony in developing hippocampal networks. *Science*, *326*(5958), 1419–1424. https://doi.org/10.1126/science.1175509

Borghi, T., Gusmeroli, R., Spinelli, A. S., & Baranauskas, G. (2007). A simple method for efficient spike detection in multiunit recordings. *Journal of Neuroscience Methods*, *163*(1), 176–180. https://doi.org/10.1016/j.jneumeth.2007.02.014

Brennand, K., Simone, A., Jou, J., Gelboin-Burkhart, C., Tran, N., Sangar, S., … Gage, F. (2011). Modeling schizophrenia using hiPSC neurons Kristen. *Nature*, *473*(7346), 221–225. https://doi.org/10.1038/nature09915.Modeling

Brennand, K. J., & Gage, F. H. (2012). Modeling psychiatric disorders through reprogramming. *Disease Models & Mechanisms*, *5*(1), 26–32. https://doi.org/10.1242/dmm.008268

Brunel, N., & Wang, X.-J. (2003). What determines the frequency of fast network oscillations with irregular neural discharges? I. Synaptic dynamics and excitation-inhibition balance. *Journal of Neurophysiology*, *90*(1), 415–430. https://doi.org/10.1152/jn.01095.2002

Buzsáki, G. (2004). Large-scale recording of neuronal ensembles. *Nature Neuroscience*, *7*(5), 446–451. https://doi.org/10.1038/nn1233

Buzsáki, G., Anastassiou, C. A., & Koch, C. (2012). The origin of extracellular fields and currents — EEG, ECoG, LFP and spikes. *Nature Reviews Neuroscience*, *13*(6), 407–420. https://doi.org/10.1038/nrn3241

Byers, B., Lee, H., & Reijo Pera, R. (2012). Modeling Parkinson's Disease Using Induced Pluripotent Stem Cells. *Current Neurology and Neuroscience Reports*, *12*(3), 237–242. https://doi.org/10.1007/s11910-012-0270-y

Bystron, I., Blakemore, C., & Rakic, P. (2008). Development of the human cerebral cortex: Boulder Committee revisited. *Nature Reviews Neuroscience*, *9*(2), 110–122. https://doi.org/10.1038/nrn2252

Canals, I., Soriano, J., Orlandi, J. G., Torrent, R., Richaud-Patin, Y., Jiménez-Delgado, S., … Raya, A. (2015). Activity and high-order effective connectivity alterations in sanfilippo C patient-specific neuronal networks. *Stem Cell Reports*, *5*(4), 546–557. https://doi.org/10.1016/j.stemcr.2015.08.016

Capogna, M., & Pearce, R. A. (2011). GABA A,slow: causes and consequences. *Trends in Neurosciences*, *34*(2), 101–112. https://doi.org/10.1016/j.tins.2010.10.005

Caselles, V., Kimmel, R., & Sapiro, G. (1995). Geodesic active contours. In *Proceedings of IEEE International Conference on Computer Vision* (Vol. 0, pp. 694–699). IEEE Comput. Soc. Press. https://doi.org/10.1109/ICCV.1995.466871

Chambers, S. M., Fasano, C. A., Papapetrou, E. P., Tomishima, M., Sadelain, M., & Studer, L. (2009). Highly efficient neural conversion of human ES and iPS cells by dual inhibition of SMAD signaling. *Nature Biotechnology*, *27*(3), 275–280. https://doi.org/10.1038/nbt.1529

Chan, T. F., & Vese, L. A. (2001). Active contours without edges. *IEEE Transactions on Image Processing*, *10*(2), 266–277. https://doi.org/10.1109/83.902291

Charlesworth, P., Morton, A., Eglen, S. J., Komiyama, N. H., & Grant, S. G. N. (2016). Canalization of genetic and pharmacological perturbations in developing primary neuronal activity patterns. *Neuropharmacology*, *100*, 47–55. https://doi.org/10.1016/j.neuropharm.2015.07.027

Chekeni, F. B., Elliott, M. R., Sandilos, J. K., Walk, S. F., Kinchen, J. M., Lazarowski, E. R., … Ravichandran, K. S. (2010). Pannexin 1 channels mediate "find-me" signal release and membrane permeability during apoptosis. *Nature*, *467*(7317), 863–867. https://doi.org/10.1038/nature09413

Chen, T.-W., Wardill, T. J., Sun, Y., Pulver, S. R., Renninger, S. L., Baohan, A., … Kim, D. S. (2013). Ultrasensitive fluorescent proteins for imaging neuronal activity. *Nature*, *499*(7458), 295–300. https://doi.org/10.1038/nature12354

Chestkov, I. V., Vasilieva, E. A., Illarioshkin, S. N., Lagarkova, M. A., & Kiselev, S. L. (2014). Patient-Specific Induced Pluripotent Stem Cells for SOD1-Associated Amyotrophic Lateral Sclerosis Pathogenesis Studies. *Acta Naturae*, *6*(1), 54–60. Retrieved from http://www.ncbi.nlm.nih.gov/pubmed/24772327

Chiappalone, M., Vato, A., Tedesco, M., Marcoli, M., Davide, F., & Martinoia, S. (2003). Networks of neurons coupled to microelectrode arrays: A neuronal sensory system for pharmacological applications. *Biosensors and Bioelectronics*, *18*(5–6), 627–634. https://doi.org/10.1016/S0956-5663(03)00041-1

Chiappalone, M., Bove, M., Vato, A., Tedesco, M., & Martinoia, S. (2006). Dissociated cortical networks show spontaneously correlated activity patterns during in vitro

development. *Brain Research*, *1093*(1), 41–53. https://doi.org/10.1016/j.brainres.2006.03.049

Cho, S., Wood, A., & Bowlby, M. (2007). Brain Slices as Models for Neurodegenerative Disease and Screening Platforms to Identify Novel Therapeutics. *Current Neuropharmacology*, *5*(1), 19–33. https://doi.org/10.2174/157015907780077105

Ciabatti, E., González-Rueda, A., Mariotti, L., Morgese, F., & Tripodi, M. (2017). Life-Long Genetic and Functional Access to Neural Circuits Using Self-Inactivating Rabies Virus. *Cell*, *170*(2), 382–392.e14. https://doi.org/10.1016/j.cell.2017.06.014

Cimetta, E., Figallo, E., Cannizzaro, C., Elvassore, N., & Vunjak-Novakovic, G. (2009). Micro-bioreactor arrays for controlling cellular environments: Design principles for human embryonic stem cell applications. *Methods*, *47*(2), 81–89. https://doi.org/10.1016/j.ymeth.2008.10.015

Clapham, D. E. (2007). Calcium Signaling. *Cell*, *131*(6), 1047–1058. https://doi.org/10.1016/j.cell.2007.11.028

Cohen, E., Ivenshitz, M., Amor-Baroukh, V., Greenberger, V., & Segal, M. (2008). Determinants of spontaneous activity in networks of cultured hippocampus. *Brain Research*, *1235*, 21–30. https://doi.org/10.1016/j.brainres.2008.06.022

Corlew, R., Bosma, M. M., & Moody, W. J. (2004). Spontaneous, synchronous electrical activity in neonatal mouse cortical neurones. *Journal of Physiology*, *560*(2), 377–390. https://doi.org/10.1113/jphysiol.2004.071621

Cornelissen, F., Verstraelen, P., Verbeke, T., Pintelon, I., Timmermans, J.-P., Nuydens, R., & Meert, T. (2013). Quantitation of Chronic and Acute Treatment Effects on Neuronal Network Activity Using Image and Signal Analysis. *Journal of Biomolecular Screening*, *18*(7), 807–819. https://doi.org/10.1177/1087057113486518

Cosgrove, K. E., & MacCaferri, G. (2012). MGlu1α-dependent recruitment of excitatory GABAergic input to neocortical Cajal-Retzius cells. *Neuropharmacology*, *63*(3), 486–493. https://doi.org/10.1016/j.neuropharm.2012.04.025

Cossart, R., Ikegaya, Y., & Yuste, R. (2005). Calcium imaging of cortical networks dynamics. *Cell Calcium*, *37*(5 SPEC. ISS.), 451–457. https://doi.org/10.1016/j.ceca.2005.01.013

Cotterill, E., Charlesworth, P., Thomas, C. W., Paulsen, O., & Eglen, S. J. (2016). A comparison of computational methods for detecting bursts in neuronal spike trains and their application to human stem cell-derived neuronal networks. *Journal of Neurophysiology*, *116*(2), 306–321. https://doi.org/10.1152/jn.00093.2016

Coyne, L., Shan, M., Przyborski, S. A., Hirakawa, R., & Halliwell, R. F. (2011). Neuropharmacological properties of neurons derived from human stem cells. *Neurochemistry International*, *59*(3), 404–412. https://doi.org/10.1016/j.neuint.2011.01.022

Crépel, V., Aronov, D., Jorquera, I., Represa, A., Ben-Ari, Y., & Cossart, R. (2007). A Parturition-Associated Nonsynaptic Coherent Activity Pattern in the Developing Hippocampus. *Neuron*, *54*(1), 105–120. https://doi.org/10.1016/j.neuron.2007.03.007

Danjo, T., Eiraku, M., Muguruma, K., Watanabe, K., Kawada, M., Yanagawa, Y., … Sasai, Y. (2011). Subregional Specification of Embryonic Stem Cell-Derived Ventral Telencephalic Tissues by Timed and Combinatory Treatment with Extrinsic Signals. *Journal of Neuroscience*, *31*(5), 1919–1933. https://doi.org/10.1523/JNEUROSCI.5128-10.2011

De Paola, V., Arber, S., & Caroni, P. (2003). AMPA receptors regulate dynamic equilibrium of presynaptic terminals in mature hippocampal networks. *Nature Neuroscience*, 491–500. https://doi.org/10.1038/nn1046

Defranchi, E., Novellino, A., Whelan, M., Vogel, S., Ramirez, T., van Ravenzwaay, B., & Landsiedel, R. (2011). Feasibility Assessment of Micro-Electrode Chip Assay as a Method of Detecting Neurotoxicity in vitro. *Frontiers in Neuroengineering*, *4*(April), 6. https://doi.org/10.3389/fneng.2011.00006

Delescluse, M., & Pouzat, C. (2006). Efficient spike-sorting of multi-state neurons using inter-spike intervals information. *Journal of Neuroscience Methods*, *150*(1), 16–29. https://doi.org/10.1016/j.jneumeth.2005.05.023

Delgado Ruz, I., & Schultz, S. R. (2014). Localising and classifying neurons from high density MEA recordings. *Journal of Neuroscience Methods*, *233*, 115–128. https://doi.org/10.1016/j.jneumeth.2014.05.037

Dolmetsch, R., & Geschwind, D. H. (2011). The Human Brain in a Dish: The Promise of iPSC-Derived Neurons. *Cell*, *145*(6), 831–834. https://doi.org/10.1016/j.cell.2011.05.034

Dombeck, D. A., Khabbaz, A. N., Collman, F., Adelman, T. L., & Tank, D. W. (2007). Imaging large scale neural activity with cellular resolution in awake mobile mice. *Neuron*, *56*(1), 43–57.

Dupont, E., Hanganu, I. L., Kilb, W., Hirsch, S., & Luhmann, H. J. (2006). Rapid developmental switch in the mechanisms driving early cortical columnar networks. *Nature*, *439*(7072), 79–83. https://doi.org/10.1038/nature04264

Dworak, B. J., & Wheeler, B. C. (2009). Novel MEA platform with PDMS microtunnels enables the detection of action potential propagation from isolated axons in culture. *Lab Chip*, *9*(3), 404–410. https://doi.org/10.1039/B806689B

Egashira, T., Yuasa, S., & Fukuda, K. (2011). Induced pluripotent stem cells in cardiovascular medicine. *Stem Cells International*, *2011*, 348960. https://doi.org/10.4061/2011/348960

Egert, U., Knott, T., Schwarz, C., Nawrot, M., Brandt, A., Rotter, S., & Diesmann, M. (2002). MEA-Tools: An open source toolbox for the analysis of multi-electrode data with MATLAB. *Journal of Neuroscience Methods*, *117*(1), 33–42. https://doi.org/10.1016/S0165-0270(02)00045-6

Egorov, A. V., & Draguhn, A. (2013). Development of coherent neuronal activity patterns in mammalian cortical networks: common principles and local hetereogeneity. *Mechanisms of Development*, *130*(6–8), 412–423. https://doi.org/10.1016/j.mod.2012.09.006

Eichele, T., Calhoun, V. D., Moosmann, M., Specht, K., Jongsma, M. L. A., Quiroga, R. Q., … Hugdahl, K. (2008). Unmixing concurrent EEG-fMRI with parallel independent component analysis. *International Journal of Psychophysiology*, *67*(3), 222–234. https://doi.org/10.1016/j.ijpsycho.2007.04.010

Einevoll, G. T., Franke, F., Hagen, E., Pouzat, C., & Harris, K. D. (2012). Towards reliable spike-train recordings from thousands of neurons with multielectrodes. *Current Opinion in Neurobiology*, *22*(1), 11–17. https://doi.org/10.1016/j.conb.2011.10.001

Eiraku, M., Watanabe, K., Matsuo-Takasaki, M., Kawada, M., Yonemura, S., Matsumura, M., … Sasai, Y. (2008). Self-organized formation of polarized cortical tissues from ESCs and its active manipulation by extrinsic signals. *Cell Stem Cell*, *3*(5), 519–532. https://doi.org/10.1016/j.stem.2008.09.002

Elkabetz, Y., Panagiotakos, G., G., A., Socci, N. D., Tabar, V., & Studer, L. (2008). Human ES cell-derived neural rosettes reveal a functionally dinstinct early neural stem cell stage. *Genes & Development*, *22*(2), 152–165. https://doi.org/10.1101/gad.1616208

Eroglu, Ç., Allen, N. J., Susman, M. W., O'Rourke, N. A., Park, C. Y., Özkan, E., … Barres, B. A. (2009). Gabapentin Receptor α2δ-1 Is a Neuronal Thrombospondin Receptor Responsible for Excitatory CNS Synaptogenesis. *Cell*, *139*(2), 380–392. https://doi.org/10.1016/j.cell.2009.09.025

Eytan, D., & Marom, S. (2006). Dynamics and effective topology underlying synchronization in networks of cortical neurons. *The Journal of Neuroscience : The Official Journal of the Society for Neuroscience*, *26*(33), 8465–8476. https://doi.org/10.1523/JNEUROSCI.1627-06.2006

Eytan, D., Minerbi, A., Ziv, N., & Marom, S. (2004). Dopamine-induced dispersion of correlations between action potentials in networks of cortical neurons. *Journal of Neurophysiology*, *92*(3), 1817–1824. https://doi.org/10.1152/jn.00202.2004

FitzGerald, J. J., Lacour, S. P., McMahon, S. B., & Fawcett, J. W. (2009). Microchannel electrodes for recording and stimulation: In vitro evaluation. *IEEE Transactions on Biomedical Engineering*, *56*(5), 1524–1534. https://doi.org/10.1109/TBME.2009.2013960

FitzGerald, J. J., Lacour, S. P., McMahon, S. B., & Fawcett, J. W. (2008). Microchannels as axonal amplifiers. *IEEE Transactions on Biomedical Engineering*, *55*(3), 1136–1146. https://doi.org/10.1109/TBME.2007.909533

Forostyak, O., Romanyuk, N., Verkhratsky, A., Sykova, E., & Dayanithi, G. (2013). Plasticity of Calcium Signaling Cascades in Human Embryonic Stem Cell-Derived Neural Precursors. *Stem Cells and Development*, *22*(10), 1506–1521. https://doi.org/10.1089/scd.2012.0624

Frantz, G. D., & McConnell, S. K. (1996). Restriction of late cerebral cortical progenitors to an upper-layer fate. *Neuron*, *17*(1), 55–61. https://doi.org/10.1016/S0896-6273(00)80280-9

Frega, M., van Gestel, S. H. C., Linda, K., van der Raadt, J., Keller, J., Van Rhijn, J.-R., … Nadif Kasri, N. (2017). Rapid Neuronal Differentiation of Induced Pluripotent Stem Cells for Measuring Network Activity on Micro-electrode Arrays. *Journal of Visualized Experiments*, (119), 1–10. https://doi.org/10.3791/54900

Freund, T. F., & Buzsáki, G. (1996). Interneurons of the hippocampus. *Hippocampus*, *6*(4), 347–470. https://doi.org/10.1002/(SICI)1098-1063(1996)6:4<347::AID-HIPO1>3.0.CO;2-I

Frey, U., Egert, U., Heer, F., Hafizovic, S., & Hierlemann, A. (2009). Microelectronic system for high-resolution mapping of extracellular electric fields applied to brain slices. *Biosensors and Bioelectronics*, *24*(7), 2191–2198. https://doi.org/10.1016/j.bios.2008.11.028

Fukuda, T. (2007). Structural organization of the gap junction network in the cerebral cortex. *The Neuroscientist : A Review Journal Bringing Neurobiology, Neurology and Psychiatry*, *13*(3), 199–207. https://doi.org/10.1177/1073858406296760

Fukushima, K., Miura, Y., Sawada, K., Yamazaki, K., & Ito, M. (2016). Establishment of a human neuronal network assessment system by using a human neuron/astrocyte co-culture derived from fetal neural stem/progenitor cells. *Journal of Biomolecular Screening*, *21*(1), 54–64. https://doi.org/10.1177/1087057115610055

Galimberti, I., Gogolla, N., Alberi, S., Santos, A. F., Muller, D., & Caroni, P. (2006). Long-Term Rearrangements of Hippocampal Mossy Fiber Terminal Connectivity in the

Adult Regulated by Experience. *Neuron*, *50*(5), 749–763. https://doi.org/10.1016/j.neuron.2006.04.026

Gao, P., Postiglione, M. P., Krieger, T. G., Hernandez, L., Wang, C., Han, Z., … Shi, S. H. (2014). Deterministic progenitor behavior and unitary production of neurons in the neocortex. *Cell*, *159*(4), 775–788. https://doi.org/10.1016/j.cell.2014.10.027

Garaschuk, O., Hanse, E., & Konnerth, A. (1998). Developmental profile and synaptic origin of early network oscillations in the CA1 region of rat neonatal hippocampus. *The Journal of Physiology*, *507 (Pt 1*(Pt 1), 219–236. Retrieved from http://www.ncbi.nlm.nih.gov/pubmed/9490842

Garaschuk, O., Linn, J., Eilers, J., & Konnerth, A. (2000). Large-scale oscillatory calcium waves in the immature cortex. *Nature Neuroscience*, *3*(5), 452–459. https://doi.org/10.1038/74823

Gaspard, N., Bouschet, T., Hourez, R., Dimidschstein, J., Naeije, G., Van Den Ameele, J., … Vanderhaeghen, P. (2008). An intrinsic mechanism of corticogenesis from embryonic stem cells. *Nature*, *455*(7211), 351–357. https://doi.org/10.1038/nature07287

Germain, N. D., Banda, E. C., Becker, S., Naegele, J. R., & Grabel, L. B. (2013). Derivation and Isolation of NKX2.1-Positive Basal Forebrain Progenitors from Human Embryonic Stem Cells. *Stem Cells and Development*, *22*(10), 1477–1489. https://doi.org/10.1089/scd.2012.0264

Germain, N., Banda, E., & Grabel, L. (2010). Embryonic stem cell neurogenesis and neural specification. *Journal of Cellular Biochemistry*, *111*(3), 535–542. https://doi.org/10.1002/jcb.22747

Gesteland, R., Howland, B., Lettvin, J., & Pitts, W. (1959). Comments on Microelectrodes. *Proceedings of the IRE*, *47*(11), 1856–1862. https://doi.org/10.1109/JRPROC.1959.287156

Giacomello, M., Girardi, S., Scorzeto, M., Peruffo, A., Maschietto, M., Cozzi, B., & Vassanelli, S. (2011). Stimulation of Ca2+signals in neurons by electrically coupled electrolyte-oxide-semiconductor capacitors. *Journal of Neuroscience Methods*, *198*(1), 1–7. https://doi.org/10.1016/j.jneumeth.2011.02.009

Glykys, J., & Mody, I. (2007). The main source of ambient GABA responsible for tonic inhibition in the mouse hippocampus. *Journal of Physiology*, *582*(3), 1163–1178. https://doi.org/10.1113/jphysiol.2007.134460

Gold, C., Henze, D. A., Koch, C., & Buzsáki, G. (2006). On the Origin of the Extracellular Action Potential Waveform: A Modeling Study. *Journal of Neurophysiology*, *95*(5), 3113–3128. https://doi.org/10.1152/jn.00979.2005

Gopal, K. V. (2003). Neurotoxic effects of mercury on auditory cortex networks growing on microelectrode arrays: a preliminary analysis. *Neurotoxicology and Teratology*, *25*(1), 69–76. https://doi.org/10.1016/S0892-0362(02)00321-5

Gourévitch, B., & Eggermont, J. J. (2007). A nonparametric approach for detection of bursts in spike trains. *Journal of Neuroscience Methods*, *160*(2), 349–358. https://doi.org/10.1016/j.jneumeth.2006.09.024

Goyal, G., & Nam, Y. (2011). Neuronal micro-culture engineering by microchannel devices of cellular scale dimensions. *Biomedical Engineering Letters*, *1*(2), 89–98. https://doi.org/10.1007/s13534-011-0014-y

Greenberg, D. S., Houweling, A. R., & Kerr, J. N. D. (2008). Population imaging of ongoing neuronal activity in the visual cortex of awake rats. *Nature Neuroscience*, *11*(7), 749–751. https://doi.org/10.1038/nn.2140

Gullo, F., Mazzetti, S., Maffezzoli, A., Dossi, E., Lecchi, M., Amadeo, A., … Wanke, E. (2010). Orchestration of "presto" and "largo" synchrony in up-down activity of cortical networks. *Frontiers in Neural Circuits*, *4*(April), 11. https://doi.org/10.3389/fncir.2010.00011

Gunhanlar, N., Shpak, G., van der Kroeg, M., Gouty-Colomer, L. A., Munshi, S. T., Lendemeijer, B., … Kushner, S. A. (2017). A simplified protocol for differentiation of electrophysiologically mature neuronal networks from human induced pluripotent stem cells. *Molecular Psychiatry*, *23*(5), 1336–1344. https://doi.org/10.1038/mp.2017.56

Gust, J., Wright, J. J., Pratt, E. B., & Bosma, M. M. (2003). Development of synchronized activity of cranial motor neurons in the segmented embryonic mouse hindbrain. *Journal of Physiology*, *550*(1), 123–133. https://doi.org/10.1113/jphysiol.2002.038737

Gähwiler, B. H., Capogna, M., Debanne, D., McKinney, R. A., & Thompson, S. M. (1997). Organotypic slice cultures: A technique has come of age. *Trends in Neurosciences*, *20*(10), 471–477. https://doi.org/10.1016/S0166-2236(97)01122-3

Göbel, W., & Helmchen, F. (2007). In Vivo Calcium Imaging of Neural Network Function. *Physiology*, *22*(6), 358–365. https://doi.org/10.1152/physiol.00032.2007

Hanganu, I. L., Kilb, W., & Luhmann, H. J. (2001). Spontaneous synaptic activity of subplate neurons in neonatal rat somatosensory cortex. *Cerebral Cortex*, *11*(5), 400–410. https://doi.org/10.1093/cercor/11.5.400

Hanganu, I. L., Okabe, A., Lessmann, V., & Luhmann, H. J. (2009). Cellular mechanisms of subplate-driven and cholinergic input-dependent network activity in the neonatal rat somatosensory cortex. *Cerebral Cortex*, *19*(1), 89–105. https://doi.org/10.1093/cercor/bhn061

Hanganu, I. L., Kilb, W., & Luhmann, H. J. (2002). Functional synaptic projections onto subplate neurons in neonatal rat somatosensory cortex. *The Journal of Neuroscience : The Official Journal of the Society for Neuroscience*, *22*(16), 7165–7176. https://doi.org/20026716

Hanganu, I. L., & Luhmann, H. J. (2004). Functional nicotinic acetylcholine receptors on subplate neurons in neonatal rat somatosensory cortex. *Journal of Neurophysiology*, *92*(1), 189–198. https://doi.org/10.1152/jn.00010.2004

Hanganu-Opatz, I. L. (2010). Between molecules and experience: role of early patterns of coordinated activity for the development of cortical maps and sensory abilities. *Brain Research Reviews*, *64*(1), 160–176. https://doi.org/10.1016/j.brainresrev.2010.03.005

Hansen, D. V., Lui, J. H., Flandin, P., Yoshikawa, K., Rubenstein, J. L., Alvarez-Buylla, A., & Kriegstein, A. R. (2013). Non-epithelial stem cells and cortical interneuron production in the human ganglionic eminences. *Nature Neuroscience*, *16*(11), 1576–1587. https://doi.org/10.1038/nn.3541

Hansen, S. K., Stummann, T. C., Borland, H., Hasholt, L. F., Tümer, Z., Nielsen, J. E., … Hyttel, P. (2016). Induced pluripotent stem cell - derived neurons for the study of spinocerebellar ataxia type 3. *Stem Cell Research*, *17*(2), 306–317. https://doi.org/10.1016/j.scr.2016.07.004

Harris, K. D., Henze, D. A., Csicsvari, J., Hirase, H., & Buzsáki, G. (2000). Accuracy of tetrode spike separation as determined by simultaneous intracellular and extracellular measurements. *Journal of Neurophysiology*, *84*(1), 401–414. https://doi.org/10.1152/jn.2000.84.1.401

Harris, K. D., Hirase, H., Leinekugel, X., Henze, D. A., & Buzsáki, G. (2001). Temporal interaction between single spikes and complex spike bursts in hippocampal

pyramidal cells. *Neuron*, *32*(1), 141–149. https://doi.org/10.1016/S0896-6273(01)00447-0

Harris, K. D., Quiroga, R. Q., Freeman, J., & Smith, S. L. (2016). Improving data quality in neuronal population recordings. *Nature Neuroscience*, *19*(9), 1165–1174. https://doi.org/10.1038/nn.4365

Harrison, J. F., Rinne, M. L., Kelley, M. R., Druzhyna, N. M., Wilson, G. L., & Ledoux, S. P. (2007). Altering DNA base excision repair: use of nuclear and mitochondrial-targeted N-methylpurine DNA glycosylase to sensitize astroglia to chemotherapeutic agents. *Glia*, *55*(14), 1416–1425. https://doi.org/10.1002/glia

Hartfield, E. M., Yamasaki-Mann, M., Ribeiro Fernandes, H. J., Vowles, J., James, W. S., Cowley, S. A., & Wade-Martins, R. (2014). Physiological characterisation of human iPS-derived dopaminergic neurons. *PLoS ONE*, *9*(2). https://doi.org/10.1371/journal.pone.0087388

Heikkilä, T. J., Ylä-Outinen, L., Tanskanen, J. M. A., Lappalainen, R. S., Skottman, H., Suuronen, R., … Narkilahti, S. (2009). Human embryonic stem cell-derived neuronal cells form spontaneously active neuronal networks in vitro. *Experimental Neurology*, *218*(1), 109–116. https://doi.org/10.1016/j.expneurol.2009.04.011

Heinemann, U., Buchheim, K., Gabriel, S., Kann, O., Kovács, R., & Schuchmann, S. (2002). Coupling of electrical and metabolic activity during epileptiform discharges. *Epilepsia*, *43 Suppl 5*(5), 168–173. Retrieved from http://www.ncbi.nlm.nih.gov/pubmed/12121315

Heman-Ackah, S. M., Bassett, A. R., & Wood, M. J. A. (2016). Precision Modulation of Neurodegenerative Disease-Related Gene Expression in Human iPSC-Derived Neurons. *Scientific Reports*, *6*(February), 1–12. https://doi.org/10.1038/srep28420

Hendriks, J., Riesle, J., & Blitterswijk, C. A. van. (2010). Co-culture in cartilage tissue engineering. *Journal of Tissue Engineering and Regenerative Medicine*, *4*(7), 524–531. https://doi.org/10.1002/term

Henze, D. a, Borhegyi, Z., Csicsvari, J., Mamiya, a, Harris, K. D., & Buzsáki, G. (2000). Intracellular features predicted by extracellular recordings in the hippocampus in vivo. *Journal of Neurophysiology*, *84*(1), 390–400. https://doi.org/84:390-400

Henze, D. A., Urban, N. N., & Barrionuevo, G. (2000). The multifarious hippocampal mossy fiber pathway: A review. *Neuroscience*, *98*(3), 407–427. https://doi.org/10.1016/S0306-4522(00)00146-9

Hochedlinger, K., & Jaenisch, R. (2006). Nuclear reprogramming and pluripotency. *Nature*, *441*(7097), 1061–1067. https://doi.org/10.1038/nature04955

Hogberg, H. T., Sobanski, T., Novellino, A., Whelan, M., Weiss, D. G., & Bal-Price, A. K. (2011). Application of micro-electrode arrays (MEAs) as an emerging technology for developmental neurotoxicity: Evaluation of domoic acid-induced effects in primary cultures of rat cortical neurons. *NeuroToxicology*, *32*(1), 158–168. https://doi.org/10.1016/j.neuro.2010.10.007

Holmgren, C. D., Mukhtarov, M., Malkov, A. E., Popova, I. Y., Bregestovski, P., & Zilberter, Y. (2010). Energy substrate availability as a determinant of neuronal resting potential, GABA signaling and spontaneous network activity in the neonatal cortex in vitro. *Journal of Neurochemistry*, *112*(4), 900–912. https://doi.org/10.1111/j.1471-4159.2009.06506.x

Holter, N. I., Zuber, N., Bruehl, C., & Draguhn, A. (2007). Functional maturation of developing interneurons in the molecular layer of mouse dentate gyrus. *Brain Research*, *1186*(1), 56–64. https://doi.org/10.1016/j.brainres.2007.09.089

Hu, J.-G., Lü, H.-Z., Wang, Y.-X., Bao, M.-S., Zhao, B.-M., & Zhou, J.-S. (2010). BMP signaling mediates astrocyte differentiation of oligodendrocyte progenitor cells. *The Tohoku Journal of Experimental Medicine*, *222*(3), 195–200. https://doi.org/10.1620/tjem.222.195

Hua, J. Y., & Smith, S. J. (2004). Neural activity and the dynamics of central nervous system development. *Nature Neuroscience*, *7*(4), 327–332. https://doi.org/10.1038/nn1218

Humpel, C. (2015). Organotypic brain slice cultures: A review. *Neuroscience*, *305*, 86–98. https://doi.org/10.1016/j.neuroscience.2015.07.086

Hyysalo, A., Ristola, M., Mäkinen, M. E.-L., Häyrynen, S., Nykter, M., & Narkilahti, S. (2017). Laminin α5 substrates promote survival, network formation and functional development of human pluripotent stem cell-derived neurons in vitro. *Stem Cell Research*, *24*. https://doi.org/10.1016/j.scr.2017.09.002

Illes, S., Fleischer, W., Siebler, M., Hartung, H. P., & Dihné, M. (2007). Development and pharmacological modulation of embryonic stem cell-derived neuronal network activity. *Experimental Neurology*, *207*(1), 171–176. https://doi.org/10.1016/j.expneurol.2007.05.020

Illes, S., Jakab, M., Beyer, F., Gelfert, R., Couillard-Despres, S., Schnitzler, A., … Aigner, L. (2014). Intrinsically active and pacemaker neurons in pluripotent stem cell-derived neuronal populations. *Stem Cell Reports*, *2*(3), 323–336. https://doi.org/10.1016/j.stemcr.2014.01.006

Illes, S., Theiss, S., Hartung, H.-P., Siebler, M., & Dihné, M. (2009). Niche-dependent development of functional neuronal networks from embryonic stem cell-derived neural populations. *BMC Neuroscience*, *10*(Aug), 93. https://doi.org/10.1186/1471-2202-10-93

Inoue, K., Furukawa, T., Kumada, T., Yamada, J., Wang, T., Inoue, R., & Fukuda, A. (2012). Taurine inhibits K +-Cl - cotransporter KCC2 to regulate embryonic Cl - homeostasis via with-no-lysine (WNK) protein kinase signaling pathway. *Journal of Biological Chemistry*, *287*(25), 20839–20850. https://doi.org/10.1074/jbc.M111.319418

Inta, D., Meyer-Lindenberg, A., & Gass, P. (2011). Alterations in postnatal neurogenesis and dopamine dysregulation in schizophrenia: A hypothesis. *Schizophrenia Bulletin*, *37*(4), 674–680. https://doi.org/10.1093/schbul/sbq134

Ishii, M. N., Yamamoto, K., Shoji, M., Asami, A., & Kawamata, Y. (2017). Human induced pluripotent stem cell (hiPSC)-derived neurons respond to convulsant drugs when co-cultured with hiPSC-derived astrocytes. *Toxicology*, *389*(June), 130–138. https://doi.org/10.1016/j.tox.2017.06.010

Ishiuchi, S., Tsuzuki, K., Yoshida, Y., Yamada, N., Hagimura, N., Okado, H., … Ozawa, S. (2002). Blockage of Ca(2+)-permeable AMPA receptors suppresses migration and induces apoptosis in human glioblastoma cells. *Nature Medicine*, *8*(9), 971–978. https://doi.org/10.1038/nm746

Ito, D., Komatsu, T., & Gohara, K. (2013). Measurement of saturation processes in glutamatergic and GABAergic synapse densities during long-term development of cultured rat cortical networks. *Brain Research*, *1534*, 22–32. https://doi.org/10.1016/j.brainres.2013.08.004

Ito, S., Yeh, F. C., Hiolski, E., Rydygier, P., Gunning, D. E., Hottowy, P., … Beggs, J. M. (2014). Large-scale, high-resolution multielectrode-array recording depicts

functional network differences of cortical and hippocampal cultures. *PLoS ONE*, *9*(8). https://doi.org/10.1371/journal.pone.0105324

Itsykson, P., Ilouz, N., Turetsky, T., Goldstein, R. S., Pera, M. F., Fishbein, I., … Reubinoff, B. E. (2005). Derivation of neural precursors from human embryonic stem cells in the presence of noggin. *Molecular and Cellular Neuroscience*, *30*(1), 24–36. https://doi.org/10.1016/j.mcn.2005.05.004

Ivenshitz, M., & Segal, M. (2010). Neuronal density determines network connectivity and spontaneous activity in cultured hippocampus. *Journal of Neurophysiology*, *104*(2), 1052–1060. https://doi.org/10.1152/jn.00914.2009

Ivenshitz, M., & Segal, M. (2010). Neuronal density determines network connectivity and spontaneous activity in cultured hippocampus. *Journal of Neurophysiology*, *104*(2), 1052–1060. https://doi.org/10.1152/jn.00914.2009

Jang, M. J., & Nam, Y. (2015). NeuroCa: integrated framework for systematic analysis of spatiotemporal neuronal activity patterns from large-scale optical recording data. *Neurophotonics*, *2*(3), 035003. https://doi.org/10.1117/1.NPh.2.3.035003

Jansen, R., Timmerman, J., Loos, M., Spijker, S., van Ooyen, A., Brussaard, A. B., … Linkenkaer-Hansen, K. (2011). Novel candidate genes associated with hippocampal oscillations. *PLoS ONE*, *6*(10). https://doi.org/10.1371/journal.pone.0026586

Jessell, T. M., & Sanes, J. R. (2000). Development. The decade of the developing brain. *Current Opinion in Neurobiology*, *10*(5), 599–611. https://doi.org/10.1016/S0959-4388(00)00136-7

Jha, P., Wang, X., & Auwerx, J. (2016). Analysis of Mitochondrial Respiratory Chain Supercomplexes Using Blue Native Polyacrylamide Gel Electrophoresis (BN-PAGE). *Current Protocols in Mouse Biology*, *6*(1), 1–14. https://doi.org/10.1002/9780470942390.mo150182

Johnson, M. A., Weick, J. P., Pearce, R. A., & Zhang, S.-C. (2007). Functional Neural Development from Human Embryonic Stem Cells: Accelerated Synaptic Activity via Astrocyte Coculture. *Journal of Neuroscience*, *27*(12), 3069–3077. https://doi.org/10.1523/JNEUROSCI.4562-06.2007

Jungblut, M., Knoll, W., Thielemann, C., & Pottek, M. (2009). Triangular neuronal networks on microelectrode arrays: An approach to improve the properties of low-density networks for extracellular recording. *Biomedical Microdevices*, *11*(6), 1269–1278. https://doi.org/10.1007/s10544-009-9346-0

Kadoshima, T., Sakaguchi, H., Nakano, T., Soen, M., Ando, S., Eiraku, M., & Sasai, Y. (2013). Self-organization of axial polarity, inside-out layer pattern, and species-specific progenitor dynamics in human ES cell-derived neocortex. *Proceedings of the National Academy of Sciences*, *110*(50), 20284–20289. https://doi.org/10.1073/pnas.1315710110

Kamioka, H., Maeda, E., Jimbo, Y., Robinson, H. P. C., & Kawana, A. (1996). Spontaneous periodic synchronized bursting during formation of mature patterns of connections in cortical cultures. *Neuroscience Letters*, *206*(2–3), 109–112. https://doi.org/10.1016/S0304-3940(96)12448-4

Kaneoke, Y., & Vitek, J. L. (1996). Burst and oscillation as disparate neuronal properties. *Journal of Neuroscience Methods*, *68*(2), 211–223. https://doi.org/10.1016/0165-0270(96)00081-7

Kaphingst, K. A., Persky, S., McCall, C., Lachance, C., Beall, A. C., & Blascovich, J. (2009). Testing Communication Strategies to Convey Genomic Concepts Using Virtual

Reality Technology. *Journal of Health Communication*, *14*(4), 384–399. https://doi.org/10.1080/10810730902873927

Kapucu, F. E., Tanskanen, J. M. A., Mikkonen, J. E., Ylä-Outinen, L., Narkilahti, S., & Hyttinen, J. A. K. (2012). Burst analysis tool for developing neuronal networks exhibiting highly varying action potential dynamics. *Frontiers in Computational Neuroscience*, *6*(June), 1–14. https://doi.org/10.3389/fncom.2012.00038

Kasteel, E. E. J., & Westerink, R. H. S. (2017). Comparison of the acute inhibitory effects of Tetrodotoxin (TTX) in rat and human neuronal networks for risk assessment purposes. *Toxicology Letters*, *270*, 12–16. https://doi.org/10.1016/j.toxlet.2017.02.014

Kayama, T., Suzuki, I., Odawara, A., Sasaki, T., & Ikegaya, Y. (2018). Temporally coordinated spiking activity of human induced pluripotent stem cell-derived neurons co-cultured with astrocytes. *Biochemical and Biophysical Research Communications*, *495*(1), 1028–1033. https://doi.org/10.1016/j.bbrc.2017.11.115

Kerr, J. N. D., Greenberg, D., & Helmchen, F. (2005). From The Cover: Imaging input and output of neocortical networks in vivo. *Proceedings of the National Academy of Sciences*, *102*(39), 14063–14068. https://doi.org/10.1073/pnas.0506029102

Khazipov, R., Esclapez, M., Caillard, O., Bernard, C., Khalilov, I., Tyzio, R., … Ben-Ari, Y. (2001). Early development of neuronal activity in the primate hippocampus in utero. *The Journal of Neuroscience : The Official Journal of the Society for Neuroscience*, *21*(24), 9770–9781. https://doi.org/21/24/9770 [pii]

Khazipov, R., Khalilov, I., Tyzio, R., Morozova, E., Ben-Ari, Y., & Holmes, G. L. (2004). Developmental changes in GABAergic actions and seizure susceptibility in the rat hippocampus. *European Journal of Neuroscience*, *19*(3), 590–600. https://doi.org/10.1111/j.0953-816X.2003.03152.x

Khazipov, R., & Luhmann, H. J. (2006). Early patterns of electrical activity in the developing cerebral cortex of humans and rodents. *Trends in Neurosciences*, *29*(7), 414–418. https://doi.org/10.1016/j.tins.2006.05.007

Khazipov, R., Sirota, A., Leinekugel, X., Holmes, G. L., Ben-Ari, Y., & Buzsáki, G. (2004). Early motor activity drives spindle bursts in the developing somatosensory cortex. *Nature*, *432*(7018), 758–761. https://doi.org/10.1038/nature03132

Khirug, S., Huttu, K., Ludwig, A., Smirnov, S., Voipio, J., Rivera, C., … Khiroug, L. (2005). Distinct properties of functional KCC2 expression in immature mouse hippocampal neurons in culture and in acute slices. *European Journal of Neuroscience*, *21*(4), 899–904. https://doi.org/10.1111/j.1460-9568.2005.03886.x

Khodagholy, D., Gelinas, J. N., Thesen, T., Doyle, W., Devinsky, O., Malliaras, G. G., & Buzsáki, G. (2015). NeuroGrid: recording action potentials from the surface of the brain. *Nature Neuroscience*, *18*(2), 310–315. https://doi.org/10.1038/nn.3905

Kilb, W., Ikeda, M., Uchida, K., Okabe, A., Fukuda, A., & Luhmann, H. J. (2002). Depolarizing glycine responses in Cajal-Retzius cells of neonatal rat cerebral cortex. *Neuroscience*, *112*(2), 299–307. https://doi.org/10.1016/S0306-4522(02)00071-4

Kilb, W., Hanganu, I. L., Okabe, A., Sava, B. A., Shimizu-Okabe, C., Fukuda, A., & Luhmann, H. J. (2008). Glycine Receptors Mediate Excitation of Subplate Neurons in Neonatal Rat Cerebral Cortex. *Journal of Neurophysiology*, *100*(2), 698–707. https://doi.org/10.1152/jn.00657.2007

Kilb, W., Kirischuk, S., & Luhmann, H. J. (2011). Electrical activity patterns and the functional maturation of the neocortex. *European Journal of Neuroscience*, *34*(10), 1677–1686. https://doi.org/10.1111/j.1460-9568.2011.07878.x

Kim, S., Harrison, R., & Solzbacher, F. (2008). Influence of system integration and packaging for a wireless neural interface on its wireless powering performance. *Conference Proceedings : ... Annual International Conference of the IEEE Engineering in Medicine and Biology Society. IEEE Engineering in Medicine and Biology Society. Annual Conference*, *2008*, 3182–3185. https://doi.org/10.1109/IEMBS.2008.4649880

Kim, S., & McNames, J. (2007). Automatic spike detection based on adaptive template matching for extracellular neural recordings. *Journal of Neuroscience Methods*, *165*(2), 165–174. https://doi.org/10.1016/j.jneumeth.2007.05.033

Kirischuk, S., Sinning, A., Blanquie, O., Yang, J.-W., Luhmann, H. J., & Kilb, W. (2017). Modulation of Neocortical Development by Early Neuronal Activity: Physiology and Pathophysiology. *Frontiers in Cellular Neuroscience*, *11*(November), 1–21. https://doi.org/10.3389/fncel.2017.00379

Kirmse, K., Witte, O. W., & Holthoff, K. (2011). GABAergic depolarization during early cortical development and implications for anticonvulsive therapy in neonates. *Epilepsia*, *52*(9), 1532–1543. https://doi.org/10.1111/j.1528-1167.2011.03128.x

Kirwan, P., Turner-Bridger, B., Peter, M., Momoh, A., Arambepola, D., Robinson, H. P. C., & Livesey, F. J. (2015). Development and function of human cerebral cortex neural networks from pluripotent stem cells in vitro. *Development*, *142*(18), 3178–3187. https://doi.org/10.1242/dev.123851

Klausberger, T., & Somogyi, P. (2008). Neuronal diversity and temporal dynamics: the unity of hippocampal circuit operations. *Science*, *321*(5885), 53–57. https://doi.org/10.1126/science.1149381

Ko, D., Wilson, C. J., Lobb, C. J., & Paladini, C. A. (2012). Detection of bursts and pauses in spike trains. *Journal of Neuroscience Methods*, *211*(1), 145–158. https://doi.org/10.1016/j.jneumeth.2012.08.013

Kolbaev, S. N., Achilles, K., Luhmann, H. J., & Kilb, W. (2011). Effect of depolarizing GABA A -mediated membrane responses on excitability of Cajal-Retzius cells in the immature rat neocortex. *Journal of Neurophysiology*, *106*(4), 2034–2044. https://doi.org/10.1152/jn.00699.2010

Kornack, D. R., & Rakic, P. (1995). Radial and horizontal deployment of clonally related cells in the primate neocortex: Relationship to distinct mitotic lineages. *Neuron*, *15*(2), 311–321. https://doi.org/10.1016/0896-6273(95)90036-5

Kuijlaars, J., Oyelami, T., Diels, A., Rohrbacher, J., Versweyveld, S., Meneghello, G., … Verheyen, A. (2016). Sustained synchronized neuronal network activity in a human astrocyte co-culture system. *Scientific Reports*, *6*(1), 36529. https://doi.org/10.1038/srep36529

Lam, R. S., Töpfer, F. M., Wood, P. G., Busskamp, V., & Bamberg, E. (2017). Functional maturation of human stem cell-derived neurons in long-term cultures. *PLoS ONE*, *12*(1), 1–26. https://doi.org/10.1371/journal.pone.0169506

Lancaster, M. A., & Knoblich, J. A. (2014). Organogenesisin a dish: Modeling development and disease using organoid technologies. *Science*, *345*(6194). https://doi.org/10.1126/science.1247125

Lancaster, M. a, Renner, M., Martin, C., Wenzel, D., Bicknell, S., Hurles, M. E., … Andrew, P. (2013). Europe PMC Funders Group Cerebral organoids model human brain development and microcephaly. *Nature*, *501*(7467), 373–379. https://doi.org/10.1038/nature12517.Cerebral

Lappalainen, R. S., Salomäki, M., Ylä-Outinen, L., Heikkilä, T. J., Hyttinen, J. A. K., Pihlajamäki, H., … Narkilahti, S. (2010). Similarly derived and cultured hESC lines

show variation in their developmental potential towards neuronal cells in long-term culture. *Regenerative Medicine*, *5*(5), 749–762. https://doi.org/10.2217/rme.10.58

Latham, P. E., Richmond, B. J., Nelson, P. G., & Nirenberg, S. (2000). Intrinsic dynamics in neuronal networks. I. Theory. *Journal of Neurophysiology*, *83*(2), 808–827. https://doi.org/10.1152/jn.2000.83.2.808

Legéndy, C. R., & Salcman, M. (1985). Bursts and recurrences of bursts in the spike trains of spontaneously active striate cortex neurons. *Journal of Neurophysiology*, *53*(4), 926–939. https://doi.org/10.1152/jn.1985.53.4.926

Leinekugel, X., Khazipov, R., Cannon, R., Hirase, H., Ben-Ari, Y., & Buzsáki, G. (2002). Correlated bursts of activity in the neonatal hippocampus in vivo. *Science*, *296*(5575), 2049–2052. https://doi.org/10.1126/science.1071111

Leonzino, M., Busnelli, M., Antonucci, F., Verderio, C., Mazzanti, M., & Chini, B. (2016). The Timing of the Excitatory-to-Inhibitory GABA Switch Is Regulated by the Oxytocin Receptor via KCC2. *Cell Reports*, *15*(1), 96–103. https://doi.org/10.1016/j.celrep.2016.03.013

Li, H., Liu, H., Corrales, C. E., Risner, J. R., Forrester, J., Holt, J. R., … Edge, A. S. B. (2009). Differentiation of neurons from neural precursors generated in floating spheres from embryonic stem cells. *BMC Neuroscience*, *10*, 122. https://doi.org/10.1186/1471-2202-10-122

Lindvall, O. (2016). Clinical translation of stem cell transplantation in Parkinson's disease. *Journal of Internal Medicine*, *279*(1), 30–40. https://doi.org/10.1111/joim.12415

Lisman, J. E., Coyle, J. T., Green, R. W., Javitt, D. C., Benes, F. M., Heckers, S., & Grace, A. A. (2008). Circuit-based framework for understanding neurotransmitter and risk gene interactions in schizophrenia. *Trends in Neurosciences*, *31*(5), 234–242. https://doi.org/10.1016/j.tins.2008.02.005

Lisman, J., & Buzsáki, G. (2008). A neural coding scheme formed by the combined function of gamma and theta oscillations. *Schizophrenia Bulletin*, *34*(5), 974–980. https://doi.org/10.1093/schbul/sbn060

Liu, X., Demosthenous, A., & Donaldson, N. (2007). On the noise performance of pt electrodes. *Conference Proceedings : ... Annual International Conference of the IEEE Engineering in Medicine and Biology Society. IEEE Engineering in Medicine and Biology Society. Annual Conference*, *2007*, 434–436. https://doi.org/10.1109/IEMBS.2007.4352316

Lütcke, H., Gerhard, F., Zenke, F., Gerstner, W., & Helmchen, F. (2013). Inference of neuronal network spike dynamics and topology from calcium imaging data. *Frontiers in Neural Circuits*, *7*(December), 1–20. https://doi.org/10.3389/fncir.2013.00201

Lütcke, H., Margolis, D. J., & Helmchen, F. (2013). Steady or changing? Long-term monitoring of neuronal population activity. *Trends in Neurosciences*, *36*(7), 375–384. https://doi.org/10.1016/j.tins.2013.03.008

Maccione, A., Gandolfo, M., Massobrio, P., Novellino, A., Martinoia, S., & Chiappalone, M. (2009). A novel algorithm for precise identification of spikes in extracellularly recorded neuronal signals. *Journal of Neuroscience Methods*, *177*(1), 241–249. https://doi.org/10.1016/j.jneumeth.2008.09.026

Maeda, E., Robinson, H. P., & Kawana, A. (1995). The mechanisms of generation and propagation of synchronized bursting in developing networks of cortical neurons. *The Journal of Neuroscience : The Official Journal of the Society for Neuroscience*, *15*(10), 6834–6845. Retrieved from http://www.ncbi.nlm.nih.gov/pubmed/7472441

Mahmud, M., Bertoldo, A., Girardi, S., Maschietto, M., & Vassanelli, S. (2012). SigMate: A Matlab-based automated tool for extracellular neuronal signal processing and analysis. *Journal of Neuroscience Methods*, *207*(1), 97–112. https://doi.org/10.1016/j.jneumeth.2012.03.009

Malchenko, S., Xie, J., de Fatima Bonaldo, M., Vanin, E. F., Bhattacharyya, B. J., Belmadani, A., … Soares, M. B. (2014). Onset of rosette formation during spontaneous neural differentiation of hESC and hiPSC colonies. *Gene*, *534*(2), 400–407. https://doi.org/10.1016/j.gene.2013.07.101

Mallat, S. G. (1989). A theory for multiresolution signal decomposition: the wavelet representation. *IEEE Transactions on Pattern Analysis and Machine Intelligence*, *11*(7), 674–693. https://doi.org/10.1109/34.192463

Mann, E. O., & Paulsen, O. (2007). Role of GABAergic inhibition in hippocampal network oscillations. *Trends in Neurosciences*, *30*(7), 343–349. https://doi.org/10.1016/j.tins.2007.05.003

Marchetto, M. C. N. M., Carromeu, C., Acab, A., Yu, D., Yeo, G. W., Mu, Y., … Muotri, A. R. (2010). A model for neural development and treatment of Rett syndrome using human induced pluripotent stem cells. *Cell*, *143*(4), 527–539. https://doi.org/10.1016/j.cell.2010.10.016.A

Maroof, A. M., Brown, K., Shi, S. H., Studer, L., & Anderson, S. A. (2010). Prospective Isolation of Cortical Interneuron Precursors from Mouse Embryonic Stem Cells. *Journal of Neuroscience*, *30*(13), 4667–4675. https://doi.org/10.1523/JNEUROSCI.4255-09.2010

Maroof, A. M., Keros, S., Tyson, J. a, Ying, S.-W., Ganat, Y. M., Merkle, F. T., … Studer, L. (2013). Directed differentiation and functional maturation of cortical interneurons from human embryonic stem cells. *Cell Stem Cell*, *12*(5), 559–572. https://doi.org/10.1016/j.stem.2013.04.008

Martin, G. R. (1981). Isolation of a pluripotent cell line from early mouse embryos cultured in medium conditioned by teratocarcinoma stem cells. *Proceedings of the National Academy of Sciences of the United States of America*, *78*(12), 7634–7638. https://doi.org/10.1073/pnas.78.12.7634

Martinez, J., Pedreira, C., Ison, M. J., & Quian Quiroga, R. (2009). Realistic simulation of extracellular recordings. *Journal of Neuroscience Methods*, *184*(2), 285–293. https://doi.org/10.1016/j.jneumeth.2009.08.017

Martinoia, S., Bonzano, L., Chiappalone, M., Tedesco, M., Marcoli, M., & Maura, G. (2005). In vitro cortical neuronal networks as a new high-sensitive system for biosensing applications. *Biosensors and Bioelectronics*, *20*(10 SPEC. ISS.), 2071–2078. https://doi.org/10.1016/j.bios.2004.09.012

Matsuda, N., Odawara, A., Katoh, H., Okuyama, N., Yokoi, R., & Suzuki, I. (2018). Detection of synchronized burst firing in cultured human induced pluripotent stem cell-derived neurons using a 4-step method. *Biochemical and Biophysical Research Communications*, *497*(2), 612–618. https://doi.org/10.1016/j.bbrc.2018.02.117

Mayer, M., Arrizabalaga, O., Lieb, F., Ciba, M., Ritter, S., & Thielemann, C. (2018). Electrophysiological investigation of human embryonic stem cell derived neurospheres using a novel spike detection algorithm. *Biosensors and Bioelectronics*, *100*(August 2017), 462–468. https://doi.org/10.1016/j.bios.2017.09.034

Mazzoni, A., Broccard, F. D., Garcia-Perez, E., Bonifazi, P., Ruaro, M. E., & Torre, V. (2007). On the dynamics of the spontaneous activity in neuronal networks. *PLoS ONE*, *2*(5). https://doi.org/10.1371/journal.pone.0000439

McCabe, A. K., Chisholm, S. L., Picken-Bahrey, H. L., & Moody, W. J. (2006). The self-regulating nature of spontaneous synchronized activity in developing mouse cortical neurones. *Journal of Physiology*, *577*(1), 155–167. https://doi.org/10.1113/jphysiol.2006.117523

McCormick, D. A., Connors, B. W., Lighthall, J. W., & Prince, D. A. (1985). Comparative electrophysiology of pyramidal and sparsely spiny stellate neurons of the neocortex. *Journal of Neurophysiology*, *54*(4), 782–806. https://doi.org/10.1152/jn.1985.54.4.782

McManus, M. F., Nasrallah, I. M., Gopal, P. P., Baek, W. S., & Golden, J. A. (2004). Axon mediated interneuron migration. *Journal of Neuropathology and Experimental Neurology*, *63*(9), 932–941. https://doi.org/10.1093/jnen/63.9.932

Minerbi, A., Kahana, R., Goldfeld, L., Kaufman, M., Marom, S., & Ziv, N. E. (2009). Long-term relationships between synaptic tenacity, synaptic remodeling, and network activity. *PLoS Biology*, *7*(6). https://doi.org/10.1371/journal.pbio.1000136

Moody, W. J., & Bosma, M. M. (2005). Ion channel development, spontaneous activity, and activity-dependent development in nerve and muscle cells. *Physiological Reviews*, *85*(0031–9333 (Print)), 883–941. https://doi.org/10.1152/physrev.00017.2004.

Morales, R., Riss, M., Wang, L., Gavín, R., Del Río, J. A., Alcubilla, R., & Claverol-Tinturé, E. (2008). Integrating multi-unit electrophysiology and plastic culture dishes for network neuroscience. *Lab on a Chip*, *8*(11), 1896–1905. https://doi.org/10.1039/b802165a

Muguruma, K., & Sasai, Y. (2012). In vitro recapitulation of neural development using embryonic stem cells: From neurogenesis to histogenesis. *Development Growth and Differentiation*, *54*(3), 349–357. https://doi.org/10.1111/j.1440-169X.2012.01329.x

Mukamel, E., Nimmerjahn, A., & Schnitzer, M. (2009). Automated analysis of cellular signals from large-scale calcium imaging data. *Neuron*, *63*(6), 747–760. https://doi.org/10.1016/j.neuron.2009.08.009.Automated

Mukhtarov, M., Ivanov, A., Zilberter, Y., & Bregestovski, P. (2011). Inhibition of spontaneous network activity in neonatal hippocampal slices by energy substrates is not correlated with intracellular acidification. *Journal of Neurochemistry*, *116*(2), 316–321. https://doi.org/10.1111/j.1471-4159.2010.07111.x

Mungenast, A. E., Siegert, S., & Tsai, L. H. (2016). Modeling Alzheimer's disease with human induced pluripotent stem (iPS) cells. *Molecular and Cellular Neuroscience*, *73*, 13–31. https://doi.org/10.1016/j.mcn.2015.11.010

Muñoz-Sanjuán, I., & Brivanlou, A. H. (2002). Neural induction, the default model and embryonic stem cells. *Nature Reviews. Neuroscience*, *3*(4), 271–280. https://doi.org/10.1038/nrn786

Murphy, R. C., & Messer, A. (2001). Gene transfer methods for CNS organotypic cultures: A comparison of three nonviral methods. *Molecular Therapy*, *3*(1), 113–121. https://doi.org/10.1006/mthe.2000.0235

Murphy, T. H., Blatter, L. a, Wier, W. G., & Baraban, J. M. (1992). Spontaneous synchronous synaptic calcium transients in cultured cortical neurons. *The Journal of Neuroscience : The Official Journal of the Society for Neuroscience*, *12*(12), 4834–4845. https://doi.org/1361198

Nageshappa, S., Carromeu, C., Trujillo, C. A., Mesci, P., Pasciuto, E., Vanderhaeghen, P., … Lupski, J. R. (2016). Altered neuronal network and rescue in a human MECP2 duplication model. *Molecular Psychiatry*, *21*(2), 178–188. https://doi.org/10.1038/mp.2015.128.Altered

Narula, U., Ruiz, A., McQuaide, M., DeMarse, T. B., Wheeler, B. C., & Brewer, G. J. (2017). Narrow microtunnel technology for the isolation and precise identification of axonal communication among distinct hippocampal subregion networks. *PLoS ONE*, *12*(5), 1–15. https://doi.org/10.1371/journal.pone.0176868

Nekrasov, E. D., Vigont, V. A., Klyushnikov, S. A., Lebedeva, O. S., Vassina, E. M., Bogomazova, A. N., … Kiselev, S. L. (2016). Manifestation of Huntington's disease pathology in human induced pluripotent stem cell-derived neurons. *Molecular Neurodegeneration*, *11*(1), 1–15. https://doi.org/10.1186/s13024-016-0092-5

Nelson, M. J., Pouget, P., Nilsen, E. A., Patten, C. D., & Schall, J. D. (2008). Review of signal distortion through metal microelectrode recording circuits and filters. *Journal of Neuroscience Methods*, *169*(1), 141–157. https://doi.org/10.1016/j.jneumeth.2007.12.010

Ng, C., Sandoval, K., Rowitch, D. H., Xu, D., Patrick, S., Huang, E. J., & Alvarez-buylla, A. (2016). Extensive migration of young neurons into the infant human frontal lobe. *Science*, *354*(6308), 1–14. https://doi.org/10.1126/science.aaf7073.Extensive

Nicholas, C. R., Chen, J., Tang, Y., Southwell, D. G., Chalmers, N., Vogt, D., … Kriegstein, A. R. (2013). Functional maturation of hPSC-derived forebrain interneurons requires an extended timeline and mimics human neural development. *Cell Stem Cell*, *12*(5), 573–586. https://doi.org/10.1016/j.stem.2013.04.005

Nicolelis, M. A. L., & Lebedev, M. A. (2009). Principles of neural ensemble physiology underlying the operation of brain-machine interfaces. *Nature Reviews Neuroscience*, *10*(7), 530–540. https://doi.org/10.1038/nrn2653

Nimmrich, V., Maier, N., Schmitz, D., & Draguhn, A. (2005). Induced sharp wave-ripple complexes in the absence of synaptic inhibition in mouse hippocampal slices. *Journal of Physiology*, *563*(3), 663–670. https://doi.org/10.1113/jphysiol.2004.079558

Obien, M. E. J., Deligkaris, K., Bullmann, T., Bakkum, D. J., & Frey, U. (2014). Revealing neuronal function through microelectrode array recordings. *Frontiers in Neuroscience*, *8*(JAN), 423. https://doi.org/10.3389/fnins.2014.00423

Odawara, A., Katoh, H., Matsuda, N., & Suzuki, I. (2016). Induction of long-term potentiation and depression phenomena in human induced pluripotent stem cell-derived cortical neurons. *Biochemical and Biophysical Research Communications*, *469*(4), 856–862. https://doi.org/10.1016/j.bbrc.2015.12.087

Odawara, A., Katoh, H., Matsuda, N., & Suzuki, I. (2016). Physiological maturation and drug responses of human induced pluripotent stem cell-derived cortical neuronal networks in long-term culture. *Scientific Reports*, *6*(February), 1–14. https://doi.org/10.1038/srep26181

Odawara, A., Saitoh, Y., Alhebshi, A. H., Gotoh, M., & Suzuki, I. (2014). Long-term electrophysiological activity and pharmacological response of a human induced pluripotent stem cell-derived neuron and astrocyte co-culture. *Biochemical and Biophysical Research Communications*, *443*(4), 1176–1181. https://doi.org/10.1016/j.bbrc.2013.12.142

O'Donovan, M. J., Wenner, P., Chub, N., Tabak, J., & Rinzel, J. (1998). Mechanisms of spontaneous activity in the developing spinal cord and their relevance to locomotion. *Annals of the New York Academy of Sciences*, *860*, 130–141. Retrieved from http://onlinelibrary.wiley.com/doi/10.1111/j.1749-6632.1998.tb09044.x/full

O'Donovan, M. J. (1999). The origin of spontaneous activity in developing networks of the vertebrate nervous system. *Current Opinion in Neurobiology*, *9*(1), 94–104. Retrieved from

https://api.istex.fr/document/04F89DA323FBCAB26E3F2D64587213820F0DB6E0/fulltext/pdf?auth=ip,fede&sid=ebsco

Ohki, K., Chung, S., Ch, Y. H., Kara, P., & Reid, R. C. (2005). Functional imaging with cellular resolution reveals precise micro- architecture in visual cortex. *Nature*, *433*(7026), 597–603. https://doi.org/10.1055/s-2004-818954

Oki, K., Tatarishvili, J., Wood, J., Koch, P., Wattananit, S., Mine, Y., … Kokaia, Z. (2012). Human-induced pluripotent stem cells form functional neurons and improve recovery after grafting in stroke-damaged brain. *Stem Cells*, *30*(6), 1120–1133. https://doi.org/10.1002/stem.1104

Owens, D. F., & Kriegstein, a R. (1998). Patterns of intracellular calcium fluctuation in precursor cells of the neocortical ventricular zone. *The Journal of Neuroscience : The Official Journal of the Society for Neuroscience*, *18*(14), 5374–5388. Retrieved from http://www.ncbi.nlm.nih.gov/pubmed/9651220

Ozden, I., Lee, H. M., Sullivan, M. R., & Wang, S. S.-H. (2008). Identification and Clustering of Event Patterns From In Vivo Multiphoton Optical Recordings of Neuronal Ensembles. *Journal of Neurophysiology*, *100*(1), 495–503. https://doi.org/10.1152/jn.01310.2007

Paavilainen, T., Pelkonen, A., Mäkinen, M. E.-L., Peltola, M., Huhtala, H., Fayuk, D., & Narkilahti, S. (2018). Effect of prolonged differentiation on functional maturation of human pluripotent stem cell-derived neuronal cultures. *Stem Cell Research*, *27*. https://doi.org/10.1016/j.scr.2018.01.018

Paredes, R. M., Etzler, J. C., Watts, L. T., & Lechleiter, J. D. (2008). Chemical Calcium Indicators. *Methods*, *46*(3), 143–151. https://doi.org/10.1016/j.ymeth.2008.09.025.Chemical

Paşca, A. M., Sloan, S. A., Clarke, L. E., Tian, Y., Makinson, C. D., Huber, N., … Paşca, S. P. (2015). Functional cortical neurons and astrocytes from human pluripotent stem cells in 3D culture. *Nature Methods*, *12*(7), 671–678. https://doi.org/10.1038/nmeth.3415

Paşca, S. P., Portmann, T., Voineagu, I., Yazawa, M., Shcheglovitov, A., Paşca, A. M., … Dolmetsch, R. E. (2011). Using iPSC-derived neurons to uncover cellular phenotypes associated with Timothy syndrome. *Nature Medicine*, *17*(12), 1657–1662. https://doi.org/10.1038/nm.2576

Pasquale, V., Martinoia, S., & Chiappalone, M. (2010). A self-adapting approach for the detection of bursts and network bursts in neuronal cultures. *Journal of Computational Neuroscience*, *29*(1–2), 213–229. https://doi.org/10.1007/s10827-009-0175-1

Patel, T. P., Man, K., Firestein, B. L., & Meaney, D. F. (2015). Automated quantification of neuronal networks and single-cell calcium dynamics using calcium imaging. *Journal of Neuroscience Methods*, *243*, 26–38. https://doi.org/10.1016/j.jneumeth.2015.01.020

Pedreira, C., Martinez, J., Ison, M. J., & Quian Quiroga, R. (2012). How many neurons can we see with current spike sorting algorithms? *Journal of Neuroscience Methods*, *211*(1), 58–65. https://doi.org/10.1016/j.jneumeth.2012.07.010

Perea, G., & Araque, A. (2010). GLIA modulates synaptic transmission. *Brain Research Reviews*, *63*(1–2), 93–102. https://doi.org/10.1016/j.brainresrev.2009.10.005

Peron, S., Chen, T.-W., & Svoboda, K. (2015). Comprehensive imaging of cortical networks. *Current Opinion in Neurobiology*, *32*, 115–123. https://doi.org/10.1016/j.conb.2015.03.016

Pfrieger, F. W., & Barres, B. A. (1997). Synaptic efficacy enhanced by glial cells in vitro. *Science*, *277*(5332), 1684–1687. https://doi.org/10.1126/science.277.5332.1684

Pickering, M., Pickering, B. W., Murphy, K. J., & O'Connor, J. J. (2008). Discrimination of cell types in mixed cortical culture using calcium imaging: A comparison to immunocytochemical labeling. *Journal of Neuroscience Methods*, *173*(1), 27–33. https://doi.org/10.1016/j.jneumeth.2008.05.014

Pimashkin, A., Kastalskiy, I., Simonov, A., Koryagina, E., Mukhina, I., & Kazantsev, V. (2011). Spiking Signatures of Spontaneous Activity Bursts in Hippocampal Cultures. *Frontiers in Computational Neuroscience*, *5*(November), 1–12. https://doi.org/10.3389/fncom.2011.00046

Pnevmatikakis, E. A., Soudry, D., Gao, Y., Machado, T. A., Merel, J., Pfau, D., … Paninski, L. (2016). Simultaneous Denoising, Deconvolution, and Demixing of Calcium Imaging Data. *Neuron*, *89*(2), 285–299. https://doi.org/10.1016/j.neuron.2015.11.037

Quilichini, P. P., Le Van Quyen, M., Ivanov, A., Turner, D. A., Carabalona, A., Gozlan, H., … Bernard, C. (2012). Hub GABA Neurons Mediate Gamma-Frequency Oscillations at Ictal-like Event Onset in the Immature Hippocampus. *Neuron*, *74*(1), 57–64. https://doi.org/10.1016/j.neuron.2012.01.026

Quirk, M. C., & Wilson, M. A. (1999). Interaction between spike waveform classification and temporal sequence detection. *Journal of Neuroscience Methods*, *94*(1), 41–52. https://doi.org/10.1016/S0165-0270(99)00124-7

Quiroga, R. Q., Nadasdy, Z., & Ben-Shaul, Y. (2004). Unsupervised Spike Detection and Sorting with Wavelets and Superparamagnetic Clustering. *Neural Computation*, *16*(8), 1661–1687. https://doi.org/10.1162/089976604774201631

Quiroga, R. Q., Reddy, L., Koch, C., & Fried, I. (2007). Decoding Visual Inputs From Multiple Neurons in the Human Temporal Lobe. *Journal of Neurophysiology*, *98*(4), 1997–2007. https://doi.org/10.1152/jn.00125.2007

Rakhade, S. N., & Jensen, F. E. (2009). Epileptogenesis in the immature brain: Emerging mechanisms. *Nature Reviews Neurology*, *5*(7), 380–391. https://doi.org/10.1038/nrneurol.2009.80

Rakic, P. (1995). Radial versus tangential migration of neuronal clones in the developing cerebral cortex. *Proceedings of the National Academy of Sciences of the United States of America*, *92*(25), 11323–11327. https://doi.org/10.1073/pnas.92.25.11323

Rakic, P. (1995). A small step for the cell, a giant leap for mankind: a hypothesis of neocortical expansion during evolution. *Trends in Neurosciences*, *18*(9), 383–388. https://doi.org/10.1016/0166-2236(95)93934-P

Rakic, P., & Caviness, V. S. (1995). Cortical development: view from neurological mutants two decades later. *Neuron*, *14*(6), 1101–1104. https://doi.org/10.1016/0896-6273(95)90258-9

Rash, B. G., & Grove, E. A. (2006). Area and layer patterning in the developing cerebral cortex. *Current Opinion in Neurobiology*, *16*(1), 25–34. https://doi.org/10.1016/j.conb.2006.01.004

Rey, H. G., Pedreira, C., & Quian Quiroga, R. (2015). Past, present and future of spike sorting techniques. *Brain Research Bulletin*, *119*, 106–117. https://doi.org/10.1016/j.brainresbull.2015.04.007

Reynolds, S., Abrahamsson, T., Schuck, R., Sjöström, P. J., Schultz, S. R., & Dragotti, P. L. (2017). ABLE: An Activity-Based Level Set Segmentation Algorithm for Two-Photon Calcium Imaging Data. *Eneuro*, *4*(5), ENEURO.0012-17.2017. https://doi.org/10.1523/ENEURO.0012-17.2017

Rheims, S., Minlebaev, M., Ivanov, A., Represa, A., Khazipov, R., Holmes, G. L., … Zilberter, Y. (2008). Excitatory GABA in Rodent Developing Neocortex In Vitro. *Journal of Neurophysiology*, *100*(2), 609–619. https://doi.org/10.1152/jn.90402.2008

Rhinn, M., Picker, A., & Brand, M. (2006). Global and local mechanisms of forebrain and midbrain patterning. *Current Opinion in Neurobiology*, *16*(1), 5–12. https://doi.org/10.1016/j.conb.2006.01.005

Rice, M. E., Okada, Y. C., & Nicholson, C. (1993). Anisotropic and heterogeneous diffusion in the turtle cerebellum: implications for volume transmission. *Journal of Neurophysiology*, *70*(5), 2035–2044. https://doi.org/10.1152/jn.1993.70.5.2035

Ridoux, V., Robert, J. J., Perricaudet, M., Mallet, J., & Le Gal La Salle, G. (1995). Adenovirus mediated gene transfer in organotypic brain slices. *Neurobiology of Disease*, *2*(1), 49–54. https://doi.org/10.1006/nbdi.1995.0005

Rivera, C., Voipio, J., Payne, J. A., Ruusuvuori, E., Lahtinen, H., Lamsa, K., … Kaila, K. (1999). The K+/Cl− co-transporter KCC2 renders GABA hyperpolarizing during neuronal maturation. *Nature*, *397*(6716), 251–255. https://doi.org/10.1038/16697

Robinson, H. P., Kawahara, M., Jimbo, Y., Torimitsu, K., Kuroda, Y., & Kawana, A. (1993). Periodic synchronized bursting and intracellular calcium transients elicited by low magnesium in cultured cortical neurons. *Journal of Neurophysiology*, *70*(4), 1606–1616. https://doi.org/10.1152/jn.1993.70.4.1606

Rose, T., Goltstein, P. M., Portugues, R., & Griesbeck, O. (2014). Putting a finishing touch on GECIs. *Frontiers in Molecular Neuroscience*, *7*(November), 1–15. https://doi.org/10.3389/fnmol.2014.00088

Roy, D., Steyer, G. J., Gargesha, M., Stone, M. E., & Wilson, D. L. (2009). 3D cryo-imaging: a very high-resolution view of the whole mouse. *Anatomical Record*, *292*(3), 342–351. https://doi.org/10.1002/ar.20849

Roy, D., Steyer, G. J., Gargesha, M., Stone, M. E., & Wilson, D. L. (2009). 3D Cryo-Imaging: A Very High-Resolution View of the Whole Mouse. *The Anatomical Record: Advances in Integrative Anatomy and Evolutionary Biology*, *292*(3), 342–351. https://doi.org/10.1002/ar.20849

Rozental, R., Srinivas, M., Gökhan, S., Urban, M., Dermietzel, R., Kessler, J. A., … Mehler, M. F. (2000). Temporal expression of neuronal connexins during hippocampal ontogeny. *Brain Research Reviews*, *32*(1), 57–71. https://doi.org/10.1016/S0165-0173(99)00096-X

Rubio, A., Luoni, M., Giannelli, S. G., Radice, I., Iannielli, A., Cancellieri, C., … Broccoli, V. (2016). Rapid and efficient CRISPR/Cas9 gene inactivation in human neurons during human pluripotent stem cell differentiation and direct reprogramming. *Scientific Reports*, *6*(October), 1–16. https://doi.org/10.1038/srep37540

Rushton, D. J., Mattis, V. B., Svendsen, C. N., Allen, N. D., & Kemp, P. J. (2013). Stimulation of GABA-induced Ca2+ influx enhances maturation of human induced pluripotent stem cell-derived neurons. *PLoS ONE*, *8*(11), 1–16. https://doi.org/10.1371/journal.pone.0081031

Saito, A., Takayama, Y., Moriguchi, H., Kotani, K., & Jimbo, Y. (2009). Developmental effects of low frequency magnetic fields on P19-derived neuronal cells. *Conference Proceedings : Annual International Conference of the IEEE Engineering in Medicine and Biology Society IEEE Engineering in Medicine and Biology Society Conference*, *2009*, 5942–5945. https://doi.org/10.1109/IEMBS.2009.5334755

Sandoe, J., & Eggan, K. (2013). Opportunities and challenges of pluripotent stem cell neurodegenerative disease models. *Nature Neuroscience*, *16*(7), 780–789. https://doi.org/10.1038/nn.3425

Satuvuori, E., Mulansky, M., Bozanic, N., Malvestio, I., Zeldenrust, F., Lenk, K., & Kreuz, T. (2017). Measures of spike train synchrony for data with multiple time scales. *Journal of Neuroscience Methods*, *287*, 25–38. https://doi.org/10.1016/j.jneumeth.2017.05.028

Sava, B. A., Chen, R., Sun, H., Luhmann, H. J., & Kilb, W. (2014). Taurine activates GABAergic networks in the neocortex of immature mice. *Frontiers in Cellular Neuroscience*, *8*(February), 1–13. https://doi.org/10.3389/fncel.2014.00026

Scelfo, B., Politi, M., Reniero, F., Palosaari, T., Whelan, M., & Zaldívar, J.-M. (2012). Application of multielectrode array (MEA) chips for the evaluation of mixtures neurotoxicity. *Toxicology*, *299*(2–3), 172–183. https://doi.org/10.1016/j.tox.2012.05.020

Schuchmann, S., Schmitz, D., Rivera, C., Vanhatalo, S., Salmen, B., Mackie, K., … Kaila, K. (2006). Experimental febrile seizures are precipitated by a hyperthermia-induced respiratory alkalosis. *Nature Medicine*, *12*(7), 817–823. https://doi.org/10.1038/nm1422

Schwartz, T. H., Rabinowitz, D., Unni, V., Kumar, V. S., Smetters, D. K., Tsiola, A., & Yuste, R. (1998). Networks of coactive neurons in developing layer 1. *Neuron*, *20*(3), 541–552. https://doi.org/10.1016/S0896-6273(00)80993-9

Seidel, D., Jahnke, H. G., Englich, B., Girard, M., & Robitzki, A. A. (2017). In vitro field potential monitoring on a multi-microelectrode array for the electrophysiological long-term screening of neural stem cell maturation. *Analyst*, *142*(11), 1929–1937. https://doi.org/10.1039/c6an02713j

Selinger, J. V., Kulagina, N. V., O'Shaughnessy, T. J., Ma, W., & Pancrazio, J. J. (2007). Methods for characterizing interspike intervals and identifying bursts in neuronal activity. *Journal of Neuroscience Methods*, *162*(1–2), 64–71. https://doi.org/10.1016/j.jneumeth.2006.12.003

Shein-Idelson, M., Ben-Jacob, E., & Hanein, Y. (2011). Engineered neuronal circuits: a new platform for studying the role of modular topology. *Frontiers in Neuroengineering*, *4*(September), 10. https://doi.org/10.3389/fneng.2011.00010

Shen, Q., Wang, Y., Dimos, J. T., Fasano, C. A., Phoenix, T. N., Lemischka, I. R., … Temple, S. (2006). The timing of cortical neurogenesis is encoded within lineages of individual progenitor cells. *Nature Neuroscience*, *9*(6), 743–751. https://doi.org/10.1038/nn1694

Sheroziya, M. G., von Bohlen und Halbach, O., Unsicker, K., & Egorov, A. V. (2009). Spontaneous Bursting Activity in the Developing Entorhinal Cortex. *Journal of Neuroscience*, *29*(39), 12131–12144. https://doi.org/10.1523/JNEUROSCI.1333-09.2009

Shew, W. L., Bellay, T., & Plenz, D. (2010). Simultaneous multi-electrode array recording and two-photon calcium imaging of neural activity. *Journal of Neuroscience Methods*, *192*(1), 75–82. https://doi.org/10.1016/j.jneumeth.2010.07.023

Shi, Y., Kirwan, P., & Livesey, F. J. (2012). Directed differentiation of human pluripotent stem cells to cerebral cortex neurons and neural networks. *Nature Protocols*, *7*(10), 1836–1846. https://doi.org/10.1038/nprot.2012.116

Shi, Y., Kirwan, P., Smith, J., Maclean, G., Orkin, S. H., & Livesey, F. J. (2014). A human stem cell model of early Alzheimer's disease pathology in Down syndrome. *Science*

Translational Medicine, *4*(124), 2–23. https://doi.org/10.1126/scitranslmed.3003771.A

Shi, Y., Kirwan, P., Smith, J., Robinson, H. P. C., & Livesey, F. J. (2012). Human cerebral cortex development from pluripotent stem cells to functional excitatory synapses. *Nature Neuroscience*, *15*(3), 477–486, S1. https://doi.org/10.1038/nn.3041

Singer, M., Deutschman, C. S., Seymour, C. W., Shankar-Hari, M., Annane, D., Bauer, M., … Angus, D. C. (2016). The Third International Consensus Definitions for Sepsis and Septic Shock (Sepsis-3). *JAMA*, *315*(8), 801–810. https://doi.org/10.1001/jama.2016.0287

Smetters, D., Majewska, A., & Yuste, R. (1999). Detecting action potential in neuronal populations with calcium imaging. *Methods*, *18*, 215–221.

Smith, S. L., & Häusser, M. (2011). Parallel processing of visual space by neighboring neurons in mouse visual cortex. *Nature Neuroscience*, *13*(9), 1144–1149. https://doi.org/10.1038/nn.2620.Parallel

Somogyvári, Z., Cserpán, D., Ulbert, I., & Érdi, P. (2012). Localization of single-cell current sources based on extracellular potential patterns: The spike CSD method. *European Journal of Neuroscience*, *36*(10), 3299–3313. https://doi.org/10.1111/j.1460-9568.2012.08249.x

Somogyvári, Z., Zalányi, L., Ulbert, I., & Érdi, P. (2005). Model-based source localization of extracellular action potentials. *Journal of Neuroscience Methods*, *147*(2), 126–137. https://doi.org/10.1016/j.jneumeth.2005.04.002

Spray, D. C., Scemes, E., & Dermietzel, R. (2014). Gap Junctions in the Nervous System. *Encyclopedia of the Neurological Sciences*, 402–408. https://doi.org/10.1016/B978-0-12-385157-4.00058-0

Spruston, N., Schiller, Y., Stuart, G., & Sakmann, B. (1995). Activity-dependent action potential invasion and calcium influx into hippocampal CA1 dendrites. *Science*, *268*(5208), 297–300. https://doi.org/10.1126/science.7716524

Stern, C. D. (2006). Neural induction: 10 years on since the "default model". *Current Opinion in Cell Biology*, *18*(6), 692–697. https://doi.org/10.1016/j.ceb.2006.09.002

Stern, C. D. (2001). Initial patterning of the central nervous system: how many organizers? *Nature Reviews. Neuroscience*, *2*(2), 92–98. https://doi.org/10.1038/35053563

Stetter, O., Battaglia, D., Soriano, J., & Geisel, T. (2012). Model-Free Reconstruction of Excitatory Neuronal Connectivity from Calcium Imaging Signals. *PLoS Computational Biology*, *8*(8). https://doi.org/10.1371/journal.pcbi.1002653

Stoppini, L., Duport, S., & Corrèges, P. (1997). A new extracellular multirecording system for electrophysiological studies: Application to hippocampal organotypic cultures. *Journal of Neuroscience Methods*, *72*(1), 23–33. https://doi.org/10.1016/S0165-0270(96)00151-3

Stosiek, C., Garaschuk, O., Holthoff, K., & Konnerth, A. (2003). In vivo two-photon calcium imaging of neuronal networks. *Proceedings of the National Academy of Sciences*, *100*(12), 7319–7324. https://doi.org/10.1073/pnas.1232232100

Stratton, P., Cheung, A., Wiles, J., Kiyatkin, E., Sah, P., & Windels, F. (2012). Action potential waveform variability limits multi-unit separation in freely behaving rats. *PLoS ONE*, *7*(6). https://doi.org/10.1371/journal.pone.0038482

Sun, J.-J., & Luhmann, H. J. (2007). Spatio-temporal dynamics of oscillatory network activity in the neonatal mouse cerebral cortex. *European Journal of Neuroscience*, *26*(7), 1995–2004. https://doi.org/10.1111/j.1460-9568.2007.05819.x

Supèr, H., Soriano, E., & Uylings, H. B. (1998). The functions of the preplate in development and evolution of the neocortex and hippocampus. *Brain Research Reviews*, *27*(1), 40–64. https://doi.org/10.1016/S0165-0173(98)00005-8

Sutor, B., & Hagerty, T. (2005). Involvement of gap junctions in the development of the neocortex. *Biochimica et Biophysica Acta*, *1719*(1–2), 59–68. https://doi.org/10.1016/j.bbamem.2005.09.005

Tabar, V., & Studer, L. (2014). Pluripotent stem cells in regenerative medicine: challenges and recent progress. *Nature Reviews Genetics*, *15*(2), 82–92. https://doi.org/10.1038/nrg3563

Takahashi, K., & Yamanaka, S. (2006). Induction of Pluripotent Stem Cells from Mouse Embryonic and Adult Fibroblast Cultures by Defined Factors. *Cell*, *126*(4), 663–676. https://doi.org/10.1016/j.cell.2006.07.024

Takayama, Y., & Kida, Y. S. (2016). In vitro reconstruction of neuronal networks derived from human iPS cells using microfabricated devices. *PLoS ONE*, *11*(2), 1–15. https://doi.org/10.1371/journal.pone.0148559

Tateno, T., Jimbo, Y., & Robinson, H. P. C. (2005). Spatio-temporal cholinergic modulation in cultured networks of rat cortical neurons: Spontaneous activity. *Neuroscience*, *134*(2), 425–437. https://doi.org/10.1016/j.neuroscience.2005.04.049

Taylor, A. M., Blurton-Jones, M., Rhee, S. W., Cribbs, D. H., Cotman, C. W., & Jeon, N. L. (2005). A microfluidic culture platform for CNS axonal injury, regeneration and transport. *Nature Methods*, *2*(8), 599–605. https://doi.org/10.1038/nmeth777

Teixeira, A. I., Ilkhanizadeh, S., Wigenius, J. A., Duckworth, J. K., Inganäs, O., & Hermanson, O. (2009). The promotion of neuronal maturation on soft substrates. *Biomaterials*, *30*(27), 4567–4572. https://doi.org/10.1016/j.biomaterials.2009.05.013

Telezhkin, V., Schnell, C., Yarova, P., Yung, S., Cope, E., Hughes, A., … Kemp, P. J. (2016). Forced cell cycle exit and modulation of GABAA, CREB, and GSK3β signaling promote functional maturation of induced pluripotent stem cell-derived neurons. *American Journal of Physiology*, *310*(7), C520-41. https://doi.org/10.1152/ajpcell.00166.2015

Theis, L., Berens, P., Froudarakis, E., Reimer, J., Román Rosón, M., Baden, T., … Bethge, M. (2016). Benchmarking Spike Rate Inference in Population Calcium Imaging. *Neuron*, *90*(3), 471–482. https://doi.org/10.1016/j.neuron.2016.04.014

Thomas, A., Kim, D. S., Fields, R. L., Chin, H., & Gainer, H. (1998). Quantitative analysis of gene expression in organotypic slice-explant cultures by particle-mediated gene transfer. *Journal of Neuroscience Methods*, *84*(1–2), 181–191. https://doi.org/10.1016/S0165-0270(98)00117-4

Tian, L., Hires, S. A., Mao, T., Huber, D., Chiappe, M. E., Chalasani, S. H., … Looger, L. L. (2009). Imaging neural activity in worms, flies and mice with improved GCaMP calcium indicators. *Nature Methods*, *6*(12), 875–881. https://doi.org/10.1038/nmeth.1398

Tibau, E., Valencia, M., & Soriano, J. (2013). Identification of neuronal network properties from the spectral analysis of calcium imaging signals in neuronal cultures. *Frontiers in Neural Circuits*, *7*(December), 1–16. https://doi.org/10.3389/fncir.2013.00199

Tomek, J., Novak, O., & Syka, J. (2013). Two-Photon Processor and SeNeCA: a freely available software package to process data from two-photon calcium imaging at speeds down to several milliseconds per frame. *Journal of Neurophysiology*, *110*(1), 243–256. https://doi.org/10.1152/jn.00087.2013

Torborg, C. L., & Feller, M. B. (2005). Spontaneous patterned retinal activity and the refinement of retinal projections. *Progress in Neurobiology*, *76*(4), 213–235. https://doi.org/10.1016/j.pneurobio.2005.09.002

Traub, R. D., Draguhn, A., Whittington, M. A., Baldeweg, T., Bibbig, A., Buhl, E. H., & Schmitz, D. (2002). Axonal gap junctions between principal neurons: A novel source of network oscillations, and perhaps epileptogenesis. *Reviews in the Neurosciences*, *13*(1), 1–30. https://doi.org/10.1515/REVNEURO.2002.13.1.1

Tukker, A. M., De Groot, M. W. G. D. M., Wijnolts, F. M. J., Kasteel, E. E. J., Hondebrink, L., & Westerink, R. H. S. (2016). Is the time right for in vitro neurotoxicity testing using human iPSC-derived neurons? *Altex*, *33*(3), 261–271. https://doi.org/10.14573/altex.1510091

Tyzio, R., Holmes, G. L., Ben-Ari, Y., & Khazipov, R. (2007). Timing of the developmental switch in GABAA mediated signaling from excitation to inhibition in CA3 rat hippocampus using gramicidin perforated patch and extracellular recordings. *Epilepsia*, *48*(SUPPL. 5), 96–105. https://doi.org/10.1111/j.1528-1167.2007.01295.x

Uhlhaas, P. J., & Singer, W. (2011). The development of neural synchrony and large-scale cortical networks during adolescence: Relevance for the pathophysiology of schizophrenia and neurodevelopmental hypothesis. *Schizophrenia Bulletin*, *37*(3), 514–523. https://doi.org/10.1093/schbul/sbr034

Umaña-Taylor, A. J., Tynes, B. M., Toomey, R. B., Williams, D. R., & Mitchell, K. J. (2015). Latino adolescents' perceived discrimination in online and offline settings: An examination of cultural risk and protective factors. *Developmental Psychology*, *51*(1), 87–100. https://doi.org/10.1037/a0038432

Wagenaar, D. A., Pine, J., & Potter, S. M. (2006). An extremely rich repertoire of bursting patterns during the development of cortical cultures. *BMC Neuroscience*, *7*, 11. https://doi.org/10.1186/1471-2202-7-11

Wagenaar, D. A., Madhavan, R., Pine, J., & Potter, S. M. (2005). Controlling Bursting in Cortical Cultures with Closed-Loop Multi- Electrode Stimulation. *Journal of Neuroscience*, *25*(3), 680–688. https://doi.org/10.1523/JNEUROSCI.4209-04.2005.Controlling

Van Pelt, J., Corner, M. A., Wolters, P. S., Rutten, W. L. C., & Ramakers, G. J. A. (2004). Longterm stability and developmental changes in spontaneous network burst firing patterns in dissociated rat cerebral cortex cell cultures on multielectrode arrays. *Neuroscience Letters*, *361*(1–3), 86–89. https://doi.org/10.1016/j.neulet.2003.12.062

Van Pelt, J., Wolters, P. S., Corner, M. A., Rutten, W. L. C., & Ramakers, G. J. A. (2004). Long-term characterization of firing dynamics of spontaneous bursts in cultured neural networks. *IEEE Transactions on Biomedical Engineering*, *51*(11), 2051–2062. https://doi.org/10.1109/TBME.2004.827936

Wang, L., Riss, M., Buitrago, J. O., & Claverol-Tinturé, E. (2012). Biophysics of microchannel-enabled neuron-electrode interfaces. *Journal of Neural Engineering*, *9*(2). https://doi.org/10.1088/1741-2560/9/2/026010

Vanhatalo, S., & Kaila, K. (2006). Development of neonatal EEG activity: From phenomenology to physiology. *Seminars in Fetal and Neonatal Medicine*, *11*(6), 471–478. https://doi.org/10.1016/j.siny.2006.07.008

Vargová, L., & Syková, E. (2014). Astrocytes and extracellular matrix in extrasynaptic volume transmission. *Philosophical Transactions of the Royal Society of London. Series B, Biological Sciences*, *369*(1654), 20130608. https://doi.org/10.1098/rstb.2013.0608

Watanabe, K., Kamiya, D., Nishiyama, A., Katayama, T., Nozaki, S., Kawasaki, H., … Sasai, Y. (2005). Directed differentiation of telencephalic precursors from embryonic stem cells. *Nature Neuroscience*, *8*(3), 288–296. https://doi.org/10.1038/nn1402

Wataya, T., Ando, S., Muguruma, K., Ikeda, H., Watanabe, K., Eiraku, M., … Sasai, Y. (2008). Minimization of exogenous signals in ES cell culture induces rostral hypothalamic differentiation. *Proceedings of the National Academy of Sciences*, *105*(33), 11796–11801. https://doi.org/10.1073/pnas.0803078105

Webb, S. J., Monk, C. S., & Nelson, C. A. (2001). Developmental neuropsychology mechanisms of postnatal neurobiological development: implications for human development. *Developmental Neuropsychology*, *19*(2), 147–171. https://doi.org/10.1207/S15326942DN1902

Weder, N., Zhang, H., Jensen, K., Yang, B. Z., Simen, A., Jackowski, A., … Kaufman, J. (2014). Child abuse, depression, and methylation in genes involved with stress, neural plasticity, and brain circuitry. *Journal of the American Academy of Child and Adolescent Psychiatry*, *53*(4), 417–24.e5. https://doi.org/10.1016/j.jaac.2013.12.025

Weinstein, D. C., & Hemmati-Brivanlou, A. (1999). Neural Induction. *Annual Review of Cell and Developmental Biology*, *15*(1), 411–433. https://doi.org/10.1146/annurev.cellbio.15.1.411

Weissman, T. A., Riquelme, P. A., Ivic, L., Flint, A. C., & Kriegstein, A. R. (2004). Calcium waves propagate through radial glial cells and modulate proliferation in the developing neocortex. *Neuron*, *43*(5), 647–661. https://doi.org/10.1016/j.neuron.2004.08.015

Wernig, M., Zhao, J.-P., Pruszak, J., Hedlund, E., Fu, D., Soldner, F., … Jaenisch, R. (2008). Neurons derived from reprogrammed fibroblasts functionally integrate into the fetal brain and improve symptoms of rats with Parkinson's disease. *Proceedings of the National Academy of Sciences*, *105*(15), 5856–5861. https://doi.org/10.1073/pnas.0801677105

Vessoni, A. T., Herai, R. H., Karpiak, J. V., Leal, A. M. S., Trujillo, C. A., Quinet, A., … Muotri, A. R. (2016). Cockayne syndrome-derived neurons display reduced synapse density and altered neural network synchrony. *Human Molecular Genetics*, *25*(7), 1271–1280. https://doi.org/10.1093/hmg/ddw008

Whittington, M. A., & Traub, R. D. (2003). Interneuron diversity series: inhibitory interneurons and network oscillations in vitro. *Trends in Neurosciences*, *26*(12), 676–682. https://doi.org/10.1016/j.tins.2003.09.016

Wieringa, P. A., Wiertz, R. W. F., De Weerd, E., & Rutten, W. L. C. (2010). Bifurcating microchannels as a scaffold to induce separation of regenerating neurites. *Journal of Neural Engineering*, *7*(1). https://doi.org/10.1088/1741-2560/7/1/016001

Vogelstein, J. T., Packer, A. M., Machado, T. A., Sippy, T., Babadi, B., Yuste, R., & Paninski, L. (2010). Fast Nonnegative Deconvolution for Spike Train Inference From Population Calcium Imaging. *Journal of Neurophysiology*, *104*(6), 3691–3704. https://doi.org/10.1152/jn.01073.2009

Wunderlich, S., Kircher, M., Vieth, B., Haase, A., Merkert, S., Beier, J., … Enard, W. (2014). Primate iPS cells as tools for evolutionary analyses. *Stem Cell Research*, *12*(3), 622–629. https://doi.org/10.1016/j.scr.2014.02.001

Xu, L., Lee, H., Jetta, D., & Oh, K. W. (2015). Vacuum-driven power-free microfluidics utilizing the gas solubility or permeability of polydimethylsiloxane (PDMS). *Lab on a Chip*, *15*(20), 3962–3979. https://doi.org/10.1039/C5LC00716J

Yaksi, E., & Friedrich, R. W. (2006). Reconstruction of firing rate changes across neuronal populations by temporally deconvolved Ca2+ imaging. *Nature Methods*, *3*(5), 377–383. https://doi.org/10.1038/nmeth874

Yamazaki, K., Fukushima, K., Sugawara, M., Tabata, Y., Imaizumi, Y., Ishihara, Y., … Okano, H. (2016). Functional Comparison of Neuronal Cells Differentiated from Human Induced Pluripotent Stem Cell-Derived Neural Stem Cells under Different Oxygen and Medium Conditions. *Journal of Biomolecular Screening*, *21*(10), 1054–1064. https://doi.org/10.1177/1087057116661291

Yang, B., Tadavarty, R., Xu, J. Y., & Sastry, B. R. (2010). Activity-mediated plasticity of GABA equilibrium potential in rat hippocampal CA1 neurons. *Experimental Neurology*, *221*(1), 157–165. https://doi.org/10.1016/j.expneurol.2009.10.017

Yang, J.-W., Reyes-Puerta, V., Kilb, W., & Luhmann, H. J. (2016). Spindle Bursts in Neonatal Rat Cerebral Cortex. *Neural Plasticity*, *2016*, 1–11. https://doi.org/10.1155/2016/3467832

Ylä-Outinen, L., Heikkilä, J., Skottman, H., Suuronen, R., Aänismaa, R., & Narkilahti, S. (2010). Human cell-based micro electrode array platform for studying neurotoxicity. *Frontiers in Neuroengineering*, *3*(September), 1–9. https://doi.org/10.3389/fneng.2010.00111

Yoshimura, Y., & Callaway, E. M. (2005). Fine-scale specificity of cortical networks depends on inhibitory cell type and connectivity. *Nature Neuroscience*, *8*(11), 1552–1559. https://doi.org/10.1038/nn1565

Yoshimura, Y., Dantzker, J. L. M., & Callaway, E. M. (2005). Excitatory cortical neurons from fine-scale functional networks. *Nature*, *5*(February), 2005–2005. https://doi.org/10.1038/nature03291.1.

Zariwala, H. A., Borghuis, B. G., Hoogland, T. M., Madisen, L., Tian, L., De Zeeuw, C. I., … Chen, T.-W. (2012). A Cre-Dependent GCaMP3 Reporter Mouse for Neuronal Imaging In Vivo. *Journal of Neuroscience*, *32*(9), 3131–3141. https://doi.org/10.1523/JNEUROSCI.4469-11.2012

Zhang, J., & Jiao, J. (2015). Molecular Biomarkers for Embryonic and Adult Neural Stem Cell and Neurogenesis. *BioMed Research International*, *2015*(727542), 727542. https://doi.org/10.1155/2015/727542

Zhang, L. I., & Poo, M. M. (2001). Electrical activity and development of neural circuits. *Nature Neuroscience*, *4 Suppl*, 1207–1214. https://doi.org/10.1038/nn753

9 ORIGINAL PUBLICATIONS

Journal of Neuroscience Methods 215 (2013) 88–96

Contents lists available at SciVerse ScienceDirect

Journal of Neuroscience Methods

journal homepage: www.elsevier.com/locate/jneumeth

Basic Neuroscience

Fluorescent probes as a tool for cell population tracking in spontaneously active neural networks derived from human pluripotent stem cells

M. Mäkinen[a,1], T. Joki[a,1], L. Ylä-Outinen[a], H. Skottman[b], S. Narkilahti[a,c], R. Äänismaa[a,*]

[a] NeuroGroup, Institute of Biomedical Technology/BioMediTech, Biokatu 12, FI-33014 University of Tampere, Finland
[b] OpthalmologyGroup, Institute of Biomedical Technology/BioMediTech, Biokatu 12, FI-33014 University of Tampere, Finland
[c] The Science Center of Pirkanmaa Hospital District, Tampere, Finland

HIGHLIGHTS

- Fluorescent labels CT and DiD can be utilized with human stem cell-derived neurons.
- Labels do not affect the cell viability and minimally affect the cell proliferation.
- Labeled cells can be successfully followed for at least 4 weeks.
- Labeled cell populations form spontaneously active neural networks.

ARTICLE INFO

Article history:
Received 27 November 2012
Received in revised form 25 February 2013
Accepted 27 February 2013

Keywords:
CellTracker
DiD
Co-culture
Fluorescent probe
Labeling
Human stem cell derived neural cells
Long term

ABSTRACT

Applications such as 3D cultures and tissue modelling require cell tracking with non-invasive methods. In this work, the suitability of two fluorescent probes, CellTracker, CT, and long chain carbocyanine dye, DiD, was investigated for long-term culturing of labeled human pluripotent stem cell-derived neural cells. We found that these dyes did not affect the cell viability. However, proliferation was decreased in DiD labeled cell population. With both dyes the labeling was stable up to 4 weeks. CT and DiD labeled cells could be co-cultured and, importantly, these mixed populations had their normal ability to form spontaneous electrical network activity. In conclusion, human neural cells can be successfully labeled with these two fluorescent probes without significantly affecting the cell characteristics. These labeled cells could be utilized further in *e.g.* building controlled neuronal networks for neurotoxicity screening platforms, combining cells with biomaterials for 3D studies, and graft development.

1. Introduction

For the development of *in vitro* cell and tissue models it is often desirable to distinguish different cell populations within co-cultures in real time. This can be performed on the basis of differences in the cell morphology. However, morphological differences can vary even within the same cell type and become difficult to observe in a three dimensional culture environment. Fluorescent probes are an alternative to morphology-based identification. These probes have been tested with animal-derived cell cultures (Honig and Hume, 1989) but only one study has earlier described the use of fluorescent probes in human-derived neural cell cultures (Rizvanov et al., 2010). Furthermore, the possible cytotoxic effects should be assessed separately for human or primate cells due to species differences in neurotoxicity (Boyce et al., 1984).

The objective of this research was to find suitable fluorescent probes for the long term labeling of human embryonic stem cell (hESC)-derived neural cell co-cultures. The suitability of two widely used dyes, CellTracker (CT, also known as chloromethylfluorescein diacetate, CMFDA) and long chain carbocyanine dye 1,1′-dioctadecyl-3,3,3′,3′-tetramethylindodicarbocyanine perchlorate (DiD or DiIC18(5)) were investigated. CT has been widely used to label living cells (Redelman et al., 1988), and has been utilized in tracking both animal (Silverman et al., 2000) and human derived (Jablonska et al., 2010) cell transplants. Lipophilic long chain dicarbocyanine dyes belong to large family of cyanine dyes (for review see Mishra et al., 2000). DiD and its analogs have been used for cell visualization both in tissue slices and cell cultures (Honig and Hume, 1986, 1989). The impact of these dyes on human-derived

* Corresponding author at: NeuroGroup, Institute of Biomedical Technology/BioMediTech, University of Tampere, Biokatu 12, 6th floor, 33520 Tampere, Finland. Tel.: +358 40 1782942; fax: +358 3 35518498.
E-mail addresses: meeri.makinen@uta.fi (M. Mäkinen), tiina.joki@uta.fi (T. Joki), laura.yla-outinen@uta.fi (L. Ylä-Outinen), heli.skottman@uta.fi (H. Skottman), susanna.narkilahti@uta.fi (S. Narkilahti), riikka.aanismaa@uta.fi (R. Äänismaa).
[1] These authors contributed equally to this work.

0165-0270/$ – see front matter © 2013 Elsevier B.V. All rights reserved.
http://dx.doi.org/10.1016/j.jneumeth.2013.02.019

neural cells has not been previously studied although they have been used in cell cultures from both animal and human origin (Packard et al., 1984; Honig and Hume, 1986; Jablonska et al., 2010; Markiewicz et al., 2011).

The optimum labeling parameters and the characteristics of cell population labeled with each of these dyes were defined. Furthermore, the effect of labeling on the proliferation and viability was studied. The behavior of CT and DiD during immunocytochemistry as well as in co-cultures was also studied. Finally, the ability of CT- and DiD-labeled hESC-derived co-cultures to form functional neural networks was investigated.

2. Materials and methods

2.1. Cells

2.1.1. HESC line derivation and maintenance

A number of hESC lines (Regea 08/056, 06/040, 08/023) were used in this study. The Regea lines were derived at Institute of Biomedical Technology (IBT), University of Tampere, Finland. IBT holds an approval from the Ethics Committee of Pirkanmaa Hospital District for derivation, characterization, and differentiation of hESC-lines (R05051, R05116) as well as an approval of Valvira, the Finnish National Supervisory Authority for Welfare and Health, for research on human embryos (1426/32/300/05). The derivation and characterization of Regea lines has been described previously (Rajala et al., 2010; Skottman, 2010). The maintenance of hESC lines was done as described earlier (Rajala et al., 2007). The hESC lines were quality controlled with frequent gene and protein expression analysis, karyotype, and mycoplasma assays.

2.1.2. Derivation of neural cultures

The neural differentiation of hESCs was performed as described by Lappalainen et al. (2010). Basic fibroblast growth factor (bFGF) was used in 20 ng/ml concentration during the neurosphere culturing step. For the final neural maturation, the neurospheres were mechanically dissected and plated onto 24- or 48-well plates coated (overnight in +4 °C or two hours in +37 °C) with laminin (10 μg/ml, mouse or human, Sigma–Aldrich, St. Louis, MO). The bFGF was withdrawn at the beginning of adherent culture. Half of the medium was replaced 2-3 times a week. For co-culturing, the adherent fluorescent labeled cultures were dissected enzymatically (TrypLe Select™, Gibco).

2.2. Fluorescent dyes

Fluorescent probe 5-chloromethylfluorescein diacetate (CellTracker Green CMFDA, CT, C2925, Molecular Probes®, Life Technologies, UK) was prepared by dissolving it to DMSO (10 mM stock). Lipophilic carbocyanine 1,1′-dioctadecyl-3,3,3′,3′-tetramethylindodicarbocyanine perchlorate (DiD, D-307, Molecular Probes®, Life Technologies) was prepared by dissolving it to 99.8% ethanol (20 mM stock). On the day of use, a labeling medium was prepared by diluting stock solution to fresh culture medium. The final concentrations recommended by the manufacturer, Molecular Probes®, were 0.5–25 μM for CT and 25 μM for DiD. However, during the experiments we came to test a wider range for CT (0.5, 2, 4, 5, 8, 10, 16, 20, 30, 40 or 60 μM). Based on the literature (Honig and Hume, 1986, 1989; Potter et al., 1996) we decided to test a larger range for DiD as well (0.2, 0.5, 1, 5, 10, 20 or 50 μM). The culture medium on the cells was replaced with the labeling medium and incubated (CT: 15, 30 or 60 min or 2, 4, 24, 48, or 72 h; DiD: 2, 10, 30 or 60 min or 2, 4, 8, 16 or 24 h) at +37 °C, 5% CO_2, humidified atmosphere. After incubation, the labeling medium was replaced with fresh culture medium and the cells were imaged at varying periods after labeling. Every parameter set was tested at least once with 2 parallel samples for both probes and the optimal parameters were tested at least 8 times with 2–20 parallel samples.

2.3. Cell viability

The LIVE/DEAD® Viability/Cytotoxicity Kit (L-3224, Molecular Probes®, Life Technologies) or the components of the kit purchased individually (Calcein AM; C1430, EthD-1; E1169, Molecular Probes®, Life Technologies) were used to assess the cell viability (Althouse and Hopkins, 1995). Briefly, Calcein AM and EthD-1 were diluted to culture medium to the final concentrations of 0.1 μM and 0.5 μM, respectively. After 30 min of dark incubation, the cells were imaged with a fluorescence microscope. Analysis was performed by manually counting the number of Calcein AM and EthD-1 labeled cells from the images.

2.4. Immunocytochemistry

Cells were fixed with cold 4% paraformaldehyde for 15 min in room temperature. To prevent unspecific binding of antibodies, cells were permeabilized with 0.1% Triton X-100 (Sigma) or 0.1% saponin (Sigma–Aldrich) and blocked with 10% normal donkey serum (NDS, Millipore) in 1% bovine serum albumin (BSA, Sigma) in DPBS. Primary antibodies were diluted to 1% NDS, 1% BSA in DPBS with 0.1% Triton X-100 or 0.1% saponin. The primary antibody solution was kept on cells overnight at +4 °C. The excess primary antibodies were removed by washing with 1% BSA in DPBS without or with 0.1% saponin. Next, the secondary antibodies were added in 1% BSA in DPBS without or with 0.1% saponin. Secondary antibodies were incubated at room temperature for one hour. Immunocytochemical staining protocol was also performed with no permeabilization. The excess secondary antibodies were removed by washing with PBS and phosphate buffer without saline. For nuclear staining and mounting, Vectashield with 4,6-diamidino-2-phenylindole (DAPI, H1200, Vector laboratories, Peterborough, UK) was utilized. Primary antibodies anti-MAP-2 (rabbit, 1:600, AB5622, Millipore, Billerica, MA, USA) for detecting neuronal cells as well as their processes, anti-GFAP (sheep, 1:600, AF2594, R&D Systems, Minneapolis, MN, USA) for detecting astrocytes and anti-Ki-67 (rabbit, 1:800, AB9260, Millipore) for detecting proliferating cells were used. AlexaFluor-488, -568 or -680 conjugates of anti-rabbit or anti-sheep secondary antibodies (1:600, Molecular Probes Invitrogen) were used. In order to quantify proliferation, DAPI and Ki-67 positive cell nuclei were counted from the microscope images.

2.5. Imaging system

Cells were visualized and imaged with a fluorescent microscope set (Olympus IX51 inverted microscope, PlanFLN 4×, 10×, 20×, and 40× objectives, Olympus DP30BW CCD camera). The light was filtered with U-MNU2 (excitation filter 360–370; emission filter 420; dichromatic filter 400), U-MNB2 (excitation filter 470–490; emission filter 520; dichromatic filter 500), U-MWG2 (excitation filter 550-510; emission filter 590; dichromatic filter 570), or U-N41023 (excitation filter 625–675; emission filter 710; dichromatic filter 680) filter cube. The images were processed with Adobe Photoshop. Briefly, the grayscale images were converted to an RGB format and the output levels were adjusted to zero, except for the channel corresponding to the color of the fluorescent light.

2.6. Microelectrode array system

The electrical activity of the neural networks were measured by culturing cells on microelectrode array (MEA)-dishes (Multi

Channel Systems, MCS, Reutlingen, Germany) ($n = 9$). The electrodes on bottom of the MEA-dish detect extracellular local field potential changes produced by the electrical activity of the overlaying neurons. Thus, MEA is a non-invasive method and can be used for long term neuronal network activity follow up studies (Wagenaar et al., 2006). The microelectrodes in the dishes used had 30 μm diameter and 200 μm inter-electrode distance. The microelectrode measurements were performed using MEA-dishes sealed with 70% ethanol cleaned semi-permeable membrane (ALA MEA-MEM, ALA Scientific Instruments Inc., Westbury, NY). MEA-dishes were placed into a faraday cage protected amplifier (MEA-1060BC, MCS) and kept warm with an external heater unit (TC02, MCS) set to +38 °C. After placing the MEA-dish into the amplifier, the system was allowed to settle for one minute after which the recording was started. The measured signals were preamplified with MEA1060-Inv-BC (gain 53, MCS) and prefiltered with FA60SBC (gain 20, MCS) producing signal with 1100 gain and 1 Hz–8 kHz bandwidth. Analog to digital conversion was performed with MC_card (MCS) with 20 kHz sampling frequency. The data acquisition card was controlled *via* MC_Rack software (MCS). The digitized recordings were further processed by removing power line noise (50 Hz band reject) and baseline fluctuations (200 Hz high pass) with 2nd order Butterworth filter. Spike detection was performed online with MC_Rack software. Threshold based detection (5 times standard deviation of noise level) was used. Both, the electrode raw data and detected spikes were saved for analysis. Signals were recorded for 5 min 1–3 times a week for each MEA. The spike counts and time stamps on each electrode were extracted with NeuroExplorer (Nex Technologies, Littleton, MA, USA) software, collected to Excel files, and combined to raster plots.

2.7. Statistical analysis

Statistical analysis were performed with IBM® SPSS (version 19) statistical software package. The data gained from manual cell counting from LIVE/DEAD- or Ki-67-stained cells were analyzed with nonparametric Kruskal-Wallis test followed by a Mann-Whitney U-test (*post hoc* test). A p-value less than 0.05 was considered significant. If more than two groups were analyzed the resulting p values were multiplied by the number of comparisons performed (Bonferroni correction).

3. Results

3.1. Optimizing labeling

A group of different labeling parameters were studied to obtain long time dye retention. A CT concentration of 0.5, 2, 4, 5, 8, 10, 16, 20, 30, 40, or 60 μM was incubated for 15 or 30 min, 1, 2, 4, 12, 24, 48, or 72 h (Fig. 1A). Properly observable labeling of the cells up to 4 weeks was obtained by incubating 10, 16, and 20 μM CT dilutions for 72 h. These labeling parameters enabled the labeling of both cell bodies and processes (Fig. 1B). Based on the comparison between fluorescent and transmission light images, CT seemed to label the whole cell population (Fig. 1B). At the end of the experiment, 4 weeks after labeling, CT labeled cells were fixed and stained with DAPI. The percentage of CT labeled cells from DAPI identified nuclei was 94% (604 cells, 6 imaged areas from 2 parallel wells). Hence, it can be argued that CT labels virtually all cells of the differentiated population. The labeling did not have effect on cell viability based on visual inspection. The cell viability was studied in more detail only in optimal concentration (Section 3.2).

DiD concentrations of 0.2, 0.5, 1, 5, 10, 20, and 50 μM were tested with 10 min, 30 min, 1, 2, 16, or 24 h incubation times (Fig. 1C). A high DiD concentration (50 μM) or a long incubation time (16 h) with over 5 μM DiD concentration had clearly adverse effect on cell viability and were not further studied. Optimal labeling was observed with 10 or 20 μM DiD concentration and 1 or 2 h incubation time (Fig 1D). During the first week of 5 weeks follow up time, the labeling was bright and cellular processes were clearly visible. After the second week, some of the labeled processes were no longer visible. During the third week, the probe concentrated into cell somas. After 4 weeks, the probe accumulated into somatic granules (data not shown).

3.2. Effect on viability and proliferation

The cytochemical effects of both CT and DiD were studied by assessing cell viability and proliferation. For these experiments, the CT labeling was performed for 72 h with 10 μM concentration and the DiD labeling was performed for 2 h with 10 μM concentration. For CT labeled cells, LIVE/DEAD staining was performed 4 or 15 days after labeling to study the acute labeling effect and long term dye retaining effect on cell viability. No clear difference was observed between labeled cells and control cells on the 4 days time point (>1000 cells from 5 parallel images from 2 parallel wells, Fig. 2A). However, at 15 days time point, there were slightly more dead cells in CT labeled cultures compared to control cultures. No significant differences were found between control and CT labeled cells in the time points studied. For studying the effect on proliferation, the CT labeled cells were fixed 6–7 or 11–13 days after labeling and immunocytochemistry was performed against Ki-67, a marker of dividing cell nucleus. The cells were counted after imaging the stained cells (>450 cells, 2 parallel wells 3 figures each, Fig. 2B) and no significant differences between control and CT labeled cells were found in either time point.

For DiD labeled cells the viability was analyzed 5 days after the labeling. A triple labeled population (Calcein-AM, DiD, ethidium homodimer) was imaged using the U-N41023 filter cube in order to distinguish DiD. This was required due to the ability of DiD to also pass the U-MWG2 filter cube used for ethidium homodimer. The ethidium homodimer was, in turn, distinguished from DiD by having clearly brighter emission. Furthermore, ethidium homodimer labeled dead cell nuclei had a distinct round morphology whereas living cells labeled with DiD had more complex morphology with somas and neurites. No difference in viability was seen between the DiD labeled and the control cells (>6900 cells counted from 3 parallel wells, Fig. 2C). Proliferation was analyzed 3 weeks after cell plating. For acute effects, the adherent cultures were labeled with DiD and fixed 2 days later. For long term effects, the adherent cultures were labeled with DiD and fixed 2 weeks after labeling. The control group was cultured adherent for 3 weeks. The population that was labeled 2 days before analysis had slight decrease in proliferation but the difference was not significant. As a long term effect (2 weeks after labeling), DiD was observed to reduce cell proliferation as the amount of Ki-67 positive cells was significantly lower in labeled population when compared to the control cells (>1500 cells counted from 2 parallel wells, Fig. 2D) ($p < 0.05$).

3.3. Optimizing immunocytochemistry

Fluorescent probes integrating to cell membranes, such as DiD, can be sensitive to reagents used to increase cell membrane permeability. Permeabilization, however, is required in order to perform immunocytochemistry against intracellular epitopes. We compared immunocytochemical stainings performed without permeabilization, with a common permeabilizer Triton X-100 or with a milder permeabilizer saponin. With DAPI there were no differences (Fig. 3A–C). The immunochemistry was performed against intracellular proteins MAP-2 and GFAP. Without permeabilization, the immunocytochemistry produced an uneven labeling and the

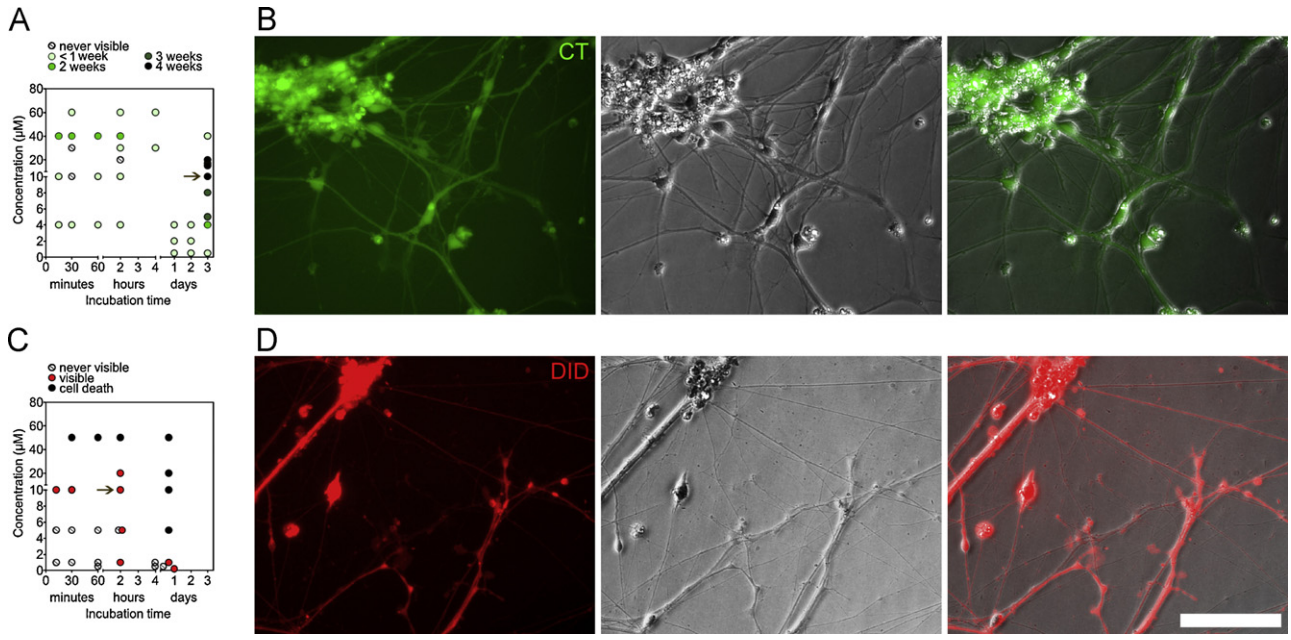

Fig. 1. Live-labeling of cells with fluorescent probes CT (A, B) and DiD (C, D). In pictures A and C, circles with slash present the labeling parameters when no labeling with CT or DiD was observed. In picture A, the CT label retention time in the cultures is presented with colored dots (from light green to dark green = from less than a week up to 3 weeks, black = up to 4 weeks). Thus, with 10 μM and 3 days incubation, CT labeling was traceable up to 4 weeks and these parameters were considered optimal (marked with arrow). Picture B shows cells labeled using the optimal parameters. In picture C, red dots shows labeling parameters for good labeling whereas black dots shows parameters that caused cell death. The dye retention was followed at least 2 weeks for each labeling parameter set. Thus, the optimal parameters for DiD were 10 μM and 2 h incubation (marked with arrow). Picture D shows cells labeled using the optimal parameters. In pictures B and D, the rightmost image is an overlay between the fluorescent and wide field image. In pictures A and C, the *x*-axis is scaled to minutes (0–60), hours (1–4), and to days (1–3) in order to show all the times in same axis. Scale bar is 100 μm.

cell morphologies were difficult to perceive (Fig. 3D). With Triton X-100 and saponin the labeling was bright and clear (Fig. 3E and F). Without permeabilization or with saponin permeabilization the DiD probe was well retained and remained clearly visible (Fig. 3G and I). However, with Triton X-100 DiD was dissolved from the membranes causing faint labeling and red background fluorescence (Fig. 3H). None of the permeabilizers used disturbed the retainment or fluorescence of CT (Fig. 3J–L). An example of immunochemistry with saponin permeabilization performed against MAP-2 or GFAP with CT or DiD labeled cells is presented in Fig. 4.

3.4. Co-culturing

To further assess the suitability of CT and DiD for mixed cell cultures, the effect of dissociating and replating previously labeled cells was studied. CT was retained during dissociation and no clear difference in the intensity of the dye was observed between the control and the replated CT labeled cells during one week follow up time (data not shown). Furthermore, it was observed that the background fluorescence of CT was diminished during replating. DiD was also found to be suitable for enzymatic cell detachment and replating. After the effect of cell dissociation was studied, mixed cell cultures of CT and DiD labeled cells were produced. The cells originating from different adherent cultures labeled with different fluorescent dyes did not avoid each other and grew as a mixed network (Fig. 5A–C). Initially, the dyes were retained in different cells. However, during the long term co-culturing the dyes became partially co-localized and granular (Fig. 5D–F).

The effect of CT and DiD labeling on the formation of the neural network activity was studied with planar MEAs (Fig. 6). Adherent hESC-derived neural cultures were labeled either with CT or DiD and dissociated to single cell suspensions. Cells from both suspensions were replated onto MEA plates ($n = 9$). The development of the network activity was followed by weekly measurements (Fig. 6B). During the follow up period, the co-cultures first developed single spikes and later semi synchronous trains (Fig. 6C). From these

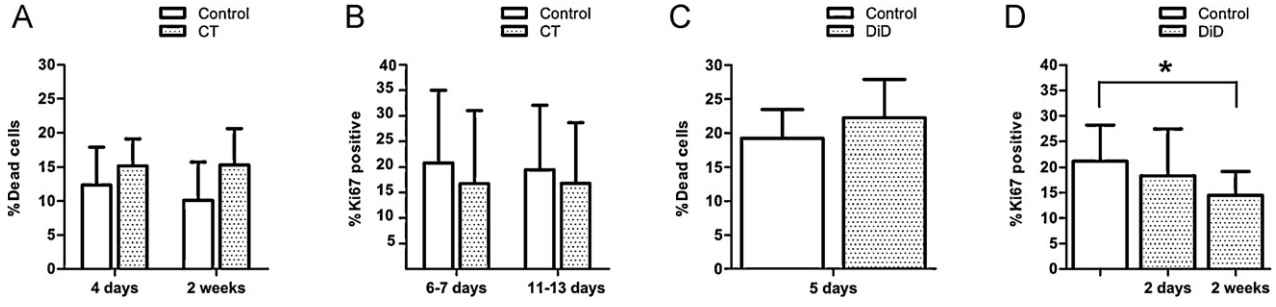

Fig. 2. Viability and proliferation studied with labeled and unlabeled populations. (A) In LIVE/DEAD analysis CT labeling slightly increased the amount the dead cells in the cultures. (B) Similarly, the amount of the Ki-67 positive proliferative cells was slightly lower in CT labeled cell populations when compared to unlabeled control cells. Similarly, DiD labeling slightly increased the amount of the dead cells (C) while decreasing the amount of proliferative Ki-67 positive cells. The decrease was significant after long term culturing (D). * represents a *p*-value less than 0.05.

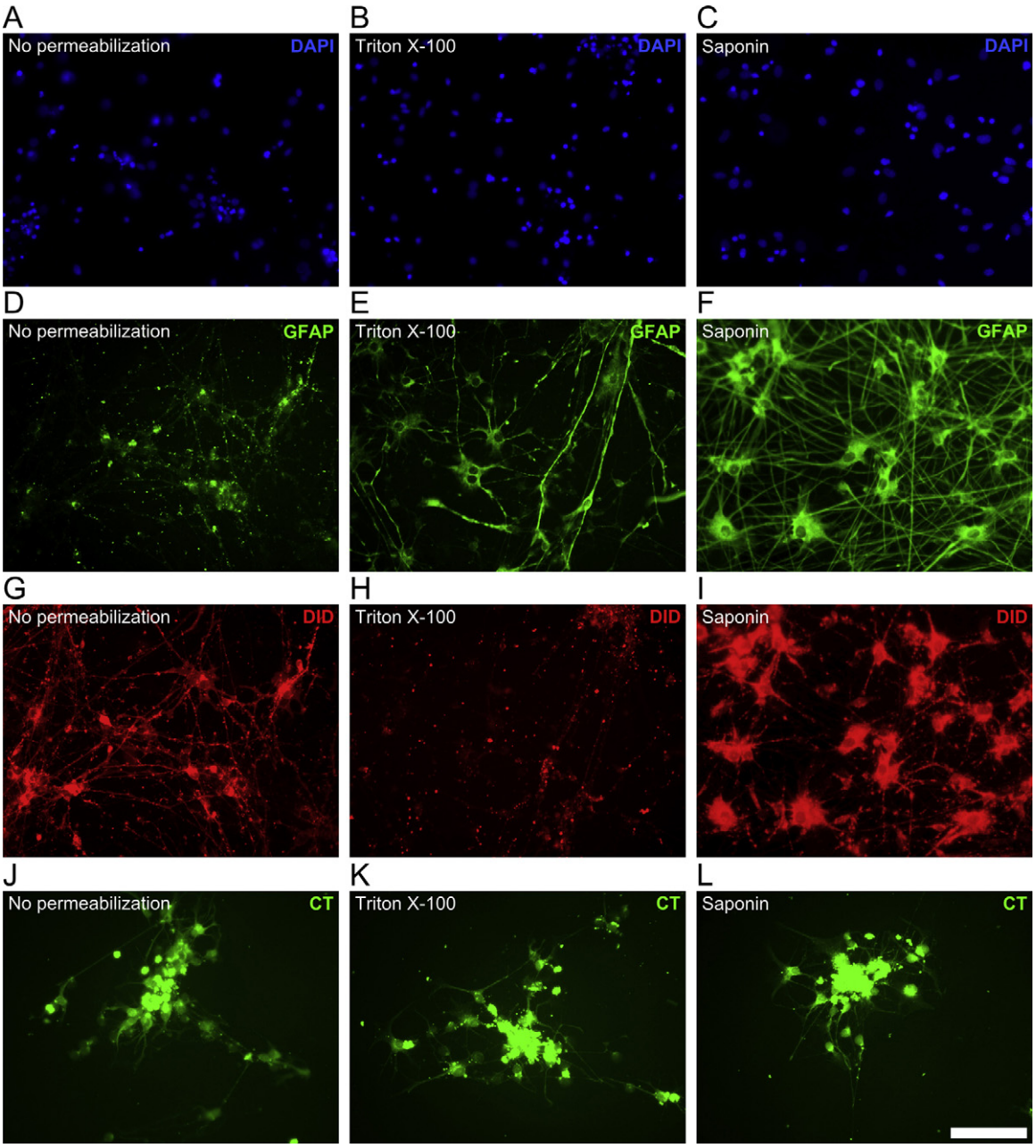

Fig. 3. Dye retention with different immunocytochemical permeabilization approaches. (A–C) DAPI stained all the nuclei regardless of the permeabilization. (D) GFAP, an antibody against intracellular protein could not be used without permeabilization whereas with either (E) Triton-X or (F) saponin the GFAP staining was successfully detected. DiD staining could be detected without permeabilization (G) and with saponin (I) whereas (H) with Triton-X DiD was extracted. CT staining was not affected by any of the permeabilization approaches (J–L). Scale bar 100 μm.

observations, it was deduced that the labeling with CT and DiD, as well as co-culturing in a mixed form, does not prevent the formation of network connections between the hESC-derived neurons.

4. Discussion

The objective of this research was to find and study the effects of fluorescent probes suitable for long term labeling of hESC-derived neural cell co-cultures. The suitability of two dyes, CT and DiD were investigated. Our results indicated that CT and DiD can be used for studying co-cultures of hESC-derived neural cells without adverse cytotoxic or functional effects.

CT at a concentration of 10 μM in cell culture medium with 72 h incubation time enabled cell visualization at least up to 4 weeks. Labeling concentration of CT used in previous experiments with neural lineage cell cultures tend to follow those recommended by the Molecular Probes (0.5–25 μM), *e.g.* 20 μM for 30 min (McMahon and McDermott, 2006), 5 μM for 60 min (Pettersson et al., 2010), and 10 μM for 30 min (Markiewicz et al., 2011). The observations about the CT retention varied as CT labeled radial glial cells were reported to be observable up to 20 days (McMahon and McDermott, 2006) while CT labeled olfactory ensheathing glial cells lost their fluorescence in under 14 days (Pettersson et al., 2010). However, the parameters used by Pettersson et al. (2010), McMahon and McDermott (2006), and Markiewicz et al. (2011) were not reported to be optimized for the cell type used. We discovered that with short incubation times (15 min–4 h) the labeling was detectable less than 2 weeks whereas with longer incubation times (toward 72 h) the

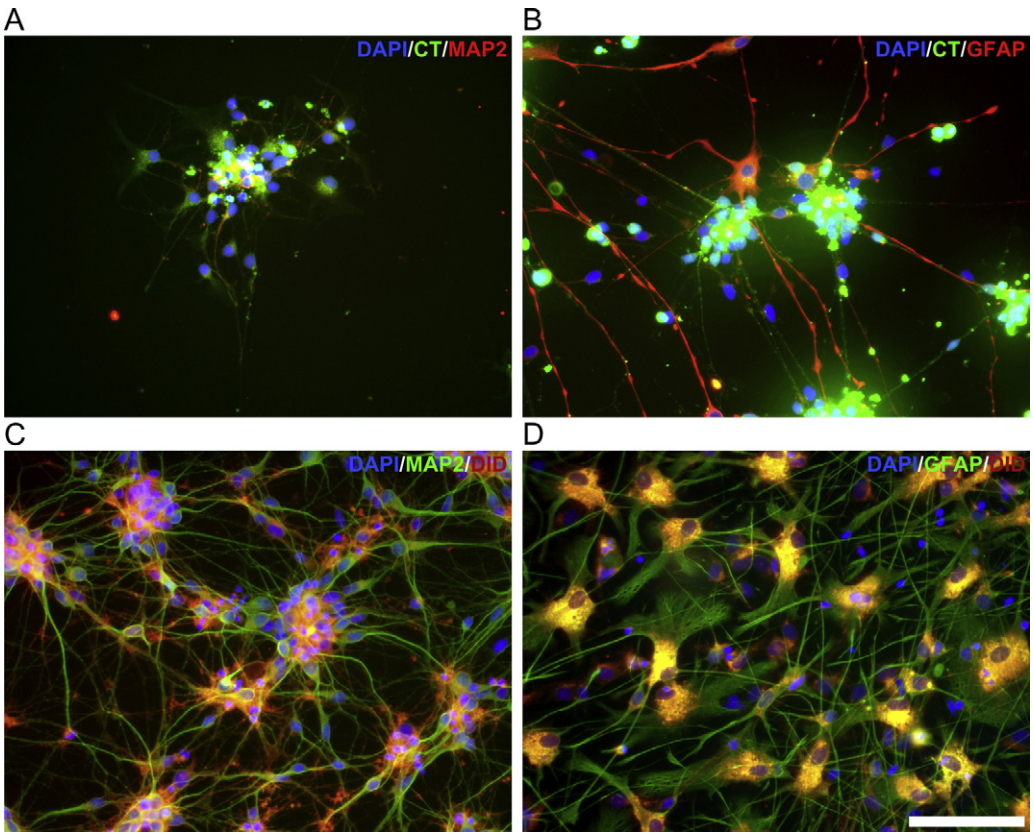

Fig. 4. Immunocytochemical staining combined with CT and DiD labeling. CT labeled cells stained positive (A) with MAP-2 and (B) with GFAP. Similarly, DiD label co-localized (C) with MAP-2 and (D) with GFAP. Scale bar 100 μm.

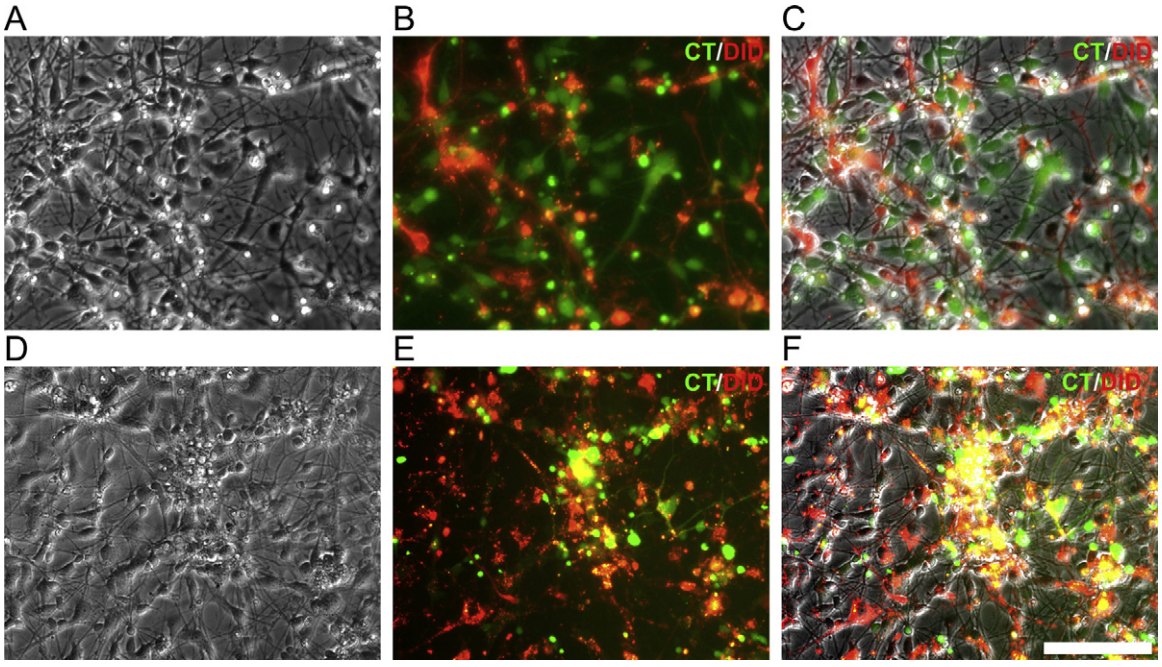

Fig. 5. Combined co-cultures of cells pre-labeled with CT (green) or DiD (red). (A–C) Four days after combining, the separately labeled cell populations could be easily detected. (A) A wide field image of the co-culture, (B) a corresponding fluorescent image from two channels, and (C) an overlay of the wide field and fluorescent images. (D–F) 17 days after combining the separate populations could still be detected. (D) A wide field image of the co-culture, (E) a corresponding fluorescent image from two channels, (F) an overlay of the wide field and fluorescent images. Scale bar 100 μm.

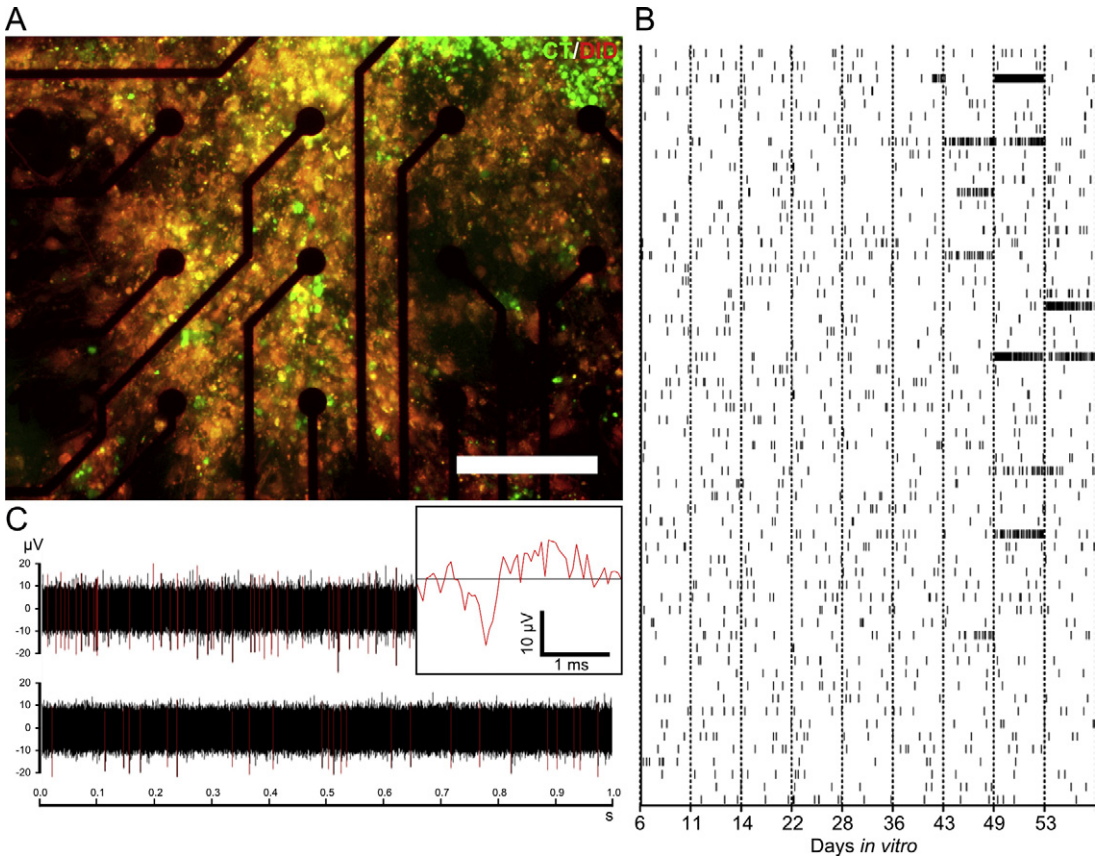

Fig. 6. Functionality of the neural network formed by mixed pre-labeled neural populations. (A) A dense network from cells stained with CT or DiD grew over microelectrode array. (B) Development of network activity from single spikes to spike trains during the culturing period of over 53 days. Each vertical tic represents a spike while each row represents activity from a single microelectrode. Measurement days are on the *x*-axis. (C) A close-up view of training from two adjacent electrodes. The red lines represent spikes. The shape of one spike is presented in larger time scale in the box in (C). The horizontal black line is 0 mV level. Scale bar in (A) is 100 μm.

probe became detectable for at least 4 weeks. Thus, at least with CT, it seems that the labeling parameters should be optimized according to the cell type. In their experiments McMahon and McDermott (2006), transplanted CT labeled radial glial cells and reported them to be traceable up to 20 days *in vivo*. Based on this, CT could also be feasible for *in vivo* studies.

With DiD, the 20 μM (19.2 μg/ml) working solution with 2 h incubation time was most suitable for hESC-derived neuronal cultures. Previously with neural applications, the probe concentration in working solution has typically been between 10 and 40 μg/ml and incubation times between 15 min and 2 h (Honig and Hume, 1986, 1989; Potter et al., 1996). In this study, DiD probe was detectable for 4 weeks in hESC-derived neuronal cultures. The detectability of DiD fluorescence was quite similar to DiO and DiI as described earlier with embryonic chick neurons which were visible for three and half weeks *in vitro* (Honig and Hume, 1986). Previously, carbocyanine dyes (DiI, DiO, DiD, DiR and analogs) have been used to study neuronal architecture in animal derived fixed or living tissue (Honig and Hume, 1986, 1989; Matsubayashi et al., 2008). In addition, DiI has been used to label rat neural cells for *ex vivo* transplantation studies (Potter et al., 1996) and to label human bone marrow fibroblasts crafted into mice or rat *in vivo* (Ferrari et al., 2001). The human fibroblast labeled with DiI (20 μM) were detectable in the craft after one month (Ferrari et al., 2001). This indicates that carbocyanine dyes are also suitable for *in vivo* applications.

The viability of hESC-derived neural cells was not changed few days after CT labeling with the optimal parameters. However, after longer period from CT labeling (>2 weeks) the proportion of dead cells was larger even though no statistical differences were found. Based on this observation, CT might induce a decrease in the cell viability after several weeks. No literature assessing the viability effect of CT was found. CT did not affect the proliferation of hESC-derived neural cells as during experiments no trend with respect to post labeling period length was observed. Contradictory, CT labeling has previously been described to reduce the proliferation rate of rat olfactory ensheathing cells (Pettersson et al., 2010). The labeling performed by Pettersson et al. (2010) was performed with a lower CT concentration and shorter incubation time compared to our study. Because these gentler labeling parameters affected proliferation, it is possible that such effects are cell type dependent. Previously, CT has been described to label human cord blood stem cell-derived neurons, astrocytes, oligodendrocytes, and microglia (Markiewicz et al., 2011). In this study the percentage of CT labeled cells was observed not to reach 100%. This is most likely due to the easier visualization of DAPI stained nuclei compared to CT stained cell bodies from groups of tightly packed cells.

With the optimal labeling parameters DiD labeling did not affect the cell viability. In the literature, the carbocyanine dyes are also commonly described as non-harmful to different animal-derived cell cultures (Honig and Hume, 1986; Ferrari et al., 2001). In this study some cytotoxic effects were seen when the cells were exposed to a high probe concentration, but this was not analyzed any further. In line, Potter et al. (1996) have also reported cytotoxic effects with neuronal cultures when exposed to high (40 μg/ml) probe concentrations for over 30 min. One previous study described that no differences in cell behavior was found between labeled and unlabeled chicken neural cell populations (Honig and Hume,

1986). In contrast, we found that the proliferation of the hESC-derived neural cells was decreased during long term culture after DiD labeling. The difference of observations might be due to different analysis method or differences in neural cell characteristics between two different species. Furthermore, when using these dyes with hESC-derived neurons the decrease in proliferation during long term culture needs to be taken into account.

All studied permeabilizations and primary antibody incubation times allowed the retention of CT and clear immunolabeling. CT was localized around virtually all DAPI stained nuclei. DiD was lost if permeabilization was performed with Triton-X. However, 0.1% Saponin permeabilization allowed DiD retainment. Both MAP-2 positive neurons and GFAP positive astrocytes were found to be labeled by DiD. Thus, both probes labeled all cell types present in hESC-derived neural cultures. Previously, both probes used in this study or their analogs have been shown to label several cell types (Redelman et al., 1988; Ferrari et al., 2001; Heinrich et al., 2007; Matsubayashi et al., 2008; Markiewicz et al., 2011).

Dissociation of labeled adherent cultures did not cause visible intensity changes in CT or DiD labeling. Co-cultures of CT and DiD labeled cells grew as mixed cell networks. Hence, no obvious signs of self-organization caused by labeling with CT and DiD were observed. CT can be argued to be suitable for replating due to the observed retainment of the dye in cells after replating. The effect of replating on the maximal visualization time, however, was not studied. Some of the co-cultured cells had both dyes in them after long term co-culturing. However, cells which were originally labeled with CT or DiD could be separated by visual inspection from cells which had taken up either of the dyes. Previous publications about carbocyanine dyes have not reported transfer from labeled population to unlabeled cells (Honig and Hume, 1986) although some dye transfer has been reported to take place *via* labeled cell debris in cultures (Potter et al., 1996). The co-localization of CT and DiD to same cells could be due to cells engulfing cell debris or parts of each other during close cell-cell interactions. To the best of our knowledge, no one else has studied the usage of dual fluorescent dye labeled neural cells in long term co-cultures *i.e.* during several weeks. One dual labeled co-culture system utilizing human cells has been described (Rizvanov et al., 2010). However, this work did not address the effects of dyes on cells and the culturing time was not mentioned (Rizvanov et al., 2010). Studying long term suitability of dyes for co-cultures is important, because it is desirable to visualize cells during long term culturing required for studying slow tissue formation processes as well as to be able to distinguish the cell populations after fixing the cultures for immunocytochemical characterization.

Co-cultures of CT and DiD labeled cells were able to develop network activity. Thus, the ability of hESC derived neurons to form functional neural networks is not compromised by CT and DiD labeling. Earlier Honig and Hume have reported that carbocyanine labeling does not affect the electrical properties of single chicken neurons (Honig and Hume, 1986). This is in line with our findings. To the best of our knowledge, our study is the first one to study the electrical functionality of fluorescent probe labeled human derived neuronal cell networks. The aspect of functionality is extremely important to consider when utilizing neural cells and aiming toward applications such as *in vitro* models, neurotoxicity studies or graft development. Thus, it is of high importance to note that labeling living cells with studied probes did not affect the formation of functional neural networks from hESC-derived neurons described earlier (Heikkilä et al., 2009). In functional neural tissue the signal is transmitted along cells *via* action potentials, and between cells *via* synaptic connections. MEAs can be used to make recordings of the action potentials in the network scale (Whitson et al., 2006). Subsequent network scale recordings allow the study of development of signal transmission in neural cultures (Wagenaar et al., 2006). Thus, the network activity measured by MEA can be argued to demonstrate that separately CT and DiD labeled co-cultured neural cells are able fire action potentials and are able to form a functional network. However, the MEA methodology does not enable the direct study of synapses or detailed electrophysiological features of single cells (Whitson et al., 2006). Hence, nothing can be concluded about the formation of synapses between the two differently labeled cell populations or about subtle effects of these dyes on the electrophysiological properties of single cells. These aspects could be studied in the future by utilizing patch clamp or calcium imaging methods, and immunocytochemical staining against synaptic structures.

Here, we have shown that human pluripotent stem cell-derived neuronal cells can be labeled with two fluorescent probes, CT and DiD, without affecting the cells' viability (and with CT, proliferation), and most importantly their electrical functionality at network level. This study clearly shows, that live-labeling is possible and can be potentially helpful in many important applicative fields such as neuronal network formation studies for building *e.g.* neurotoxicity testing platforms or actual graft development. Presumably this method can also be used when studying these cells in biomaterials, however, the reactivity of CT chloromethyl moieties with protein thiols should be taken into account when staining cell cultures in biomaterials containing thiol groups.

Acknowledgements

The personnel of IBT Stem cell unit is acknowledged for the support in stem cell research. This study was funded by Competitive Research funding of the Tampere University Hospital (Grant 9M064) and SpareBrain project, Academy of Finland (139345). These organizations were not involved in study design, execution, and manuscript preparation.

References

Althouse GC, Hopkins SM. Assessment of boar sperm viability using a combination of two fluorophores. Theriogenology 1995;43:595–603.
Boyce S, Kelly E, Reavill C, Jenner P, Marsden C. Repeated administration of N-methyl-4-phenyl 1,2,5,6-tetrahydropyridine to rats is not toxic to striatal dopamine neurones. Biochem Pharmacol 1984;1:1747–52.
Ferrari A, Hannouche D, Oudina K, Bourguignon M, Meunier A, Sedel L, et al. In vivo tracking of bone marrow fibroblasts with fluorescent carbocyanine dye. J Biomed Mater Res 2001;56:361–7.
Heikkilä TJ, Ylä-Outinen L, Tanskanen JMa, Lappalainen RS, Skottman H, Suuronen R, et al. Human embryonic stem cell-derived neuronal cells form spontaneously active neuronal networks in vitro. Exp Neurol 2009;218:109–16.
Heinrich L, Freyria A, Melin M, Tourneur Y, Maksoud R, Bernengo J, et al. Confocal laser scanning microscopy using dialkylcarbocyanine dyes for cell tracing in hard and soft biomaterials. J Biomed Mater Res 2007;81:153–61.
Honig MG, Hume RI. Fluorescent carbocyanine dyes allow living neurons of identified origin to be studied in long-term cultures. J Cell Biol 1986;103:171–87.
Honig MG, Hume RI. Dil and diO: versatile fluorescent dyes for neuronal labelling and pathway tracing. Trends Neurosci 1989;12:333–41.
Jablonska A, Kozlowska H, Markiewicz I, Domanska-Janik K, Lukomska B. Transplantation of neural stem cells derived from human cord blood to the brain of adult and neonatal rats. Acta Neurobiol 2010;70:337–50.
Lappalainen RS, Salomaki M, Yla-Outinen L, Heikkila TJ, Hyttinen JA, Pihlajamaki H, et al. Similarly derived and cultured hESC lines show variation in their developmental potential towards neuronal cells in long-term culture. Regen Med 2010;5:749–62.
Markiewicz I, Sypecka J, Domanska-Janik K, Wyszomirski T, Lukomska B. Cellular environment directs differentiation of human umbilical cord blood-derived neural stem cells in vitro. J Histochem Cytochem 2011;59:289–301.
Matsubayashi Y, Iwai L, Kawasaki H. Fluorescent double-labeling with carbocyanine neuronal tracing and immunohistochemistry using a cholesterol-specific detergent digitonin. J Neurosci Methods 2008;174:71–81.
McMahon SS, McDermott KW. A comparison of cell transplantation and retroviral gene transfection as tools to study lineage and differentiation in the rat spinal cord. J Neurosci Methods 2006;152:243–9.
Mishra A, Behera RK, Behera PK, Mishra BK, Behera GB. Cyanines during the 1990: a review. Chem Rev 2000;100:1973–2012.
Packard BS, Karukstis KK, Klein MP. Intracellular dye heterogeneity determined by fluorescence lifetimes. BBA Biomembr 1984;769:201–8.

Pettersson J, Lobov S, Novikova LN. Labeling of olfactory ensheathing glial cells with fluorescent tracers for neurotransplantation. Brain Res Bull 2010;81:125–32.
Potter SM, Pine J, Fraser SE. Neural transplant staining with DiI and vital imaging by 2-photon laser-scanning microscopy. Scanning Microsc Suppl 1996;10:189–99.
Rajala K, Hakala H, Panula S, Aivio S, Pihlajamäki H, Suuronen R, et al. Testing of nine different xeno-free culture media for human embryonic stem cell cultures. Hum Reprod 2007;22:1231–8.
Rajala K, Lindroos B, Hussein SM, Lappalainen RS, Pekkanen-Mattila M, Inzunza J, et al. A defined and xeno-free culture method enabling the establishment of clinical-grade human embryonic, induced pluripotent and adipose stem cells. PLoS ONE 2010;5:e10246.
Redelman D, Butler S, Robison J, Garner D. Identification of inflammatory cells in bovine milk by flow cytometry. Cytometry 1988;9:463–8.
Rizvanov AA, Yalvaç ME, Shafigullina AK, Salafutdinov II, Blatt NL, Sahin F, et al. Interaction and self-organization of human mesenchymal stem cells and neuro-blastoma SH-SY5Y cells under co-culture conditions:a novel system for modeling cancer cell micro-environment. Eur J Pharm Biopharm 2010;76:253–9.
Silverman AJ, Sutherland AK, Wilhelm M, Silver R. Mast cells migrate from blood to brain. J Neurosci 2000;20:401–8.
Skottman H. Derivation and characterization of three new human embryonic stem cell lines in Finland. In Vitro Cell Dev Biol 2010;46:206–9.
Wagenaar DA, Pine J, Potter SM. An extremely rich repertoire of bursting patterns during the development of cortical cultures. BMC Neurosci 2006;7:11.
Whitson J, Kubota D, Shimono K, Jia Y. Multi-electrode arrays enhancing traditional methods and enabling network physiology. In: Advances in Network Electrophysiology. 2006 ed. Signapore: Springer; 200638–68.

Journal of Neuroscience Methods 259 (2016) 143–155

Contents lists available at ScienceDirect

Journal of Neuroscience Methods

journal homepage: www.elsevier.com/locate/jneumeth

Computational Neuroscience

Joint analysis of extracellular spike waveforms and neuronal network bursts

Fikret Emre Kapucu[a,*,1], Meeri E.-L. Mäkinen[b], Jarno M.A. Tanskanen[a], Laura Ylä-Outinen[b], Susanna Narkilahti[b], Jari A.K. Hyttinen[a]

[a] Tampere University of Technology, Department of Electronics and Communications Engineering, Computational Biophysics and Imaging Group, BioMediTech, Biokatu 6, FI-33520 Tampere, Finland
[b] University of Tampere, NeuroGroup, BioMediTech, Biokatu 12, FI-33014 Tampere, Finland

HIGHLIGHTS

- Spike and burst statistics give limited information on changes in networks.
- Here, spike sorting combined with burst detection.
- Spike waveform type participation in bursts revealed.
- Spike type compositions of bursts change under network modifications.
- New kind of information obtained on the changes in bursting networks.

ARTICLE INFO

Article history:
Received 2 June 2015
Received in revised form
23 November 2015
Accepted 24 November 2015
Available online 7 December 2015

Keywords:
Neuronal network
Microelectrode array
Burst detection
Spike waveform
Spike sorting
Electrophysiological signal analysis

ABSTRACT

Background: Neuronal networks are routinely assessed based on extracellular electrophysiological microelectrode array (MEA) measurements by spike sorting, and spike and burst statistics. We propose to jointly analyze sorted spikes and detected bursts, and hypothesize that the obtained spike type compositions of the bursts can provide new information on the functional networks.
New method: Spikes are detected and sorted to obtain spike types and bursts are detected. In the proposed joint analysis, each burst spike is associated with a spike type, and the spike type compositions of the bursts are assessed.
Results: The proposed method was tested with simulations and MEA measurements of *in vitro* human stem cell derived neuronal networks under different pharmacological treatments. The results show that the treatments altered the spike type compositions of the bursts. For example, 6-cyano-7-nitroquinoxaline-2,3-dione almost completely abolished two types of spikes which had composed the bursts in the baseline, while bursts of spikes of two other types appeared more frequently. This phenomenon was not observable by spike sorting or burst analysis alone, but was revealed by the proposed joint analysis.
Comparison with existing methods: The existing methods do not provide the information obtainable with the proposed method: for the first time, the spike type compositions of bursts are analyzed.
Conclusions: We showed that the proposed method provides useful and novel information, including the possible changes in the spike type compositions of the bursts due to external factors. Our method can be employed on any data exhibiting sortable action potential waveforms and detectable bursts.

* Corresponding author. Tel.: +358 40 849 0023; fax: +358 3 364 1385 (departmental fax: +not at the corresponding author's location, usage discouraged).
E-mail addresses: fikret.kapucu@tut.fi (F.E. Kapucu), meeri.makinen@uta.fi (M.E.-L. Mäkinen), tanskanen@ieee.org (J.M.A. Tanskanen), laura.yla-outinen@uta.fi (L. Ylä-Outinen), susanna.narkilahti@uta.fi (S. Narkilahti), jari.hyttinen@tut.fi (J.A.K. Hyttinen).
[1] Department of Electronics and Communications Engineering, Tampere University of Technology

http://dx.doi.org/10.1016/j.jneumeth.2015.11.022
0165-0270/

1. Introduction

Regardless of decades of research, neuronal networks, and their development and functioning, are still not fully understood. The analysis of electrophysiological data is one of the methodologies for advancing our knowledge. Developing new methods to derive more information from the available measurement data is highly desirable. Here, we propose a new joint spike and burst analysis method for analyzing extracellular network electrophysiology data. We illustrate the method with simulated signals, and as the test bench we use human stem cell derived neuronal networks cultured on microelectrode arrays (MEAs). Such networks have been shown to develop spontaneous electrical activity and show histiotypic behavior (Bużańska et al., 2005, 2006; Heikkilä et al., 2009).

MEAs are commonly employed in the assessment of the electrical activity of neuronal networks both *in vitro* and *in vivo*. MEA recordings carry information on the electrical activity in tissues and cell cultures at network and cell levels (Gross et al., 1977; Thomas et al., 1972; Pine, 1980; Egert et al., 1998), *e.g.*, from neurons in the vicinity of the MEA electrodes. Physically, MEAs record extracellular field potentials as voltage signals, which can exhibit contributions from both action potentials and lower frequency neuronal activity, in addition to noise. Here, we consider that an action potential is synonymous with a voltage spike over any area of neuronal cell membrane recorded via a MEA electrode. In the recordings, spikes may occur as individual spikes, or as trains or bursts manifesting network activity (Kandel and Spencer, 1961; Connors et al., 1982; Gray and McCormick, 1996).

To use neuronal networks on MEAs as biosensors was proposed by Gross and Rhoades (1995), who described the effects of several pharmacological agents on bursting, and also mentioned the possibility to measure average spike waveforms. Several studies have suggested various spike and burst related metrics to quantify neuronal network behavior (Bal-Price et al., 2008; Johnstone et al., 2010; Defranchi et al., 2011; Hogberg et al., 2011; Novellino et al., 2011; Alloisio et al., 2015). In previous studies, parameters such as spike count, the number of bursts, mean spike rate, mean burst rate, the number of spikes in bursts, burst duration, interburst interval, and the percentage of spikes in bursts have been commonly used (Johnstone et al., 2010; Novellino et al., 2011; Uchida et al., 2012). Furthermore, patterns and spatial distributions of activity are inherent and crucial aspects in network electrophysiology (Banerjee and Ellender, 2009; Uhlhaas et al., 2009; Crumiller et al., 2011).

Burst analysis is necessary in analyzing network activity and the network effects of different *in vitro* treatments (Johnstone et al., 2010). Previously, several different burst detection methods, mostly based on experimentally pre-defined parameters such as interspike interval (ISI) and the number of spikes in bursts (Chiappalone et al., 2005; Turnbull et al., 2005; Wagenaar et al., 2006; Pasquale et al., 2010), have been proposed, for example, to study rat cortical or hippocampal neuronal networks. Burst definitions which are more adaptive to the analyzed network have also been proposed (Pasquale et al., 2010; Kapucu et al., 2012). Such adaptability is called for in the analysis of maturing networks, such as human stem cell derived networks (Kapucu et al., 2012).

In spike analysis, spike waveform cut-outs are sorted, and the waveforms in each resulting class, or cluster, can be averaged to obtain the representative spike waveform types (Gibson et al., 2012). Despite its challenges, spike sorting is required for isolating or identifying single neuronal cell activities in a population firing in an orchestrated manner (Buzsáki, 2004), and different spike sorting algorithms have been utilized in various studies (Santhanam et al., 2006; Sun et al., 2010; Truccolo et al., 2011). Most related to our work, Illes et al. (2014) utilized raster plots of the sorted spikes.

In this paper, a novel joint analysis of sorted spike waveforms and detected bursts is proposed. The joint analysis provides information on the participation of the spike types in bursts for the particular data at hand. In other words, spike type compositions of the bursts, and their changes, *e.g.*, in time or due to external effects, can be assessed using the proposed framework. To our best knowledge, such a joint analysis has not been proposed previously.

A motivation for the development of the joint analysis has been an earlier study on the relationship between single spike features and network bursting in hippocampal pyramidal cells (Harris et al., 2001), which indicated that conditions that cause high firing rates do not necessarily produce high bursting in pyramidal cells. Moreover, the relation between firing rate and bursting may change differently for bursts with different intraburst ISIs (Harris et al., 2001). This may also be the case with our cells, or with any other neuronal network. If this is the case, increase in the activity of a spike type would not guarantee a higher probability of its participation in bursts. Thus, joint analysis would be necessary to assess the burst participations of different spike types.

The joint analysis is illustrated with simulated data containing spikes with different waveforms, organized as individual spikes and bursts, and demonstrated with real MEA data from *in vitro* human neuronal networks undergoing a pharmacological experiment to alter the networks. We show that the proposed framework yields information on the networks and on the changes therein, which is not obtainable by spike and burst analysis nor by spike sorting alone.

The methods presented in this paper were implemented in Matlab and run in a standard laptop PC. The Matlab code for the proposed joint framework is publicly freely available in the Matlab Central File Exchange (http://www.mathworks.com/matlabcentral/fileexchange/54277-joint-analysis-of-extracellular-spike-waveforms-and-neuronal-network-bursts).

2. Materials and methods

In this paper we demonstrate our proposed joint analysis together with the conventional methods. The methods are organized in three sections: Section 2.1 Cell preparations and the pharmacological experiment; Section 2.2 MEA measurements; and Section 2.3 MEA measurement analysis, describing the spike count statistics, spike sorting, burst detection, the proposed joint analysis (Fig. 1) illustrated with simulated data, and mathematical considerations on the proposed joint analysis.

2.1. Cell preparations and the pharmacological experiment

2.1.1. Cell culturing

Human stem cells were used as the starting material for neuronal cultures (Lappalainen et al., 2010). University of Tampere has ethical approval from Pirkanmaa Hospital District to derivate, culture, and differentiate human embryonic stem cells (Skottman, R05116), and the permission from the National Authority for Medicolegal Affairs (1426/32/300/05) to conduct human stem cell research. After differentiation and subsequent plating on MEAs (Heikkilä et al., 2009), the cultures were grown on the MEAs for seven weeks. Each MEA well was considered as one cell culture.

2.1.2. Pharmacological experiment

The proposed method is demonstrated by analyzing MEA data measured from 12 neuronal cell cultures which were pharmacologically manipulated for different effects on neuronal networks. The pharmacological experiment consisted of the following phases

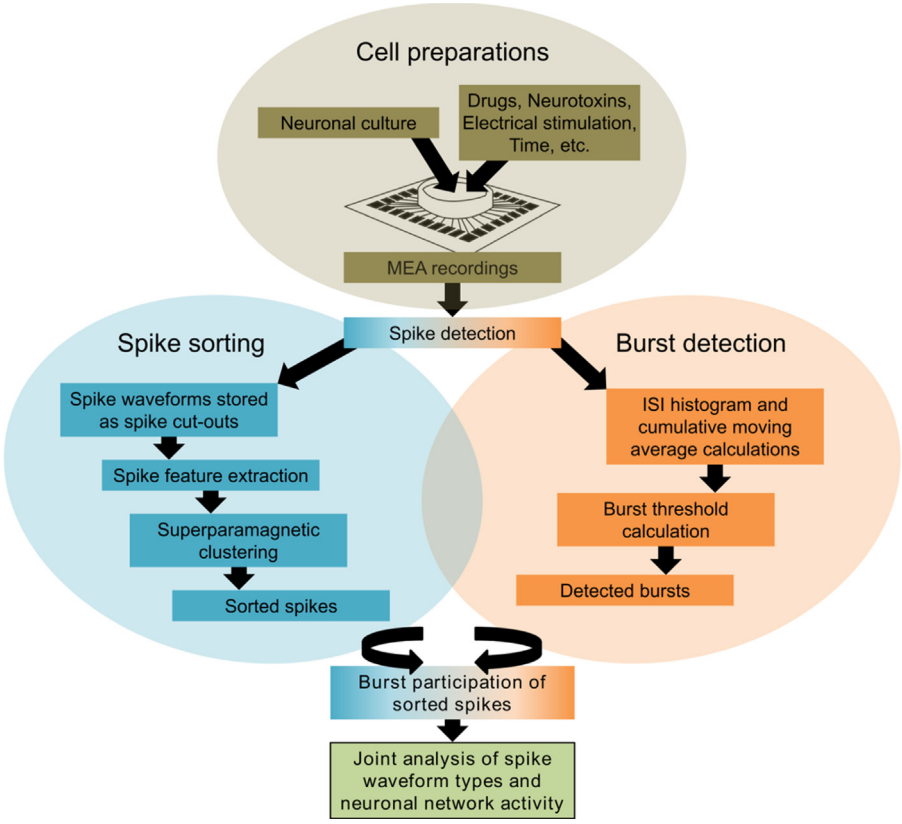

Fig. 1. A schematic presentation of the proposed joint analysis. The proposed framework consists of spike sorting and burst detection, followed by the analysis of the participation of the spikes of different types observed in bursts. Here, the spike sorting by Quiroga et al. (2004) and burst detection by Kapucu et al. (2012) were employed.

with MEA data acquired at each phase immediately after pharmacological manipulation or wash, and before any manipulations:

(i) Baseline.
(ii) 1st wash with fresh medium, to observe the effects of immediate medium change.
(iii) CNQX (20 μmol, AMPA/kainate receptor antagonist 6-cyano-7-nitroquinoxaline-2,3-dione, Abcam), to block AMPA/kainate mediated signaling.
(iv) CNQX (20 μmol, Abcam) + D-AP5 (30 μmol, D(-)-2-amino-5-phosphonopentanoic acid, Abcam) AMPA/kainate and NMDA receptor antagonist, to block glutamatergic signaling.
(v) 2nd wash with fresh medium.
(vi) GABA (100 μmol, Sigma), to boost GABAergic signaling.
(vii) Bicuculline (30 μmol, $GABA_A$ antagonist bicuculline methiobromide, Sigma), to inhibit GABAergic signaling.

2.2. MEA measurements

MEA measurements were performed with the MEA wells sealed with semi-permeable membranes (ALA MEA-MEM, ALA Scientific Instruments, Westbury, NY, USA) or custom made PDMS blocks (Kreutzer et al., 2012). The signals from the MEAs were amplified with a preamplifier MEA1060-Inv-BC (Multi Channel Systems MCS GmbH, Reutlingen, Germany, MCS) and analog filtered and amplified with a filter amplifier FA60S-BC (MCS) (bandwidth: 1 Hz–8 kHz, total gain: 1100). The temperature was controlled with an external heater unit (TC02, MCS) set to +38 °C, and the cultures were allowed to settle for 1 min in the preamplifier before each 5-minute recording. Analog to digital conversion was performed at 20 kHz sampling frequency with MC_Card (MCS) in a PC computer, and the measurement was controlled via MC_Rack software (MCS). The digitized recordings were further processed with MC_Rack to obtain cleaner high frequency spike information using a 50 Hz notch filter to remove mains noise, and a second order Butterworth highpass filter with 200 Hz cutoff frequency to alleviate baseline fluctuations and low frequency local field potential effects. MCS MEA data was imported to Matlab (MathWorks, Inc., Natick, MA, USA) using Neuroshare library (Neuroshare Library, 2003) for offline analysis.

2.3. MEA measurement analysis

At each phase of the pharmacological experiment (see Section 2.1.2), one 300 s recording was made from each culture (MEA well). The numbers of independent cultures included in the analyses are given in Table S1 along with the inclusion/exclusion criteria for the different analyses.

2.3.1. Spike count statistics

Traditional spike count (the total numbers of spikes in one recording) was calculated for each recording. Only the MEA wells which exhibited sufficient action potential activity were included in burst detection: It was required that at least 50 spikes were detected from an electrode of a MEA well in any 300 s recording of the baseline or at one of the pharmacological experiment phases. (See Table S2 for the numbers of channels fulfilling this criterion in each well at each phase of the experiment.) The same criterion has been used previously in burst analysis for human embryonic stem cell derived neuronal networks (Kapucu et al., 2012).

To obtain descriptive statistics for the spike counts at the different phases of the experiment, and to compare them with the respective spike counts in the baseline recordings, data from all electrodes of each well was pooled and medians were calculated over the wells. The upper and lower quartiles were calculated along with the differences between the upper and lower quartiles, *i.e.*, the interquartile ranges (IQRs) containing 50% of the data. In the sequel,

IQRs are shown in all relevant figures displaying the results. All the spike count statistics calculations were performed in GraphPad Prism 6 (GraphPad Software, Inc., La Jolla, CA, USA).

2.3.2. Spike detection and sorting

Data analysis was performed on data from a single channel and on data pooled from all electrodes. For the single channel analysis, we selected a channel whose firing rate at baseline was the closest to the average firing rate over all channels at the baseline. The average firing rate for the selected channel at the baseline was approximately 1.61 spikes/s, whereas the average firing rate for all baseline recordings per channel was 1.58 spikes/s with the maximum firing rate 14.04 spikes/s.

For the pooled data analysis, spike sorting was performed per well for each phase of the pharmacological experiment. Spike sorting classifies spikes to classes corresponding to the neuronal action potential waveforms. First, spikes were detected by thresholding at five times the median of the baseline noise, and the spike time stamps and waveform cut-outs (spanning 1 ms prior and 2.2 ms after the maximum of the spike) were stored. The obtained spike waveform cut-outs were sorted using the Wave clus algorithm (Quiroga et al., 2004), which gave the average cluster waveforms and the associated lower and upper standard deviation waveforms. In Wave clus, the cluster size was initially set for the baseline according to the number of spikes to be sorted. All the detected spikes were included in the spike count and spike sorting analysis (the total of 172,750 spikes). Minimum cluster size for baseline recordings was five spikes for single electrode analysis (the total of 483 spikes were analyzed for the baseline) and 50 spikes for pooled data (the total of 51,230 spikes were analyzed for the baseline). However, the cluster sizes were altered for the different phases of the pharmacological experiment, since the activity and spike counts varied between the phases.

After automatic clustering, supervised tuning of the temperature was performed as suggested in the tutorial of Wave clus (Wave_clus., 2004), improving the spike sorting. Still, such spike sorting is less subjective than completely supervised spike sorting. Tuning the temperature was the only supervised correction performed. After unsupervised clustering, the temperature was tuned to observe if more clusters could be formed: If the average spike waveforms of the new clusters due to tuning could be considered as spike types different from those obtained without tuning, the new clusters were retained.

In this work, the effects of overlapping spikes are later discussed based on the analysis results. This matter has been wider addressed, *e.g.*, by Quiroga et al. (2004). Performances of spike sorting algorithms, including Wave clus, have been addressed by Wild et al. (2012), also providing references to methods aimed at solving the spike overlapping problem.

2.3.3. Spike type identification and labeling

To track the occurrence of the spikes types over the pharmacological experiment, it was necessary to identify the representative spike types, and label all the average waveforms observed at the different phases of the experiment with the spike types. This was done by selecting the representative average waveforms as spike types, as described below, and performing correlation analysis of the average waveforms and their respective standard deviation waveforms with those of the spike type waveforms. A simple operator-guided method was devised for the single electrode data analysis and a fully automated method for the full data analysis.

For the single electrode data analysis, the most prominent and distinguished average spike waveforms amongst all the average waveforms for the entire experiment were selected as the representative spike types by visual assessment. Thereafter, cross correlations between each of the remaining average waveforms with all the spike type waveforms were calculated, and the waveforms were tentatively labeled with spike types according to the highest cross correlations. Thus, each cluster produced by Wave clus was assigned a tentative spike label. To take into account the waveform variability, analogous cross correlation analysis was also performed between the standard deviation waveforms: To confirm the tentative spike type labeling, the highest cross correlations had to be found between the standard deviation waveforms of the tentatively labeled cluster and the corresponding standard deviation waveforms of its tentative spike type. Otherwise, the average waveform was considered to represent a new spike type.

For the full data analysis, an automated version of the above cross correlation analysis was devised: Instead of visual identification of the spike types, the average waveforms given by Wave clus for the baseline measurements were used as the spike types. Thereafter, the cross correlation analysis to label the average waveforms with spike types, and the adoption of new spikes types was performed alike described for the single electrode data analysis.

2.3.4. Burst detection

To analyze network activity, an adaptive burst detection algorithm, the cumulative moving average algorithm (CMA; Kapucu et al., 2012), was employed. CMA utilizes ISI statistics to objectively define and detect bursts. Here, CMA was employed with the same parameters as in (Kapucu et al., 2012). The exclusion/inclusion criterion was the same as for the spike count statistics (see Table S1).

2.3.5. The proposed joint analysis

In our proposed joint analysis (Fig. 1), first, spikes are detected and sorted. In parallel with spike sorting, burst detection is performed. After spike sorting and burst detection, every detected spike is labeled as either a burst spike or an individual spike, and carries a spike type label. Thus, the participation of different types of spikes in the network activity is unraveled. The wells which did not exhibit any bursting were excluded from the joint analysis of spike types and bursts (see Table S1).

Here, the joint analysis was implemented with the spike detection, spike sorting, and burst detection methods described earlier. To illustrate the proposed joint analysis, we simulated noisy single channel MEA data carrying spikes of three different waveforms (denoted as ASp 1, ASp 2, and ASp 3). The waveforms were modified from the data in the Wave clus distribution package (Wave_clus., 2004). The ISIs were set to at least 30 ms for the spikes in bursts and 300 ms for the individual spikes. Thus, no spike overlapping was introduced to concentrate on the joint analysis without having to consider the performances of spike detection and sorting for overlapping spikes. A 60 s simulation exhibited 10 bursts with seven ASp 1s and three ASp 2s in each burst. Four spikes (one ASp 1, one ASp 2 and two ASp 3s) were placed between all bursts. Background noise added to the formed spike signal was a random signal with uniformly distributed values between −3 mV and 3 mV. The spike waveforms are shown in Fig. 2A, and a section of the simulated signal in Fig. 2C. From the simulated signal, spikes were detected and sorted, and burst and joint analysis were performed to illustrate the methodology.

In the results of this illustrative toy analysis, three average spike waveforms (Fig. 2A), *i.e.*, the spike types, appeared as expected and were sorted with 100% accuracy. The burst detection result (Fig. 2B) shows that all the bursts were correctly detected. An exemplary burst shown in Fig. 2C illustrates the outcome of the proposed analysis framework: **the spike type composition of the burst**. The burst shown in Fig. 2C was composed of the spikes of types ASp 1 and ASp 2 as expected, with one individual ASp 3 types spike observed before the burst. The obtained numbers of spikes of different types in bursts and outside of the bursts are presented in Fig. 2D, from which it is seen that all the bursts were composed

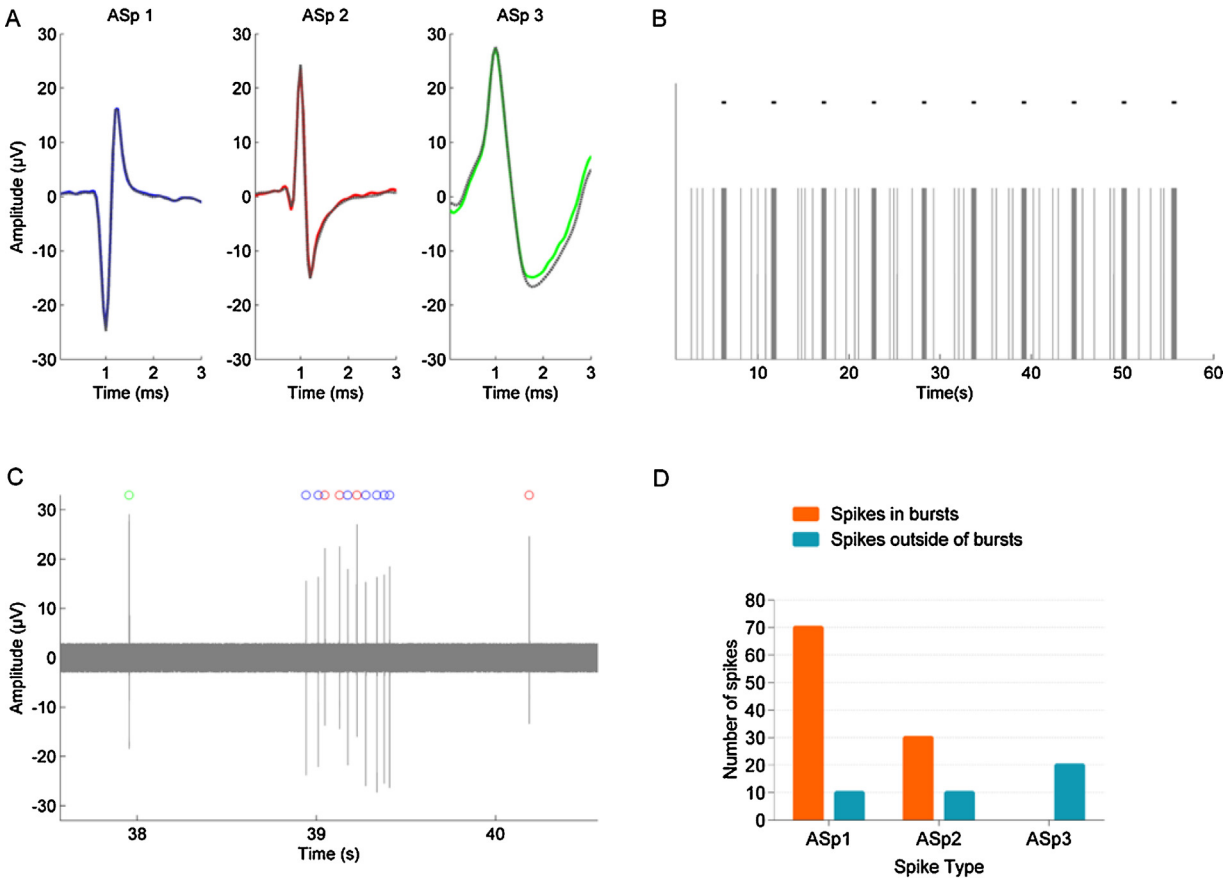

Fig. 2. Simulated toy data and its illustrative joint analysis results. (A) The simulated spike waveforms **ASp 1 (blue)**, **ASp 2 (red)**, and **ASp 3 (green)**, along with the corresponding average waveforms (grey dotted curves) calculated based on the detected and sorted noisy spikes. (B) The time points of the detected spikes (grey vertical bars), and the detected bursts (black horizontal lines). (C) A section of the simulated signal with sorted spikes indicated by circles with the colors indicating the particular waveforms as shown in (A). (D) The results of the joint analysis showing the counts of the different types of spikes participating in the bursts, along with those occurring outside of the bursts. (For interpretation of the references to color in this figure legend, the reader is referred to the web version of this article.)

solely of the spikes of types ASp 1 and ASp 2, whereas spikes of all spike types appeared as individual spikes outside of the bursts, which was 100% in accordance with the simulation setup.

2.3.6. *Mathematical considerations regarding the proposed joint analysis*

To formulate a mathematical expression of the spike compositions of the bursts in a measurement, a measured signal during a burst with the different identified spike type waveforms can be expressed as

$$s_t(t) = \sum_{j=1}^{J_i} W_{swt_{i,j},t^o_{i,j}}(t) + n_i(t)$$

where, $s_i(t)$ is the measured signal sample at discrete time t during the ith burst; J_i is the number of the detected spikes in the ith burst; and $W_{swt_{i,j},t^o_{i,t}}(t)$ is the sample of a spike waveform signal (of the length of the ith burst in samples) which is zero except for the period $t^o_{i,t} \le t \le t^o_{i,t} + L - 1$ during which the L samples long swtth type spike waveform occurs ($swt_{i,j}$ denotes that the type of the jth spike of the ith burst is swt). $n_i(t)$ is the corresponding measured background noise sample accounting for all other signal components except for the identified spike type waveforms. This formulation effectively dissects the bursts in to their constituent spike types. The spike type compositions of the bursts in an entire measured signal is then given by all the pairs $\{swt_{i,t}, t^o_{i,t}\}$.

The information gain due to the proposed joint analysis compared to merely detecting the burst spikes corresponds to that of observing a string of letters formed from the alphabet of the size equal to the number of the spike types plus one (each letter corresponding to a spike type and a symbol '0' to denote 'no waveform') *vs.* a binary string ('1' corresponding to a detected spike). For example, with three detected spike waveform types denoted A, B, and C, the information gain would result from observing a burst as a string, for example, like '00A0B0000A0CC' (for illustrative purposes, only a few 0s are shown), as compared to observing the same burst with mere spike detection as '0010100001011. Here, possible spike overlapping has not been considered. For the binary alphabet with equal symbol probabilities, the information content is $\log_2(2) = 1$ bit per symbol, whereas an alphabet of size four with equal symbol probabilities results in the information content of $\log_2(4) = 2$ bits per symbol (Shannon, 1948). Naturally the same amount of information per spike waveform is provided by spike sorting alone, but with the proposed joint analysis, this information is extracted specifically for each burst. For a real MEA measurement, the probability of an occurrence of the 'no waveform' symbol is much larger than that of a symbol denoting a spike; thus, the information contents of the spike symbols are larger than in the example, but the principal difference between the two approaches remains. Thereafter, the information gain achievable by the analyzes of the spike type waveforms themselves, their changes, and their occurrences in time, compared to the analysis of mere time stamps of the burst spikes, depends on the following neurobiological analysis,

and the associated information gain is not simply formally quantifiable.

3. Results

To demonstrate the proposed method and the obtainable results, we first present the analysis results for a signal measured via one electrode (Figs. 3 and 4); this example illustrates from phase to phase of the pharmacological experiment, what happened in a vicinity of one electrode, *i.e.*, in a local part of the neuronal network seen via one electrode. Next, we present the analysis results for the entire data set at every phase of the pharmacological experiment. See Table S1 for the number of the cultures at each phase.

3.1. Results of single channel pharmacological experiment data analysis

In the analysis of single electrode data, spike sorting resulted in four different spike types (Fig. 3): one negative and one positive monophasic spike waveform (Spike-I, Fig. 3A, and Spike-II, Fig. 3B), and two biphasic spike waveforms (Spike-III, Fig. 3C, and Spike-IV, Fig. 3D).

Spike counts are shown in Fig. 4A: the total number of spikes detected decreased with the 1st wash compared to the baseline, and also with the application of CNQX. Application of CNQX + D-AP5 increased the number of spikes from that observed with CNQX alone. In the subsequent phases of the pharmacological experiment, the number of spikes did not change much. On the other hand, observing the numbers of spikes of particular types (Fig. 4B), and the changes in the numbers of spikes of different types relative to the baseline (Fig. 4C), different phenomena can be observed: In the baseline, most of the spikes were of the type Spike-I, which decreased in numbers at the 1st wash and further due to CNQX (Fig. 4B). The number of Spike-II type spikes exhibited a roughly similar trend (Fig. 4B). At the 2nd wash (Fig. 4B) and thereafter, spikes of types Spike-III and Spike-IV were the most prominent. In summary, with the near extinction of spikes of types Spike-I and Spike-II, spikes of types Spike-III and Spike-IV appeared (Fig. 4B). Observing the numbers of spikes of the different types relative to the baseline (Fig. 4C), it is seen that as the pharmacological experiment progressed, the number spike of type Spike-III went through great changes. Since Spike-IV did not appear at baseline, its results cannot be shown relative to the baseline in Fig. 4C. It is clear that the information gained from the analysis of spike statistics for the different spike types (Fig. 4B and C) cannot be obtained from the mere total numbers of spikes (Fig. 4A).

Traditional burst analysis results presented as the relative number of bursts, relative average burst duration, and relative average numbers of spikes in a burst, all compared to their respective baselines, are shown in Fig. 4D–F, respectively. For example: The 1st wash greatly increased the number of bursts, duration, and the number of spikes in a burst (Fig. 4D–F, respectively). CNQX, compared to the previous experiment phase, decreased the relative number of bursts (Fig. 4D), but did not change the burst duration (Fig. 4E), and brought the number of spikes in a burst close to that at the baseline (Fig. 4F). The 2nd wash nearly extinguished bursting activity, whereas the subsequent application of GABA restored approximately half of the number of bursts compared to the baseline (Fig. 4D), and had a tremendous increasing effect on both the burst duration (Fig. 4E) and the number of spikes in a burst (Fig. 4F). Regarding the extreme increase in burst duration for GABA in Fig. 4E, the average burst duration at the baseline was 0.1 s, whereas after GABA application it was 67.3 s, resulting in the shown 67,300% increase in the average duration.

The results of the joint analysis of spike types and bursts are presented in Fig. 4G and H. For clarification, the results in Fig. 4G are presented in Fig. S1A in percentages relative to the total numbers of spikes. To compare the burst spike types and individual spike types for completeness, the different spike types seen in individual spikes are shown in Fig. S2A. To demonstrate the proposed joint analysis, for example, in the baseline the bursts were composed merely of spikes of types Spike-I and II (Fig. 4G), whereas later in the experiment, under CNQX + D-AP5, the bursts were composed far mostly of the spikes of type Spike-II, and the 2nd wash nearly abolished bursting (Fig. 4G and H). However, the picture is totally changed by the application GABA: Under the influence of GABA

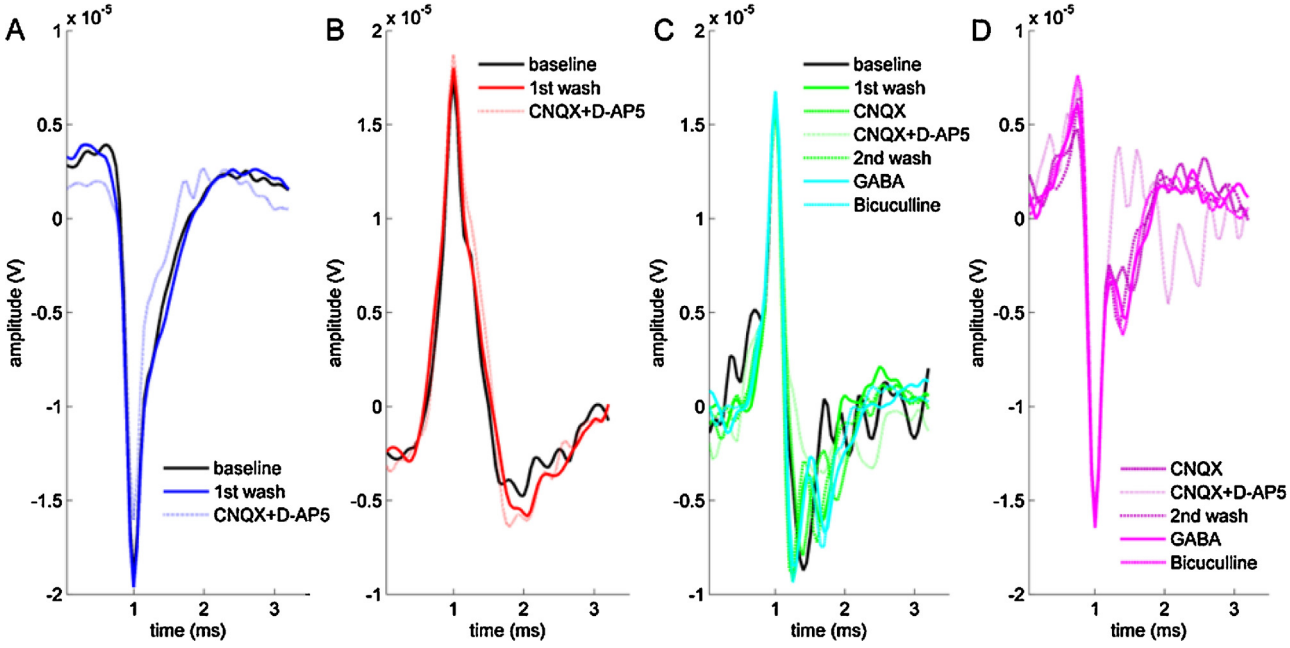

Fig. 3. The average spike waveforms observed in one channel in the pharmacological experiment, shown for the phases of the pharmacological experiment at which the particular waveforms were observed (see the legend in each panel). The spike types: (A) Spike-I (blue), (B) Spike-II (red), (C) Spike-III (green), and (D) Spike-IV (purple). (For interpretation of the references to color in this figure legend, the reader is referred to the web version of this article.)

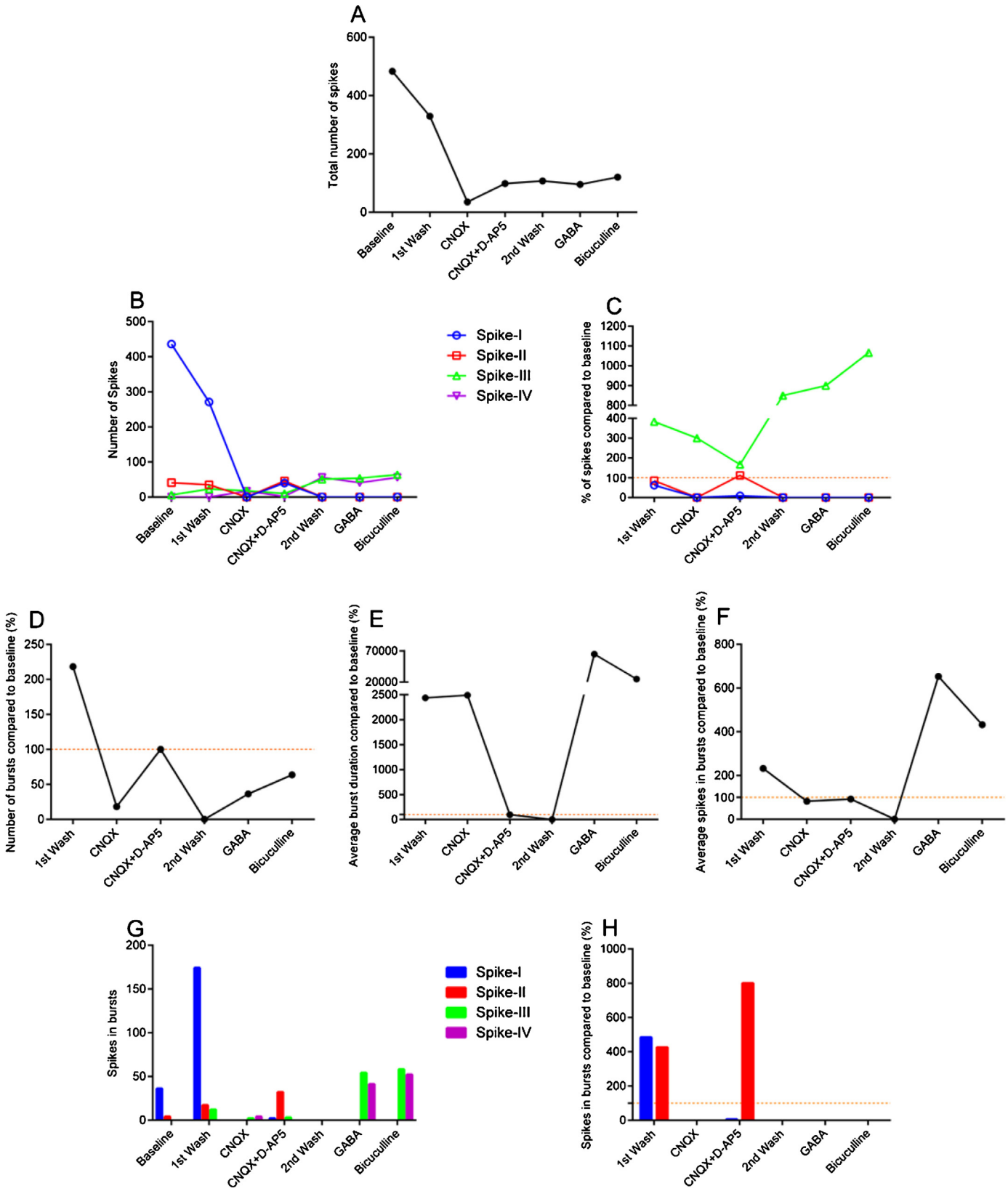

Fig. 4. The results of the traditional spike and burst analysis (A–F) and the joint analysis (G and H) at all the phases of the pharmacological experiment for one MEA channel. (A) The total number of spikes. (B) and (C) The numbers of the different types of spikes, and their relative amounts, respectively. (D) The relative numbers of bursts. (E) The relative average durations of bursts. (F) The relative average numbers of spikes in a burst. (G) The numbers of spikes of each type in bursts. (H) The relative numbers of spikes of each type in bursts. The relative quantities are with respect the corresponding values at the respective baselines. The spike types: Spike-I (blue), Spike-II (red), Spike-III (green), and Spike-IV (purple). (For interpretation of the references to color in this figure legend, the reader is referred to the web version of this article.)

and thereafter of GABA and bicuculline, the bursts were composed merely of the spikes of types Spike-III and Spike-IV. Thus, the joint analysis of spike types and bursts (Fig. 4G and H) provided more information on the network effects of pharmacological than the traditional burst analysis alone (Fig. 4D–F).

Alike with the spike counts (Fig. 4B and C), also here observing the numbers of spikes in burst (Fig. 4G) and the same relative to the baseline (Fig. 4H), different views to the phenomena are obtained. For example, the increase in the number of Spike-I type spikes after the 1st wash was far greater than that of Spike-II type spikes, but the increase in percentages (Fig. 4H) is roughly equal.

To explicitly point out new information given by the proposed joint analysis, for example, in Fig. 4B it is seen that after the 1st wash, there was a notable decrease in the occurrence of Spike-I type spikes and a slight decrease in the number of Spike-II type spikes, whereas in Fig. 4D it is seen that simultaneously the number of bursts more than doubled compared to baseline. For this experiment phase, the joint analysis results in Fig. 4G show a notable increase in the burst participation of Spike-I type spikes and slight increase in the burst participation of Spike-II type spikes. This is also reflected in the percentual amounts of the spikes of these types appearing in bursts compared to the total spike counts (Fig. S1A), whereas individual spikes (Fig. S2A) of both types decreased. This information on the changes in the burst participation of the different types of spikes cannot be obtained by the traditional analysis results in Fig. 4B and D.

Also, new information provided by the joint analysis can be demonstrated by observing the activity in Fig. 4B after the CNQX + D-AP5 application when the number of Spike-II type spikes recovered to the approximately same level as it was at the baseline. Spike-I type spikes also recovered approximately to the same level as Spike-II type spikes, however remaining still greatly fewer than at the baseline. At this point of the experiment, the number of bursts, average burst durations, and the average numbers of spikes in bursts were close to what they had been at the baseline (Fig. 4D–F, respectively). The joint analysis results in Fig. 4G show that at this time, the bursts were mostly composed of Spike-II type spikes, whereas at the baseline, the burst spikes had been mainly Spike-I type spikes. In conclusion, although the traditional burst characteristics (Fig. 4D–F) were approximately equal at base line and after the CNQX + D-AP5 application, the joint analysis revealed that the main burst spike type was different between these two experiment phases. This information on the burst composition change cannot be obtained from results of the traditional analyses in Fig. 4B and D, but only with the proposed joint analysis.

3.2. Results of full pharmacological experiment data analysis

In the analysis of the full data set, data from all the MEAs and MEA wells was pooled (see Table S1), and analyzed for each phase of the pharmacological experiment. The average spike waveforms (Fig. 5) obtained from the pooled data exhibited naturally more variation than the spike waveforms obtained from the signal measured via one electrode (Fig. 3). It is to be noted that the variability in the data was quite large, as seen from the IQRs in Fig. 6; therefore we chose not to draw biological conclusions. Nevertheless, the results clearly demonstrate the usability of the proposed joint analysis. In the analysis results in Fig. 6, the quantities shown are the medians over the analyzed wells with the whiskers covering the 50% IQRs. For burst durations (Fig. 6E) and the number of spikes in a burst (Fig. 6F), shown are the medians of the per-well averages (See the numbers of the analyzed wells in Table S1).

Spike sorting analysis of the pooled data resulted in five different spike types (Spike-I, Spike-II, Spike-III, Spike-IV, and Spike-V, seen in Fig. 5A–E, respectively). In Fig. 5, the average waveforms for each spike type are shown for the phases of the pharmacological experiment at which they were observable.

For this data, two monophasic (one negative (Spike-I, Fig. 5A), and one positive (Spike-II, Fig. 5B)) and two biphasic spike waveforms were obtained (Spike-III, Fig. 5C, and Spike-IV, Fig. 5D), but not all of them were observed at all phases of the pharmacological experiment. Also obtained was Spike-V (Fig. 5E), which appeared only at the 1st wash and under the influence of CNQX + D-AP5. Spike-V was composed of greatly varying individual spike waveforms which could not be clustered together.

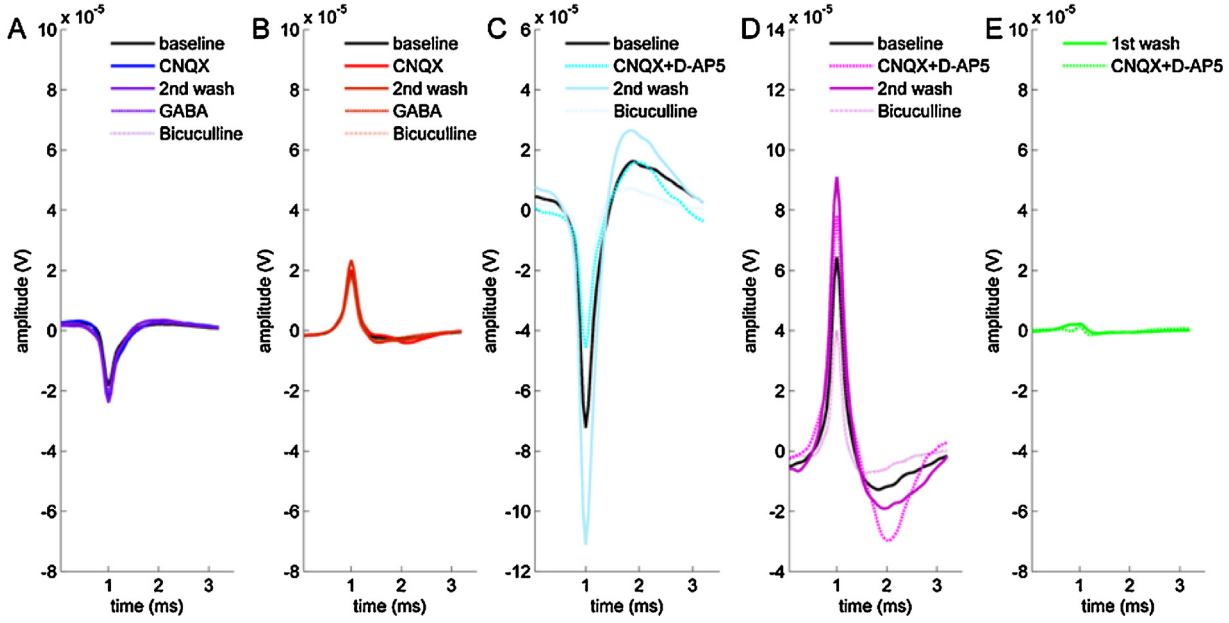

Fig. 5. The average spike waveforms observed in the entire pharmacological experiment data set, shown for the phases of the pharmacological experiment at which the particular waveforms were observed (see the legend in each panel). The spike types: (A) Spike-I (blue), (B) Spike-II (red), (C) Spike-III (cyan), (D) Spike-IV (purple), and (C) Spike-V (green). (For interpretation of the references to color in this figure legend, the reader is referred to the web version of this article.)

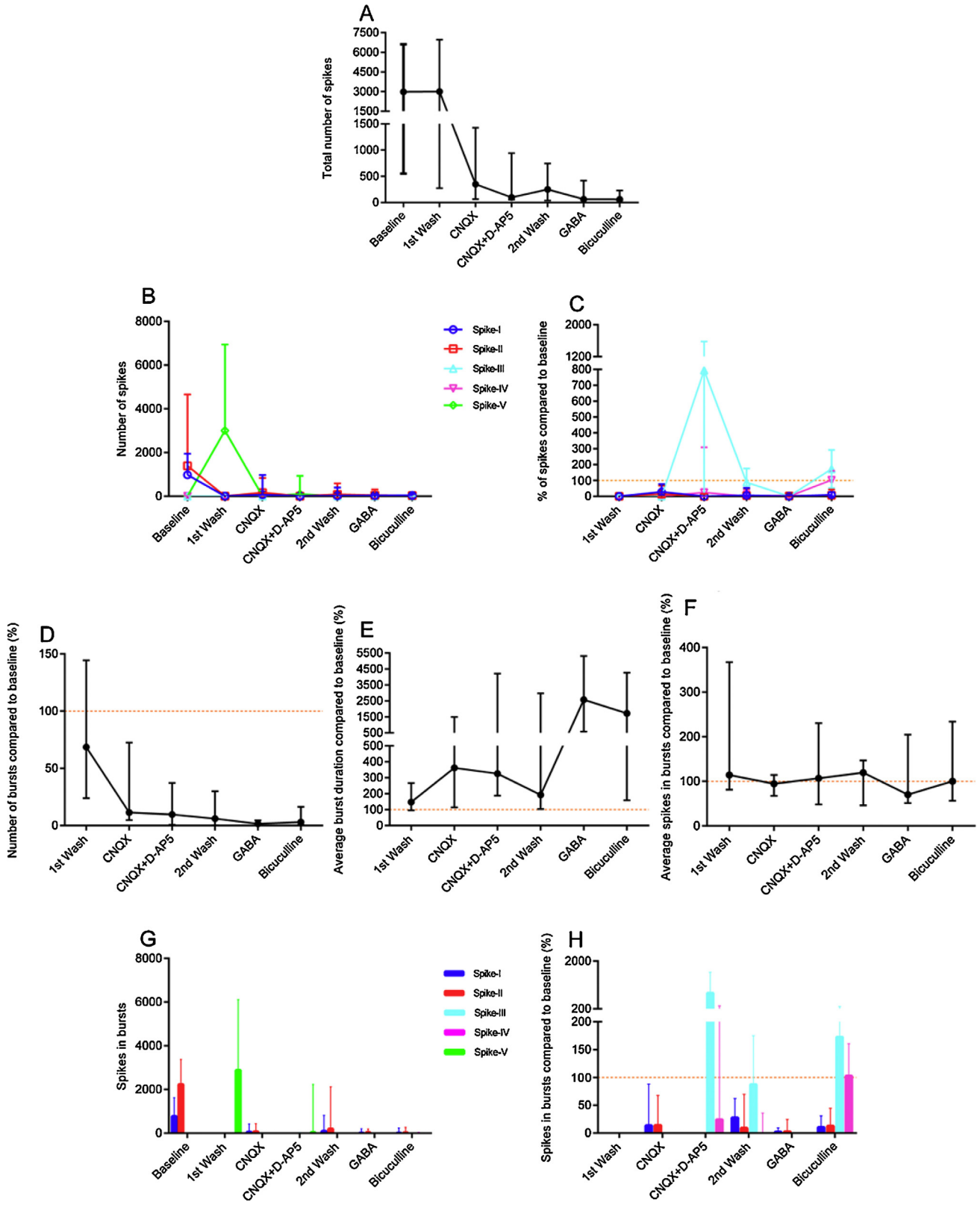

Fig. 6. The results of the traditional spike and burst analysis (A–F) and the joint analysis (G and H) at all the phases of the pharmacological experiment for the entire data set. (A) The total number of spikes. (B) and (C) The numbers of the different types of spikes, and their relative amounts, respectively. (D) The relative numbers of bursts. (E) The relative average durations of bursts. (F) The relative average numbers of spikes in a burst. (G) The numbers of spikes of each type in bursts. (H) The relative numbers of spikes of each type in bursts. The quantities shown are the medians over the number of analyzed wells (see Table S1) with the whiskers covering the 50% IQRs. The relative quantities are with respect the corresponding values at the respective baselines. The spike types: Spike-I (blue), Spike-II (red), Spike-III (cyan), Spike-IV (purple), and Spike-V (green). (For interpretation of the references to color in this figure legend, the reader is referred to the web version of this article.)

In the spike count analysis (Fig. 6A), variability in the total number of spikes was high at the baseline and 1st wash. At the CNQX application, the median of the total number of spikes decreased drastically and remained low compared to the baseline through the rest of the pharmacological experiment. Alike for the single channel data, more information can be obtained by observing the numbers of spikes of different types (Fig. 6B and C). At baseline, Spike-I and II were observed in higher numbers than the other types of spikes. The 1st wash changed the situation drastically, making the Spike-V the most prominent; let us recall that Spike-V was composed of greatly varying spike waveforms which could not be clustered, *i.e.*, the 1st wash greatly disturbed the spike waveforms. Also, Spike-V did not appear at the baseline, and is thus not shown in Fig. 6C and H. CNQX caused some spikes of types Spike-I and II to reappear, whereas CNQX + D-AP5 caused an uprising of Spike-III type spikes (Fig. 6C), which dominated also at the 2nd wash and at the application of bicuculline. GABA nearly shut down spiking (Fig. 6C). Naturally, the spike-type specific phenomena (Fig. 6B and C) cannot be observed from the mere total number of spikes (Fig. 6A).

Traditional burst analysis results presented as the relative number of bursts, relative median of the well-wise average burst durations, and the relative median of the well-wise average number of spikes in a burst, all compared to their respective baselines, are shown in Fig. 6D–F. The relative number of bursts decreased through the pharmacological experiment (Fig. 6D). Burst duration (Fig. 6E) increased slightly at the 1st wash, and more prominently under the influence of CNQX, whereas the 2nd wash decreased the burst duration. GABA caused a large increase in the burst duration (Fig. 6E), to which bicuculline had little effect. Interestingly, the fraction of the total number of spikes appearing in burst remained approximately constant through the experiment (Fig. 6F).

The proposed joint analysis results (Fig. 6G) reveal that at the baseline, the bursts were composed almost completely composed of the spikes of types Spike-I and II, *i.e.*, the monophasic negative (Fig. 5A) and positive (Fig. 5B) spikes, respectively. (For clarification, the results in Fig. 6G are presented in Fig. S1B as the relative numbers of the burst spikes with respect to the total numbers of spikes in percentages. To compare the burst spike types and individual spike types for completeness, the different spike types seen in individual spikes are shown in Fig. S2B.) This means that the networks were operating with the spikes of types Spike-I and II. The 1st wash caused the burst to be composed of almost entirely of Spike-V type spikes (Fig. 6G) which did not represent a well-defined waveform (Fig. 5E). CNQX partially recovered Spike-I and II type spikes also in bursts, whereas CNQX + D-AP5 again removed them from bursts (Fig. 6G and H). The 2nd wash brought the spikes of types Spike-I and II partially back to the bursts, which were now composed of spikes of types Spike-I, II, III, and IV. Under the influence of GABA, there were almost no spikes in bursts (Fig. 6G and H), as there were almost no bursts (Fig. 6D). Nevertheless, the few remaining bursts had approximately the same number of spikes in a burst as at the baseline (Fig. 6F). Bicuculline caused the bursts to be composed mainly of the spikes of types Spike-I and II (Fig. 6G) with a few Spike-III and IV type spikes also present in the bursts (Fig. 6H).

Again, observing the results as counts (Fig. 6B and G) and in percentages (Fig. 6C and H) provided clearly different and complimentary views to the results. Although in this pooled data experiment the spike type change trends (Fig. 6G and H) in the joint analysis in general followed those observed in the traditional analyses (Fig. 6B and C), the proposed joint analysis of spikes and bursts nevertheless provided the actual data on the spike type compositions of the bursts, which was naturally not obtainable by the means of the traditional analyses.

4. Discussion and conclusions

In this paper, we have proposed a novel analysis method for the joint analysis of action potentials and network events observed in local field potential measurements. The main usage of the proposed method is to test a hypothesis that spike types in bursts and spikes in general have different dynamics, *e.g.*, in response to external effects. We have demonstrated that this hypothesis is worth testing, and that the tool developed will provide deeper information on the activity of neuronal networks and their alterations. The essence of the proposed joint analysis was illustrated by a simulation (Fig. 2C), in which a spike type composition of a burst was seen for the first time. The value of the method was demonstrated by analyzing the MEA measurements from a pharmacological experiment with several different chemical applications; the effects of the pharmacological agents were observed with both traditional spike and burst analysis, and with the proposed joint analysis of spikes and bursts, where we demonstrated that the proposed joint analysis reveals information on the network activity which is not obtainable by the traditional analyses, *i.e.*, **the burst participation of the different types of spikes,** and the changes of this by chemical modification of the neuronal activity.

In the analysis of the pooled data, the overall results were calculated in each phase of the pharmacological experiment per well and not per electrode. With this approach, we aimed to study the general behavior of the networks in the different experimental phases. We are confident that regardless of the variability in our data (Heikkilä et al., 2009; Kapucu et al., 2012), the function of the proposed method was described, and the new information obtainable by the method demonstrated. We observed that indeed there are different dynamics of spike waveform types contributing to the bursts and spikes in general.

To investigate the stability of the signals, especially motivated by the large deviation seen in Spike-V, we took a look at the stability of the spike waveforms during the 300-second measurement after the 1st wash when the Spike-V appeared (Fig. 6B and G). We analyzed each disjoint 100-second section separately. Especially the first and third 100-second sections of the recording had similar clustering results as the complete recording, exhibiting a cluster of highly varying spike waveforms. However, spike waveforms in the second 100-second section were different. This demonstrates that the network function was changing during the recording. In general, one possible disturbing effect may have been the relatively short 1-minute stabilizing period before the measurement after the MEAs were placed in the measurement device. However, due to the described observed behavior during the 100-second sections, we can assume that a longer stabilizing period would not have resulted in more stable networks.

Another issue is the effect of overlapping spikes. Especially for bursting action potentials, spike sorting has been always challenging (Lewicki, 1998; Quiroga et al., 2004; Wild et al., 2012). In our work, especially for the pooled data, spike sorting represents average waveform types obtained from large datasets. Waveform distortions caused by overlapping spikes can be expected to be seen as average and standard deviation waveforms which greatly differ from the general spike average and standard deviation waveforms. Here, highly distorted spikes which could not be assigned to any cluster during spike sorting, accounted for approximately 3.7% of all the analyzed spikes (3.36% for the burst spikes and 0.34% for the individual spikes). Additionally, average and standard deviation waveforms of the obtained spike types were consistent over the different phases of the experiment for both burst and individual spikes. In conclusion, even though the effects of overlapping could be seen in our analysis, they are not expected to change our results or conclusions.

Using the proposed method, here, we show that the burst spike types and the spikes in general may have different dynamics. By assessing the results both as percentual changes with respect to the baseline activity for each spike type, and as changes in the actual burst spike counts, different views were gained to the changes in the network activity. In the literature, either absolute counts, such as spike and burst counts (Gopal, 2003; Brewer et al., 2009; Hogberg et al., 2011) or changes of percentual values (Gramowski et al., 2000; Ylä-Outinen et al., 2010) are given. Keefer et al. (2001) and Johnstone et al. (2010) provided the results partially in both forms. However, simultaneous analysis of both quantities has not been common practice, and not utilized in drawing comparative conclusions. Here, we demonstrated the usefulness of utilizing both approaches simultaneously in the joint analysis.

The polarity of the measured waveforms has been described to depend on the location of the neuron relative to the electrode (Henze et al., 2000; Gold et al., 2006). Thus, the observed changes in the spike waveforms and the spike type compositions of the bursts may have resulted from chemical induced functional changes in the cells or networks, morphological effects on the cells, different cell compartments contributing to the measurements, or from any combination of these. Nevertheless, we conclude that the observable effects are not random, but consistent manifestations of the changes in the networks. In long-term experiments, cell movement may also affect spike waveforms, which should naturally be evident also in the controls. Here, the experiment was acute, spike sorting was equally successful in all phases of the pharmacological experiment, and the spike type formation and assignment worked consistently; thus, the observed changes in spike waveforms due to the pharmacological applications did not interfere with spike sorting. It is also to be noted that the number of spikes available for the analysis may also affect the spike sorting results. Here, spike sorting worked consistently.

The pharmacological effects observed in the joint analysis are clear and interesting. Joint analysis results do provide more information on the network changes. Unraveling the actual reasons for, and the consequences of the observed spike type compositions of the bursts, and their changes due to pharmacological and other treatments, call for detailed studies with in-depth neuronal network analysis providing information on the sources of spikes, including information on active neuronal types and cell compartments. This is naturally called for in any spike sorting based analysis.

4.1. Further applicability

Here, the spike sorting by Quiroga et al. (2004) and burst detection by Kapucu et al. (2012) were employed. However, the proposed joint analysis framework (Fig. 1) can be implemented with any spike sorting and burst detection algorithms appropriate for the measurement data at hand. This is important to facilitate both different analysis approaches, and the different characteristics of spikes and bursts in the *in vitro* networks derived from different species and origins; the differences in network behavior have substantial influence on the applicability of different spike sorting and burst detection methods, and also call for more objective and automated methods (Kapucu et al., 2012). For spike sorting, the advantages and drawbacks of supervised and unsupervised algorithms can be argued: An automatic classification can be corrected or optimized by the user with unsupervised approaches in a final classification step which makes the approach still supervised but less subjective and less time consuming (Martínez and Quiroga, 2013). Certainly it would be preferable to have an accurate and fully unsupervised algorithm, which still remains a largely open question (Martínez and Quiroga, 2013). The only assumptions imposed by the proposed joint analysis framework itself are that there are sortable action potential waveforms and detectable bursts present in the data.

To possibly alleviate the effects of high variability in the data, the single channel analysis used here merely to demonstrate the method, could also be employed in the analysis of the entire MEA by analyzing each channel separately. Thereafter, should the single channel analyzes produce mutually corroborative results, overall conclusions could be drawn. However, combining the single channel analyses results to an overall result would require the development of a separate statistically valid method. Straighter forward, the analysis of single channel data can be employed to reveal the spatial distributions of the different types of spikes composing the bursts. This analysis technique would be promising, *e.g.*, for tracking the spike waveforms and their network participations. Single electrode data analysis naturally considers the local network in the vicinity of the electrode, whereas the analysis pooled data provides a better view to the overall activity and allows statistical analysis, while possibly losing information on particular local network phenomena.

The proposed joint analysis can be performed on all detected spikes, or alternatively, separately on burst spikes and non-burst spikes. In applying the analysis on such different sets of spikes, one needs to consider the possibly different functions of spikes occurring in different circumstances, such as in bursts or individually (Valiante and Carlen, 2014). Here, our main aim was the analysis of bursts, which can be assumed to manifest actual network activity. Similarly, instead of bursts, spike trains can be analyzed with the proposed method providing the spike types and their changes in the spike trains. Naturally, the same can be done also with individual spikes, *i.e.*, for the spikes not in bursts or trains as demonstrated in Fig. S2. Thus, complementary information on the different processes in the networks can be obtained by the selection of the data to be analyzed. Given spike sorting and burst and/or train detection methods appropriate for the data at hand, the framework is applicable in the analysis of any electrophysiological data, not only in the analysis of *in vitro* measurements.

4.2. Conclusions

Currently, there is a great call for methods to analyze neuronal network function from *in vitro* MEA recordings in more detail, for example, for research on basic biological questions such as neuronal network development and learning, for the assessment of various culturing methods, and for drug research and neurotoxicology (Coecke and Price, 2007; LeFew et al., 2013). Here, we propose a new joint analysis method that provides the spike type compositions of the bursts. We showed that the spike type compositions of bursts may change subject to environmental effects. Specifically, based on the presented results, pharmacological substances may affect the spike type compositions of the bursts, which are not seen in traditional spike and burst analysis, including spike sorting as traditionally utilized. Thus, with our joint analysis, more detailed information on the network behavior and its changes can be obtained.

Acknowledgments

The work of F. E. Kapucu has been supported by the Finnish Cultural Foundation (the Central Fund and Pirkanmaa Regional Fund), by the Ella and Georg Ehrnrooth Foundation, by the Human Spare Parts Project funded by the Finnish Funding Agency for Technology and Innovation (Tekes), and by the 3DNeuroN project in the European Union's Seventh Framework Programme, Future and Emerging Technologies, grant agreement no. 296590. The works of M. E.-L. Mäkinen, L. Ylä-Outinen, and S. Narkilahti have been supported by the Human Spare Parts Project funded by the Finnish

Funding Agency for Technology and Innovation (Tekes). The work of J. M. A. Tanskanen has been supported by the 3DNeuroN project in the European Union's Seventh Framework Programme, Future and Emerging Technologies, grant agreement no. 296590.

Appendix A. Supplementary data

Supplementary data associated with this article can be found in the online version at http://dx.doi.org/10.1016/j.jneumeth.2015.11.022.

References

Alloisio S, Nobile M, Novellino A. Multiparametric characterisation of neuronal network activity for *in vitro* agrochemical neurotoxicity assessment. NeuroToxicology 2015;48:152–65, http://dx.doi.org/10.1016/j.neuro.2015.03.013.

Bal-Price AK, Suñol C, Weiss DG, van Vliet E, Westerink RHS, Costa LG. Application of *in vitro* neurotoxicity testing for regulatory purposes: symposium III summary and research needs. NeuroToxicology 2008;29(3):520–31, http://dx.doi.org/10.1016/j.neuro.2008.02.008.

Banerjee A, Ellender TJ. Oscillations in the developing cortex: a mechanism for establishing and synchronizing an early network? J Neurosci 2009;29(48):15029–30, http://dx.doi.org/10.1523/JNEUROSCI. 4567-09.2009.

Brewer GJ, Boehler MD, Ide AN, Wheeler BC. Chronic electrical stimulation of cultured hippocampal networks increases spontaneous spike rates. J Neurosci Methods 2009;184(1):104–9, http://dx.doi.org/10.1016/j.jneumeth.2009.07.031.

Bużańska L, Jurga M, Stachowiak EK, Stachowiak MK, Domańska-Janik K. Neural stem-like cell line derived from a nonhematopoietic population of human umbilical cord blood. Stem Cells Dev 2006;15(3):391–406, http://dx.doi.org/10.1089/scd.2006.15.391.

Bużańska L, Habich A, Jurga M, Sypecka J, Domańska-Janik K. Human cord blood-derived neural stem cell line—possible implementation in studying neurotoxicity. Toxicol *in vitro* 2005;19(7):991–9, http://dx.doi.org/10.1016/j.tiv.2005.06.036.

Buzsáki G. Large-scale recording of neuronal ensembles. Nat Neurosci 2004;7(5):446–51, http://dx.doi.org/10.1038/nn1233.

Chiappalone M, Novellino A, Vajda I, Vato A, Martinoia S, van Pelt J. Burst detection algorithms for the analysis of spatio-temporal patterns in cortical networks of neurons. Neurocomputing 2005;65–66:653–62, http://dx.doi.org/10.1016/j.neucom.2004.10.094.

Coecke S., Price A. Why *in vitro* neurotoxicity approaches are not formally validated and used for regulatory purposes: The way forward, ⟨http://www.alttox.org/ttrc/toxicity-tests/neurotoxicity/way-forward/coecke-price/⟩; 2007 [updated 06.12.07; cited 01.11.13].

Connors BW, Gutnick MJ, Prince DA. Electrophysiological properties of neocortical neurons *in vitro*. J Neurophysiol 1982;48(6):1302–20, http://jn.physiology.org/content/48/6/1302.

Crumiller M, Knight B, Yu Y, Kaplan E. Estimating the amount of information conveyed by a population of neurons. Front Neurosci 2011;5:90, http://dx.doi.org/10.3389/fnins.2011.00009.

Defranchi E, Novellino A, Whelan M, Vogel S, Ramirez T, van Ravenzwaay B, et al. Feasibility assessment of micro-electrode chip assay as a method of detecting neurotoxicity *in vitro*. Front Neuroeng 2011;4:6, http://dx.doi.org/10.3389/fneng.2011.00006.

Egert U, Schlosshauer B, Fennrich S, Nisch W, Fejtl M, Knott T, et al. A novel organotypic long-term culture of the rat hippocampus on substrate-integrated multielectrode arrays. Brain Res Protoc 1998;2(4):229–42, http://dx.doi.org/10.1016/S1385-299X(98)00013-0.

Gibson S, Jack WJ, Markovic D. Spike sorting: the first step in decoding the brain. IEEE Signal Process Mag 2012;29(1):124–43, http://dx.doi.org/10.1109/MSP.2011.941880.

Gold C, Henze DA, Koch C, Buzsáki G. On the origin of the extracellular action potential waveform: a modeling study. J Neurophysiol 2006;95:3113–28, http://dx.doi.org/10.1152/jn.00979.2005.

Gopal KV. Neurotoxic effects of mercury on auditory cortex networks growing on microelectrode arrays: a preliminary analysis. Neurotoxicol Teratol 2003;25(1):69–76, http://dx.doi.org/10.1016/S0892-0362(02)00321-5.

Gramowski A, Schiffmann D, Gross GW. Quantification of acute neurotoxic effects of trimethyltin using neuronal networks cultured on microelectrode arrays. NeuroToxicology 2000;21(3):331–42, http://europepmc.org/abstract/MED/10894123.

Gray CM, McCormick DA. Chattering cells: superficial pyramidal neurons contributing to the generation of synchronous oscillations in the visual cortex. Science 1996;274(5284):109–13, http://dx.doi.org/10.1126/science.274.5284.109.

Gross GW, Rhoades BK. The use of neuronal networks on multielectrode arrays as biosensors. Biosens Bioelectron 1995;10(6–7):553–67, http://dx.doi.org/10.1016/0956-5663(95)96931-N.

Gross GW, Rieske E, Kreutzberg GW, Meyer A. A new fixed-array multi-microelectrode system designed for long-term monitoring of extracellular single unit neuronal activity *in vitro*. Neurosci Lett 1977;6(2–3):101–5, http://dx.doi.org/10.1016/0304-3940(77)90003-9.

Harris KD, Hirase H, Leinekugel X, Henze DA, Buzsáki G. Temporal interaction between single spikes and complex spike bursts in hippocampal pyramidal cells. Neuron 2001;32(1):141–9, http://dx.doi.org/10.1016/S0896-6273(01)00447-0.

Heikkilä TJ, Ylä-Outinen L, Tanskanen JMA, Lappalainen RS, Skottman H, Suuronen R, et al. Human embryonic stem cell-derived neuronal cells form spontaneously active neuronal networks *in vitro*. Exp Neurol 2009;218(1):109–16, http://dx.doi.org/10.1016/j.expneurol.2009.04.011.

Henze DA, Borhegyi Z, Csicsvari J, Mamiya A, Harris KD, Buzsáki G. Intracellular features predicted by extracellular recordings in the hippocampus *in vivo*. J Neurophysiol 2000;84(1):390–400, http://jn.physiology.org/content/84/1/390.

Hogberg HT, Sobanski T, Novellino A, Whelan M, Weiss DG, Bal-Price AK. Application of micro-electrode arrays (MEAs) as an emerging technology for developmental neurotoxicity: evaluation of domoic acid-induced effects in primary cultures of rat cortical neurons. NeuroToxicology 2011;32(1):158–68, http://dx.doi.org/10.1016/j.neuro.2010.10.007.

Illes S, Jakab M, Beyer F, Gelfert R, Couillard-Despres S, Schnitzler A, et al. Intrinsically active and pacemaker neurons in pluripotent stem cell-derived neuronal populations. Stem Cell Rep 2014;2(3):323–36, http://dx.doi.org/10.1016/j.stemcr.2014.01.006.

Johnstone AFM, Gross GW, Weiss DG, Schroeder OH-U, Gramowski A, Shafer T. Microelectrode arrays: a physiologically based neurotoxicity testing platform for the 21st century. NeuroToxicology 2010;31(4):331–50, http://dx.doi.org/10.1016/j.neuro.2010.04.001.

Kandel ER, Spencer WA. Electrophysiology of hippocampal neurons. II. After-potentials and repetitive firing. J Neurophysiol 1961;24(3):243–59, http://jn.physiology.org/content/24/3/243.

Kapucu FE, Tanskanen JMA, Mikkonen JE, Ylä-Outinen L, Narkilahti S, Hyttinen JAK. Burst analysis tool for developing neuronal networks exhibiting highly varying action potential dynamics. Front Comput Neurosci 2012;6:38, http://dx.doi.org/10.3389/fncom.2012.00038.

Keefer EW, Norton SJ, Boyle NAJ, Talesa V, Gross GW. Acute toxicity screening of novel AChE inhibitors using neuronal networks on microelectrode arrays. NeuroToxicology 2001;22(1):3–12, http://dx.doi.org/10.1016/S0161-813X(00)00014-0.

Kreutzer J, Ylä-Outinen L, Kärnä P, Kaarela T, Mikkonen J, Skottman H, et al. Structured PDMS chambers for enhanced human neuronal cell activity on MEA platforms. J Bionic Eng 2012;9(1):1–10, http://dx.doi.org/10.1016/S1672-6529(11)60091-7.

Lappalainen RS, Salomäki M, Ylä-Outinen L, Heikkilä TJ, Hyttinen JAK, Pihlajamäki H, et al. Similarly derived and cultured hESC lines show variation in their developmental potential towards neuronal cells in long-term culture. Regen Med 2010;5(5):749–62, http://dx.doi.org/10.2217/rme.10.58.

LeFew WR, McConnell ER, Crooks JL, Shafer TJ. Evaluation of microelectrode array data using Bayesian modeling as an approach to screening and prioritization for neurotoxicity testing. NeuroToxicology 2013;36:34–41, http://dx.doi.org/10.1016/j.neuro.2013.02.006.

Lewicki MS. A review of methods for spike sorting: the detection and classification of neural action potentials. Netw: Comput Neural Syst 1998;9(4):R53–78, http://dx.doi.org/10.1088/0954-898X_9_4_001.

Martínez J, Quiroga RQ. Spike sorting. In: Quiroga RQ, Panzeri S, editors. Principles of neural coding. London, UK: CRC Press; London, UK; 2013. p. 61–74, http://dx.doi.org/10.1201/b14756-6.

Neuroshare Library, ⟨http://www.multichannelsystems.com/software/neuroshare-library⟩; [September 2003, accessed March 2015].

Novellino A, Scelfo B, Palosaari T, Price A, Sobanski T, Shafer TJ, et al. Development of micro-electrode array based tests for neurotoxicity: assessment of interlaboratory reproducibility with neuroactive chemicals. Front Neuroeng 2011;4:4, http://dx.doi.org/10.3389/fneng.2011.00004.

Pasquale V, Martinoia S, Chiappalone M. A self-adapting approach for the detection of bursts and network bursts in neuronal cultures. J Comput Neurosci 2010;29(1–2):219–29, http://dx.doi.org/10.1007/s10827-009-0175-1.

Pine J. Recording action potentials from cultured neurons with extracellular microcircuit electrodes. J Neurosci Methods 1980;2(1):19–31, http://dx.doi.org/10.1016/0165-0270(80)90042-4.

Quiroga RQ, Nadasdy Z, Ben-Shaul Y. Unsupervised spike detection and sorting with wavelets and superparamagnetic clustering. Neural Comput 2004;16(8):1661–87, http://dx.doi.org/10.1162/089976604774201631.

Santhanam G, Ryu SI, Yu BM, Afshar A, Shenoy KV. A high-performance brain-computer interface. Nature 2006;442(7099):195–8, http://dx.doi.org/10.1038/nature04968.

Shannon CE. A mathematical theory of communication. Bell Syst Tech J 1948;XXVII(3):379–423, http://dx.doi.org/10.1002/j. 1538-7305.1948.tb01338.x.

Sun JJ, Kilb W, Luhmann HJ. Self-organization of repetitive spike patterns in developing neuronal networks *in vitro*. Eur J Neurosci 2010;32(8):1289–99, http://dx.doi.org/10.1111/j. 1460-9568.2010.07383.x.

Thomas CA Jr, Springer PA, Loeb GE, Berwald-Netter Y, Okun LM. A miniature microelectrode array to monitor the bioelectric activity of cultured cells. Exp Cell Res 1972;74(1):61–6, http://dx.doi.org/10.1016/0014-4827(72)90481-8.

Truccolo W, Donoghue JA, Hochberg LR, Eskandar EN, Madsen JR, Anderson WS, et al. Single-neuron dynamics in human focal epilepsy. Nat Neurosci 2011;14(5):635–41, http://dx.doi.org/10.1038/nn.2782.

Turnbull L, Dian E, Gross G. The string method of burst identification in neuronal spike trains. J Neurosci Methods 2005;145(1–2):23–35, http://dx.doi.org/10.1016/j.jneumeth.2004.11.020.

Uchida T, Suzuki S, Hirano Y, Ito D, Nagayama M, Gohara K. Xenon-induced inhibition of synchronized bursts in a rat cortical neuronal network. Neuroscience 2012;214:149–58, http://dx.doi.org/10.1016/j.neuroscience.2012.03.063.

Uhlhaas PJ, Pipa G, Lima B, Melloni L, Neuenschwander S, Nikolić D, et al. Neural synchrony in cortical networks: history, concept and current status. Front Integr Neurosci 2009;3:17, http://dx.doi.org/10.3389/neuro.07.017.2009.

Valiante TA, Carlen PL. Electrophysiological mechanisms of network control: bursting in the brain—from cells to networks. In: Faingold C, Blumenfeld H, editors. Neuronal networks in brain function, CNS disorders, and therapeutics. London, UK: Academic Press; 2014. p. 121–33, http://dx.doi.org/10.1016/B978-0-12-415804-7. 00009-5.

Wagenaar DA, Pine J, Potter SM. An extremely rich repertoire of bursting patterns during the development of cortical cultures. BMC Neurosci 2006;7(7):11, http://dx.doi.org/10.1186/1471-2202-7-11.

Wave_clus. Unsupervised spike detection and sorting, ⟨http://www2.le.ac.uk/departments/engineering/research/bioengineering/neuroengineering-lab/spike-sorting⟩; 2004 [accessed 11.12.15].

Wild J, Prekopcsak Z, Sieger T, Novak D, Jech R. Performance comparison of extracellular spike sorting algorithms for single-channel recordings. J Neurosci Methods 2012;203(2):369–76, http://dx.doi.org/10.1016/j.jneumeth.2011.10.013.

Ylä-Outinen L, Heikkilä J, Skottman H, Suuronen R, Äänismaa R, Narkilahti S. Human cell-based micro electrode array platform for studying neurotoxicity. Front Neuroeng 2010;3:111, http://dx.doi.org/10.3389/fneng.2010.00111.

Joint analysis of extracellular spike waveforms and neuronal network bursts

Fikret Emre Kapucu, Meeri E.-L. Mäkinen, Jarno M. A. Tanskanen, Laura Ylä-Outinen, Susanna Narkilahti, Jari A. K. Hyttinen

Journal of Neuroscience Methods

Supplementary Material

Table S1

The experiment and analysis structure. The MEAs, MEA wells, and the numbers of wells (i.e., the numbers of separate cultures, *n*) included in each test and analysis, along with the well inclusion criteria. The individual MEAs are identified by numbers. On each MEA chip, there were six wells with nine microelectrodes in each well.

Analysis method	Test	MEAs and MEA wells included in the analysis	Number of wells (*n*)	Well inclusion criteria
Spike Sorting Based Analysis	Baseline	MEA 1, all wells MEA 2, all wells	12	All wells (no exclusion criteria)
	1st Wash	MEA 1, all wells MEA 2, all wells	12	
	CNQX	MEA 1, all wells MEA 2, all wells	12	
	CNQX+D-AP5	MEA 1, all wells MEA 2, all wells	12	
	2nd Wash	MEA 1, all wells MEA 2, all wells	12	
	GABA	MEA 1, all wells MEA 2, all wells	12	
	Bicuculline	MEA 1, all wells MEA 2, all wells	12	
Spike Activity Analysis and Burst Detection	Baseline	MEA 1, wells A, B, C, D, F MEA 2, wells A, B, C, E, F	10	Minimum of 50 spikes detected in a 300 s recording from an electrode of a well in at least one phase of the experiment (Kapucu et al., 2012)
	1st Wash	MEA 1, wells A, B, C, D, F MEA 2, wells A, B, C, E, F	10	
	CNQX	MEA 1, wells A, B, C, D, F MEA 2, wells A, B, C, E, F	10	
	CNQX+D-AP5	MEA 1, wells A, B, C, D, F MEA 2, wells A, B, C, E, F	10	
	2nd Wash	MEA 1, wells A, B, C, D, F MEA 2, wells A, B, C, E, F	10	
	GABA	MEA 1, wells A, B, C, D, F MEA 2, wells A, B, C, E, F	10	
	Bicuculline	MEA 1, wells A, B, C, D, F MEA 2, wells A, B, C, E, F	10	
Burst Analysis and Proposed Joint Analysis	Baseline	MEA 1, wells A, B, C, D, F MEA 2, wells A, B, C, E, F	10	Minimum of 50 spikes, and at least one burst detected with the employed burst detection algorithm (Kapucu et al., 2012) in a 300 s recording from an electrode of a well
	1st Wash	MEA 1, wells A, B, C, D, F MEA 2, wells A, B, C, E, F	10	
	CNQX	MEA 1, wells A, B, C, D, F MEA 2, wells A, B, C, E, F	10	
	CNQX+D-AP5	MEA 1, wells A, B, C, F MEA 2, wells A, B, C, E, F	9	
	2nd Wash	MEA 1, wells A, B, C, F MEA 2, wells A, B, C, E	8	
	GABA	MEA 1, wells A, B, C, D, F MEA 2, wells A, B, C	8	
	Bicuculline	MEA 1, wells A, B, C, D, F MEA 2, wells A, B, E, F	9	

Joint analysis of extracellular spike waveforms and neuronal network bursts

Fikret Emre Kapucu, Meeri E.-L. Mäkinen, Jarno M. A. Tanskanen, Laura Ylä-Outinen, Susanna Narkilahti, Jari A. K. Hyttinen

Journal of Neuroscience Methods

Supplementary Material

Table S2

The numbers of channels in the wells which exhibited more than 50 spikes in 300 s for different experiment phases. The individual MEAs are identified by numbers whereas the individual wells are identified by capital letters. On each MEA chip, there were six wells with nine microelectrodes in each well.

Wells	Baseline	1st Wash	CNQX	CNQX+D-AP5	2nd Wash	GABA	Bicuculline
MEA 1, well A	7	6	3	3	1	0	2
MEA 1, well B	6	5	4	0	0	0	0
MEA 1, well C	9	7	8	8	7	5	5
MEA 1, well D	7	4	2	0	0	0	0
MEA 1, well E	0	0	0	0	0	0	0
MEA 1, well F	3	4	1	3	4	1	1
MEA 2, well A	9	6	1	0	4	3	0
MEA 2, well B	9	9	9	5	9	9	8
MEA 2, well C	7	3	0	1	0	0	0
MEA 2, well D	0	0	0	0	0	0	0
MEA 2, well E	5	4	1	0	2	0	0
MEA 2, well F	0	1	0	0	0	0	0

Joint analysis of extracellular spike waveforms and neuronal network bursts

Fikret Emre Kapucu, Meeri E.-L. Mäkinen, Jarno M. A. Tanskanen, Laura Ylä-Outinen, Susanna Narkilahti, Jari A. K. Hyttinen

Journal of Neuroscience Methods

Supplementary Material

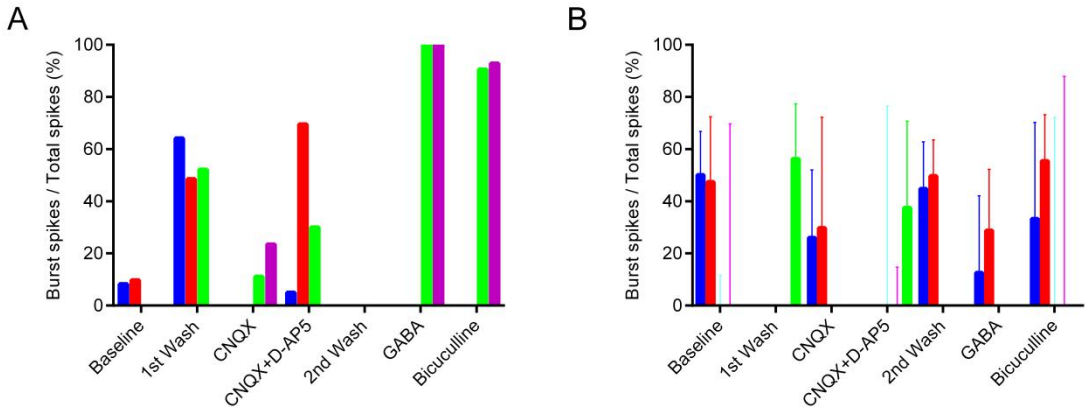

Fig. S1. The numbers of each type of spikes in bursts relative to the total numbers of spikes (A) for the single channel analysis (c.f. Fig. 4G), and (B) for the pooled data analysis (c.f. Fig. 6G).

Joint analysis of extracellular spike waveforms and neuronal network bursts

Fikret Emre Kapucu, Meeri E.-L. Mäkinen, Jarno M. A. Tanskanen, Laura Ylä-Outinen, Susanna Narkilahti, Jari A. K. Hyttinen

Journal of Neuroscience Methods

Supplementary Material

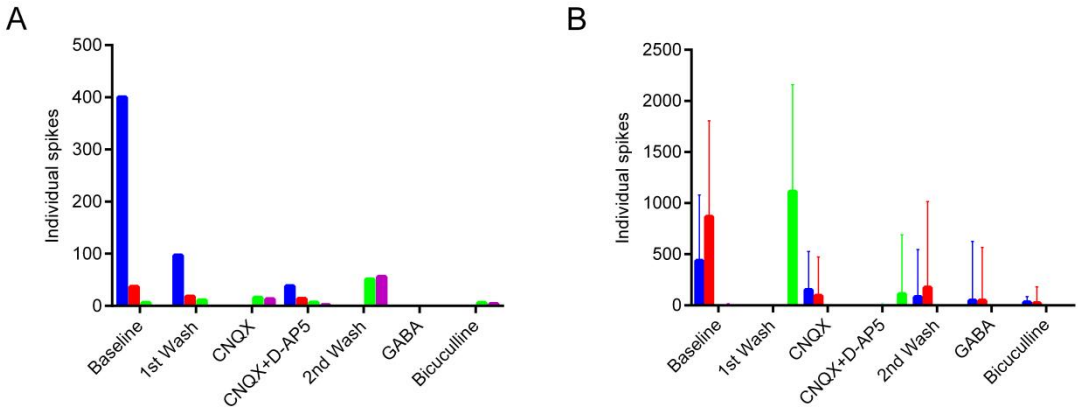

Fig. S2. The numbers of each type of spikes in individual spikes (A) for the single channel analysis (c.f. Fig. 4G), and (B) for the pooled data analysis (c.f. Fig. 6G).

frontiers in Neuroscience

ORIGINAL RESEARCH
published: 31 October 2017
doi: 10.3389/fnins.2017.00606

Optimised PDMS Tunnel Devices on MEAs Increase the Probability of Detecting Electrical Activity from Human Stem Cell-Derived Neuronal Networks

Maria Toivanen[1†], Anssi Pelkonen[1†], Meeri Mäkinen[1], Laura Ylä-Outinen[1], Lassi Sukki[2], Pasi Kallio[2], Mervi Ristola[1†] and Susanna Narkilahti[1*†]*

[1] NeuroGroup, BioMediTech Institute and Faculty of Medicine and Biosciences, University of Tampere, Tampere, Finland, [2] Micro and Nanosystems Research Group, BioMediTech Institute and Faculty of Biomedical Sciences and Engineering, Tampere University of Technology, Tampere, Finland

OPEN ACCESS

Edited by:
Michele Giugliano,
University of Antwerp, Belgium

Reviewed by:
Anja Kunze,
Montana State University, United States
Sophie Pautot,
USR3505 Institut des Technologies Avancées en sciences du Vivant (ITAV), France
Marc Heuschkel,
High School of Landscape Engineering and Architecture, University of Applied Sciences Western Switzerland, Switzerland

***Correspondence:**
Mervi Ristola
mervi.ristola@uta.fi
Susanna Narkilahti
susanna.narkilahti@uta.fi

[†] These authors have contributed equally to this work.

Specialty section:
This article was submitted to Neural Technology, a section of the journal Frontiers in Neuroscience

Received: 25 July 2017
Accepted: 17 October 2017
Published: 31 October 2017

Citation:
Toivanen M, Pelkonen A, Mäkinen M, Ylä-Outinen L, Sukki L, Kallio P, Ristola M and Narkilahti S (2017) Optimised PDMS Tunnel Devices on MEAs Increase the Probability of Detecting Electrical Activity from Human Stem Cell-Derived Neuronal Networks. Front. Neurosci. 11:606. doi: 10.3389/fnins.2017.00606

Measurement of the activity of human pluripotent stem cell (hPSC)-derived neuronal networks with microelectrode arrays (MEAs) plays an important role in functional *in vitro* brain modelling and in neurotoxicological screening. The previously reported hPSC-derived neuronal networks do not, however, exhibit repeatable, stable functional network characteristics similar to rodent cortical cultures, making the interpretation of results difficult. In earlier studies, microtunnels have been used both to control and guide cell growth and amplify the axonal signals of rodent neurons. The aim of the current study was to develop tunnel devices that would facilitate signalling and/or signal detection in entire hPSC-derived neuronal networks containing not only axons, but also somata and dendrites. Therefore, MEA-compatible polydimethylsiloxane (PDMS) tunnel devices with 8 different dimensions were created. The hPSC-derived neurons were cultured in the tunnel devices on MEAs, and the spontaneous electrical activity of the networks was measured for 5 weeks. Although the tunnel devices improved the signal-to-noise ratio only by 1.3-fold at best, they significantly increased the percentage of electrodes detecting neuronal activity (52–100%) compared with the controls (27%). Significantly higher spike and burst counts were also obtained using the tunnel devices. Neuronal networks inside the tunnels were amenable to pharmacological manipulation. The results suggest that tunnel devices encompassing the entire neuronal network can increase the measured spontaneous activity in hPSC-derived neuronal networks on MEAs. Therefore, they can increase the efficiency of functional studies of hPSC-derived networks on MEAs.

Keywords: human pluripotent stem cells, microelectrode array, neuronal network, tunnel device, *in vitro* model

INTRODUCTION

Analysis of neuronal network activity *in vitro* is a pivotal part of modern brain disease modelling, neuropharmacological testing, and neurotoxicological screening (Johnstone et al., 2010; Valdivia et al., 2014). *In vitro* neuronal networks derived from human pluripotent stem cells (hPSCs) can replace animal-derived models and better predict responses in humans (Cavanaugh et al., 2014; Hunsberger et al., 2015; Pei et al., 2016). Furthermore, their activity can be measured using

microelectrode arrays (MEAs) (Johnstone et al., 2010; Jones et al., 2011; Moser, 2011). For example, the effect of a neurotoxin on the MEA-activity of a hPSC-derived network can be observed before any morphological changes (Ylä-Outinen et al., 2010). However, analyses of MEA data from hPSC-derived networks can be very challenging due to low percentage of electrodes (often <20%), or entire arrays, that detect neuronal activity (Ylä-Outinen et al., 2010; Tukker et al., 2016). Even when the hPSC-derived networks produce robust, measurable activity, the necessary differentiation and functional development can be very slow, taking up to several months (Odawara et al., 2016). The variable and slow development of neuronal network activity on MEA appears to be characteristic to all neuronal cultures of human origin; in primary human neurons, which do not require pre-differentiation, the emergence of electrical activity can take nearly 40 days, where as in corresponding rat neurons the same development happens in only 10 days (Napoli and Obeid, 2016). Therefore, it is clear that new approaches are needed to facilitate the analysis of hPSC-derived neuronal network functions.

Microengineered polydimethylsiloxane (PDMS) devices can be used to answer specific questions on mechanisms of neural function and pathology (Taylor et al., 2005; Scott et al., 2013; Ren et al., 2015), and they can also be used to facilitate the analysis of electrical function of hPSC-derived networks. PDMS devices consisting an open chamber (or "well") can guide the network to grow more densely on top of the measuring electrodes, and thus facilitate the development and detection of neuronal activity (Kreutzer et al., 2012). PDMS microtunnel devices, on the other hand, increase the detected activity by amplifying extracellular electrical signals detected by the MEA (FitzGerald et al., 2009; Wieringa et al., 2010; Wang et al., 2012). According to a generally accepted theory in the field this occurs because signal amplitudes measured by MEA in tunnels are influenced by a derivative of Ohm's law ($U = R\ I$), where the resistance of the medium inside the tunnel increases as the tunnels height (h) and width (w), i.e., cross section (A) decreases and length (l) increases ($R = \rho\ (l\ /\ A)$). The increased resistance, in turn, manifests as higher potential differences during electrical activity of the measured cells, which translates to an increased signal-to-noise ratio (SNR) in the MEA recordings. However, the microtunnels providing the best amplification (cross sections $\leq 100\ \mu m^2$, $h \leq 5\,\mu m$) are designed to encompass only neurites and not neuronal somata or entire neuronal networks, and often require a custom made electrode array (FitzGerald et al., 2008; Dworak and Wheeler, 2009; Hong et al., 2017). These neurite-encompassing microtunnels are useful for analysing certain parameters such as the speed of signal conduction along axons, but there is a need for larger tunnel devices which can provide robust MEA data from entire neuronal networks containing also dendrites and cell somata.

In this study, the objective was to develop tunnel devices that are compatible with a commercially available MEA platform, and are able to house entire hPSC-derived neuronal networks and concomitantly possess sufficiently small features to amplify the extracellular signals on MEAs in comparison to standard cultures. Therefore, hPSC-derived neuronal networks were cultured on MEAs in tunnel devices with different dimensions. The spontaneous electrical activity of the neuronal networks in the tunnels was measured up to 5 weeks and compared to data from standard MEA controls. We observed that while the tunnels provided little or no improvement of signal detection, they increased the measured network activity considerably. Thus, the use of the tunnel devices solved one of the main problems in studying hPSC-derived networks using MEAs, which is the low percentage of active electrodes.

MATERIALS AND METHODS

Production of MEA-Compatible PDMS Tunnel Devices

Custom PDMS tunnel devices and SU-8 moulds for the devices were fabricated using rapid prototyping methods (Duffy et al., 1998). The outer diameter of the PDMS devices (**Figure 1A**) was 15 mm and the height was approximately 3 mm to be compatible with the MEA array (60MEA200/30iR-Ti MEAs, MultiChannelSystem [MCS], Germany) and amplifier (MEA2100, MCS). The PDMS devices contained two cell plating areas that were interconnected by tunnels and a reference electrode well. The designed tunnel dimensions were varied as presented in **Table 1** and **Figure 1**. The cell cultivation area in front of the tunnels is covered by a PDMS lid. The different PDMS tunnels were aligned on top of the MEA electrodes as illustrated in **Figures 1B–F**.

PDMS (Sylgard 184, Dow Corning) devices were fabricated using methods described by Park et al. (2006). The moulds were fabricated from SU-8 3050 (Micro Resist Technology GmbH) on top of a silicon wafer. A 15-mm-diameter punching tool was used to punch individual devices out of PDMS sheets. A 3-mm-diameter manual punching tool was used to create inlets (cell plating areas; **Figure 1A**) at a distance of 100–1,000 μm from the tunnel mouth, and an opening for the reference electrode. The use of circular cell supply inlets and the need to have equal tunnel lengths created a lid around the punching hole. Thus, the MEA electrodes placed in front of the tunnels were covered by the PDMS lid located either 43 or 105 μm above the MEA surface depending on the tunnel height. Hereafter, these electrodes located underneath the PDMS lid but outside the tunnels are referred as outside electrodes.

The dimensions of the tunnel devices were characterised using both light microscopy and profilometry. A Zeiss Axio Imager.A1m (Carl Zeiss AG) was used to inspect the mould for potential faults. A Bruker Dektak XT stylus profilometer (Bruker Corporation) was used to measure the heights of the microstructures from the mould. According to the measurements, the mould heights were $43 \pm 7\,\mu m$ and $105 \pm 15\,\mu m$. The variation in heights was caused by the slight bending of the silicon wafers by the spinner vacuum during spin-coating, which caused the features to be thicker in the middle of the moulds.

TABLE 1 | Tunnel dimensions and number of tunnels, electrodes and MEAs.

w (μm)	*h* (μm)	*l* (μm)	Number of MEA plates	Electrodes per tunnel, outside area or MEA well	Total *n* of analysed tunnels, outside areas or MEA wells	Total *n* of analysed electrodes	Total *n* of active electrodes per week				
							1	2	3	4	5
6-well MEA control			5\–	9	30\–\–	270\–	75	107	120	146	101
1-well MEA control			4\–	59	4\–\–	236\–	–	1	18	39	42
Outside	43	–	13\8	12	13\8\–	156\96	29	87	112	119	118
Outside	105	–	21\15	12	21\15\–	254\180	9	74	150	157	154
100	43	1,000	5\4	4	6\4\5	24\16	13	18	24	24	24
100	105	1,000	7\5	4	9\5\7	36\20	2	14	24	34	31
500	43	1,000	1\–	11–12	2\–\2	23\–	3	2	12	21	23
500	105	1,000	2\–	11–12	4\–\3	46\–	1	6	34	40	44
750	43	1,000	3\2	15–16	4\2\2	63/32	8	24	40	47	48
750	105	1,000	7\5	15–16	9\5\6	142/80	7	48	71	92	91
1,500	43	1,000	5\2	31	5\2\4	155/62	11	69	127	131	127
1,500	105	1,000	7\5	31	7\5\3	217\155	4	39	167	111	137

*The tunnel width (w), height (h) and length (l) are presented in the first three columns. "Outside" refers to electrodes outside the actual tunnels but underneath the PDMS lid (**Figure 1**). The second number after the backslash indicates the corresponding number in the pharmacological experiment (**Figure 6**), and the third number after the second backslash indicates n in the CytoSpectre network orientation analysis (**Figure 3E**).*

Preparation of PDMS Tunnel Devices and MEAs for Cell Culture

The MEAs were always cleaned before use according to manufacturer's instructions (washed with 1% Tergazyme [Sigma-Aldrich], rinsed with distilled H_2O and autoclaved). MEAs were coated with 0.05% polyethylenimine as previously described (Ylä-Outinen et al., 2010). To make the tunnels hydrophilic and thus amenable to coating, the PDMS devices were treated with oxygen plasma in a PICO plasma system (Diener electronic) for 3 min at 50 W. They were manually aligned under a microscope on the MEA electrodes and reversibly bonded to the MEAs, i.e., they could still be manually removed. Mouse laminin (20 μg/ml; Sigma-Aldrich) was pipetted into the PDMS tunnel devices on MEAs through both cell plating areas (**Figure 1A**). Cell culture control plates (4-well plate, Nunc, Thermo Fisher Scientific, Inc.) were coated with 20 μg/ml or 10 μg/ml mouse laminin in wells with or without coverslips (Ø = 13 mm, VWR), respectively. The MEAs and the control plates were incubated with the laminin solutions at +4°C overnight as previously described (Ylä-Outinen et al., 2010).

Neural Differentiation and Cell Culture

The human embryonic stem cell (hESC) line Regea 08/023 and the human induced pluripotent stem cell (hiPSC) line 04311.WT were used in the experiments. BioMediTech has approval from the Finnish Medicines Agency (FIMEA) to perform research with human embryos (Dnro 1426/32/300/05). There are also supportive statements from the regional ethical committee of Pirkanmaa Hospital District for the derivation, culturing, and differentiation of hESCs (R05116) and hiPSCs (R08070). This study was carried out in accordance with the recommendations of FIMEA and Pirkanmaa Hospital District with written informed consent from all subjects who provided cell material. All subjects gave written informed consent in accordance with the Declaration of Helsinki.

The timeline for the experiments is shown in **Figure 2**. The hESCs and hiPSCs were differentiated into neural cells for 8–10 weeks in neurosphere cultures in differentiation medium (NDM) consisting of 1:1 Dulbecco's Modified Eagle's Medium/F12:Neurobasal Medium supplemented with 2 mM GlutaMax, 1x B27 supplement, 1x N2 supplement (all from Gibco Invitrogen), 25 U/ml penicillin/streptomycin (Lonza Group Ltd) and, in this neurosphere differentiation stage, 20 ng/ml basic fibroblast growth factor (bFGF, R&D Systems) as previously described (Lappalainen et al., 2010) with or without low-dose naltrexone LDN193189 (100 nM; Stemcell Technologies, Inc.).

The neurospheres containing pre-differentiated neural cells were manually dissected into small cell aggregates (Ø∼50–200 μm). Approximately 15 small aggregates (50,000–150,000 cells in total) were plated in both cell plating areas of the PDMS devices (i.e., both ends of the tunnels) as close to the tunnels as possible to ensure tunnel colonization, and similarly on control plate wells. The plating procedure was identical for each device. The PDMS devices on the MEAs were submerged in the cell culture medium (1 ml). The cells were maintained in a humidified incubator at 37°C and 5% CO_2. Half of the medium was changed three times a week. After 1 week in adherent culture, 4 ng/ml bFGF and 5 ng/ml brain-derived neurotrophic factor (BDNF) (Gibco Invitrogen) were added to the medium.

Immunocytochemistry

The control cells were fixed after 14 days in adherent culture, and immunocytochemical (ICC) staining was performed as previously described (Lappalainen et al., 2010) to verify the neural identity of the cells. Primary antibodies, rabbit anti-beta-III Tubulin (β-tub) (1:2000; GenScript) and rabbit

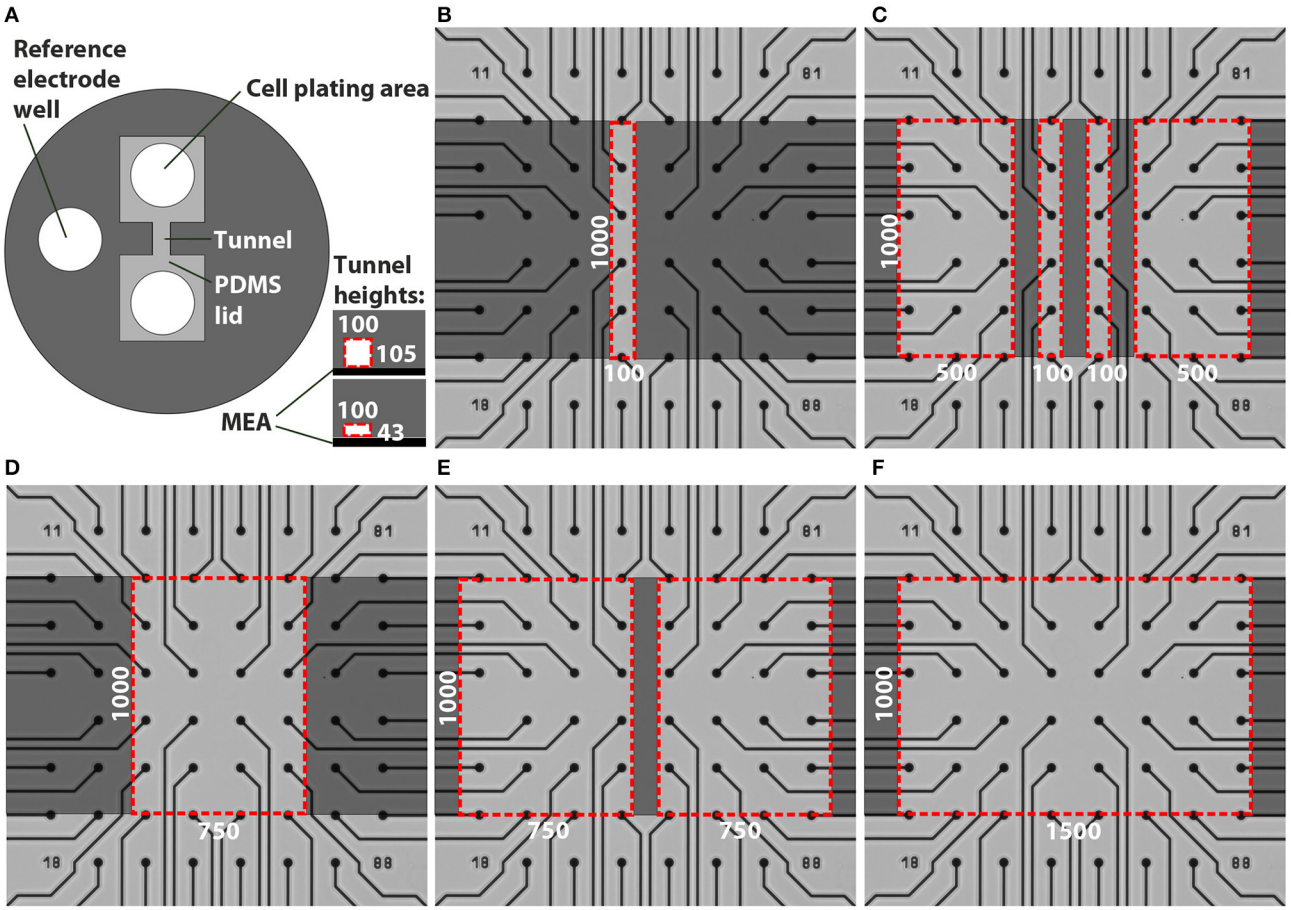

FIGURE 1 | Designs of the tunnel devices. The PDMS tunnel devices **(A)** consist of two cell plating areas that are interconnected by tunnels, and a reference electrode well. The two tunnel heights are presented in the lower right corner in **(A)**. The red dashed lines indicate the cross section of a tunnel, in this case 100 μm wide. The numbers in **(A)** provide the tunnel widths (*w*) and heights (*h*) in μm. Tunnels with different dimensions were aligned on MEAs **(B–F)**. Dark gray indicates PDMS bonded to the MEA surface, light grey represents cell cultivation areas in the tunnels and areas under the PDMS lid, while the red dashed lines indicate tunnel perimeters. The numbers in **(B–F)** provide the tunnel widths (*w*) and lengths (*l*) in μm.

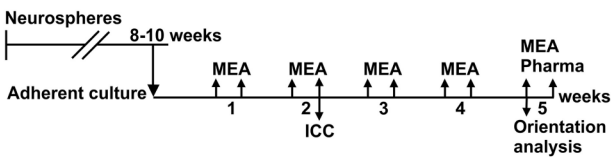

FIGURE 2 | Timeline of the experiments. Neurons were differentiated in neurosphere culture for 8–10 weeks before adherent culture in tunnel devices on MEAs and in standard cell culture wells (control cells). MEA measurements were performed twice weekly over 5 weeks, and a pharmacological test was performed at the end of the culture. Neurite orientation analysis was performed from the phase contrast images taken at the 5th week. Immunocytochemistry was performed on control cells after 2 weeks in adherent culture for both cell lines.

polyclonal anti-Microtubule-Associated Protein 2 (MAP2) (1:400; Millipore), were used together with secondary antibodies, Alexa 488 anti-rabbit and Alexa 568 anti-mouse (both 1:400; Molecular Probes). In addition, the nuclei of the cells were stained with 4′,6-diamidino-2 phenylindole (DAPI), which was included in the mounting medium (Vectashield Mounting Medium with DAPI, Vector Laboratories). The cells were imaged with a fluorescence microscope (Olympus IX51, Olympus Corporation).

Phase Contrast Microscopy and Neurite Orientation Analysis

The cells were imaged with a phase contrast microscope (Nikon Eclipse TE2000-S, Nikon Corporation) once per week to follow the neuronal morphology, migration and network formation. The cell culture control plates were used as a normal microenvironment cell control to evaluate neuronal viability, morphology and migration. The control plates were followed for 2 weeks.

The orientation of the neurites was analysed using CytoSpectre 1.2 software (http://www.tut.fi/cytospectre)

(Kartasalo et al., 2015). The software utilises spectral analysis and calculates the orientations of image components, in this case neurites (Hyysalo et al., 2017), and describes their variance with a circular variance value, which is 1 when the components are randomly aligned, and 0 when all components are completely unidirectional. The software was used in the mixed component mode and spectral resolution/noise was set to balanced. Wavelength settings (component size) were set to 1 μm (minimum) and 30 μm (maximum). The orientation of neurites inside the tunnels was analysed using phase contrast images obtained at week 5 after plating, and compared to images of the freely growing networks on cell culture control plates. The electrodes and their tracks were excluded from the image analysis by using a custom MATLAB script which automatically detected the electrodes and the tracks and replaced their pixel values with local mean intensities computed from the corresponding regions of each image, and by using CytoSpectre's component size filtering.

MEA Measurements

MEA measurements were performed with an MEA system consisting of a filter amplifier MEA2100, software MC_Rack and temperature controllers TC02 set at 37°C (all from MCS). The electrical activity of the neuronal networks was measured twice a week for 5 weeks (**Figure 2**). The duration of each recording was 10 min and the sampling rate was 25 kHz. To analyse the noise, signal amplitude and SNR in the tunnel devices, the MEA data were compared to earlier recordings from the same 60MEA200/30iR-Ti MEAs with no PDMS tunnel devices, referred to as the 1-well MEA control. The 1-well MEA control is an open volume system with no liquid volume restrictions. To analyse the development of network activity, the data were compared to recordings from 60-6wellMEA200/30iR-Ti MEAs (MCS), in which the individual wells were separated using SpikeBooster devices (BioMediTech) (Kreutzer et al., 2012), and is referred to as the 6-well MEA control. The dimensions of the cell culturing areas on the SpikeBooster devices are the same as the cell plating areas on the tunnel devices, and the 6-well MEA control can be considered a partially restricted volume system. The combination of 6-well MEAs and SpikeBooster is the most used MEA setup in our laboratory, and it typically provides the best network activity development. All used MEAs had the same surface material (Si_3N_4), electrode material (TiN), electrode diameter (30 μm) and electrode-to-electrode distance (200 μm).

Pharmacological testing with tetrodotoxin (TTX; 1 μM, Tocris Bioscience) was performed at the end of the study (**Figure 2**). MEA activity was measured for 5 min after addition of fresh medium to the MEA and after addition of TTX to the medium where the PDMS device was submerged. TTX and the equipment used for handling it were stored, handled and disposed according to institutional safety regulations (BioMediTech institute and Faculty of Medicine and Biosciences, University of Tampere).

Signal Analysis and Statistics

Spikes were detected from the MEA data using MATLAB (The MathWorks, Inc.) with a custom-made analysis program based on Quiroga et al. (2004). Analysis was performed separately for each electrode (modified from Quiroga et al., 2004). First, the voltage signal was filtered (200–3,000 Hz band pass). Next, the noise was calculated as the median (md) of the absolute values from the filtered recording divided by 0.6745. Signal values which exceeded five times this noise value were considered as spikes. Both negative and positive spikes were detected. Spikes larger than 500 times noise were removed as artefacts. For spike waveform analysis, 0.8 and 1.76 ms of voltage signal was clipped before and after the largest absolute value of the spike from the filtered data. The detector dead time between two waveforms was 1.48 ms. The peak-to-peak amplitudes were measured as the difference between the highest and lowest voltage values in the stored waveforms. A peak-to-peak md was obtained from all waveforms from one channel to identify a single value per channel. SNR was calculated by dividing the md peak-to-peak spike amplitudes by the corresponding noise values. An electrode was regarded as an active electrode (measuring neuronal activity) if more than 2 spikes were recorded in a minute (spike frequency 0.033 Hz). The threshold was determined by measuring the spike rates from empty MEAs and MEAs with TTX-silenced neuronal cultures (data not shown). Percentage of active electrodes was calculated for each tunnel and control well separately and electrodes underneath the PDMS devices were excluded from the analysis. Data from the electrodes at the tunnels mouth (under the red dashed line in **Figures 1B–F**) were not included in analyses because they could be considered neither outside nor tunnel electrodes. Bursts (clusters of spikes) were detected separately for each electrode using a method based on Kapucu et al. (2012) which defines bursts using the cumulative moving average of inter-spike intervals.

The number of repeats (n) in different analyses are presented in **Table 1**. Statistical analyses were performed in SPSS (IBM). The MEA data were found to have a non-normal distribution, and therefore the nonparametric Kruskal-Wallis test with Dunn's *post hoc* test was used to determine whether there were statistically significant differences among the different tunnels and controls. The data from the neurite orientation analysis (CytoSpectre results) were found to be normally distributed and thus were analysed by univariate analysis of variance with Bonferroni's *post hoc* test. A p-value less than 0.05 was considered significant.

RESULTS

Neuronal Network Cultures in Tunnel Devices

After cell plating, the neurons started to migrate and elongate neurites into the tunnels. The first neurites and neurons entered the tunnels as early as 3 days after plating, and typically by 2–3 weeks the neurons had formed a network covering approximately the entire area inside the tunnels. Examples of network growth from the narrowest (w = 100 μm) and widest tunnels (w = 1,500 μm) are shown in **Figures 3A,B**, respectively. Occasionally, the reversible PDMS-MEA bonding led to partial detachment of some of the PDMS devices from

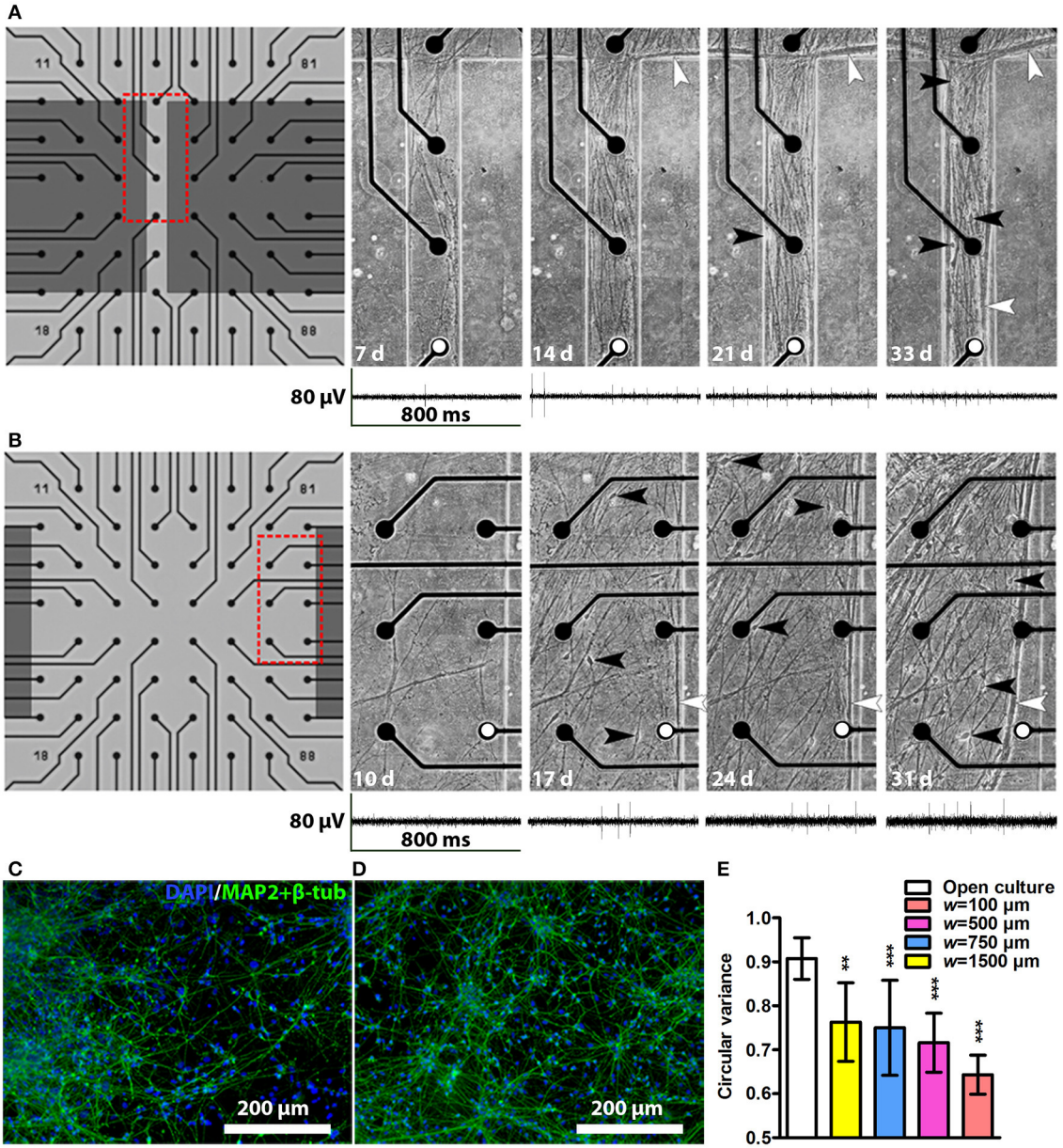

FIGURE 3 | Network development in tunnels and immunocytochemistry images of neuronal cultures. Network development in an $h = 43\,\mu m$, $w = 100\,\mu m$ tunnel **(A)** and an $h = 43\,\mu m$, $w = 1{,}500\,\mu m$ tunnel **(B)**. The electrode-to-electrode distance is 200 µm. Red dashed boxes in **(A,B)** show the location of the corresponding subfigures on the right, where somata are indicated by black and neurite bundles by white arrowheads, d, days. Representative MEA traces from the same week are shown under each tunnel image. The electrodes from which the traces were obtained are marked with white dots. Immunocytochemistry images of two cell lines: **(C)** the hiPSC line 04311.WT and **(D)** the hESC line 08/023 growing on cell culture controls plates. The cell nuclei (DAPI, blue) and neuronal markers (microtubule-associated protein 2 [MAP2] and class III tubulin [β-tub], green) were stained. **(E)** Neurite orientation analysis confirmed significantly smaller circular variances of the networks in tunnels than in freely growing open cultures. $n_{\text{open culture}}$ is 8 and n otherwise is 2–7 (**Table 1**). Statistical difference between the groups was analysed using univariate analysis of variance, and the * symbols indicate significance based on Bonferroni's *post hoc* test vs. freely growing open cultures (*$0.05 > p \geq 0.01$; **$0.01 > p \geq 0.001$; ***$p > 0.001$).

the MEAs. The cultures with insufficient PDMS-MEA bonding were excluded from the experiments. The neuronal nature of the used cells was verified by immunocytochemical staining for known neuronal markers (**Figures 3C,D**). Cell viability in the tunnels was good, and no significant cell death or detachment was observed with phase contrast microscopy during the 5-week culture period. The tunnels contained neurites and cell somata migrated into the tunnels. Toward the end of the culture the neurites tended to form thick bundles that were typically next to the PDMS walls regardless of the tunnel width. All tunnels

affected neuronal network development by causing neurite orientation (**Figures 3A,B**) compared with random neuronal networks without tunnels (**Figures 3C,D**). This observation was verified by the neurite orientation analysis, which showed that the mean circular variance values in the networks inside tunnels were significantly smaller than in freely growing networks [$F_{(3, 31)} = 6.63$, $p = 0.001$; **Figure 3E**]. The tunnel height had no significant effect on the neurite orientation [$F_{(1, 31)} = 2.94$, $p = 0.097$].The neurites in the narrowest ($w = 100\,\mu m$) tunnels were the most unidirectional (**Figures 3A,E**,).

MEA Signal Detection Inside Tunnel Devices

To determine whether the different tunnel dimensions affected the signal detection on MEA, we calculated the noise values, md peak-to-peak signal amplitudes, and from these, the corresponding SNRs in each active electrode using a custom-made MATLAB algorithm (**Figure 4**). Examples of the neuronal signals are shown in the narrow tunnel ($w = 100\,\mu m$) and wide tunnel ($w = 1{,}500\,\mu m$) (**Figures 3A,B**).

Data from standard 1-well MEAs served as the relevant control for these parameters because the tunnel device data were obtained using the same individual MEAs. The 1-well MEA control data did not contain measurements from the first week after plating, and week 1 data were therefore omitted from this analysis but are presented in Supplementary Figure 1. The outside-group refers to the electrodes outside the tunnels but under the PDMS lid (**Figure 1**), and thus have the same h as the tunnel electrodes.

The md noise values were higher in the electrodes inside the PDMS tunnels in comparison to the 1-well MEA control (md 1.3 μV; **Figures 4A,B**). In the $h = 43\,\mu m$ tunnels, noise was significantly increased in the electrodes inside $w = 100\,\mu m$, $w = 750\,\mu m$, and $w = 1{,}500\,\mu m$ tunnels (md 1.8, 2.0, and 2.0, $p < 0.001$; **Figure 4A**). The 6-well MEA control had a comparatively high noise level (md 3.1 μV). In the $h = 105\,\mu m$, the tunnels noise was significantly increased in $w = 500\,\mu m$, $w = 750\,\mu m$, and $w = 1{,}500\,\mu m$ tunnels (md 1.9, 1.9, and 1.8; $p < 0.001$; **Figure 4B**). In the $h = 105\,\mu m$ devices, the noise was particularly high at the first week after plating (Supplementary Figure 1), probably due to system stabilization and/or protein adsorption to the electrode surface. However, inclusion of the data in the analyses had no significant effect on the results. In general, noise was significantly higher in the $h = 43\,\mu m$ devices compared with the $h = 105\,\mu m$ devices ($p < 0.001$; **Figure 4A** vs. **Figure 4B**). These results suggest that PDMS tunnels can increase noise in MEA recordings depending on the tunnel dimensions.

In agreement with the increased noise values, the md peak-to-peak signal amplitudes were increased in electrodes inside tunnel devices when compared with the 1-well MEA control (md 13.3 μV; **Figures 4C,D**). In the $h = 43\,\mu m$ tunnel devices, the amplitudes were significantly increased in the outside electrodes as well as the electrodes in $w = 100\,\mu m$, $w = 750\,\mu m$ and $w = 1{,}500\,\mu m$ tunnels (md 18.4, 18.9, 20.1, and 19.5 μV, respectively; $p < 0.001$; **Figure 4C**). The 6-well MEA control had relatively high signal amplitudes (md 24.3 μV). In the $h = 105\,\mu m$ tunnels, the amplitudes were significantly increased in

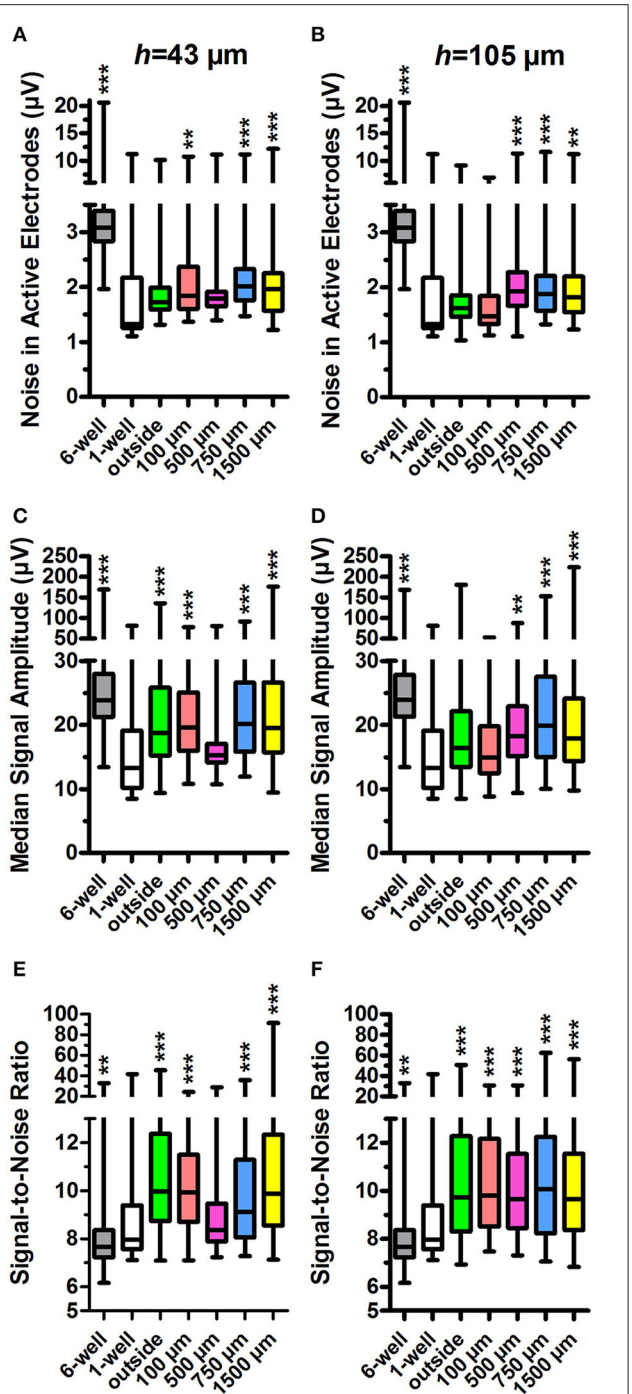

FIGURE 4 | Noise in active electrodes, signal amplitude and signal-to-noise ratio. The noise was calculated for active electrodes in $h = 43\,\mu m$ **(A)** and $h = 105\,\mu m$ tunnel devices **(B)** and controls (6 and 1-well MEAs). The tunnel width or control group is indicated on the x-axes. The median signal amplitude in active electrodes in $h = 43\,\mu m$ **(C)** and $h = 105\,\mu m$ devices **(D)** and controls was also calculated. The signal-to-noise-ratio (SNR) in $h = 43\,\mu m$ **(E)** and $h = 105\,\mu m$ devices **(F)** was calculated from the noise and median signal amplitude in active electrodes. n (active electrodes) is 61–547 (weekly numbers of active electrodes are in **Table 1**). Please note that the low number of $h = 43\,\mu m$, $w = 500\,\mu m$ tunnels (2) may affect the results. Statistical differences between groups were analysed using the Kruskal-Wallis test, and the * symbols indicate significant differences using Dunn's *post hoc* test vs. the 1-well control (*$0.05 > p \geq 0.01$; **$0.01 > p \geq 0.001$; ***$p > 0.001$).

the electrodes in $w = 500\,\mu m$, $w = 750\,\mu m$, and $w = 1{,}500\,\mu m$ tunnels (md 18.2, 20.0, and 18.0 μV; $p < 0.001$; **Figure 4D**). In general, signal amplitudes were significantly higher in the electrodes in the $h = 43\,\mu m$ devices compared with the $h = 105\,\mu m$ devices ($p < 0.001$; **Figure 4C** vs. **Figure 4D**). These results suggest that PDMS tunnel devices can increase MEA signal amplitude depending on the device dimensions.

SNR was found to be higher in the electrodes in tunnel devices compared with the 1-well MEA control (md 8.0, **Figures 4E,F**). In the $h = 43\,\mu m$ tunnel devices, SNR was significantly increased in the outside electrodes under the PDMS lid as well as electrodes in $w = 100\,\mu m$, $w = 750\,\mu m$, and $w = 1{,}500\,\mu m$ tunnels (md 10.0, 9.9, 9.1, and 9.9, respectively; $p < 0.001$; **Figure 4E**). SNR was lowest in the 6-well MEA controls (md 7.7). In the $h = 105\,\mu m$ tunnel devices, SNR was significantly increased in the outside electrodes as well as electrodes in $w = 100\,\mu m$, $w = 500\,\mu m$, $w = 750\,\mu m$, and $w = 1{,}500\,\mu m$ tunnels (md 9.7, 9.8, 9.6, 10.1, and 9.7, respectively; $p < 0.001$; **Figure 4F**). The tunnel height had no significant effect on SNR ($p = 0.244$; **Figure 4E** vs. **Figure 4F**). In summary, the SNRs recorded from inside the tunnel devices were very similar, thus making the differences in noise and signal amplitudes between different designs irrelevant in terms of MEA signal detection. However, it appears that a PDMS tunnel device on the MEA in general improves SNR.

Tunnel Devices Increase Spike and Burst Activity on MEA

To assess whether the tunnel devices could affect the spike and burst activity on MEA, we analysed the percentage of active electrodes, spike count and burst count in active electrodes using our custom-made MATLAB algorithm (**Figure 5**). We compared the activity data from tunnel electrodes to the 6-well MEA control. The statistical analyses between the tunnel devices and controls were performed separately each week because the activity in the tunnel electrodes increased dramatically over time.

The percentage of active electrodes increased in the tunnel devices (**Figures 5A,B**). At week 1, the percentage of active electrodes was highest in the 6-well MEA controls. However, while the percentage in the 6-well MEA controls decreased from 46 to 27% over 5 weeks, the percentage in the tunnel devices steadily increased, surpassing the 6-well MEA controls 2–4 weeks after plating and finally reaching 52–100% at week 5. The percentage of active electrodes was especially high in the $w = 100\,\mu m$ and $w = 500\,\mu m$ tunnels, reaching 80–100% by week 5. The percentages were also higher in the $h = 43\,\mu m$ tunnels compared with the $h = 105\,\mu m$ tunnels (69–100% vs. 52–85% at week 5; **Figure 5A** vs. **Figure 5B**). The smallest tunnels ($h = 43\,\mu m$, $w = 100\,\mu m$) were best in terms of the percentage of active electrodes, reaching 100% as early as week 3 (**Figure 5A**).

There were significantly more spikes per active electrode in the tunnel devices compared with the 6-well MEA controls (**Figures 5C,D**). The md spike count in the 6-well MEA controls never reached higher than 125 over 10 min (week 4). The md spike count was highest, with 3,449 spikes over 10 min, in the smallest tunnels ($h = 43\,\mu m$, $w = 100\,\mu m$) at week 5 ($p < 0.001$; **Figure 5C**). The outside electrodes in the $h = 43\,\mu m$ tunnel devices also had high spike counts, with md reaching 2,715 at week 5. The spike counts between the outside electrodes and the $w = 100\,\mu m$ tunnels did not differ significantly during any week. The spike counts were also significantly increased in higher ($h = 105\,\mu m$) devices compared with the 6-well MEA controls (**Figure 5D**). The maximal spike count in the $h = 105\,\mu m$ devices was reached at week 4, when the md spike count in the $w = 500\,\mu m$ tunnels was 992 ($p < 0.001$). The md spike count was nearly as high in the $w = 100\,\mu m$ tunnels for the corresponding time point (964). In general, the spike count was higher in the $h = 43\,\mu m$ tunnel devices compared with the $h = 105\,\mu m$ devices. For example, in the $w = 100\,\mu m$ tunnels, the difference was significant at weeks 4 (2,886 and 964, respectively; $p = 0.013$) and 5 (3,449 vs. 907, respectively; $p = 0.002$; **Figure 5C** vs. **Figure 5D**). Taken together, the spike count data showed that the $w = 100\,\mu m$ tunnels and outside area of the $h = 43\,\mu m$ tunnel devices were the best to increase the amount of measured network activity.

As with the spike counts, the burst counts were also increased in the tunnel devices compared with the 6-well MEA controls. In the 6-well MEA controls, the md burst count was highest at week 5, with 6 bursts over 10 min (**Figures 5E,F**). In the smallest tunnels ($h = 43\,\mu m$, $w = 100\,\mu m$), the burst count reached a maximum, 373, at week 4 ($p < 0.001$; **Figure 5E**). The burst counts were also very high in the outside electrodes of the $h = 43\,\mu m$ tunnel devices, with 250 bursts at week 5 ($p < 0.001$). The burst counts between the outside electrodes and the $w = 100\,\mu m$ tunnels did not differ significantly during any week. The burst counts were also significantly increased in the higher ($h = 105\,\mu m$) tunnels compared with the 6-well MEA controls, achieving a maximum of 108 at week 4 in the $w = 500\,\mu m$ tunnels ($p < 0.001$; **Figure 5F**). The md burst count was also high in the $w = 100\,\mu m$ tunnels at the same week, with 80 bursts. However, the number of bursts in the $h = 105\,\mu m$ tunnels was generally less than in the $h = 43\,\mu m$ tunnels. For example, in the $w = 100\,\mu m$ tunnels, the difference was significant at weeks 4 (80 and 373, respectively; $p = 0.006$) and 5 (56 and 368, respectively; $p = 0.002$; **Figure 5E** vs. **Figure 5F**). The burst count data suggested that the MEA activity was highest in $w =$ 100-μm-wide tunnels and the outside area of the $h =$ 43-μm-high tunnel devices, which is consistent with the spike count results (**Figures 5C,D**). However, considering also the percentage of active electrodes (**Figures 5A,B**), it is not the area outside the tunnels, but particularly the smallest tunnels ($h = 43\,\mu m$, $w = 100\,\mu m$), that had the greatest ability to increase the amount of measured network activity.

MEA Activity Inside Tunnel Devices Can Be Affected by Pharmacological Treatment

To test whether the MEA signals inside the tunnel devices originated from neuronal activity, we measured the MEA activity inside the devices before and after TTX treatment (**Figures 6A,B**). TTX inhibits the function of neuronal voltage-gated sodium channels and, therefore, blocks the electrical

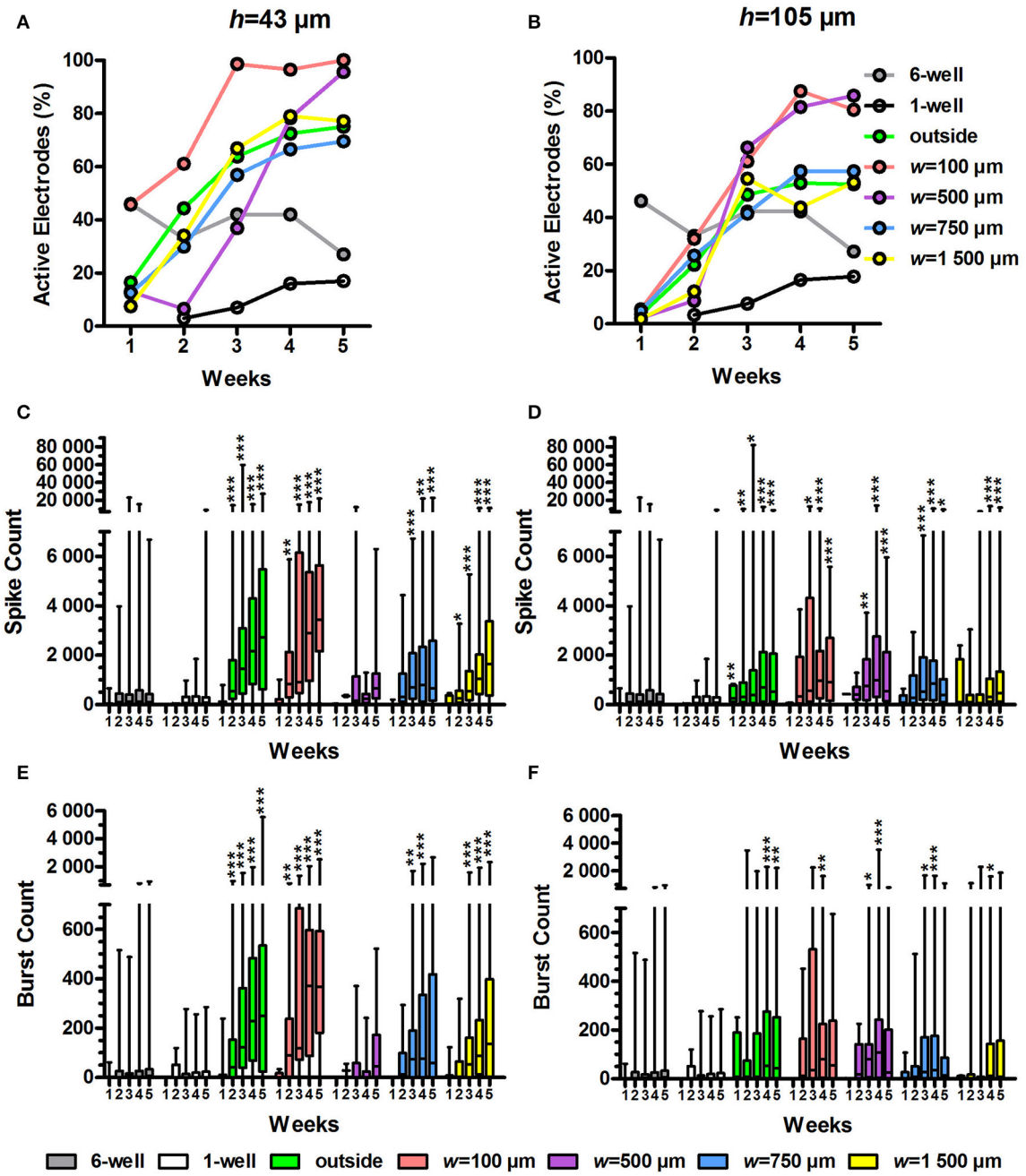

FIGURE 5 | Percentage of active electrodes, spike count and burst count. The percentage of active electrodes was calculated from the MEA data for the $h = 43\,\mu m$ **(A)** and h=105 µm tunnel devices **(B)** as well as the controls (6 and 1-well MEAs). Total n of analysed electrodes was 23-270 (**Table 1**). The spike count in the active electrodes over 10 min was also analysed for the $h = 43\,\mu m$ **(C)** and $h = 105\,\mu m$ tunnel devices **(D)** and controls. The number of bursts over 10 min was analysed from the spike data for the $h = 43\,\mu m$ **(E)** and h = 105-µm-high tunnel devices **(F)** and the controls. n (active electrodes) was 1-167 (**Table 1**). Please note that the low number of $h = 43\,\mu m$, $w = 500\,\mu m$ tunnels (2) may affect the results. Statistical differences between groups each week were analysed using the Kruskal-Wallis test, and * symbols indicate significant differences using Dunn's *post hoc* test vs. the 6-well control (*$0.05 > p \geq 0.01$; **$0.01 > p \geq 0.001$; ***$p > 0.001$).

activity of neurons. After addition of regular medium, the percentage of active electrodes was between 26% ($h = 105\,\mu m$, outside electrodes) and 94% ($h = 43\,\mu m$, $w = 100\,\mu m$). After the addition of TTX to the medium, the percentage of active electrodes dropped between 5% ($h = 105\,\mu m$, $w = 1{,}500\,\mu m$) and 0% (e.g., $h = 43\,\mu m$, $w = 100\,\mu m$). The effect of TTX on MEA activity in tunnel devices was prompt and clear, showing that the measured activity was of neuronal origin and that the tunnel devices can be used in pharmacological experiments.

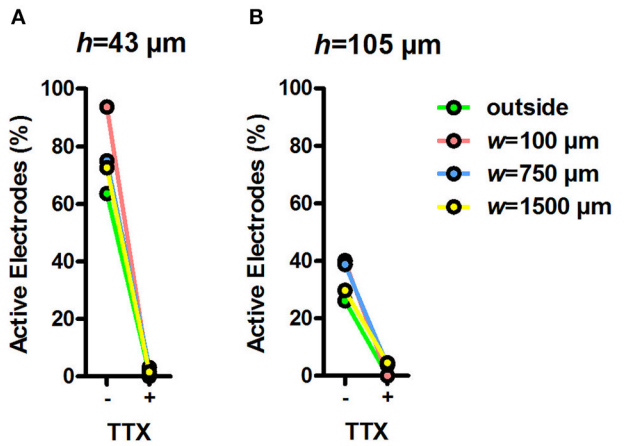

FIGURE 6 | Percentage of active electrodes before and during TTX. Percentage of active electrodes in $h = 43\,\mu m$ **(A)** and $h = 105\,\mu m$ tunnel devices **(B)** during 5-min recordings after changing the medium and adding TTX. Total *n* of analysed electrodes was 16–180 (**Table 1**).

DISCUSSION

The aim of this study was to develop novel tunnel devices that would facilitate and enhance the detection and analysis of extracellular electrical signals recorded from hPSC-derived neuronal networks. Neurons were cultured on MEAs covered by PDMS tunnel devices with varying dimensions, and the spontaneous electrical activity was measured for 5 weeks. The tunnels induced unidirectional growth of neurites, and the neuronal networks filled the tunnels in 2–3 weeks. The PDMS tunnel devices in general improved SNR, although none of the tested tunnel devices improved the MEA signal detection more than others. The tunnel devices increased network activity, and the smallest tunnels ($h = 43\,\mu m$, $w = 100\,\mu m$) were the best ones in this regard. The neuronal activity inside the tunnels was affected by TTX treatment.

Previously, tunnel devices on MEAs have been studied using rodent derived networks (Goyal and Nam, 2011), but the current setup is, to the best of our knowledge, the first to test the compatibility of PDMS tunnels with neuronal networks of human origin. Cells were plated to both ends of the tunnels, and this ensured neurite growth and cell migration into the tunnels. The hPSC-derived networks remained viable and active for the entire 5-week follow-up period, and we did not observe viability problems that could result from too small medium volume or flow inside the tunnels. The tunnels induced unidirectional growth of neurites, in contrast to the random orientation in freely growing cultures. Interestingly, similar tunnels in the study of Goyal and Nam (2011) appeared to instead induce more random neurite orientation and to increase branching of rat primary hippocampal neurons. This difference may reflect both the developmental stage of the neurons and their region-specific morphology (Dotti et al., 1988). It is also possible that there is some selectivity in the tunnels for axons over dendrites, which can explain some of the observed neurite orientation. However, the tunnels did not exclude dendrites because plenty of cell somas, from which dendrites branch off, migrated into the tunnels. The two cell populations attracting each other from the opposite ends of the tunnel probably also cause the neurites to grow in a more oriented manner. Overall, the results suggest that hPSC-derived neuronal networks are compatible with PDMS tunnel devices on MEA.

In this study, we aimed to improve the detection of electrical activity from human stem cell-derived neuronal networks on MEA using tunnel devices. A generally accepted theory in the field states that signal amplitudes measured by MEA in tunnels are influenced by a derivative of Ohm's law, where the resistance of the medium inside the tunnel increases as the tunnels cross section (*h* and *w*) decreases and length increases (FitzGerald et al., 2008, 2009; Wang et al., 2012). The increased resistance, in turn, manifests as higher potential differences during electrical activity of the measured cells, i.e., higher signal amplitudes measured by the MEA. However, apart for the slightly higher signal amplitudes in the $h = 43\,\mu m$ in comparison to the $h = 105\,\mu m$ tunnels, there was no clear connection between tunnel the cross section (*h* and *w*) and the signal amplitudes. Additionally, earlier studies examining tunnel devices have reported significant, considerably larger increases in noise and signal amplitudes when measuring rodent neurons (Morales et al., 2008; Dworak and Wheeler, 2009; FitzGerald et al., 2009; Goyal and Nam, 2011; Habibey et al., 2015). The *w* and *h* of our smallest tunnels ($w = 100\,\mu m$, $h = 43\,\mu m$) were most similar to the tunnels described by Goyal and Nam ($w = 50$ or $100\,\mu m$, $h = 50\,\mu m$) (Goyal and Nam 2011), who obtained spike amplitudes of several hundred µV, considerably higher than in our tunnels. This difference is most likely due to different tunnel lengths, since the length of the tunnels described by Goyal and Nam was 7-fold compared with our tunnels, and such an increase in the tunnel length has been shown to amplify the signal significantly (FitzGerald et al., 2008, 2009). However, in terms of signal detection, it is most useful to study the ratio between the noise and signal amplitude (SNR). Here, SNR in any of the tested tunnels did not increase more than 1.3-fold, reaching a value of 10. Although the increase was statistically significant, the median SNRs were rather modest in comparison to those reported earlier for the much smaller, axon-encompassing microtunnels, where SNR has reached as high as 80 (Wang et al., 2012) or even 450 (Pan et al., 2014) depending on the tunnel dimensions. Furthermore, the SNR in the current study did not depend on tunnel dimensions. Thus, it seems likely that the slight improvement in SNR occurred because the PDMS device guided the neurons to grow on or near the electrodes, and shortened the distance between the signal source and detector (Obien et al., 2015). It is also possible that the cleaning procedures between the experiments have affected the signal detection properties of the MEAs. All and all, the results concur with earlier simulation studies and the general theory in the field (FitzGerald et al., 2008, 2009; Wang et al., 2012), which suggest that the current, comparatively high and wide, but short, tunnels do not provide high enough resistance to improve signal detection on MEA.

Although the tested PDMS tunnel devices had no major effects on SNR, we found that the tunnel devices dramatically increased the percentage of active electrodes and the amount of detected

spike and burst activity on those electrodes when measuring hPSC-derived neuronal networks. Despite the advantages and potential of hPSC-derived networks in *in vitro* modelling (Hunsberger et al., 2015), they can be very slow (Odawara et al., 2016) and unpredictable in developing neuronal activity, and the low percentage of activity-detecting electrodes can especially complicate MEA data acquisition and analysis (Ylä-Outinen et al., 2010; Tukker et al., 2016). In our setup, the smallest of the tested tunnels were able to increase the portion of active electrodes up to 100% in only 3 weeks, increasing spike activity 12-fold and burst activity 30-fold at the same time. It is possible that the observed activity increases because the electrodes in the tunnels observe the same signal from multiple sites of the same neuron or network. However, in this case the signals in the tunnel electrodes would appear synchronous, and we observed synchronous activity only occasionally (spanning to two or three adjacent electrodes), while majority of the activity was non-synchronous. Increasing spike activity and temporal clustering of spikes into bursts are generally considered as signs of network activity maturation (Kapucu et al., 2012; Biffi et al., 2013; Odawara et al., 2016). It is possible that the maturation here was accelerated because the tunnels increased the density of neurons by limiting the area on which they can grow. However, according to earlier results from primary rodent cultures, simply increasing cell density cannot make the percentage of active electrodes exceed 60%, and once the maximum has been reached, increasing cell density merely decreases activity (Biffi et al., 2013). According to our own experience the maximum of active electrodes in hPSC-derived cultures is ∼50%. This suggest that some additional feature of the smallest tunnels, such as the effect on neurite orientation or efficient placing of the network on the electrodes, can significantly increase the detected network activity.

Not only the smallest but also larger tunnels significantly increased the amount of detected activity in comparison to control MEAs, and in particular the electrodes outside the actual tunnels but under the PDMS lid detected very high spike and burst activity. This finding implies that either the outer walls of the tunnels (at a right angle to the tunnel itself, **Figure 1**) function as guiding barriers that localize the developing networks on the outside electrodes, or that the tunnels funnel the networks from the outside area (**Figure 3A**), or both. However, we cannot exclude the possibility that the increase in detected activity reflects an increase in sensitivity of the system because the extracellular signals are detected when they cross a threshold, which depends on the noise level. This phenomenon could explain the increased activity in the $h = 43\,\mu m$ devices in comparison to the $h = 105\,\mu m$ devices. Besides changes in measurement sensitivity, the differences in results between the tunnel heights can be influenced by the batch-to-batch variation of hPSCs. Still, the increased activity inside the tunnels followed the observed growth of the neuronal network, and differences in activity between the controls and PDMS device electrodes increased over time, indicating a facilitation of network activity development. The results suggest that PDMS tunnel devices are a valuable tool for increasing the measurable activity on MEA and can therefore save time and money when using hPSC-derived neurons in disease modelling, pharmacological testing or toxicological screening *in vitro*.

If tunnel devices are to be used for *in vitro* modelling, the activity inside the tunnels must be amenable to pharmacological manipulation. To date, reports from pharmacological experiments in tunnel devices are lacking, except one (Dworak and Wheeler, 2009). Here, we evaluated the effects of a well-established blocker of neuronal activity (TTX) on the MEA signals from entire neuronal networks inside PDMS tunnels. The MEA measurements were performed directly after addition of TTX to the medium, and the results showed that the pharmacological effect of a neuron-specific toxicant inside the tunnels was clear and manifested immediately.

We conclude that PDMS tunnel devices on MEAs are a suitable environment for cultivating neuronal networks of human origin. Although the effects of the tunnel devices on SNR were modest, the devices substantially increased the percentage of active electrodes and amount of detected neuronal network activity in a design-dependent and robust fashion. The tunnels are also suitable for pharmacological testing. Therefore, PDMS tunnel devices encompassing neuronal networks are a promising tool for reducing time and costs in analyses of the activity of hPSC-derived neuronal models on MEAs.

AUTHOR CONTRIBUTIONS

PK, MR, and SN supervised the project; PK, MR, SN, LY, and MM designed experiments; MT performed experiments; MM assisted with the pharmacological experiments; LS produced the PDMS devices; MM, MT, and AP analysed data; MT and AP drafted the manuscript; MT, AP, MM, LY, LS, PK, MR, and SN revised the manuscript.

FUNDING

This work was funded the Finnish Funding Agency for Technology and Innovation (TEKES), and Academy of Finland grants to LY and MR (grant numbers 286990 and 296415, respectively). AP received support from Juliana von Wendt Fund.

ACKNOWLEDGMENTS

The authors thank Kimmo Kartasalo for invaluable help and advice in image processing for the neurite orientation analysis, and Risto-Pekka Pölönen for the introduction to the CytoSpectre software. We are also very grateful to the iPS Cells core facility, University of Tampere, for providing the undifferentiated hiPSCs, the Tampere Facility of Electrophysiological Measurements, University of Tampere (Juha Heikkilä), for facilitating functional measurements, and Hanna Mäkelä and Eija Hannuksela for technical assistance with cell maintenance.

SUPPLEMENTARY MATERIAL

The Supplementary Material for this article can be found online at: https://www.frontiersin.org/articles/10.3389/fnins.2017.00606/full#supplementary-material

REFERENCES

Biffi, E., Regalia, G., Menegon, A., Ferrigno, G., and Pedrocchi, A. (2013). The influence of neuronal density and maturation on network activity of hippocampal cell cultures: a methodological study. *PLoS ONE* 8:e83899. doi: 10.1371/journal.pone.0083899

Cavanaugh, S. E., Pippin, J. J., and Barnard, N. D. (2014). Animal models of Alzheimer disease: historical pitfalls and a path forward. *ALTEX* 31, 279–302. doi: 10.14573/altex.1310071

Dotti, C., Sullivan, C., and Banker, G. (1988). The establishment of polarity by hippocampal-neurons in culture. *J. Neurosci.* 8, 1454–1468.

Duffy, D., McDonald, J., Schueller, O., and Whitesides, G. (1998). Rapid prototyping of microfluidic systems in poly(dimethylsiloxane). *Anal.Chem.* 70, 4974–4984. doi: 10.1021/ac980656z

Dworak, B. J., and Wheeler, B. C. (2009). Novel MEA platform with PDMS microtunnels enables the detection of action potential propagation from isolated axons in culture. *Lab Chip* 9, 404–410. doi: 10.1039/B806689B

FitzGerald, J. J., Lacour, S. P., McMahon, S. B., and Fawcett, J. W. (2008). Microchannels as axonal amplifiers. *IEEE Trans. Biomed. Eng.* 55, 1136–1146. doi: 10.1109/TBME.2007.909533

FitzGerald, J. J., Lacour, S. P., McMahon, S. B., and Fawcett, J. W. (2009). Microchannel electrodes for recording and stimulation: *in vitro* evaluation. *IEEE Trans. Biomed. Eng.* 56, 1524–1534. doi: 10.1109/TBME.2009.2013960

Goyal, G., and Nam, Y. (2011). Neuronal micro-culture engineering by microchannel devices of cellular scale dimensions. *Biomed. Eng. Lett.* 1, 89–98. doi: 10.1007/s13534-011-0014-y

Habibey, R., Golabchi, A., Latifi, S., Difato, F., and Blau, A. (2015). A microchannel device tailored to laser axotomy and long-term microelectrode array electrophysiology of functional regeneration. *Lab Chip* 15, 4578–4590. doi: 10.1039/C5LC01027F

Hong, N., Joo, S., and Nam, Y. (2017). Characterization of axonal spikes in cultured neuronal networks using microelectrode arrays and microchannel devices. *IEEE Trans. Biomed. Eng.* 64, 492–498. doi: 10.1109/TBME.2016.2567424

Hunsberger, J. G., Efthymiou, A. G., Malik, N., Behl, M., Mead, I. L., Zeng, X., et al. (2015). Induced pluripotent stem cell models to enable *in vitro* models for screening in the central nervous system. *Stem Cells Dev.* 24, 1852–1864 doi: 10.1089/scd.2014.0531

Hyysalo, A., Ristola, M., Joki, T., Honkanen, M., Vippola, M., and Narkilahti, S. (2017). Aligned poly(epsilon-caprolactone) nanofibers guide the orientation and migration of human pluripotent stem cell-derived neurons, astrocytes, and oligodendrocyte precursor cells *in vitro*. *Macromol. Biosci.* doi: 10.1002/mabi.201600517. [Epub ahead of print].

Johnstone, A. F. M., Gross, G. W., Weiss, D. G., Schroeder, O. H. U., Gramowski, A., and Shafer, T. J. (2010). Microelectrode arrays: a physiologically based neurotoxicity testing platform for the 21st century. *Neurotoxicology* 31, 331–350. doi: 10.1016/j.neuro.2010.04.001

Jones, I. L., Livi, P., Lewandowska, M. K., Fiscella, M., Roscic, B., and Hierlemann, A. (2011). The potential of microelectrode arrays and microelectronics for biomedical research and diagnostics. *Anal. Bioanal. Chem.* 399, 2313–2329. doi: 10.1007/s00216-010-3968-1

Kapucu, F. E., Tanskanen, J. M. A., Mikkonen, J. E., Ylä-Outinen, L., Narkilahti, S., and Hyttinen, J. A. K. (2012). Burst analysis tool for developing neuronal networks exhibiting highly varying action potential dynamics. *Front. Comput. Neurosci.* 6:38. doi: 10.3389/fncom.2012.00038

Kartasalo, K., Pölönen, R., Ojala, M., Rasku, J., Lekkala, J., Aalto-Setälä, K., et al. (2015). CytoSpectre: a tool for spectral analysis of oriented structures on cellular and subcellular levels. *BMC Bioinformatics* 16:344. doi: 10.1186/s12859-015-0782-y

Kreutzer, J., Ylä-Outinen, L., Karna, P., Kaarela, T., Mikkonen, J., Skottman, H., et al. (2012). Structured PDMS chambers for enhanced human neuronal cell activity on MEA platforms. *J. Bionic. Eng.* 9, 1–10. doi: 10.1016/S1672-6529(11)60091-7

Lappalainen, R. S., Salomaki, M., Ylä-Outinen, L., Heikkilä, T. J., Hyttinen, J. A. K., Pihlajamäki, H., et al. (2010). Similarly derived and cultured hESC lines show variation in their developmental potential towards neuronal cells in long-term culture. *Regen. Med.* 5, 749–762. doi: 10.2217/rme.10.58

Morales, R., Riss, M., Wang, L., Gavin, R., Del Rio, J. A., Alcubilla, R., et al. (2008). Integrating multi-unit electrophysiology and plastic culture dishes for network neuroscience. *Lab Chip* 8, 1896–1905. doi: 10.1039/b802165a

Moser, V. C. (2011). Functional assays for neurotoxicity testing. *Toxicol. Pathol.* 39, 36–45. doi: 10.1177/0192623310385255

Napoli, A., and Obeid, I. (2016). Comparative analysis of human and rodent brain primary neuronal culture spontaneous activity using micro-electrode array technology. *J. Cell Biochem.* 117, 559–565. doi: 10.1002/jcb.25312

Obien, M. E., Deligkaris, K., Bullmann, T., Bakkum, D. J., and Frey, U. (2015). Revealing neuronal function through microelectrode array recordings. *Front. Neurosci.* 8:423. doi: 10.3389/fnins.2014.00423

Odawara, A., Katoh, H., Matsuda, N., and Suzuki, I. (2016). Physiological maturation and drug responses of human induced pluripotent stem cell-derived cortical neuronal networks in long-term culture. *Sci. Rep.* 6:26181. doi: 10.1038/srep26181

Pan, L., Alagapan, S., Franca, E., DeMarse, T., Brewer, G. J., and Wheeler, B. C. (2014). Large extracellular spikes recordable from axons in microtunnels. *IEEE Trans. Neural. Syst. Rehabil. Eng.* 22, 453–459. doi: 10.1109/TNSRE.2013.2289911

Park, J. W., Vahidi, B., Taylor, A. M., Rhee, S. W., and Jeon, N. L. (2006). Microfluidic culture platform for neuroscience research. *Nat. Protoc.* 1, 2128–2136. doi: 10.1038/nprot.2006.316

Pei, Y., Peng, J., Behl, M., Sipes, N. S., Shockley, K. R., Rao, M. S., et al. (2016). Comparative neurotoxicity screening in human iPSC-derived neural stem cells, neurons and astrocytes. *Brain Res.* 1638, 57-73. doi: 10.1016/j.brainres.2015.07.048

Quiroga, R., Nadasdy, Z., and Ben-Shaul, Y. (2004). Unsupervised spike detection and sorting with wavelets and superparamagnetic clustering. *Neural Comput.* 16, 1661–1687. doi: 10.1162/089976604774201631

Ren, Y., Kunze, A., and Renaud, P. (2015). "Compartmentalized microfluidics for *in vitro* Alzheimer's disease studies," in *Microfluidic and Compartmentalized Platforms for Neurobiological Research*, *1st Edn.* ed E. Biffi (New York, NY: Humana Press), 197–215.

Scott, A., Weir, K., Easton, C., Huynh, W., Moody, W. J., and Folch, A. (2013). A microfluidic microelectrode array for simultaneous electrophysiology, chemical stimulation, and imaging of brain slices. *Lab Chip* 13, 527–535. doi: 10.1039/C2LC40826K

Taylor, A. M., Blurton-Jones, M., Rhee, S. W., Cribbs, D. H., Cotman, C. W., and Jeon, N. L. (2005). A microfluidic culture platform for CNS axonal injury, regeneration and transport. *Nat. Methods* 2, 599–605. doi: 10.1038/nmeth777

Tukker, A. M., de Groot, M. W. G. D. M., Wijnolts, F. M. J., Kasteel, E. E. J., Hondebrink, L., and Westerink, R. H. S. (2016). Is the time right for *in vitro* neurotoxicity testing using human ipsc-derived neurons? *ALTEX* 33, 261–271. doi: 10.14573/altex.1510091

Valdivia, P., Martin, M., LeFew, W. R., Ross, J., Houck, K. A., and Shafer, T. J. (2014). Multi-well microelectrode array recordings detect neuroactivity of ToxCast compounds. *Neurotoxicology* 44, 204–217. doi: 10.1016/j.neuro.2014.06.012

Wang, L., Riss, M., Buitrago, J. O., and Claverol-Tinture, E. (2012). Biophysics of microchannel-enabled neuron-electrode interfaces. *J. Neural Eng.* 9:026010. doi: 10.1088/1741-2560/9/2/026010

Wieringa, P. A., Wiertz, R. W. F., de Weerd, E. L., and Rutten, W. L. C. (2010). *In vitro* verification of a 3-D regenerative neural interface design: examination of neurite growth and electrical properties within a bifurcating microchannel structure. *Proc. IEEE* 98, 389–397. doi: 10.1109/JPROC.2009.2038950

Ylä-Outinen, L., Heikkilä, J., Skottman, H., Suuronen, R., Äänismaa, R., and Narkilahti, S. (2010). Human cell-based micro electrode array platform for studying neurotoxicity. *Front. Neuroeng.* 3:111. doi: 10.3389/fneng.2010.00111

Conflict of Interest Statement: The authors declares that the research was conducted in the absence of any commercial or financial relationships that could be construed as a potential conflict of interest.

Supplementary Material

PDMS Tunnel Devices on MEAs Increase the Measurable Activity of Human Stem Cell-Derived Neuronal Networks

Maria Toivanen, Anssi Pelkonen, Meeri Mäkinen, Laura Ylä-Outinen, Lassi Sukki, Pasi Kallio, Mervi Ristola*, Susanna Narkilahti*

*** Correspondence:** Mervi Ristola, mervi.ristola@uta.fi; Susanna Narkilahti, susanna.narkilahti@uta.fi

1 Supplementary Figures and Tables

1.1 Supplementary Figures

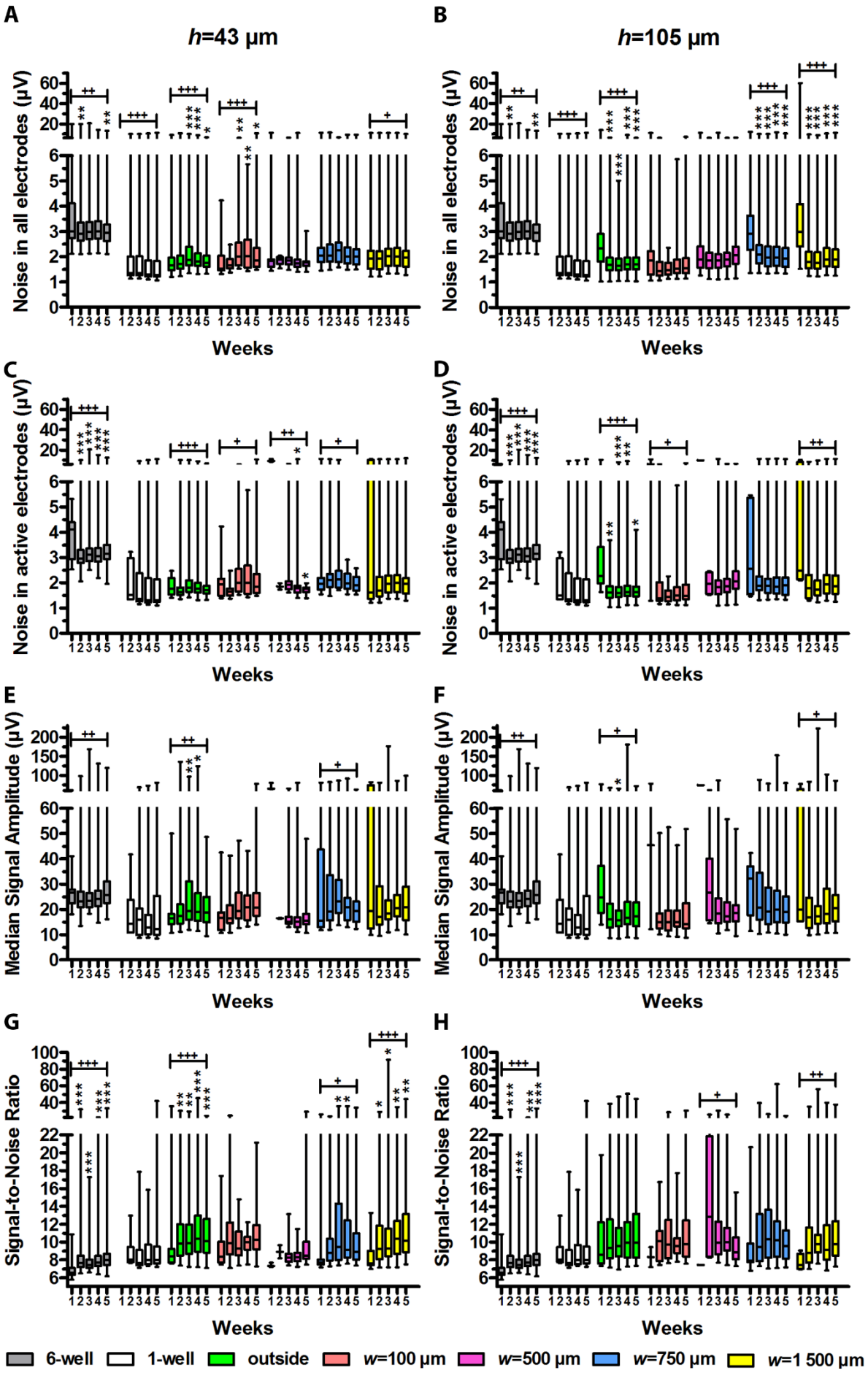
A
h=43 µm
B
h=105 µm
Noise in all electrodes (µV)
C
D
Noise in active electrodes (µV)
E
F
Median Signal Amplitude (µV)
G
H
Signal-to-Noise Ratio
Weeks
6-well
1-well
outside
w=100 µm
w=500 µm
w=750 µm
w=1 500 µm

Supplementary Figure 1. Weekly noise in all and in active electrodes, signal amplitude and signal-to-noise ratio. The weekly noise was calculated for all electrodes in *h*=43 µm **(A)** and *h*=105 µm devices **(B)** and controls (6- and 1-well MEAs). Total *n* of analysed electrodes was 23-270 **(Table 1)**. The weekly noise was also calculated for the active electrodes in *h*=43 µm **(C)** and *h*=105 µm devices **(D)** and controls. Below these is presented the weekly median signal amplitude in active electrodes in *h*=43 µm **(E)** and *h*=105 µm devices **(F)** and controls. The weekly signal-to-noise-ratio in *h*=43 µm **(G)** and *h*=105 µm devices **(H)** and controls was calculated from the noise and median signal amplitude in active electrodes. *n* (active electrodes) was 1-167 **(Table 1)**. The + symbols indicate whether measurement week affected the results according to Kruskal-Wallis test (+: $0.05>p\geq0.01$; ++: $0.01>p\geq0.001$; +++: $p>0.001$). The * symbols indicate the significance of the difference between the particular week and week 1 within the particular tunnel device or control according to Dunn's *post hoc* test (*: $0.05>p\geq0.01$; **: $0.01>p\geq0.001$; ***: $p>0.001$).

frontiers in Cellular Neuroscience

ORIGINAL RESEARCH
published: 06 March 2018
doi: 10.3389/fncel.2018.00056

GABA and Gap Junctions in the Development of Synchronized Activity in Human Pluripotent Stem Cell-Derived Neural Networks

Meeri Eeva-Liisa Mäkinen, Laura Ylä-Outinen and Susanna Narkilahti*

NeuroGroup Laboratory, BioMediTech Institute and Faculty of Medicine and Life Sciences, University of Tampere, Tampere, Finland

The electrical activity of the brain arises from single neurons communicating with each other. However, how single neurons interact during early development to give rise to neural network activity remains poorly understood. We studied the emergence of synchronous neural activity in human pluripotent stem cell (hPSC)-derived neural networks simultaneously on a single-neuron level and network level. The contribution of gamma-aminobutyric acid (GABA) and gap junctions to the development of synchronous activity in hPSC-derived neural networks was studied with GABA agonist and antagonist and by blocking gap junctional communication, respectively. We characterized the dynamics of the network-wide synchrony in hPSC-derived neural networks with high spatial resolution (calcium imaging) and temporal resolution microelectrode array (MEA). We found that the emergence of synchrony correlates with a decrease in very strong GABA excitation. However, the synchronous network was found to consist of a heterogeneous mixture of synchronously active cells with variable responses to GABA, GABA agonists and gap junction blockers. Furthermore, we show how single-cell distributions give rise to the network effect of GABA, GABA agonists and gap junction blockers. Finally, based on our observations, we suggest that the earliest form of synchronous neuronal activity depends on gap junctions and a decrease in GABA induced depolarization but not on $GABA_A$ mediated signaling.

Keywords: human pluripotent stem cells, stem cell derived neurons, microelectrode array, calcium imaging, synchrony, gap junctions, neural network, excitatory GABA

OPEN ACCESS

Edited by:
Enrico Cherubini, Scuola Internazionale Superiore di Studi Avanzati (SISSA), Italy

Reviewed by:
Werner Kilb, Johannes Gutenberg-Universität Mainz, Germany
Annalisa Scimemi, University at Albany (SUNY), United States

****Correspondence:***
Meeri Eeva-Liisa Mäkinen
meeri.makinen@uta.fi

Received: *15 December 2017*
Accepted: *16 February 2018*
Published: *06 March 2018*

Citation:
Mäkinen ME-L, Ylä-Outinen L and Narkilahti S (2018) GABA and Gap Junctions in the Development of Synchronized Activity in Human Pluripotent Stem Cell-Derived Neural Networks. Front. Cell. Neurosci. 12:56. doi: 10.3389/fncel.2018.00056

INTRODUCTION

A better understanding of the human brain and its development would allow us to answer questions such as how the brain functions, how the brain malfunctions, and how the brain can be cured. Despite scientific progress, the nature and function of the human brain remains to be fully understood. The brain carries out cognitive functions and behavior using electrical activity. The electrical activity of the brain arises from single neurons communicating with each other. Groups of communicating neurons form neural networks, which function as the computing hubs of the brain. How single neurons give rise to neural network activity remains poorly understood. Patterned neural network activity arises when asynchronous neurons self-organize their firing patterns into synchronous activity (for review Corlew et al., 2004; Blankenship and Feller, 2010; Kerschensteiner, 2014; Luhmann et al., 2016). Different patterns of activity arising during development have been

described in several systems and uniformly consist of events of synchronous firing of neurons throughout the neural network separated by periods of silence (Blankenship and Feller, 2010; Moore et al., 2011). These patterns differ in the extent of activity propagation and the fraction of cells recruited (Kerschensteiner, 2014). This synchronous firing has been observed *in vivo* (Landmesser and Szente, 1986; Khazipov et al., 1997) and *ex vivo* (Ben-Ari et al., 1989; Garaschuk et al., 1998; Menendez De La Prida et al., 1998; Corlew et al., 2004), as well as *in vitro* both in primary (Khalilov et al., 1997; Leinekugel et al., 1998) and stem cell-derived cultures (Illes et al., 2007; Heikkilä et al., 2009). However, the series of mechanisms that initiate the events of synchronous network activity and the mechanisms suppressing activity during the quiescent periods are not fully understood (Kerschensteiner, 2014).

The mechanisms responsible for controlling the patterned activity are currently thought to consist of a combination of pacemaker-like membrane properties of single neurons and the network interactions between them (Blankenship and Feller, 2010; Momose-Sato and Sato, 2013; Kerschensteiner, 2014). The network interactions mediated by traditional synaptic neurotransmitters in developing neural networks have been shown to work also via extra synaptic transmission (Blankenship and Feller, 2010). Additionally, the mechanisms act homeostatically, adapting to induced impairments by employing an alternative mechanism (Blankenship and Feller, 2010; Kerschensteiner, 2014). However, patterned activity has also been shown to arise in *in vitro* cell cultures, which provide a simpler system for studying its basic mechanisms (Opitz et al., 2002; Sun et al., 2010). Despite the complexity of the environment during development, the network interactions that participate in the patterning of activity during synchronous network events have been found to include a traditional synaptic neurotransmitter gamma-aminobutyric acid (GABA) and gap junctions (Momose-Sato and Sato, 2013). GABA is an inhibitory synaptic neurotransmitter of the adult brain, but in the immature brain, GABA can also excite neurons (Feller, 1999; O'Donovan, 1999; Ben-Ari, 2002). Similarly, gap junctional coupling in an adult brain differs from that of an immature one (Blankenship and Feller, 2010). The role of both GABA and gap junctions in driving the patterned network activity remains uncertain as the reports from different *in vivo* and *ex vivo* preparations contradict each other (Conhaim et al., 2011; Kerschensteiner, 2014). Furthermore, species differences in preparations might also interfere in the translatability across species, which has been shown to be especially poor in the brain (Haston and Finkbeiner, 2016).

Several aspects differ between the primate and the rodent brain (Finlay and Darlington, 1995). For example, developing primate neural networks contain primate-specific stem cell populations and neurons (Hill and Walsh, 2005; Rakic, 2009). The cellular constituents of human-specific neural development can be successfully captured in human pluripotent stem cell (hPSC)-derived neural cultures (Shi et al., 2012). Here, we studied the contribution of GABA and gap junctions to the development of synchronous activity in hPSC-derived neural networks. Developing networks were measured simultaneously at a single neuron resolution with calcium imaging and on a network level with microelectrode arrays (MEAs). The single-neuron responses were associated with the network responses by comparing the calcium imaging and MEA recordings as well as by employing a large scale single-cell analysis. In this article, we show that the strength of GABA excitation played a key role in the formation of network-wide synchrony. Furthermore, synchronous network activity was produced by neurons of different functional maturity levels acting in concert. Finally, we show that the synchronous network activity in hPSC-derived neural networks was not mediated by endogenous GABA and is modulated by gap junctions.

MATERIALS AND METHODS

Human Embryonic Stem Cells

The neural networks used in this study were differentiated from the human embryonic stem cell line Regea 08/023 (Regea 08/023, European Human Embryonic Stem Cell Registry). Regea 08/023 has been previously derived (Skottman, 2010) and was maintained as previously described (Toivonen et al., 2013). This work was conducted under the approval of the Ethics Committee of Pirkanmaa Hospital District for the derivation, characterization, and differentiation of hESC-lines (Skottman, R05116) and under an approval of Valvira, the Finnish National Authority for Medicolegal Affairs, for research on human stem cells (1426/32/300/05).

Neural Cell Derivation, Cell Plating and Coating

The neural differentiation of hESCs was performed as described by Lappalainen et al. (2010). Basic fibroblast growth factor (bFGF) was used at 20 ng/ml during the neurosphere phase. After suspension differentiation, the neurospheres were mechanically dissected.

The pieces of aggregates were plated on thin MEA dishes with a 180-μm-thin recording area, 59 substrate-embedded titanium nitride microelectrodes, a silicon nitride isolator, and an internal reference electrode (60ThinMEA200/30iR-ITO, Multi Channel Systems MCS GmbH). Electrodes with a 30-μm diameter were organized in an 8 × 8 grid with 200 μm spacing. MEA dishes were coated (overnight at +4°C or 2 h at +37°C) with PEI (0.1% polyethylenimine, Sigma-Aldrich) and subsequently with mouse laminin (20 μg/ml, Sigma-Aldrich, St. Louis, MO, USA). Altogether, 36 (29/36 were successful) neural networks were plated onto MEAs. The bFGF was withdrawn at the beginning of adherent culture in MEA. Half of the culture medium was replaced three times a week. The timeline for the experiments is shown in **Figure 1**.

Follow-Up Recordings

MEA follow-up measurements were performed twice a week for 4 weeks or until the end-point measurement. The follow up measurements were performed with the MEA wells sealed with semi-permeable membranes (ALA MEA-MEM, ALA

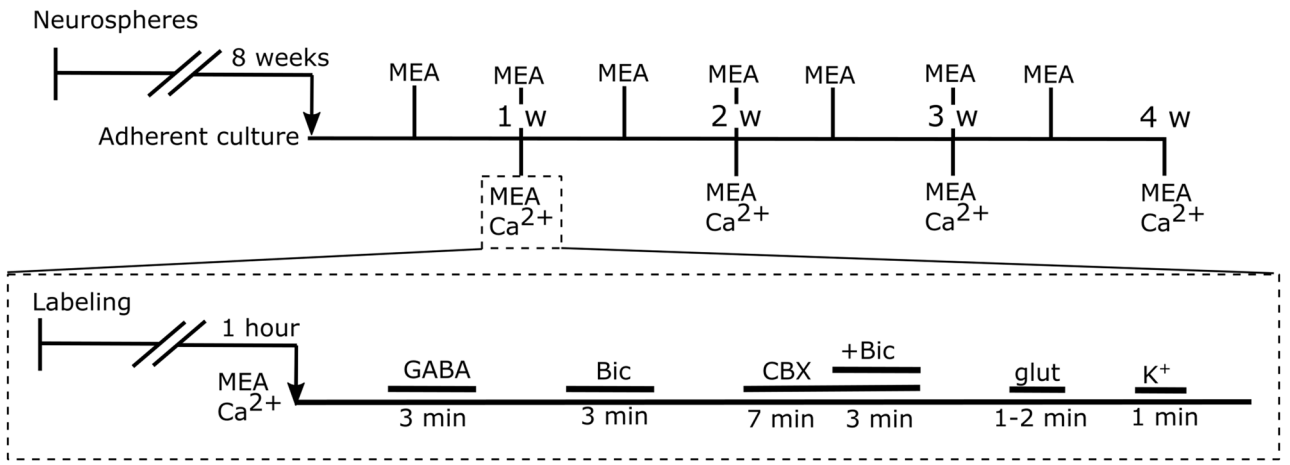

FIGURE 1 | Timeline for the experiments. Top timeline: human pluripotent stem cell (hPSC)-derived neural precursors were cultured as neurospheres for 8 weeks. Next, neural precursors were plated and cultured as adherent cells in order to form neural networks. The functional maturation of the networks was followed by microelectrode array (MEA) measurements twice a week. At each of the 4 weeks, an end-point measurement, MEA and Ca^{2+}, was performed for 5–9 neural cultures (**Table 1**, column 1). Bottom timeline: first, neural cells were labeled for calcium imaging. Next, simultaneous MEA and Ca^{2+} recording was performed, and a series of pharmacological agents were applied. The series consisted of gamma-aminobutyric acid (GABA), the GABAA receptor antagonist bicuculline (Bic), the gap junction blocker carbenoxolone (CBX), glutamate (glut) and high potassium (K+).

Scientific Instruments, Westbury, NY, USA). The voltage from the microelectrodes was measured with a filter amplifier MEA2100 (Multi Channel Systems MCS GmbH, Reutlingen, Germany). The temperature was controlled with an external heater unit (TC02, MCS) set to +38°C, and the cultures were allowed to settle for 1 min in the system before each 5-min follow-up recording. An analog-to-digital conversion was performed at a 50-kHz sampling frequency. The same recording setup was used during combined MEA recording and calcium imaging except the semi-permeable membrane was not used.

End-Point Recordings

Preparation for Calcium Imaging

For the end-point measurement, neural cells (**Table 1**, 1st column) were loaded with Fluo-4 AM (4 μM, F14201, Thermo Fisher Scientific) diluted in fresh cell culture medium for 30 min at 37°C and 5% CO_2. This was followed by a wash with fresh Ringer's solution for 30 min at 37°C and 5% CO_2. The Ringer's solution contained 140 mM NaCl, 10 mM HEPES, 10 mM D glucose, 3.5 mM KCl, 1.25 mM NaH_2PO_4, 2 mM $CaCl_2$ and 1 mM $MgCl_2$ (all from Sigma-Aldrich) dissolved in dH_2O, pH adjusted to 7.4 with NaOH.

Pharmacology

In the beginning of each combined MEA recording and calcium imaging session (**Table 1**, 1st column), a baseline was measured after the culture was perfused with Ringer's solution for at least 10 min. Pharmacological substances were applied to neural cultures via a gravitation-fed perfusion system (2 ml/min, ALA Scientific). Before the cells were perfused, the substances were diluted to their final concentrations. Treatments were applied in the following order: GABA (100 μM, GABA, A5835-10 g, Sigma), $GABA_A$ receptor antagonist bicucullinemethionine (10 μM, Bic, 14343-10MG, Sigma-Aldrich), gap junction blocker carbenoxolone (CBX; 25 μM, CBX, C4790, Sigma-Aldrich), L-glutamic acid (30 μM, glut, G8415-100 g, Sigma), and KCl (5 mM, K+, P9541-500G, Sigma-Aldrich). Each substance application was separated by a 3–5-min perfusion with Ringer's solution.

TABLE 1 | Numbers of measured and analyzed samples.

Age at endpoint	Calcium imaged (& MEA measured) networks	Analyzed calcium imaged networks (on MEA)	Analyzed ROIs (networks)	Analyzed synchronous networks (ROIs)
1 w	7 (5)	5 (4)	3496 (5)	-
2 w	13 (6)	4 (3)	2132 (4)	-
3 w	11 (7)	4 (3)	2136 (4)	3 (1358)
4 w	11 (9)	4 (4)*	2018 (3)	2 (1216)
Total	42 (27)	17 (14)	9782 (16)	5 (2574)

*All the networks measured with MEAs were simultaneously calcium imaged. Likewise, the calcium imaging was analyzed from all the networks whose MEA activity was analyzed. *One of the networks was excluded from detailed quantification (Analyzed ROIs) due to the amount of noise in the recording. w refers to week, MEA refers to microelectrode array, ROI refers to region of interest, in this case, individual neuron.*

Calcium Imaging

During calcium imaging, the neural network activity was imaged every 0.5 s (2 Hz) with a fluorescent imaging system consisting of an Olympus IX61 inverted microscope (10× objective, NA = 0.5), an Andor iXon 885 EMCCD camera (Andor Technology, Belfast, Northern Ireland) and a Polychrom V monochromator (TILL Photonics, Munich, Germany). Images were acquired with TILL Photonics Live Acquisition software. Images were exported into TIFF-stacks from TILL Photonics Offline Analysis software and loaded into MATLAB.

MEA Analysis

Altogether, recordings from 14 neural networks (3–4 per timepoint, **Table 1**, 2nd column), all also included in the calcium analysis, were analyzed (Supplementary Figure S1). The digitized recordings were imported to MATLAB (MathWorks, Inc., Natick, MA, USA) using the NeuroShare library (NeuroShare Library, 2003). The recorded raw MEA signals were noisy due to the noise caused by the perfusion and imaging system. Noise was removed by subtracting the median voltage of all electrodes from the voltage of each individual electrode. The signal was bandpass filtered (200–3000 Hz). Several windows (0.05, 0.1, 0.5, 1, 10, 30, 50, 70, 90, 100, 300 s) with different overlap (30%, 50% and 80%) were compared for optimal noise reduction. Finally, the signal was analyzed in 30-s windows with an 80% overlap. The median of window noise was calculated, and spikes were detected as events that crossed five times the median threshold similar to Quiroga et al. (2004). Detector dead time was 1.5 ms. Spike timestamps and cut-out waveforms (spanning 1 ms prior and 2.2 ms after the maximum of the spike) were stored.

Quantification and Presentation of MEA Data

A grayscale spike rate raster plot was obtained by calculating the spike rate from the spike timestamps for each electrode with 2-s binning. The spike rate was then represented as a grayscale from white to black [0, 0.5 Hz]. For network-level analysis, a combined spike rate (10-s bins, 80% overlap) from all electrodes, with the exception of the ground electrode, was calculated. Network-wide peaks in spike rate were detected using the MATLAB Signal Processing Toolbox. The prominence of an activity peak was calculated as the difference in activity between the peak and the surrounding baseline. Thus, the prominence allowed for the comparison of the increase in activity whether the baseline contained a high or low amount of activity. A prominence of 0.05 was used as a criterion for activity peaks. Peak detection provided values for peak width, prominence, height and timing. The values are represented in images per peak (dots in **Figure 2F**) and as medians of detected peaks (horizontal lines in **Figure 2F**).

Calcium Imaging Analysis

To extract information from all of the cells in the imaged area, an automated segmentation was performed in MATLAB. Altogether, recordings from 17 neural networks (we randomly selected a set of measurements to reach 4–5 measurements per timepoint, **Table 1**, 2nd column) were analyzed. All of the imaging recordings corresponding to the analyzed MEA recordings were analyzed.

Segmentation

In MATLAB, images taken during calcium imaging were segmented with a foreground and background marker-guided watershed transformation (Supplementary Figure S2). Images were preprocessed in MATLAB by averaging 50 subsequent frames and scaling pixel values to range [0, 1].

Foreground markers were generated by a sequence of morphological operations. A threshold marker was used to identify high-intensity objects when performing morphological opening on the preprocessed image. The result of the morphological opening was subtracted from the averaged and scaled image. The resulting image was eroded with a flat morphological disk-shaped structuring element with a radius of 2. Next, the regional maxims were detected from the processed image, and the result was first eroded and then dilated by using a 3 by 3 neighborhood for both operations.

Background markers were generated by setting the value of the pixels in the foreground marker locations on the preprocessed image to the same value. The image was converted to a black-and-white image by thresholding with Otsu's (1979) method. The resulting binary image was used to compute the Euclidean distance transform further used in the Fernand Meyer watershed algorithm (Meyer, 1994). The watershed regions were set to 0, thus leaving the outside areas background markers with a value of 1. To ensure that none of the foreground and background markers were touching, the background markers were dilated with a flat morphological disk-shaped structuring element with a radius of 2, and the resulting pixels were removed from the set of foreground pixels.

For the final watershed transformation, the preprocessed image was parallel filtered with a predefined Sobel horizontal edge-emphasizing 2D-filter and its transpose. The values outside the bounds were assumed to be equal to the array border value for both operations. A watershed transformation was performed on an image generated from the square root of the sum of the exponents of the filtering operations with regional minimums imposed to locations specified by foreground and background markers.

Tracking

The segmentation results were tracked by minimizing the distance between the centroids of detected cells. This was performed by using a cost matrix generated from the distances between the centroids of areas resulting from segmentation. A gating threshold of 20 was used for distances together with a gating cost of 5000. The cost of non-assignment was set to 500. The minimum track age was set to 20 and visibility to 0.5 of the time. The optimal track was calculated with the James Munkres's variant of the Hungarian assignment algorithm (Munkres, 1957).

The track information was used to generate a fluorescence intensity trace for each cell. Altogether, traces from 9782 cells were collected. Each fluorescent intensity trace was normalized to [0, 1]. Thus, the intensity value 1 reflects the maximum intensity of a cell during the recording, and measured responses are

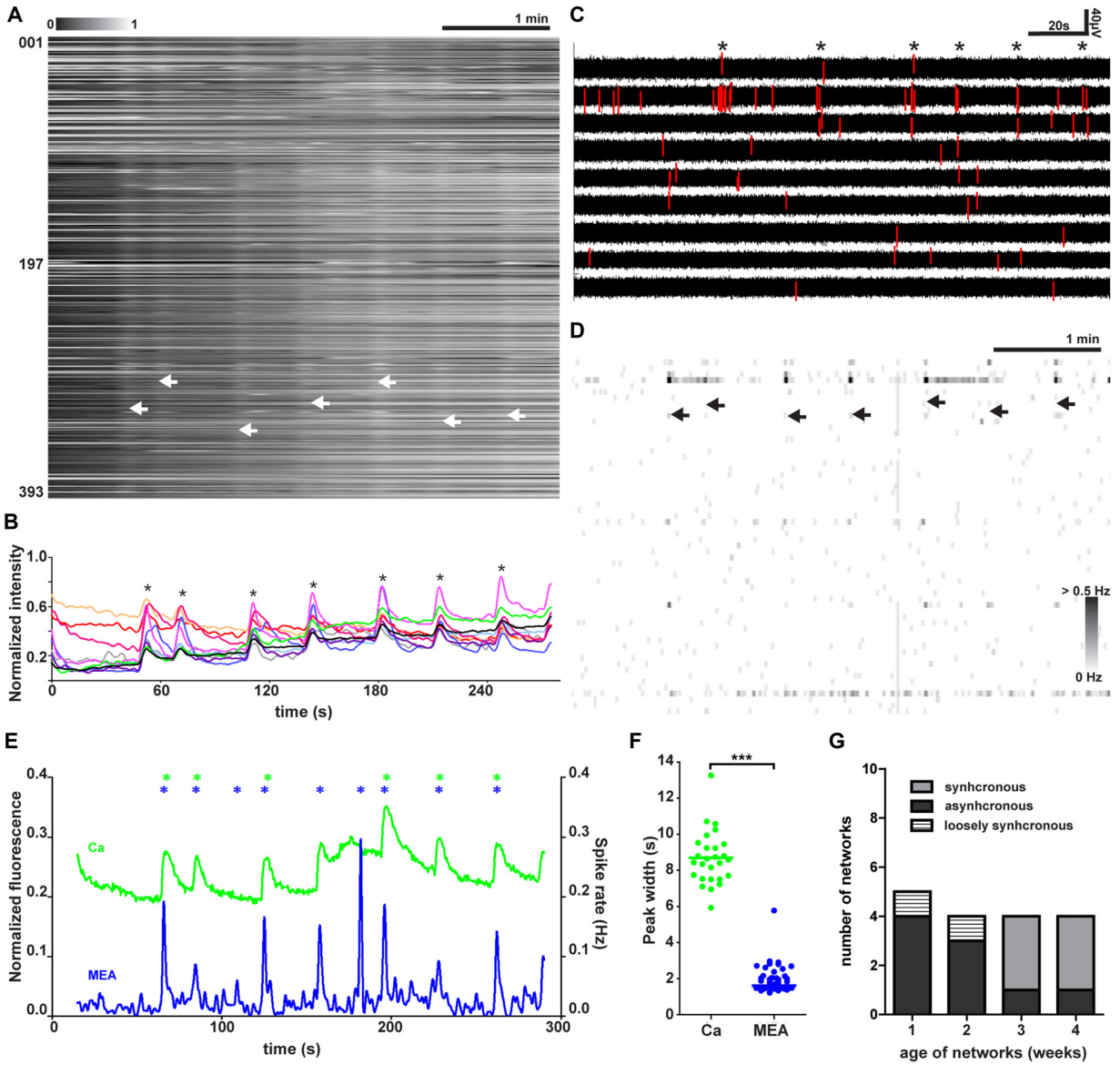

FIGURE 2 | Spontaneous synchronized network activity during baseline. **(A)** Normalized raster plot of spontaneous intracellular Ca^{2+} fluctuations from all neurons (n = 393) in the imaged area from one synchronous network. Each row of pixels (y-axis, number of neuron) contains normalized intensity changes (gray scale bar) during a 5-min (x-axis) recording from one neuron. Vertical stripes (arrow heads) denote network-wide synchronous intracellular calcium rises. **(B)** Representative single-neuron intracellular calcium level traces (y-axis) from 10 representative synchronously active neurons. Neurons are selected from the recording shown in **(A)**. Traces show the normalized fluorescent calcium dye intensity (y-axis) over time (x-axis). The asterisks mark synchronous intracellular calcium rises. **(C)** MEA recording from nine selected electrodes during baseline activity in one network. Each row contains a voltage trace from one electrode. Asterisks mark the moments of synchronous activity. Voltage values associated with detected spikes are drawn in red. Vertical scale bar denotes a 40-μV change in the measured voltage, and the horizontal scale bar denotes 20 s of time. **(D)** MEA recording as a grayscale spike rate raster plot during synchronous baseline activity from the same network at the same time as in **(A)**. Spikes detected from individual electrodes are indicated by gray levels according to the associated scale bar. Each row represents the spike rate (gray scale bar) detected by one electrode (n = 60, y-axis) on one row in the grayscale raster plot. Synchronous network activity marked with arrow heads. **(E)** Network activity as summed Ca^{2+} fluctuations (green) and global MEA firing rate (blue) from one representative network (393 neurons) during baseline. Vertical scale bar corresponds to a 20% change in fluorescence (green trace) and 0.02-Hz change in spike rate (blue trace). Asterisks mark the peaks of network activity detected during the baseline for the summed calcium signal (green) and whole MEA spike rate (blue). **(F)** Widths of the network activity peaks from summed Ca^{2+} fluctuations (green, n = 27 peaks) and global MEA firing rate (blue, n = 46 peaks) for all networks (n = 5 networks). ***marks significant ($p < 0.001$) difference between peak widths measured by calcium imaging or MEA during baseline. **(G)** Number and relative proportion of synchronous, asynchronous and loosely synchronous network activity found at each time point.

expressed as a fraction of the saturation level of the fluorescent signal (Carmignoto et al., 1998; Maravall et al., 2000).

The collected traces were filtered with a Butterworth bandpass filter (0.0013–0.02 Hz), and traces with a standard deviation

greater than 0.05 were removed as noisy. Traces with less than a 10% increase in normalized fluorescence during the application of high potassium were removed as inactive or originating from cells other than neurons. The amount of remaining traces in a network was always more than 98% of the initial traces.

Quantification and Presentation of Calcium Imaging Data

The images of all included calcium traces (117–1354 traces per image) were formed by aligning all individual calcium traces of a recording (n = 17 networks, **Table 1**, 2nd column). To estimate the network response (n = 5 networks), the individual traces were bandpass filtered [0.005–0.2 Hz] with a Butterworth filter and normalized. The traces were then summed, and the sum was normalized. Network activity peaks were detected when the peak prominence exceeded 0.025. The same criterion was used for individual traces (n = 2574 traces from synchronous networks). Peak detection for both individual traces and network traces was done with the MATLAB Signal Processing Toolbox. Peak detection provided values for peak width, prominence, height and timing. The values are represented in result images per peak (dots in **Figures 2F**, **5C**, **6D**, **7D,E**) and as medians of detected peaks (asterisks in **Figures 5E,F**, **6F**, **7F,G**). The change in peak prominence or inter-peak interval was counted as difference from baseline. Relative change was obtained by dividing the change with the baseline value. The distribution of peak prominences and inter-peak intervals were represented as histograms obtained with 0.005 and 1-s binning, respectively. Change distributions were also represented as a histogram, all with 5% binning. Cumulative sums were obtained from the aforementioned histograms. Excitatory GABA responses were calculated by low-pass filtering traces with a 0.024-Hz Butterworth filter and summed during baseline and GABA application. The difference between these two was taken as the excitatory GABA response.

Statistical Analysis

For data represented in **Figures 2F**, **5C**, **6D**, **7D,E** Wilcoxon signed rank test (paired, two-tailed, nonparametric) was performed in GrapPad Prim 5.02. For data represented in **Figures 5D**, **6E** the Pearson correlation coefficients and p-values were calculated in MATLAB.

RESULTS

Emergence and Properties of Synchronous Network Activity

To study the development of neuronal network functionality, hPSC-derived neural cells were plated on top of MEAs and allowed to spontaneously form neural networks (n = 17, Supplementary Figure S3). The development of activity in neural cell cultures was followed by measuring extracellular voltage signals twice a week with the underlying MEA. In addition, at 1-week, 2-week, 3-week, and 4-week, and 4-w time points, intracellular calcium level changes were measured simultaneously with MEA recording (**Table 1**, column 1). During this measurement, a series of pharmacological agents (see "Materials and Methods" section **Figure 1**) was applied.

Live-cell calcium imaging during baseline revealed three distinct patterns of activity. We labeled these patterns of activity as synchronous, asynchronous and loosely synchronous activity. A representative recording from one synchronous network is shown in **Figure 2A**. The synchronous activity was marked by tightly synchronous rises of intracellular calcium seen as white vertical stripes with clear borders when measurements from all neurons in the imaged field of view were aligned. A representative recording from one asynchronous network is shown in Supplementary Figure S4C. The aligned traces from asynchronous networks did not show any stripes. A representative recording from one loosely synchronous network is shown in Supplementary Figure S4D. Loosely synchronous networks were distinguished from asynchronous by the presence of stripes, but when compared to synchronous networks their borders were not clear-cut and contained staggered ends of calcium traces. The difference between synchronous and loosely synchronous networks was more clear when comparing individual neuronal traces (**Figure 2B** and Supplementary Figure S4B, respectively). In synchronous networks the neurons were mostly silent between network events and had their highest activity during the event, while the activity during events was not remarkably different from the activity between network events in the loosely synchronous networks.

These synchronous network events occurred at a median rate of 0.03 Hz (∼2 per minute, n = 5 networks, **Table 1**, column 4), but the interval between events varied on average from 18 s to 49 s. The activity was studied more closely at the level of a single trace, and the activity of 10 individual neurons from a synchronous network is shown in **Figure 2B**. From single-neuron traces, it was possible to see that the participating neurons were not active during every network event and that the level of increase in calcium in a cell during synchronous activity varied between events.

Synchronized activity was also detected in the simultaneously performed MEA recordings (n = 5, **Table 1**, column 4). On MEA recordings, the synchronous network events were seen as an increase in the number of detected spikes occurring in a limited time window across several electrodes. **Figure 2C** shows a representative recording from selected electrodes from one network. When the spikes trains were observed more closely, the number of detected spikes associated with network events clearly varied between events. Furthermore, few spikes were also detected during the less active intervals between the network events. Electrodes measuring the highest levels of activity within one network were usually participating in the synchronous activity as well. Spike rates across the MEA during several network events in one neural culture are shown in **Figure 2D**.

Next, the network responses of the calcium imaging and MEA recordings were formed by summing the signal of individual components, single-neuron calcium traces or single-electrode spike rates, respectively (n = 5, **Table 1**, column 4). Aligned network responses from calcium imaging and the MEA recording from one representative network are shown

in **Figure 2E**. The intracellular calcium rises and the fast extracellular field potential changes on MEA were temporally associated with each other. The temporal association between the calcium imaging and MEA recording indicates that the recorded intracellular calcium rises arise from action potential firing. However, one of five networks with synchronous activity associated with the intracellular calcium rises did not show any synchronous activity on the MEA recording. Compared to the intracellular calcium rises, the extracellular signals recorded during the synchronous activity peaked higher above baseline and returned back to baseline faster. This was further studied by quantifying the width of network activity peaks. The widths of network activity peaks of network events are shown in **Figure 2F**. The action potential firing window (1.6 s, median of 27 peaks from five synchronous networks) was significantly ($p < 0.001$) smaller and more stable than the window of intracellular calcium fluctuation (8.7 s, median of 46 peaks from five synchronous networks).

The synchronous activity, seen as stripes in aligned Ca^{2+} traces, was detected in neural networks earliest after 3 weeks of adherent culture. The amount of different types of network activity patterns at each week of adherent culture is shown in **Figure 2G** (n = 17, **Table 1**, 2nd column). Before 3 weeks, network activity was mainly asynchronous (78%, 7 of 9, Supplementary Figure S4), with a minority (22%, 2 of 9) of networks loosely synchronous (Supplementary Figure S4). After 3 weeks, the majority (80%, 6 of 8) of the recorded networks manifested synchronous activity, with a minority of asynchronous networks (20%, 2 of 8).

To summarize, we observed the emergence of synchronous activity in hPSC-derived neural networks earliest at 3 weeks. The synchronous activity was observed as population-wide increases in activity measured simultaneously by calcium imaging and MEA.

GABA Response in Single Cells

The responses to GABA application during combined calcium imaging and MEA recording were analyzed. The assessment of aligned intensities from whole networks (n = 17) revealed that loosely synchronized neural networks (n = 2 networks, n = 1419 neurons) contained strongly GABA-depolarized neurons that did not participate in synchronous network events. A representative recording during GABA application from a loosely synchronous network is shown in **Figure 3A**.

The role of the depolarizing GABA response of individual neurons in relation to the generation of a synchronously active network was further studied by quantifying the single-neuron responses (n = 8959, **Table 1**, column 3) to GABA application. There was no clear connection between the network age and response to GABA. Thus, we formed three groups based on the network activity pattern (synchronous, loosely synchronous, and asynchronous). The proportions of neurons within each network with respect to the GABA response level are shown in **Figures 3B,C**. The stronger the GABA depolarization, the smaller the proportion of those responses in synchronous networks compared to the proportion in asynchronous and

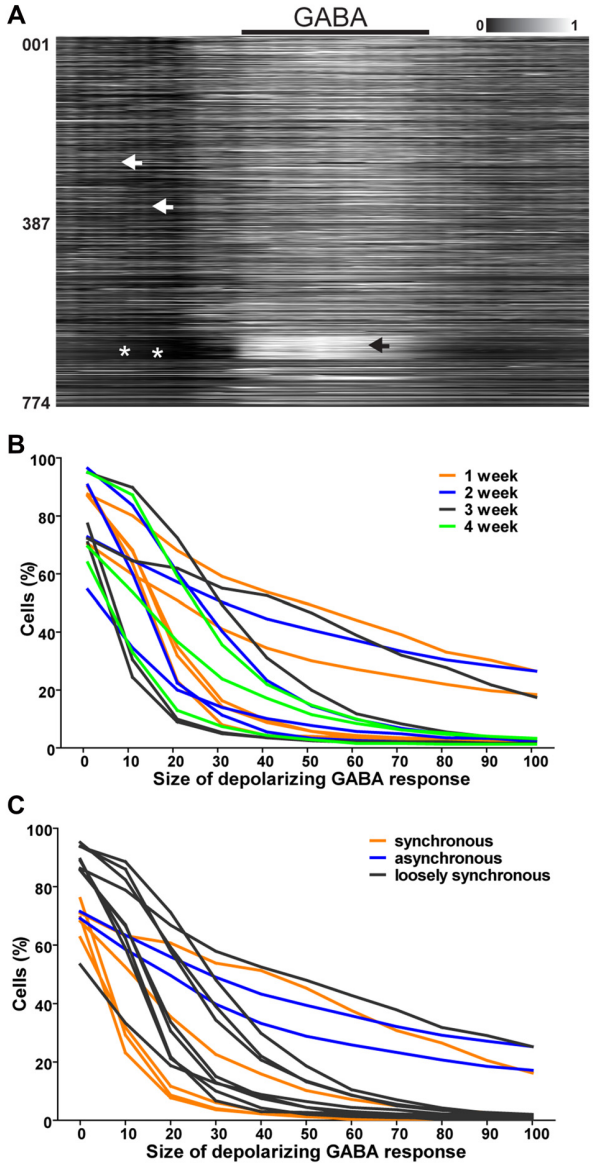

FIGURE 3 | GABA responses in single neurons. **(A)** Normalized raster plot of spontaneous intracellular Ca^{2+} fluctuations from all neurons (n = 774) in the imaged area from one loosely synchronous network during GABA application (black bar, 3 min). Each row of pixels (y-axis, number of neuron) contains normalized intensity (gray scale bar) changes during a 10-min (x-axis) recording from one neuron. Black arrow head points to a group of neurons with a high intracellular calcium rise in response to GABA application. White arrow heads point to events of loose synchronous activity. White asterisks mark the lack of synchrony. **(B)** Reverse cumulative sum of % of neurons in the field of view (y-axis) with respect to the depolarizing response of single neurons to GABA application (x-axis) is shown for each network. Neurons from 1 (n = 774, 1354, 472, 493 and 403), 2 (n = 645, 454, 538 and 495), 3 (778, 117, 670 and 571) and 4 (n = 585, 823, 393) weeks old networks are represented with orange, blue, black and green respectively. **(C)** Reverse cumulative sum of % of neurons in the field of view (y-axis) with respect to the depolarizing response of single neurons to GABA application (x-axis) is shown for each network. Neurons from networks with synchronous activity (n = 117, 670, 571, 823 and 393 neurons), no synchrony (n = 585, 778, 454, 1354, 493, 495, 472, 403 and 531 neurons) and loose synchrony (n = 774 and 645 neurons) are represented with orange, blue and black, respectively.

loosely synchronous networks. No clear change in the network composition was observed regarding the culture age. Thus, synchronous networks were the least GABA depolarized when compared to asynchronous and loosely synchronous networks. Furthermore, each of the synchronous networks (5 of 5) had a distribution of GABA responses from depolarizing to inhibitory.

Individual traces were compared more closely to study their participation in the network-wide synchronous activity. Four representative traces from three types of observed responses are shown in **Figure 4A**. The individual neurons within one network could, for example, be moderately depolarized, have no response or be inhibited as a response to GABA application. Traces representing different responses were combined to study if there was synchrony between neurons with different responses to GABA. A representative alignment is shown in **Figure 4B**. Neuronal cells with different GABA responses were observed to participate in the synchronous activity together within the network (5 of 5).

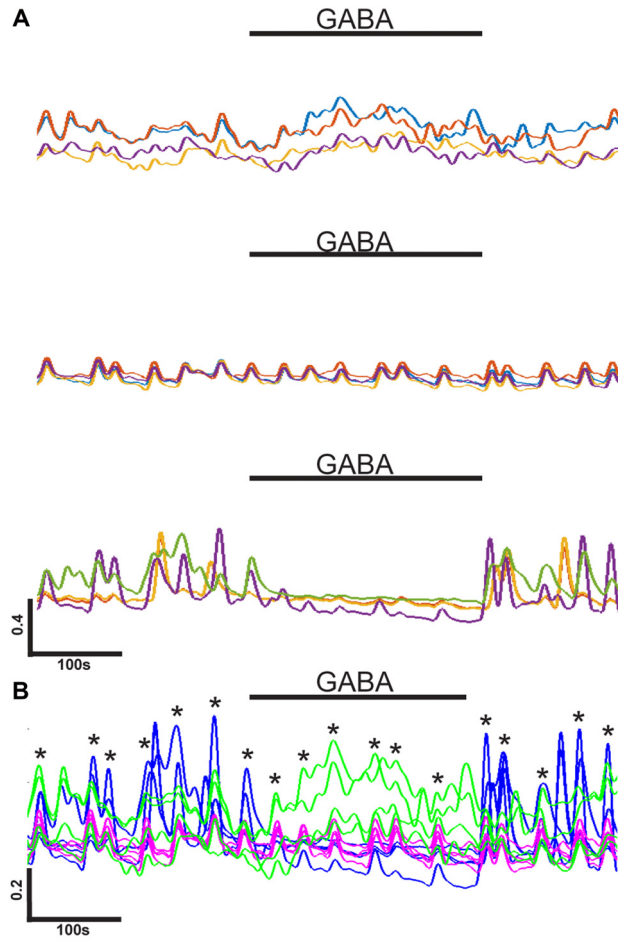

FIGURE 4 | Heterogeneous GABA responses in single network. **(A)** Groups of four representative normalized calcium level (y-axis) traces with different responses to GABA application (black bars) within one network. Traces are examples of a slight increase in intracellular calcium (top), no response (middle), and an inhibition of activity (bottom) during GABA application. Horizontal scale bar corresponds to 100 s. Vertical scale bar corresponds to a 0.4 (40% of max) increase in calcium indicator fluorescence intensity. **(B)** Example of synchrony between differently behaving neurons in the same network [same as in **(A)**]. Traces are from four neurons exited by GABA (green), four neurons not responding to GABA (purple/pink), and four neurons inhibited by GABA (blue). Black bar corresponds to GABA application. Asterisks mark the moments on synchronous activity peaks. Horizontal scale bar corresponds to 100 s. Vertical scale bar corresponds to a 0.2 (20% of max) increase in calcium indicator fluorescence intensity.

In summary, we observed that the presence of synchronous spontaneous activity in hPSC-derived networks was associated with a lack of strongly GABA-depolarized neurons and a smaller proportion of neurons depolarized by GABA than in asynchronous and loosely synchronous networks. Furthermore, we observed that strongly GABA-depolarized neurons are often not participating in network activity patterns.

GABA Response in Synchronously Active Networks on the Network Level

To reveal any spatial organization of neurons within the networks with respect to GABA responses, the neurons of the imaged area were pseudo-colored based on their GABA response. A pseudo-colored image of the area is shown in **Figure 5A**. No organizational pattern based on the different maturity level of the neurons, as defined by the GABA response, was observed in the networks.

To assess how the heterogeneous network responded as a whole to increased GABA, calcium imaging and MEA recordings were studied on the network level. Synchronously active networks (five networks, 1702 neurons, **Table 1**, column 4) were used in this analysis because they were the only networks that showed stable network-wide activity. The global network activity was assessed as summed calcium fluctuations for calcium imaging and as firing rate of the whole MEA for one representative network as shown in **Figure 5B**. To compare the synchronous networks to each other, the network-level events, peaks of synchronous activity, were quantified with respect to their prominence from the baseline level of activity between peaks. The global activity peak prominence during calcium imaging at baseline and during GABA application is shown for each synchronous network ($n = 5$) in **Figure 5C**. The synchronous networks responded to GABA application in two different manners. The network-level activity was either strongly and significantly ($p < 0.05$) inhibited or not significantly ($p > 0.05$) affected, even though the networks contained cells excited by GABA. Furthermore, these two response groups differed in their baseline activity. The initial activity during synchrony was high (over 0.1 peak prominence) for networks strongly blocked by GABA and low (less than 0.05 peak prominence) for networks that barely responded to GABA. The change in interval between synchronous peaks of activity during GABA application was also analyzed but no clear change was observed.

The connection between the initial activity level and the GABA response was further studied on the single-neuron level by measuring the initial peak prominence and change in peak prominence during GABA application. The peak prominence

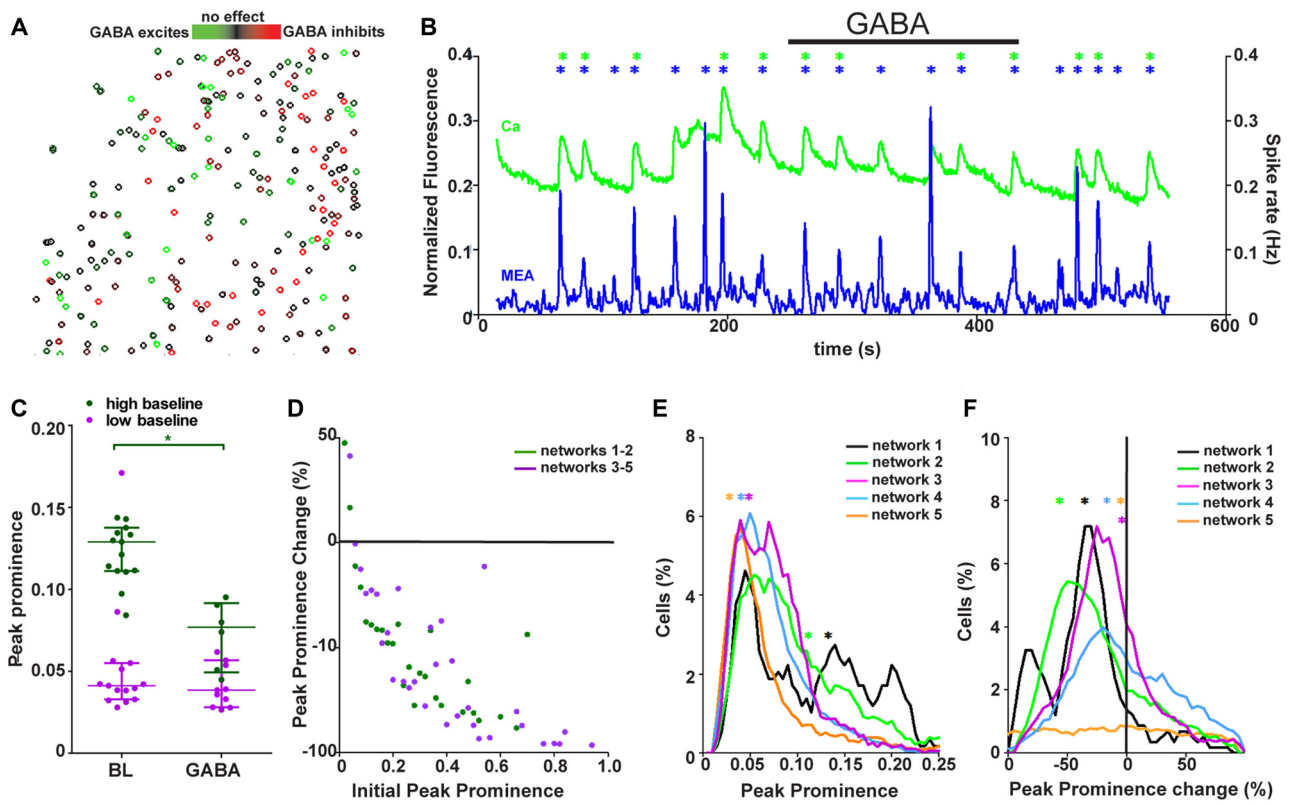

FIGURE 5 | Synchronously active networks are a heterogeneous mixture of synchronously active neurons with different GABA responses. **(A)** Spatial distribution of neurons (n = 393) colored based on their response to GABA (from green to black = strongly excited to not responding, from black to red = not responding to strongly inhibited) from one representative network. **(B)** Network activity as summed Ca^{2+} fluctuations (green, 393 neurons) and global MEA firing rate (blue) from one representative network during GABA application (back bar, 4 min). Black bar shows the time of GABA application. Asterisks mark the population activity peaks detected from the network activity traces (calcium imaging = green, MEA = blue). **(C)** Peak prominence of Ca^{2+} network activity [example trace represented in green in **(B)**]. Each dot represents an individual peak prominence (marked with asterisks in **B**) of network activity during baseline and GABA application. Peaks of activity from different groups of networks are represented by different colors. Horizontal bars represent the median network activity peak prominence for each network group. *marks significant ($p < 0.05$) difference between peak prominence during baseline and GABA application. **(D)** The single-neuron responses to GABA as a change in peak prominence (y-axis) plotted against the initial peak prominence (x-axis) from 688 (dark green, neurons from networks with strong GABA inhibition) and 1886 (purple, neurons from networks with barely any GABA response) neurons from the synchronous networks. **(E)** Distributions of the single-neuron peak prominence during baseline for all synchronous networks. Different networks are represented by different colors (black: 117, orange: 670, green: 571, blue: 823 and purple: 393 neurons). Distribution depicts the peak prominence (x-axis) and the % of neurons in the network with the corresponding peak prominence (y-axis). The asterisks represent the medians of the peak prominence of the network activity. **(F)** Distributions of single-neuron peak prominence changes in response to GABA application for all synchronous networks. Different networks are represented by different colors (black: 117, orange: 670, green: 571, blue: 823, and purple: 393 neurons). Distribution depicts the peak prominence % change (x-axis) and the % of neurons in the network with the corresponding peak prominence change (y-axis). The asterisks represent the medians of the peak prominence change in the network activity.

associated with the initial activity is shown in **Figure 5D**. During GABA application, similar to the network-level responses, the individual neurons with a higher initial activity were more strongly inhibited than neurons with a low initial activity. The correlation between initial activity and strength of GABA effect for neurons within strongly or barely inhibited networks was -0.7273 ($p < 0.0002$) and -0.7175 ($p < 0.000005$), respectively. This seemed to be independent of the network they were from. To see if the composition of the neural networks was connected to the network-level response, the proportion of neurons with respect to their initial activity (**Figure 5E**) and strength of GABA inhibition (**Figure 5F**) was quantified for each network. The synchronous networks with higher initial activity contained a larger proportion of neurons with higher initial activity. This pattern was seen as an increased proportion of neurons with a peak prominence of 0.1–0.2. Likewise, the networks inhibited more strongly with GABA contained larger proportions of neurons with stronger GABA inhibition.

In summary, the network was observed to be a heterogeneous mixture of neurons with different responses to GABA. Furthermore, the synchronous networks were either highly active at baseline and strongly inhibited by GABA or less active during baseline and barely affected by GABA. Furthermore, on the single-cell level, initial activity was related to the GABA response in a network-independent manner. The proportion of neurons

with high initial activity correlated with the network response to GABA.

GABAergic Signaling in Synchronously Active Networks

The role of endogenous GABAergic signaling in synchronous network activity (five networks, 1702 neurons, **Table 1**, column 4) was studied by blocking $GABA_A$ receptors with bicuculline (Bic). Responses to endogenous GABAergic activity blockade were analyzed from combined calcium imaging and MEA recordings. A representative calcium imaging and MEA recording from one network is shown in **Figures 6A–C**. Despite the presence of the $GABA_A$ receptor blocker and the presence of GABA-responsive neurons, no disruption of the synchronous activity was observed. Thus, the synchronous activity is not completely dependent on GABAergic signaling.

The network-level response to blockade of endogenous GABAergic signaling was quantified to study if there was an effect. The global activity peak prominence during calcium imaging at baseline and during $GABA_A$ receptor blockade is shown for each synchronous network (n = 5) in **Figure 6D**. The synchronous networks responded to GABAergic signaling

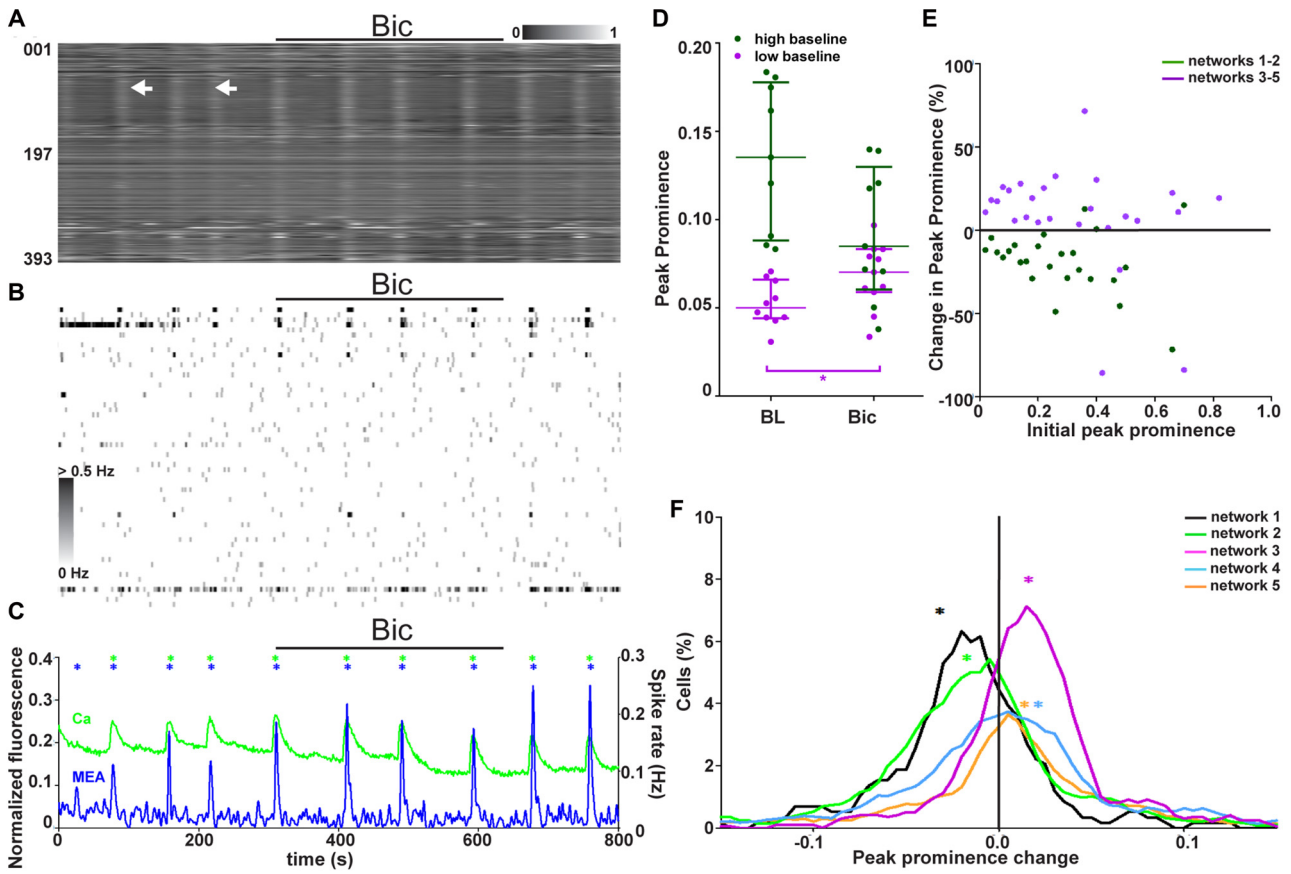

FIGURE 6 | Two classes of networks with different GABAergic signaling. **(A)** Normalized raster plot of spontaneous intracellular Ca^{2+} fluctuations from all neurons (n = 393) in the imaged area from one synchronous network during GABAA receptor blocker (bicuculline (Bic), 3 min) application (black bar). Each row of pixels (y-axis, number of neuron) contains the normalized intensity (gray scale bar) changes during a 7-min (x-axis) recording from one neuron. Vertical stripes (arrow heads) denote synchronous intracellular calcium rises. **(B)** A grayscale spike rate raster plot of an MEA recording from the same network at the same time as calcium imaging in **(A)**. Spikes detected from individual electrodes (n = 60, y-axis) are indicated by gray levels according to the associated scale bar. Black bar denotes GABA receptor blocker (Bic) application. Timescale (x-axis) is the same as in **(A)**. **(C)** Network activity as summed Ca^{2+} fluctuations (green) and global MEA firing rate (blue) from one representative network (393 neurons, same as in **A,B**) during GABAA receptor blocker (Bic) application (back bar). Asterisks mark the population activity peaks detected from the network activity traces (calcium imaging = green, MEA = blue). **(D)** Peak prominence of the Ca^{2+} level-based network activity (example trace represented green in **C**). Each dot represents an individual peak prominence (marked with asterisks in **C**) of network activity during baseline and GABAA receptor blocker (Bic) application. Peaks of activity from different groups of networks are represented by different colors. Horizontal bars represent the median network activity peak prominence for each network group. *marks significant ($p < 0.05$) difference between peak prominence during baseline and blocker application. **(E)** The single-neuron responses to $GABA_A$ receptor blockade as a change in the peak prominence (y-axis) plotted against the initial peak prominence (x-axis) from 688 (dark green, neurons from networks with high initial activity) and 1886 (purple, neurons from networks with low initial activity) neurons from the synchronous networks. **(F)** Distributions of single-neuron peak prominence changes in response to $GABA_A$ receptor blockade for all synchronous networks. Different networks are represented by different colors (black: 117, orange: 670, green: 571, blue: 823, and purple: 393 neurons). The distribution depicts the peak prominence % change (x-axis) and the % of neurons in the network with the corresponding change (y-axis). The asterisks represent the medians of the peak prominence changes in the network activity.

blockade on the network level in two different manners. These two groups of networks were the same as those seen during GABA application and baseline. Endogenous GABAergic signaling blockade did not significantly ($p > 0.05$) inhibit the networks with a high initial activity but significantly significant ($p < 0.05$) increased activity in the networks with low initial

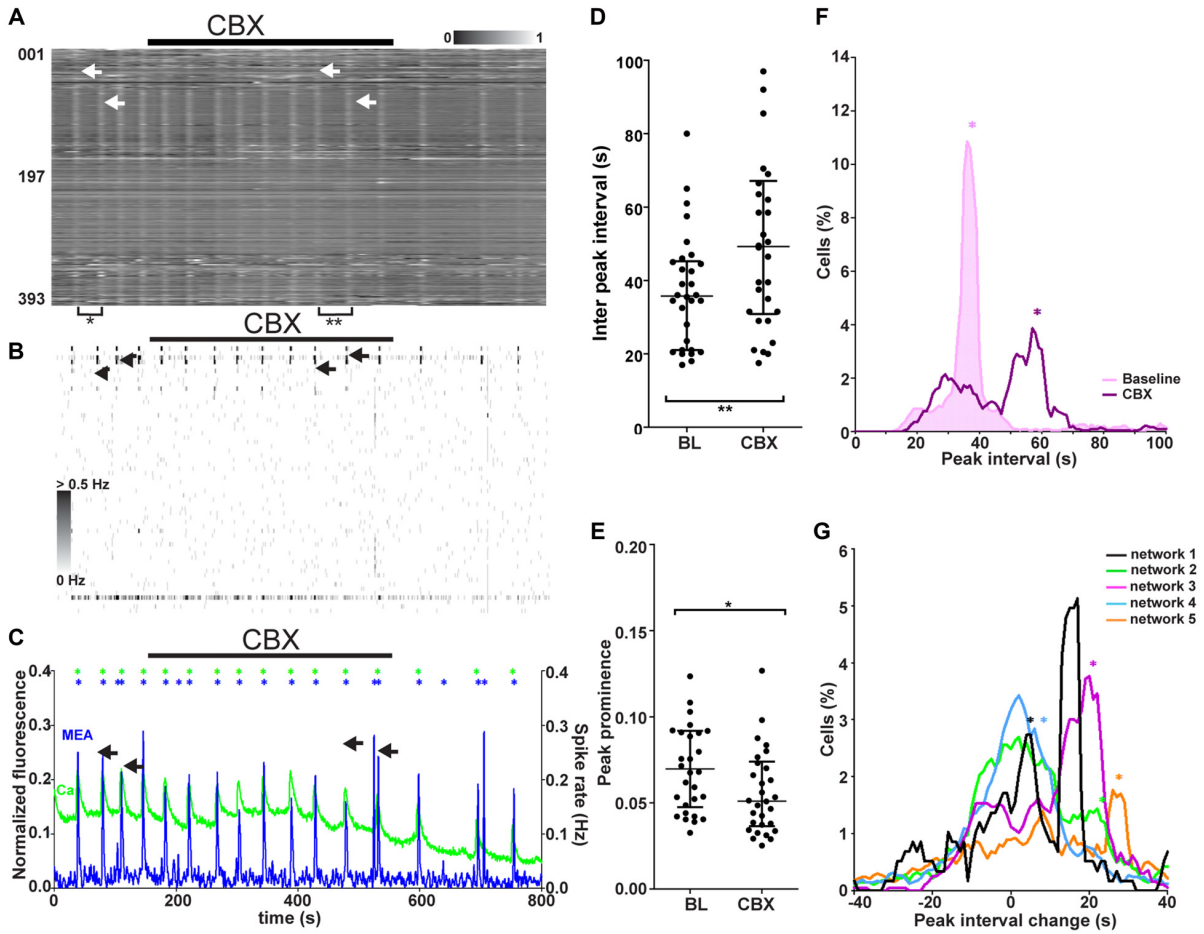

FIGURE 7 | Network responses to blockade of gap junction-mediated signaling in synchronous networks. **(A)** Normalized raster plot of spontaneous intracellular Ca^{2+} fluctuations recorded from all neurons ($n = 393$) in the imaged area from one synchronous network during baseline (BL) and gap junction blocker (CBX) application (black bar). Each row of pixels (y-axis, number of neuron) contains the normalized intensity (gray scale bar) changes during a 14.5-min (x-axis) recording from one neuron. Vertical stripes (arrow heads) denote synchronous intracellular calcium rises. Brackets mark the gap between vertical lines of synchronous activity, the inter-peak interval, during baseline (*) and CBX application (**). The arrows indicate two adjacent network events, one during baseline and one during CBX application. **(B)** A grayscale spike rate raster plot of an MEA recording from the same network at the same time as the calcium imaging in **(A)**. Spikes detected from individual electrodes ($n = 60$, y-axis) are indicated by gray levels according to the associated scale bar. Black bar denotes gap junction blocker (CBX) application. Timescale (x-axis) same as in **(A)**. The arrows indicate two adjacent network events, one during baseline and one during CBX application. **(C)** Network activity as summed Ca^{2+} fluctuations (green) and global MEA firing rate (blue) from one representative network (393 neurons, same as in **A,B**) during gap junction blocker (CBX) application (back bar). Asterisks mark the population activity peaks detected from the network activity traces (calcium imaging = green, MEA = blue). Duration of the shown signals is the same as in **(A)**. The arrows indicate two adjacent network events, one during baseline and one during CBX application. **(D)** Inter-peak interval of Ca^{2+} level-based network activity (example trace represented green in **C**). Each dot represents an individual value between two adjacent peaks (marked with asterisks in **C**) of network activity during baseline or gap junction blocker (CBX) application (3 min during the end of application). Horizontal bars represent the median network activity peak intervals. **marks significant ($p < 0.01$) difference between inter-peak interval during baseline and blocker application. **(E)** Peak prominence of Ca^{2+} level-based network activity (example trace represented green in **C**). Each dot represents an individual peak prominence (marked with asterisks in **C**) of network activity during BL and gap junction blocker (CBX) application. Only the last 3 min of activity during CBX application were taken into consideration due to the slow effect of CBX. Horizontal bars represent the median network activity peak prominence. *marks significant ($p < 0.05$) difference between peak prominence during baseline and blocker application. **(F)** Single-neuron ($n = 393$) inter-peak interval distribution of one representative network during baseline (pink shaded area) and gap junction blocker application (purple non-shaded area). The distribution depicts the inter-peak interval (x-axis) and the % of neurons in the network with the corresponding interval (y-axis). The asterisks (now vertical lines) represent the inter-peak interval of the network activity (same as horizontal lines in **D**) during baseline (pink) and gap junction blockade (purple). **(G)** Distributions of single-neuron inter-peak interval changes in response to gap junction signaling blockade for all synchronous networks. Different networks are represented by different colors (black: 117, orange: 670, green: 571, blue: 823, and purple: 393 neurons). The distribution depicts the inter-peak interval % change (x-axis) and the % of neurons in the network with the corresponding change (y-axis). The asterisks represent the medians of the inter-peak interval changes in the network activity.

activity (). The change in interval between synchronous peaks of activity during Bic application was analyzed but no clear change was observed.

The connection between the initial activity level and the response to GABAergic signaling blockade (with Bic) was further studied on the single-neuron level. The neuron responses as peak prominence with respect to initial activity are shown in **Figure 6E**. Unlike responses to GABA, the responses to blockade of GABAergic signaling did not depend on the initial activity of the neuron. The correlation between the initial activity and strength of $GABA_A$ blockade for neurons within strongly or barely inhibited networks was 0.2022 ($p = 0.293$) and −0.2451 ($p = 0.238$), respectively. However, the single-neuron response was dependent on the behavior of the network it resided in. The proportions of neurons with respect to their response to GABAergic signaling blockade was quantified (**Figure 6F**). The distribution of single-neuron responses within the network seemed to determine the network-level response. Networks inhibited or stimulated by blockade of GABAergic signaling had larger proportions of neurons inhibited or stimulated by blockade of GABAergic signaling, respectively.

In summary, the blockade of endogenous GABAergic signaling did not disrupt the synchronous activity. However, the activity was decreased in networks with high and increased in networks with low initial activity. The response of the single neurons did not depend on their own initial activity but on the network in which they resided. Additionally, the distribution of single-neuron responses seemed to determine the network-level response to GABAergic signaling blockade.

Role of Gap Junction-Mediated Signaling in Synchronously Active Networks

The role of gap junction-mediated signaling in synchronous network activity (five networks, 1702 neurons, **Table 1**, column 4) was studied by blocking gap junctions with CBX. The responses to application of the gap junction blocker during combined calcium imaging and MEA recording were analyzed. A representative calcium imaging and MEA recording from one network is shown in **Figures 7A–C**. The gap junction blocker used is known to have a slowly appearing effect. Thus, only the last 3–4 min of application were used for analysis. The gap junction blocker visibly decreased (4 of 5) or gradually abolished (1 of 5) the occurrence of synchronous peaks of activity. This was seen in both synchronous calcium rises (example recording in **Figure 5A**) and MEA recordings (example recording in **Figure 5B**). There was no clear change in the dynamics (rise time, decay time, peak width) of the single network-level peaks to gap junction blockade; however, the interval between peaks increased visibly.

To compare the network responses between synchronous networks, calcium imaging and MEA recordings were quantified on the network level, and peaks of network-level activity were detected from both data sets. The global activity peak interval and peak prominence during calcium imaging at baseline and during gap junction blockade are shown for each synchronous network ($n = 5$) in **Figures 7D,E**, respectively. Quantification of network activity peaks confirmed that the interval between peaks increased significantly ($p < 0.01$) in all synchronous networks with gap junction blockade Furthermore, the gap junction blocker caused a slight but significant ($p < 0.05$) reduction in peak prominence in all synchronous networks.

The synchronous networks were further studied on the single-neuron level by quantifying the inter-peak interval distribution for each network. Representative single-neuron peak interval histograms containing all neurons ($n = 393$) in one network during baseline and gap junction blockage are shown in **Figure 7F**. The network-level values seemed to correspond to a subpopulation within the distribution both before and after gap junction signaling blockade. To study if there was correlation between the network and subpopulation response, the distributions of single-neuron responses were analyzed for each network. Inter-peak interval change histograms for all synchronously active networks with their respective network changes are shown in **Figure 7G**. The gap junction blocker increased the interval between peaks in a subpopulation of neurons. Of the synchronous networks, 80% (4 of 5) contained a subpopulation of neurons that showed a similar inter-peak interval change compared to the change in the whole network. The distinct histogram peaks corresponding to the whole-network response suggests that there exists a gap junction-dependent population that regulates the activity of the whole network. We could not further identify this subpopulation based on physiological responses.

In summary, blockade of gap junction-mediated signaling was found to affect the synchronously active networks by decreasing the size and occurrence of the synchronous peak of activity. Furthermore, a subpopulation of neurons was observed to have an inter-peak interval change that was similar to that in the network response.

DISCUSSION

In this article, we describe the synchronous neuronal activity on a single-neuron and network level in hPSC-derived neural networks. Furthermore, we address two mechanisms generally responsible for the development of synchronous activity. In hPSC-derived neural cultures, synchronous activity was detected after 3 weeks of culture with calcium imaging and MEA recordings. The emergence of synchronous activity was found to associate with the decrease in excitatory GABA responses. Furthermore, the synchronous network activity did not depend on endogenous GABAergic signaling. Also, neurons with GABA responses varying from excitatory to inhibitory were found to act synchronously to give rise to the network activity. Large-scale analysis revealed that the network response was dependent on the responses at the single-neuron level. A subpopulation of neurons connected by gap junctions had a modulatory role in the synchronous network activity. Together, these results suggest that the earliest form of synchronous neuronal activity depends on gap junctions and a decrease in GABA excitability but not on endogenous GABAergic signaling.

hPSC-derived neurons form network-level activity patterns through their synchronization. This synchronization is

dependent on decreased GABA excitability. Neurons with strong GABA induced depolarization did not participate in the synchronous activity. Furthermore, strong GABA depolarization of neurons was seen only in loosely synchronized and asynchronous networks. However, weakly GABA-depolarized neurons participated in the network activity in synchrony with strongly GABA-inhibited neurons. This observation is in line with previous studies where developing circuits in mouse PSC-derived networks (Illes et al., 2007, 2009, 2014; Risner-Janiczek et al., 2011) and rodent cortical cultures (Baltz et al., 2010) have been shown to also contain neurons inhibited by GABA. The very strong depolarizing GABA response might be due to the activation of higher affinity, extrasynaptic $GABA_A$ receptors. These receptors are activated by ambient GABA as opposed to synaptic GABA and cause a very strong depolarization (Sipilä et al., 2005). The disappearance of the strongly GABA-depolarized neurons could mark the replacement of the extrasynaptic receptors with synaptic, lower affinity GABA receptors along with the maturation of network connectivity. The weak GABA depolarization, on the other hand, could be related to the dual role (Ben-Ari et al., 1997; Khazipov et al., 1997; Leinekugel et al., 1997; Lamsa et al., 2000; Cherubini and Ben-Ari, 2011) of GABA during network oscillations. The dual role arises from reversal of the Cl- gradient during activity and manifests as initial depolarization followed by inhibition. Such a switch would be possible with a lower but still depolarizing intracellular Cl- concentration. On the network level, we observed that the proportion of GABA-depolarized neurons was smaller in synchronous networks than in loosely synchronous and asynchronous networks. This difference is in line with previous studies that showed a decrease in the excitatory actions of GABA during network maturation in cortical cultures (Baltz et al., 2010) and *in vivo* (Ge et al., 2006). Furthermore, the addition of GABA inhibited network activity or had no effect. This result contrasts with the observations of excitatory GABA-driven network-level activity in *ex vivo* rat preparations (Leinekugel et al., 1997). The combination of the large-scale single-cell data with network activity showed that in our culture system, the switch from a depolarizing (excitatory) to inhibitory GABA response seemed to be a switch in individual neurons rather than in the whole network.

Here, the occurrence of synchronous network events did not depend on the GABAergic connections; however, the GABAergic connections did regulate network activity levels during synchronous events. The synchronous events occurred despite the presence of a $GABA_A$ receptor antagonist. The use of Bic, however, does not allow the direct assessment of Bic insensitive $GABA_C$ receptors or extrasynaptic receptors. Our observation is in line with previous reports of regular GABA-independent correlation in networks with functional GABA receptors from *ex vivo* rat (Garaschuk et al., 2000; Allene et al., 2008), *ex vivo* mouse cortex (Dupont et al., 2006; McCabe et al., 2006), *ex vivo* chick retina (Catsicas et al., 1998), embryonic rat cortical culture (Opitz et al., 2002; Baltz et al., 2010), and hPSC cultures (Kirwan et al., 2015). In contrast, GABAergic signaling has been shown to be required for correlated firing in *ex vivo* rat (Schwartz et al., 1998; Allene et al., 2008) and mouse (Aguiló et al., 1999) as well as embryonic rat cortical culture (Voigt et al., 2001). We observed that while the occurrence was not affected, the level of activity during the synchronous network events was decreased (similar to *ex vivo* mouse, Hunt et al., 2006) or increased in networks with high or low initial activity and strong or no response to externally applied GABA, respectively. The low initial activity, no response to externally applied GABA and stimulation by $GABA_A$ receptor blockade could all be caused by tonic inhibition of the continuous activation of extrasynaptic GABA receptors (Glykys and Mody, 2007; Holter et al., 2007). On the other hand, the combination of high baseline activity, a strong inhibitory response to externally applied GABA and inhibition by $GABA_A$ receptor blockade could in turn arise from activity-dependent depression via the GABA receptor (Chub and O'Donovan, 2001). Thus, the networks that respond differently to applied GABAergic modulators seem to contain differently acting GABAergic circuits that both regulate firing during network events. A shift in the behavior of developing GABAergic circuitry has previously been observed in *ex vivo* mouse cortex, where a $GABA_A$ receptor blocker was initially inhibitory to network activity but became stimulatory during network maturation (Allene et al., 2008; Conhaim et al., 2011).

Gap junctions modulate the periodicity of the synchronous network activity by modulating the activity of a subpopulation of neurons. The gap junction blocker used (CBX) has been reported to have a broad range of nonspecific effects (Tovar et al., 2009). Here, the nonspecific effects were avoided by using a concentration <50 μM and observing the effect of CBX after 5 min of application. The gap junction blocker decreased the occurrence of synchronous events by increasing the interval between events. The change in the interval of the network events matched the change in the interval of the activity of a group of single neurons. Our results are in agreement with previous results obtained *in vivo* from the developing rat cortex (Yang et al., 2009), *ex vivo* fetal human tissue (Moore et al., 2014), and rat cortex (Yuste et al., 1995; Peinado, 2001; Molchanova et al., 2016), as well as *ex vivo* adult rat (Lamsa and Taira, 2003) and chick retina (Catsicas et al., 1998) where gap junction blockers decreased the occurrence of synchronous events. Thus, the gap junction-based mechanism for modulating the occurrence of synchronous network events can be argued to be retained in several biological models of developing neural networks. In contrast, the results obtained in mouse cortex *ex vivo* show that gap junction blockade completely blocks synchronous activity (Dupont et al., 2006; Hunt et al., 2006; Sun and Luhmann, 2007). Thus, this difference may suggest that the developing neural networks in mice may differ from those in rats, chicks and, ultimately, humans in this aspect.

Developing neural networks are affected by their constituent neural cells, and the formation of network functionality has been suggested to be impaired in cultured neural networks that lack astrocytes (Kuijlaars et al., 2016). The neural networks studied here have been shown to be primarily composed of neurons with a minor astrocyte population (Lappalainen et al., 2010). In this study, network activity was measured via functionality of its neuronal component, recorded by calcium imaging and

MEAs. Similar to our previous studies (Heikkilä et al., 2009), synchronous activity was observed in MEA recordings from the hPSC-derived neural networks. This synchronous activity is a hallmark of developing neural networks and is a shared feature between *in vitro* (van Pelt et al., 2005; Illes et al., 2014) and *in vivo* (Garaschuk et al., 2000; Khazipov and Luhmann, 2006; Moore et al., 2011) networks, suggesting that developing neural networks can be accurately modeled with cell cultures. A difference between the developing networks *in vitro* and *in vivo* is the lack of the laminar structure in the former. However, a special network structure (i.e., cortical lamination) has previously been shown to be unnecessary for the formation of functional networks with rhythmic synchronized activity *in vivo* (Simmons and Pearlman, 1982), or *ex vivo* (Opitz et al., 2002). Thus, the observations from this study add to the growing body of evidence that the development of early network functionality in neuronal networks is not dependent on orderly structure. In conclusion, the described culture system and the observed network phenomena are a useful tool for studying the development of synchronous activity in developing neural circuits of human origin and the mechanisms behind the emergence of said activity. Studies performed with networks containing neurons starting from their most immature stage are important as they capture the mechanisms and spontaneous activity specific to a restricted period of development, not emerging in the adult brain (Blankenship and Feller, 2010; Momose-Sato and Sato, 2013). Furthermore, transient cell populations, some of which differ between primates and rodents (Hill and Walsh, 2005; Rakic, 2009), emerge and disappear during early network formation, laying the groundwork for further network development (Luskin and Shatz, 1985). Such populations and their contribution to the network activity development can only be observed in human-derived immature neural cell cultures.

Summary

In conclusion, we showed that the single-neuron excitatory response to GABA decreases as neurons start to participate in synchronous network activity. As this change occurs, these neurons give up their individual activity pattern and jointly give rise to the network activity pattern. In hPSC-derived networks, this activity pattern is at least partially modulated by connections between neurons. Furthermore, we showed that gap junction-mediated connections modulate the interval between events, allowing network events to occur more frequently. In addition, GABAergic connections are not necessary for the occurrence of network events but act as limiters of activity during synchronous events. Together this control over the occurrence and level of activity during synchronous events allows the networks to control the activity of its single-neuron components. The control over activity in turn allows the immature neural networks to form an internally controlled activity pattern.

AUTHOR CONTRIBUTIONS

ME-LM designed the overall study, performed the experiments, designed, programmed and tested the analysis used, interpreted the data for the work, as well as wrote the manuscript. LY-O and SN supervised the study and gave valuable comments on the manuscript. All authors contributed to manuscript revision, read and approved the submitted version.

FUNDING

This work was funded by Academy of Finland grant to LY-O (#286990), Finnish Funding Agency for Technology and Innovation (TEKES), Tampere University Doctoral Programme of Medicine and Life Science and Oskar Öflunds Stiftelse.

ACKNOWLEDGMENTS

The authors acknowledge Tampere Facility of Electrophysiological Measurements for their service and Hanna Mäkelä and Eija Hannuksela for technical assistance with cell maintenance. The University statistician Heini Huhtala is acknowledged for her assistance in the statistical analysis.

SUPPLEMENTARY MATERIAL

The Supplementary Material for this article can be found online at: https://www.frontiersin.org/articles/10.3389/fncel.2018.00056/full#supplementary-material

REFERENCES

Aguiló, A., Schwartz, T. H., Kumar, V. S., Peterlin, Z. A., Tsiola, A., Soriano, E., et al. (1999). Involvement of cajal-retzius neurons in spontaneous correlated activity of embryonic and postnatal layer 1 from wild-type and reeler mice. *J. Neurosci.* 19, 10856–10868.

Allene, C., Cattani, A., Ackman, J. B., Bonifazi, P., Aniksztejn, L., Ben-Ari, Y., et al. (2008). Sequential generation of two distinct synapse-driven network patterns in developing neocortex. *J. Neurosci.* 28, 12851–12863. doi: 10.1523/JNEUROSCI.3733-08.2008

Baltz, T., de Lima, A. D., and Voigt, T. (2010). Contribution of GABAergic interneurons to the development of spontaneous activity patterns in cultured neocortical networks. *Front. Cell. Neurosci.* 4:15. doi: 10.3389/fncel.2010.00015

Ben-Ari, Y. (2002). Excitatory actions of GABA during development: the nature of the nurture. *Nat. Rev. Neurosci.* 3, 728–739. doi: 10.1038/nrn920

Ben-Ari, Y., Cherubini, E., Corradetti, R., and Gaiarsa, J. L. (1989). Giant synaptic potentials in immature rat CA3 hippocampal neurones. *J. Physiol.* 416, 303–325. doi: 10.1113/jphysiol.1989.sp017762

Ben-Ari, Y., Khazipov, R., Leinekugel, X., Caillard, O., and Gaiarsa, J. L. (1997). $GABA_A$, NMDA and AMPA receptors: a developmentally regulated 'ménage à trois'. *Trends Neurosci.* 20, 523–529. doi: 10.1016/s0166-2236(97)01147-8

Blankenship, A. G., and Feller, M. B. (2010). Mechanisms underlying spontaneous patterned activity in developing neural circuits. *Nat. Rev. Neurosci.* 11, 18–29. doi: 10.1038/nrn2759

Carmignoto, G., Pasti, L., and Pozzan, T. (1998). On the role of voltage-dependent calcium channels in calcium signaling of astrocytes *in situ*. *J. Neurosci.* 18, 4637–4645.

Catsicas, M., Bonness, V., Becker, D., and Mobbs, P. (1998). Spontaneous Ca^{2+} transients and their transmission in the developing chick retina. *Curr. Biol.* 8, 283–288. doi: 10.1016/s0960-9822(98)70110-1

Cherubini, E., and Ben-Ari, Y. (2011). The immature brain needs GABA to be excited and hyper-excited. *J. Physiol.* 589, 2655–2656. doi: 10.1113/jphysiol.2011.208884

Chub, N., and O'Donovan, M. J. (2001). Post-episode depression of GABAergic transmission in spinal neurons of the chick embryo. *J. Neurophysiol.* 85, 2166–2176. doi: 10.1152/jn.2001.85.5.2166

Conhaim, J., Easton, C. R., Becker, M. I., Barahimi, M., Cedarbaum, E. R., Moore, J. G., et al. (2011). Developmental changes in propagation patterns and transmitter dependence of waves of spontaneous activity in the mouse cerebral cortex. *J. Physiol.* 589, 2529–2541. doi: 10.1113/jphysiol.2010.202382

Corlew, R., Bosma, M. M., and Moody, W. J. (2004). Spontaneous, synchronous electrical activity in neonatal mouse cortical neurones. *J. Physiol.* 560, 377–390. doi: 10.1113/jphysiol.2004.071621

Dupont, E., Hanganu, I. L., Kilb, W., Hirsch, S., and Luhmann, H. J. (2006). Rapid developmental switch in the mechanisms driving early cortical columnar networks. *Nature* 439, 79–83. doi: 10.1038/nature04264

Feller, M. B. (1999). Spontaneous correlated activity in developing neural circuits. *Neuron* 22, 653–656. doi: 10.1016/s0896-6273(00)80724-2

Finlay, B. L., and Darlington, R. (1995). Linked regularities in the development and evolution of mammalian brains. *Science* 268, 1578–1584. doi: 10.1126/science.7777856

Garaschuk, O., Hanse, E., and Konnerth, A. (1998). Developmental profile and synaptic origin of early network oscillations in the CA1 region of rat neonatal hippocampus. *J. Physiol.* 507, 219–236. doi: 10.1111/j.1469-7793.1998.219bu.x

Garaschuk, O., Linn, J., Eilers, J., and Konnerth, A. (2000). Large-scale oscillatory calcium waves in the immature cortex. *Nat. Neurosci.* 3, 452–459. doi: 10.1038/74823

Ge, S., Goh, E. L. K., Sailor, K. A., Kitabatake, Y., Ming, G. L., and Song, H. (2006). GABA regulates synaptic integration of newly generated neurons in the adult brain. *Nature* 439, 589–593. doi: 10.1038/nature04404

Glykys, J., and Mody, I. (2007). Activation of $GABA_A$ receptors: views from outside the synaptic cleft. *Neuron* 56, 763–770. doi: 10.1016/j.neuron.2007.11.002

Haston, K. M., and Finkbeiner, S. (2016). Clinical trials in a dish: the potential of pluripotent stem cells to develop therapies for neurodegenerative diseases. *Annu. Rev. Pharmacol. Toxicol.* 56, 489–510. doi: 10.1146/annurev-pharmtox-010715-103548

Heikkilä, T. J., Ylä-Outinen, L., Tanskanen, J. M. A., Lappalainen, R. S., Skottman, H., Suuronen, R., et al. (2009). Human embryonic stem cell-derived neuronal cells form spontaneously active neuronal networks *in vitro*. *Exp. Neurol.* 218, 109–116. doi: 10.1016/j.expneurol.2009.04.011

Hill, R. S., and Walsh, C. A. (2005). Molecular insights into human brain evolution. *Nature* 437, 64–67. doi: 10.1038/nature04103

Holter, N. I., Zuber, N., Bruehl, C., and Draguhn, A. (2007). Functional maturation of developing interneurons in the molecular layer of mouse dentate gyrus. *Brain Res.* 1186, 56–64. doi: 10.1016/j.brainres.2007.09.089

Hunt, P. N., Gust, J., McCabe, A. K., and Bosma, M. M. (2006). Primary role of the serotonergic midline system in synchronized spontaneous activity during development of the embryonic mouse hindbrain. *J. Neurobiol.* 66, 1239–1252. doi: 10.1002/neu.20259

Illes, S., Fleischer, W., Siebler, M., Hartung, H., and Dihné, M. (2007). Development and pharmacological modulation of embryonic stem cell-derived neuronal network activity. *Exp. Neurol.* 207, 171–176. doi: 10.1016/j.expneurol.2007.05.020

Illes, S., Jakab, M., Beyer, F., Gelfert, R., Couillard-Despres, S., Schnitzler, A., et al. (2014). Intrinsically active and pacemaker neurons in pluripotent stem cell-derived neuronal populations. *Stem Cell Reports* 2, 323–336. doi: 10.1016/j.stemcr.2014.01.006

Illes, S., Theiss, S., Hartung, H.-P., Siebler, M., and Dihné, M. (2009). Niche-dependent development of functional neuronal networks from embryonic stem cell-derived neural populations. *BMC Neurosci.* 10:93. doi: 10.1186/1471-2202-10-93

Kerschensteiner, D. (2014). Spontaneous network activity and synaptic development. *Neuroscientist* 20, 272–290. doi: 10.1177/1073858413510044

Khalilov, I., Esclapez, M., Medina, I., Aggoun, D., Lamsa, K., Leinekugel, X., et al. (1997). A novel *in vitro* preparation: the intact hippocampal formation. *Neuron* 19, 743–749. doi: 10.1016/s0896-6273(00)80956-3

Khazipov, R., Leinekugel, X., Khalilov, I., Gaiarsa, J. L., and Ben-Ari, Y. (1997). Synchronization of GABAergic interneuronal network in CA3 subfield of neonatal rat hippocampal slices. *J. Physiol.* 498, 763–772. doi: 10.1113/jphysiol.1997.sp021900

Khazipov, R., and Luhmann, H. J. (2006). Early patterns of electrical activity in the developing cerebral cortex of humans and rodents. *Trends Neurosci.* 29, 414–418. doi: 10.1016/j.tins.2006.05.007

Kirwan, P., Turner-Bridger, B., Peter, M., Momoh, A., Arambepola, D., Robinson, H. P. C., et al. (2015). Development and function of human cerebral cortex neural networks from pluripotent stem cells *in vitro*. *Development* 142, 3178–3187. doi: 10.1242/dev.123851

Kuijlaars, J., Oyelami, T., Diels, A., Rohrbacher, J., Versweyveld, S., Meneghello, G., et al. (2016). Sustained synchronized neuronal network activity in a human astrocyte co-culture system. *Sci. Rep.* 6:36529. doi: 10.1038/srep36529

Lamsa, K. P., Palva, J. M., Ruusuvuori, E., Kaila, K., and Taira, T. (2000). Synaptic $GABA_A$ activation inhibits AMPA-kainate receptor-mediated bursting in the newborn (*P0-P2*) rat hippocampus. *J. Neurophysiol.* 83, 359–366. doi: 10.1152/jn.2000.83.1.359

Lamsa, K., and Taira, T. (2003). Use-dependent shift from inhibitory to excitatory $GABA_A$ receptor action in SP-O interneurons in the rat hippocampal CA3 area. *J. Neurophysiol.* 90, 1983–1995. doi: 10.1152/jn.00060.2003

Landmesser, L. T., and Szente, M. (1986). Activation patterns of embryonic chick hind-limb muscles following blockade of activity and motoneurone cell death. *J. Physiol.* 380, 157–174. doi: 10.1113/jphysiol.1986.sp016278

Lappalainen, R. S., Salomäki, M., Ylä-Outinen, L., Heikkilä, T. J., Hyttinen, J. A. K., Pihlajamäki, H., et al. (2010). Similarly derived and cultured hESC lines show variation in their developmental potential towards neuronal cells in long-term culture. *Regen. Med.* 5, 749–762. doi: 10.2217/rme.10.58

Leinekugel, X., Khalilov, I., Ben-Ari, Y., and Khazipov, R. (1998). Giant depolarizing potentials: the septal pole of the hippocampus paces the activity of the developing intact septohippocampal complex *in vitro*. *J. Neurosci.* 18, 6349–6357.

Leinekugel, X., Medina, I., Khalilov, I., Ben-Ari, Y., and Khazipov, R. (1997). Ca^{2+} oscillations mediated by the synergistic excitatory actions of $GABA_A$ and NMDA receptors in the neonatal hippocampus. *Neuron* 18, 243–255. doi: 10.1016/s0896-6273(00)80265-2

Luhmann, H. J., Sinning, A., Yang, J.-W., Reyes-Puerta, V., Stüttgen, M. C., Kirischuk, S., et al. (2016). Spontaneous neuronal activity in developing neocortical networks: from single cells to large-scale interactions. *Front. Neural Circuits* 10:40. doi: 10.3389/fncir.2016.00040

Luskin, M. B., and Shatz, C. J. (1985). Studies of the earliest generated cells of the cat's visual cortex: cogeneration of subplate and marginal zones. *J. Neurosci.* 5, 1062–1075.

Maravall, M., Mainen, Z. F., Sabatini, B. L., and Svoboda, K. (2000). Estimating intracellular calcium concentrations and buffering without wavelength ratioing. *Biophys. J.* 78, 2655–2667. doi: 10.1016/s0006-3495(00)76809-3

McCabe, A. K., Chisholm, S. L., Picken-Bahrey, H. L., and Moody, W. J. (2006). The self-regulating nature of spontaneous synchronized activity in developing mouse cortical neurones. *J. Physiol.* 577, 155–167. doi: 10.1113/jphysiol.2006.117523

Menendez De La Prida, L., Bolea, S., and Sanchez-Andres, J. V. (1998). Origin of the synchronized network activity in the rabbit developing hippocampus. *Eur. J. Neurosci.* 10, 899–906. doi: 10.1046/j.1460-9568.1998.00097.x

Meyer, F. (1994). Topographic distance and watershed lines. *Signal Process.* 38, 113–125. doi: 10.1016/0165-1684(94)90060-4

Molchanova, S. M., Huupponen, J., Lauri, S. E., and Taira, T. (2016). Gap junctions between CA3 pyramidal cells contribute to network synchronization in neonatal hippocampus. *Neuropharmacology* 107, 9–17. doi: 10.1016/j.neuropharm.2016.02.033

Momose-Sato, Y., and Sato, K. (2013). Large-scale synchronized activity in the embryonic brainstem and spinal cord. *Front. Cell. Neurosci.* 7:36. doi: 10.3389/fncel.2013.00036

Moore, A. R., Zhou, W.-L., Jakovcevski, I., Zecevic, N., and Antic, S. D. (2011). Spontaneous electrical activity in the human fetal cortex *in vitro*. *J. Neurosci.* 31, 2391–2398. doi: 10.1523/JNEUROSCI.3886-10.2011

Moore, A. R., Zhou, W.-L., Sirois, C. L., Belinsky, G. S., Zecevic, N., and Antic, S. D. (2014). Connexin hemichannels contribute to spontaneous electrical activity

in the human fetal cortex. *Proc. Natl. Acad. Sci. U S A* 111, E3919–E3928. doi: 10.1073/pnas.1405253111

Munkres, J. (1957). Algorithms for the assignment and transportation problems. *J. Soc. Ind. Appl. Math.* 5, 32–38. doi: 10.1137/0105003

O'Donovan, M. J. (1999). The origin of spontaneous activity in developing networks of the vertebrate nervous system. *Curr. Opin. Neurobiol.* 9, 94–104. doi: 10.1016/s0959-4388(99)80012-9

Opitz, T., De Lima, A. D., and Voigt, T. (2002). Spontaneous development of synchronous oscillatory activity during maturation of cortical networks *in vitro*. *J. Neurophysiol.* 88, 2196–2206. doi: 10.1152/jn.00316.2002

Otsu, N. (1979). A threshold selection method from gray-level histograms. *IEEE Trans. Syst. Man Cybern.* 9, 62–66. doi: 10.1109/tsmc.1979.4310076

Peinado, A. (2001). Immature neocortical neurons exist as extensive syncitial networks linked by dendrodendritic electrical connections. *J. Neurophysiol.* 85, 620–629. doi: 10.1152/jn.2001.85.2.620

Quiroga, R. Q., Nadasdy, Z., and Ben-Shaul, Y. (2004). Unsupervised spike detection and sorting with wavelets and superparamagnetic clustering. *Neural Comput.* 16, 1661–1687. doi: 10.1162/089976604774201631

Rakic, P. (2009). Evolution of the neocortex: perspective from developmental biology. *Nat. Rev. Neurosci.* 10, 724–735. doi: 10.1038/nrn2719

Risner-Janiczek, J. R., Ungless, M. A., and Li, M. (2011). Electrophysiological properties of embryonic stem cell-derived neurons. *PLoS One* 6:e24169. doi: 10.1371/journal.pone.0024169

Schwartz, T. H., Rabinowitz, D., Unni, V., Kumar, V. S., Smetters, D. K., Tsiola, A., et al. (1998). Networks of coactive neurons in developing layer 1. *Neuron* 20, 541–552. doi: 10.1016/s0896-6273(00)80993-9

Shi, Y., Kirwan, P., Smith, J., Robinson, H. P., and Livesey, F. J. (2012). Human cerebral cortex development from pluripotent stem cells to functional excitatory synapses. *Nat. Neurosci.* 15, 477–486. doi: 10.1038/nn.3041

Simmons, P. A., and Pearlman, A. L. (1982). Retinotopic organization of the striate cortex (area 17) in the reeler mutant mouse. *Brain Res.* 256, 124–126. doi: 10.1016/0165-3806(82)90105-5

Sipilä, S. T., Huttu, K., Soltesz, I., Voipio, J., and Kaila, K. (2005). Depolarizing GABA acts on intrinsically bursting pyramidal neurons to drive giant depolarizing potentials in the immature hippocampus. *J. Neurosci.* 25, 5280–5289. doi: 10.1523/JNEUROSCI.0378-05.2005

Skottman, H. (2010). Derivation and characterization of three new human embryonic stem cell lines in Finland. *In Vitro Cell. Deve. Biol. Anim.* 46, 206–209. doi: 10.1007/s11626-010-9286-2

Sun, J. J., Kilb, W., and Luhmann, H. J. (2010). Self-organization of repetitive spike patterns in developing neuronal networks *in vitro*. *Eur. J. Neurosci.* 32, 1289–1299. doi: 10.1111/j.1460-9568.2010.07383.x

Sun, J.-J., and Luhmann, H. J. (2007). Spatio-temporal dynamics of oscillatory network activity in the neonatal mouse cerebral cortex. *Eur. J. Neurosci.* 26, 1995–2004. doi: 10.1111/j.1460-9568.2007.05819.x

Toivonen, S., Ojala, M., Hyysalo, A., Ilmarinen, T., Rajala, K., Pekkanen-Mattila, M., et al. (2013). Comparative analysis of targeted differentiation of human induced pluripotent stem cells (hiPSCs) and human embryonic stem cells reveals variability associated with incomplete transgene silencing in retrovirally derived hiPSC lines. *Stem Cells Transl. Med.* 2, 83–93. doi: 10.5966/sctm.2012-0047

Tovar, K. R., Maher, B. J., and Westbrook, G. L. (2009). Direct actions of carbenoxolone on synaptic transmission and neuronal membrane properties. *J. Neurophysiol.* 102, 974–978. doi: 10.1152/jn.00060.2009

van Pelt, J., Vajda, I., Wolters, P. S., Corner, M. A., and Ramakers, G. J. A. (2005). Dynamics and plasticity in developing neuronal networks *in vitro*. *Prog. Brain Res.* 147, 171–188. doi: 10.1016/S0079-6123(04)47013-7

Voigt, T., Opitz, T., and de Lima, A. D. (2001). Synchronous oscillatory activity in immature cortical network is driven by GABAergic preplate neurons. *J. Neurosci.* 21, 8895–8905.

Yang, J.-W., Hanganu-Opatz, I. L., Sun, J.-J., and Luhmann, H. J. (2009). Three patterns of oscillatory activity differentially synchronize developing neocortical networks *in vivo*. *J. Neurosci.* 29, 9011–9025. doi: 10.1523/JNEUROSCI.5646-08.2009

Yuste, R., Nelson, D. A., Rubin, W. W., and Katz, L. C. (1995). Neuronal domains in developing neocortex: mechanisms of coactivation. *Neuron* 14, 7–17. doi: 10.1016/0896-6273(95)90236-8

Conflict of Interest Statement: The authors declare that the research was conducted in the absence of any commercial or financial relationships that could be construed as a potential conflict of interest.

Supplementary Material

GABA and gap junctions in the development of synchronized activity in human pluripotent stem cell-derived neural networks

Meeri Eeva-Liisa Mäkinen*, Laura Ylä-Outinen, Susanna Narkilahti

*** Correspondence:** Corresponding Author: meeri.makinen@uta.fi

1 Supplementary Figures and Tables

1.1 Supplementary Figures

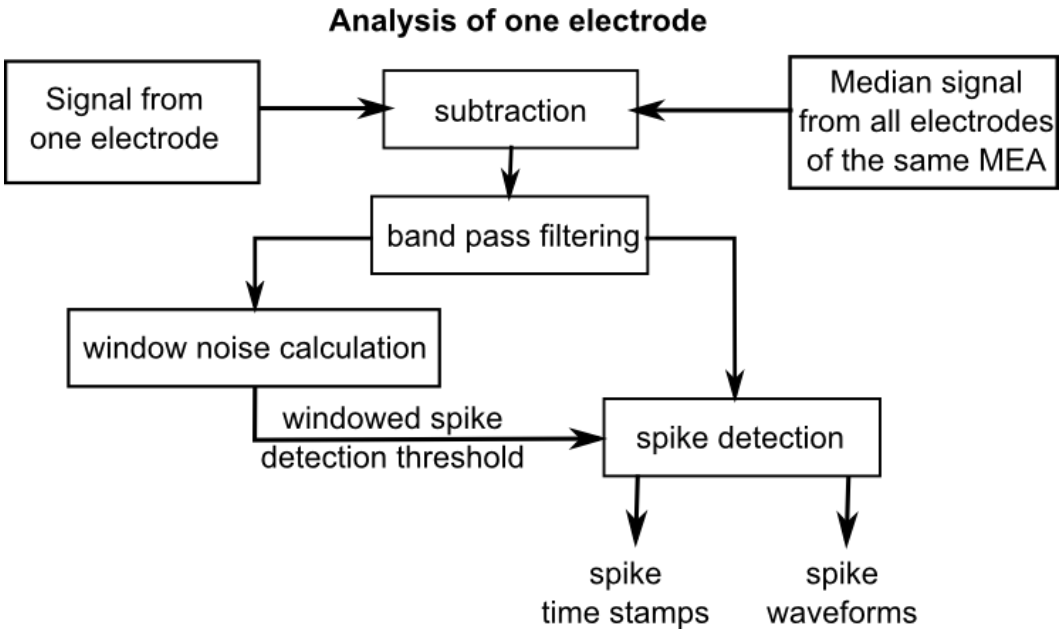

Supplementary Figure 1. The analysis process for one electrode during the MEA analysis. The median signal calculated across all electrodes is subtracted from the electrode signal. This subtraction is followed by filtering. The filtered signal is divided into windows, and the noise of each window is used to set the spike detection threshold for that window. The spike detection threshold is then used to detect spikes in the filtered signal. The output results are spike timestamps and cut-out waveforms.

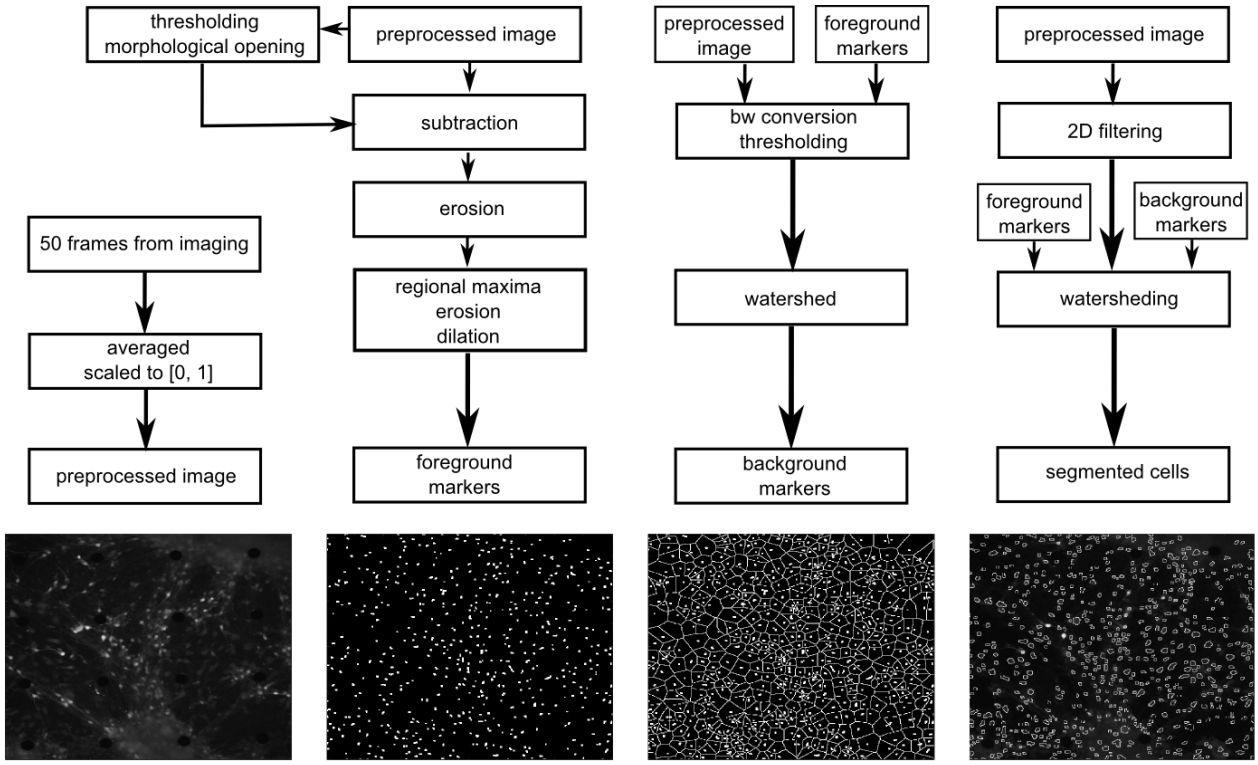

Supplementary Figure 2. The analysis process for a set of 50 subsequent images from the calcium imaging analysis. The first column depicts the preprocessing of the 50 frames into an averaged image. The second column depicts the analysis process for the generation of foreground markers from the preprocessed image. The third column depicts the analysis process for generating the background markers. The fourth column depicts the final segmentation analysis process from the preprocessed image, foreground and background markers. The bottom row contains images from different parts of the analysis of the same set of images. From left to right: preprocessed image, foreground markers, background markers and the final segmentation result.

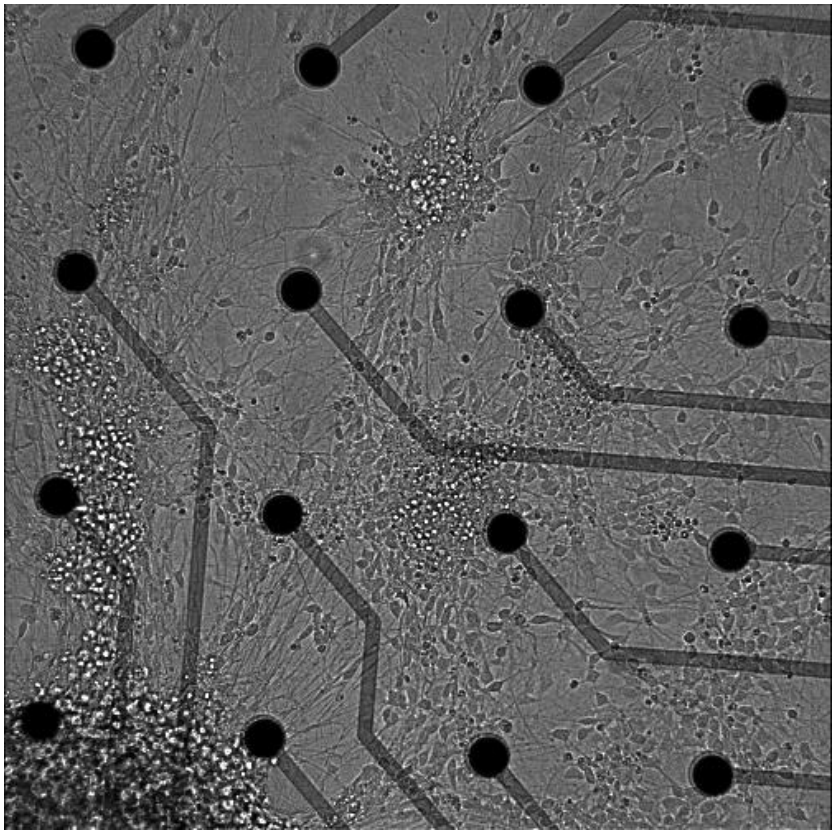

Supplementary Figure 3. Two-week-old hPSC-derived neural culture on top of a thin MEA (MEA dishes with 180 µm thick recording area) a few minutes prior to calcium imaging. The distance between two electrodes is 200 µm.

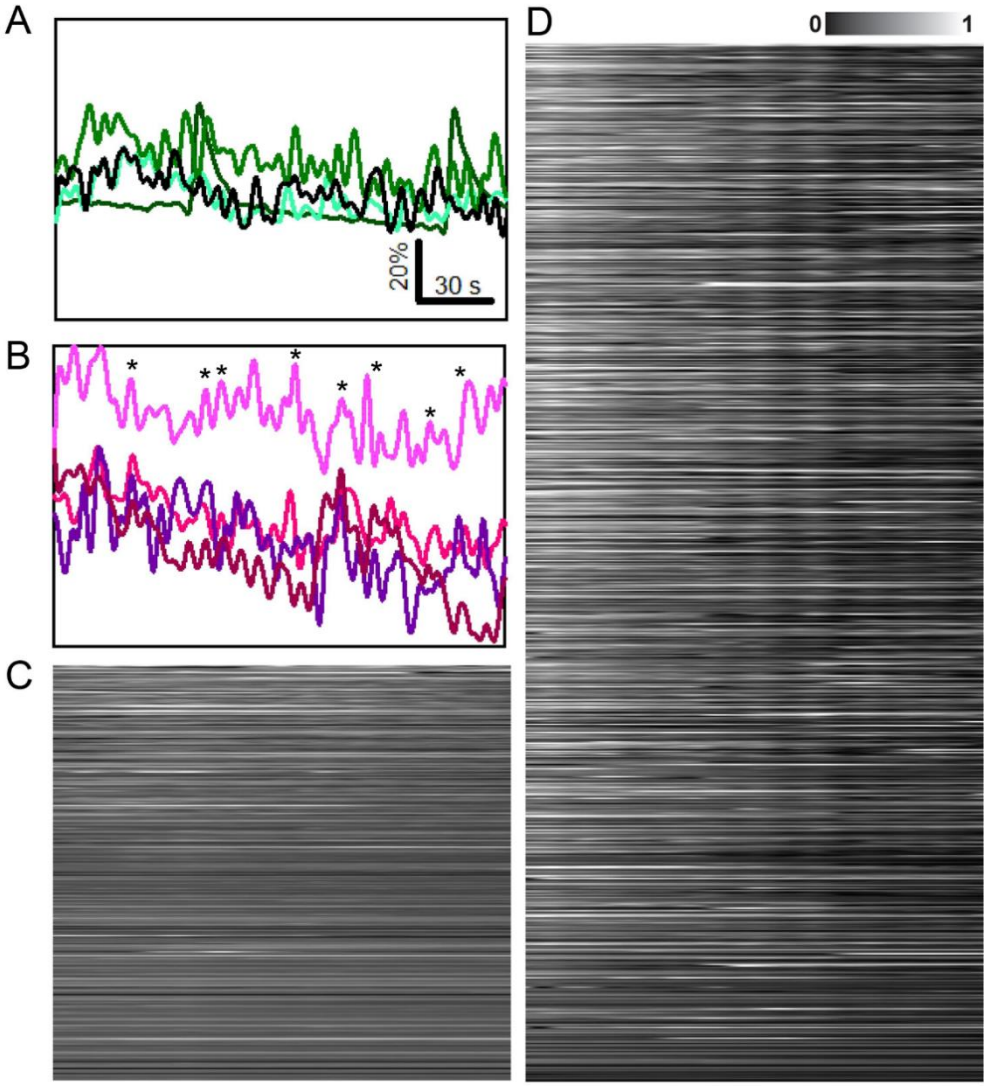

Supplementary Figure 4. (A) Representative single-neuron intracellular calcium level traces from 4 asynchronously active neurons. Neurons are selected from the recording shown in (C). Traces show the normalized fluorescent calcium dye intensity (y-axis) over time (x-axis). **(B)** Representative single-neuron intracellular calcium level traces from 4 loosely synchronously active neurons. Neurons are selected from the recording shown in (D). Traces show the normalized fluorescent calcium dye intensity (y-axis) over time (x-axis). Scale same as in (A). The asterisks mark the moments of synchronous activity. **(C)** Normalized (scalebar) raster plot of spontaneous intracellular Ca2+ fluctuations from all neurons (n = 403) in the field of view from one asynchronous network. Each row of pixels (y-axis) contains the normalized intensity changes during a 5-min (x-axis) recording from one neuron. **(D)** Normalized (scalebar) raster plot of spontaneous intracellular Ca2+ fluctuations from all neurons (n = 774) in the field of view from one loosely synchronous network. Each row of pixels (y-axis) contains the normalized intensity changes during a 5-min (x-axis) recording from one neuron.